1995

Seismic performance of concrete filled steel tube to wide flange beam moment connections with diaphragms

Garry W. Vermaas
Lehigh University

Vermaas,
Garry W.

Seismic Performance of Concrete Filled Steel Tube to Wide Flange Beam Moment...

January 14, 1995

Seismic Performance of Concrete Filled Steel Tube to Wide Flange Beam Moment Connections With Diaphragms

by

Garry W. Vermaas

A Thesis

Presented to the Graduate and Research Committee

of Lehigh University

in Candidacy for the Degree of

Master of Science

in

Civil Engineering

Lehigh University

December 6, 1995

This thesis is accepted and approved in partial fulfillment of the requirements for the Master of Science.

December 6, 1995
Date

Thesis Advisor

Chairperson of Department

Table of Contents

List of Tables

List of Tables (cont.)

List of Tables (cont.)

List of Figures

List of Figures

List of Figures

List of Figures

List of Figures

List of Figures

List of Figures

ABSTRACT

An experimental study was undertaken to investigate the cyclic stiffness, strength, and ductility of concrete filled steel tube-to-wide flange beam moment connections with diaphragms subjected to simulated seismic loading conditions. Two full scale specimens were designed, fabricated, and tested, each consisting of two wide flange beams attached to a structural steel tube column filled with unreinforced concrete (CFT). One specimen had a pair of interior diaphragms, while the other utilized exterior diaphragms, constructed of structural tees to transfer the beam forces into the connection. Both specimens were designed to have an elastic response occur primarily in the beams. The contribution to inter-story drift by the panel zone, the beams, and the column were studied by evaluating measurements associated with each taken during testing. The results of the test program indicated that the specimens possess exceptional ductility and strength under cyclic loading. Test results also concluded that the interior diaphragm within the panel zone of the CFT may be replaced by an exterior diaphragm for seismic resistant design.

The beams in both specimens were found to develop maximum moments in the plastic hinge zones that ranged from 1.16 to 1.28 times the plastic flexural capacity M_p. The beams accounted for a majority of the interstory drift, where the maximum plastic beam rotation was 0.0038 and 0.0023 rad in the two specimens. The rotation capacity and ductility of the beams was found to be

affected by strain concentrations that developed at the location of transition between the beam and connector elements (e.g. diaphragms). The elastic stiffness (EI) of the column appears to be well represented by the transformed uncracked section up to an inter-story drift of 3% to 6% of the story height.

This report is the Master of Science Thesis of Garry W. Vermaas, under the supervision of Professor James Ricles while at Lehigh University. Assessment of the results and writing of this report was completed at the Center for Advanced Technology for Large Structural Systems (ATLSS) located at Lehigh University. Subsequent related research on composite connections is continuing at ATLSS under Dr. Ricles.

Chapter 1
Introduction

1.1 Conventional Use of Structural Materials

In structural engineering, the two most traditionally used materials for large buildings are structural steel and reinforced concrete. Steel has often been used for the design of tall buildings since its important role in the construction of the skyscraper in the early 1900's. The advantage of structural steel is that it is a light material which can be erected relatively easily in any type of weather conditions. This characteristic also reduces the weight of the building in order to maintain economical foundations. Steel columns are also able to carry heavy loads due to the strength characteristics of steel. Currently, studies are ongoing related to in steel alloying which will lead to improvements in both a steel's strength and durability.

Reinforced concrete has also played an important role in high rise construction, due to its ability to carry large shear wall or column loads at lower costs. Extremely large column loads in high rise buildings can be supported by reasonably sized reinforced concrete columns with a concrete compressive strength between 7000 psi and 14,000 psi. Recent developments in reinforced concrete have allowed it to become a much more viable building material. New concrete admixtures, such as plastizers, increase the workability of the concrete

with no degradation of its strength. This workability of the concrete eases the placement in congested heavily reinforced columns. New developments in concrete mixing and batching allow concrete to be placed year round at reasonable costs. New types of lightweight aggregates offer a lightweight concrete which provides adequate strength, lessens the dead weight of the structure, and lowers the amount of cracking in elevated floor slabs. New developments in forming systems have increased the placement of concrete to a rate which is comparable to that of steel.

A study was performed to analyze the relative cost effectiveness of steel and concrete columns for tall buildings in which the necessary strength and stiffness was provided [Griffis, 1987]. It was found that reinforced concrete columns are approximately 11 times more cost affective in resisting axial load strength wise, than structural steel columns. Reinforced columns are also approximately 8.5 times more cost effective from an axial stiffness standpoint, in providing resistance to axial deformation, than structural steel columns. On the contrary structural steel columns, for a given axial load, are only 25% as large in area and weigh only 80% as much as concrete columns. It was also found, when comparing the two different structural materials in damping effectiveness, that well-confined concrete structures and welded structural steel systems at service loads have approximately 2% to 3% viscous damping. Structural steel systems at yielding stress levels develop 5% to 7% viscous damping, while

reinforced concrete structures, which have considerable cracking from ultimate loads, develop 7% to 10% viscous damping. Reinforced concrete structures, because of their stiffness, will develop 30% less acceleration under wind loading than will structural steel.

1.2 Composite Construction

Composite construction is a combination of structural steel and reinforced concrete design. This particular design concept has developed composite structural members which are commonly used in today's high rise construction. These composite elements are designed to provide adequate strength, stiffness, and ductility, as well as, resist high bending moments and large axial loads. Composite construction was used in early high rise design, where the structural steel members were encased with concrete for reasons of fire and corrosion protection. This protective reinforced concrete coating added strength, stiffness and ductility to the structural steel members, and as a result, engineers in the 1960's attempted to develop design criteria in order to take advantage of these material attributes. From that point on designers were using the distinct advantages of each separate building material, together in composite construction, in order to design more economical structural members. In addition, the advancement of concrete pumping systems, which could pump

concrete vertically over 1000 feet, made composite construction a viable option in high rise design.

There are three basic forms of composite construction in composite column design, namely ; (1) a structural circular or (2) square steel tube filled with reinforced or unreinforced concrete (CFT); and (3) the more commonly used (iii.) structural steel shape encased in reinforced concrete (SRC). these types of columns are illustrated in Figure 1.1. The construction method for CFT columns used in Japan first erects the box column frame of the whole or partitioned structure, and second, fills the columns with concrete. Typically interior diaphragm plates, with centered holes to enable concrete flow, are used at the column to beam connection. These plates are usually connected to three sides of the square box column using full penetration welds. After the box column is closed, the weld between the diaphragm plate and the fourth side of the box is made using the electroslag welding process. Connections of this type require a considerable amount of fabrication time in the shop and tend to be quite expensive.

The construction method for SRC composite construction has a different approach. The erection of the steel frame proceeds ten to twelve floors ahead of the forming and placing of the reinforced concrete. Hydraulic slip and jump form framing systems are used which can place large segments of the composite frame in short periods of time, and which utilize the concept of formwork

repetition (see Figure 1.2). In SRC construction the composite frame is not fully stable until the concrete has been placed and cured, and because of this, must be braced during the construction phase. On the other hand, CFT construction with moment connections does not require bracing nor formwork during construction.

This study focuses on composite concrete filled tube (CFT) columns used in perimeter moment resisting frames (MRF) to resist lateral loads. The lateral stiffness of an MRF is greatly influenced by the flexural stiffness of the beams and columns, as well as connection rigidity. If the columns are closely spaced, an increase in the lateral stiffness occurs due to tube action [Linderman, 1990]. At the building corners moments are developed about both axes of the column cross section. These columns are also subjected to high axial loads due to overturning effects in addition to bending moments about both axes. In order to avoid problems of dissymmetry of the wide flange shapes and at the same time maintain three dimensional continuity of the MRF, designers are tending to use box columns or structural tubes for corner columns. Box sections or structural tubes are extremely efficient for carrying axial loads due to the larger radius of gyration for a given column dimension, and have superior torsional properties. A CFT column is ideally suited for corner columns in a MRF, for these members combine structural steel tubes, with their light weight and speed of erection, with high strength concrete's inherent properties of mass, stiffness, and damping.

There are several buildings built in the United States which have been designed to resist vertical dead and live loads as well as lateral loads by the use of composite columns. Feasibility studies were conducted on the basis of these projects in order to determine the most cost effective type of construction. These studies showed in concept that composite structural members offered the best overall advantages in time and economics compared to conventional steel structures and reinforced concrete structures.

The Three Houston Center Gulf Tower in Houston, Texas (Figure 1.3) presents an excellent example of a composite design. This high rise building maintains an all steel frame below the third floor and a composite moment resisting frame having SRC columns above the third floor, with no internal bracing or bracing walls. During the construction phase of this project, the steel frame was erected 10 to 12 floors above the concrete forming and placement, which moved along at a steady pace. The combined use of steel and concrete provided a decrease in cost while easing the construction phase.

A second example of a composite design building is the First City Tower, located in Houston, Texas (Figure 1.4) [Griffis, 1987]. This high rise is designed to resist lateral loads through its composite MRF (having SRC columns) and shear walls located in the central core. The two shorter sides of the building have steel wide flange composite columns, which provide full moment connections to the girders. During the construction of this project, the perimeter

columns were erected at the same time that the building core was framed, while the composite columns were constructed 10 to 12 floors behind the steel frame.

Momentum Place, located in Dallas, Texas (Figure 1.5) [Griffis, 1987], is a third example of composite design. This 60 story composite structure consisted of jump-formed perimeter corner shear wall with punched openings, perimeter SRC composite columns, and steel interior columns. The ultimate design of this building was based on the preliminary value studies and design for efficient wind resistant building systems, where the final composite design was chosen on the basis of economics.

The IBM Atlantic Center Tower in Atlanta, Georgia [Griffis, 1987] is yet another example of a composite high rise design. This 50 story building, the tallest one in Atlanta, resists lateral loads by an interior concrete core, composite exterior SRC columns, and composite floor beams. The interior concrete core was constructed by the use of slip forms and remains to be the tallest core slip formed to date. Prior to the design of this structure a value engineering study was performed on three types of frames: (1) an interior concrete core with composite exterior SRC columns; (2) an interior concrete core with reinforced concrete exterior columns; and (3) a perimeter concrete tube with reinforced concrete interior columns. The design which utilized composite construction proved to be the most advantageous system for the construction of the building.

A composite column example where the columns consist of concrete filled steel tubes can be found in the Southern part of Tokyo [Endoh, Yamamoto, Araki, and Yagi, 1991]. This high rise condominium stands at a height of 373 feet and consists of 37 stories with 2 floors of basement and 461 separate units (see Figure 1.6). The shape of the floor plan is almost rectangular with a size of 107' x 129'. The structural frames are spaced at 17.6 feet in the transverse direction and 22 feet in the longitudinal direction with a standard floor height of 9.7 feet. There are six frames in the longitudinal direction and eight frames in the transverse direction from the second floor up. A perimeter MRF tube structure created by four frames is designed to resist earthquake loads. Shear walls are only used for the basement floors. The building has interior square CFT columns, which are 25.6 inches by 25.6 inches in cross section. The wall thickness of the steel portion of the CFTs were reported to range from 1/2 inch at the roof level to 1.4 inch at the bottom floor level. The corner columns of the building were reported to consist of circular CFTs, contrary to the floor plan in Figure 1.6, which had a diameter of 16 inches.

This building was designed for safety against earthquakes as well as comfort from wind loading effects. Interior diaphragm plates were used for beam-to-column connections. These connections and diaphragm plates were analyzed using the finite element method, through which it was found that the maximum stress in the diaphragm was located at the edge of the hole at an

angle of about 50 degrees from the beam axis (see Figure 1.7). A structural test was also conducted in order to evaluate the capacity of the frame against lateral load, load-deflection relationship and state of stress flow in the diaphragm. A construction test of casting concrete into the steel tubes was conducted for the following reasons:

(1) To develop a casting apparatus for three floors at a time and for casting concrete from the top level.

(2) To confirm the performance of this apparatus.

(3) To prove that sound concrete can be cast according to design specifications.

(4) To confirm that concrete can fill the space under the diaphragm using a real size model.

This building was the first high rise in Japan to be constructed with concrete filled structural tube composite columns. Through the experimental process the designers of this structure learned the following: (1) design methods for concrete filled tubes must be established, especially for the beam-to-column connections; (2) structural tolerances of steel tubes were poor and more effort is needed in the fabrication of the steel tubes; and (3) less fire resistive coverage of the CFT is needed if the concrete inside the column is taken into account due to the fact that the concrete provides a heat sink.

While composite design and construction has many merits, some problems can be encountered with this type of construction. First, there is the problem of differential column shortening. Concrete in the column shortens because of creep and shrinkage effects, beyond the normal range of elastic axial shortening. Second, when the steel frame is constructed prior to placement or pumping of the concrete, the structural steel columns undergo differential axial shortening due to construction loading, causing floor leveling problems. A third problem with composite construction is the different trade unions responsible for each independent material. Even though a composite design might offer the best economical solution in terms of material costs, that does not mean that it will be the cheapest to build. Complications of labor agreement during the construction phase can cause large unexpected costs.

1.3 Previous Research on CFTs

An experimental an analytical study was undertaken at Lehigh University in order to assess the performance of the CFT panel zone under shear. The test setup is shown in Figure 1.8. The study included the comparison of effective parameters of the panel zone which influenced the strength, ductility, and deformation of the composite panel zone under direct shear. The test set up used one test specimen, which essentially modeled two connection panel zones, in order to simulate to force state of the panel zone caused by the combination

of seismic and gravity loading. The details of the panel zone included: (1) the width-to-thickness (b/t) ratio of the steel tube; (2) the compressive strut angle, which was the resulting angle between the transverse axis of the column and the developed diagonal compression strut; (3)the width of the compression strut; and, (4) the effect of steel plate diaphragms on the panel zone's performance.

The results of the test were compared with shear capacity predictions for the panel zone. Three models which were evaluated were the Kanatani Model [Kantani et al., 1985], Modified Strut Model, and the ACI Model. All three of these models assumed that the shear strength of the panel is the sum of the shear strengths of steel and concrete, but differ in their methods of calculation for the concrete capacity. The Kanatani model (see Figure 1.9) assumes that the shear strength of concrete depends on the concrete compressive strength, f'_c, the compression strut angle, α, and the strut width, B_e (see Figure 1.8), where the latter is dependent on the bearing width, S, and the strut angle. The limiting steel panel zone capacity is determined using the von Mises yield criteria. Expressions for the Kanatani shear strength model are as follows:

Steel

$$A_s = 2(b - t)t \tag{1.1}$$

$$\tau_y = \frac{\sigma_y}{\sqrt{3}} \tag{1.2}$$

$$V_s = \tau_y A_s \tag{1.3}$$

where V_s, A_s, b, t, and σ_y are the shear strength of steel, cross-sectional area of the steel tube, width of panel zone, thickness of steel tube, and the yield stress of the steel tube, and

Concrete

$$D_c = D - 2t \tag{1.4}$$

without diaphragm

$$V_c = S*D_c*\cos^2\alpha*f'_c \tag{1.5}$$

with diaphragm

$$V_c = 2S*D_c*\cos^2\alpha*f'_c \tag{1.6}$$

The shear capacity in the sum of the steel and concrete shear resistance:

$$V_{pred} = V_s + V_c \tag{1.7}$$

The modified concrete truss model (see Figure 1.9) is based on a combination of the strut and tie model and the compression field model. The shear strength of the steel is calculated using the area of the steel found within the panel zone, where overall width of the tube is D. The compression strut width, B_e, is calculated using a 45 degree hydrostatic prism formed in the concrete adjacent to bearing plates (see Figure 1.10). For specimens with diaphragms, a component of secondary compression field is believed to be mobilized and should be included in the shear capacity of the panel [Ricles et al., 1993] (see Figure 1.9). Also, the strength of the confined concrete within the

compression strut is assumed to be $0.85f_c$. Expressions for the shear strength determined by the Modified Strut Model are shown below:

Steel

$$A_s = 2(b - t)*t \tag{1.8}$$

$$\tau_y = \frac{\sigma_y}{\sqrt{3}} \tag{1.9}$$

$$V_s = \tau_y A_s \tag{1.10}$$

Concrete

$$D_c = D - 2t \tag{1.11}$$

without diaphragm

$$V_c = S^* D_c *\cos(45°)\cos(\alpha)*0.85f'_c \tag{1.12}$$

with diaphragm

$$A_v = (D - 2t)(a - t_d) \tag{1.13}$$

$$\sin^2\beta = 0.5*\left(1 - \frac{\frac{a}{D}}{\sqrt{1+\left(\frac{a}{D}\right)^2}}\right) \tag{1.14}$$

$$V_c = S*D_c*\cos(45°)\cos(\alpha)*0.85f'_c + A_v*\sin^2\beta*0.85f'_c \tag{1.15}$$

where the total panel zone shear capacity is

$$V_{cap} = V_s + V_c \tag{1.16}$$

In the above expressions a and t_d are the beam depth and diaphragm plate thickness. The ACI model predicts the shear capacity of the panel using the von Mises yield criterion, and the ACI specifications to calculate the shear strength of the concrete within the panel zone. In this model the shear strength of concrete is independent of the compression strut angle and the bearing width, and is only a function of the confinement. Expressions for the ACI Model are as follows:

Steel

$$A_s = 2(b - t)*t \tag{1.17}$$

$$\tau_y = \frac{\sigma_y}{\sqrt{3}} \tag{1.18}$$

$$V_s = \tau_y A_s \tag{1.19}$$

Concrete

$$D_c = (D - 2t) \tag{1.20}$$

$$h = (b - 2t) \tag{1.21}$$

without diaphragm

$$V_c = D_c*h*15\sqrt{f'_c} \tag{1.22}$$

with diaphragm

$$V_c = D_c*h*20\sqrt{f'_c} \tag{1.23}$$

where the total shear strength is

$$V_{cap} = V_s + V_c \tag{1.24}$$

A comparison of the predicted shear versus the experimental shear for each of the four specimens can be see in Figure 1.11. The conclusions from this previous study include the following:

1. Steel and concrete both contribute to CFT panel zone shear capacity.

2. Panel zone behavior is ductile due to concrete confinement and local buckling being inhibited in panel zone.

3. Interior diaphragm plates provide additional confinement and bearing capacity, leading to greater panel zone capacity.

4. Change in strut angle did not lead to an appreciable affect.

5. Analytical methods, particularly the Kanatani and modified strut models, predict CFT panel zone shear capacity reasonable well.

The results of this study also showed that the shear capacity in the shear force-deformation response decreased slightly after reaching peak load, but regained strength, offering high ductility (see Figure 1.12). It was evident that internal diaphragms in the panel zone improve the shear capacity (see Figure 1.13). Also a decrease in width to thickness ratio b/t results in a higher shear capacity (due to the larger steel shear area for a constant width, b) as shown in Figure 1.14.

The amount of ductility and energy dissipation that the CFT offers gives reason to explore more viable and reliable connections in order to maximize the

potential of a CFT. It is therefore apparent from this and other research that the concept of CFT is one which should be explored more rigorously

Research on hollow box column, fabricated from steel plate, to wide flange beam moment connections was conducted at the University of Idaho [Linderman, 1990]. The prototype box columns used in these test procedures were 11 inch square columns with wall thickness varying from 3/4 inch to 1 1/4 in. The prototype beams selected were W16X40 and W16X26. These sizes are approximately one-half the size of a typical section. The moment capacity and ductility of a typical connection for each specimen was evaluated under cyclic loading tests. Box sections with and without diaphragm plates were considered in tests which included axial load on the column. Specimen 9, a W16X40 beam welded to a box column having 1/2" interior continuity plates, sustained 11 loading cycles above the nominal plastic moment capacity prior to failure. The maximum beam load of 80 kips was 55% above nominal yield. Specimen 4, a W16X40 beam welded to a box column having a 1 1/4 inch face plate with no interior continuity plate, sustained 7 cycles above nominal plastic moment capacity prior to failure of the connection. Failure occurred due to a crack which propagated across the top flange. The results following conclusions based on the results include:

(1) Designing box column to wide flange beam connections with the internal diaphragm plate results in ultimate connection behavior which is

comparable to the standard connection of a beam to a wide flange column, but the initial stiffness may be as much as 18% less.

(2) The web cope in the beam can be a source of crack initiation which can impair the ultimate load carrying capacity of the connection.

(3) For a given beam, a wall thickness of the box column can be designed in order to eliminate internal diaphragms, although the initial stiffness of the connection may be reduced as much as 30%.

These last results simply say that it may be possible to design CFTs with ample wall thickness whereby interior diaphragms are not needed in the connection region.

The results of experimental research on CFT columns was reported by Richard W. Furlong [1967, 1968]. In the analysis of CFTs under axial load it was suggested that the proportion of the total load carried by steel increases as strains increase because the stiffness of steel does not tend to decrease as much as the stiffness of concrete under such circumstances. It was also suggested that it was not possible to justify any effective lateral confinement offered by square or rectangular structural tubing, for the cross section tends to ovalize and is not very stiff against pressure perpendicular to the walls of the tube.

Furlong also conducted 17 ultimate strength tests on CFTs in order to determine the moment-axial interaction relationships. A summary of the axially

loaded specimens is given in table 1.1, while Table 1.2 contains the same information for specimens subjected to bending in addition to axial force. Furlong found from strain measurements that the steel and concrete sustain load somewhat independent of one another. Also there appeared to be little, if any, additional strength due to the confinement of the concrete by the structural tube. On the other hand, it was concluded that the concrete did stabilize the thin walled steel encasements from local buckling.

Furlong conducted an additional 21 stiffness and capacity tests in order to develop a more complete hypothesis. Each of the square CFT specimens were about 36 inches long, with an outside dimension that varied from 4.50 to 6 inches. He found in these tests that the adhesive bond between the steel wall and the concrete core was too weak to prohibit separation or sliding at relatively low stress levels. Also, tests on plain rolled steel tubing revealed that there were extensive residual stresses in cold-rolled and welded steel tubing such that proportional limit in the axial loading of stub columns was less than 50% of the nominal yield strength.

Extensive research on CFTs has been conducted in Japan related to the seismic performance of the members in moment resisting frames. In experimental studies on concrete filled steel tubular columns under concentric loading by Tomii et al. [1977], it was found that the capacity of concrete filled steel tubular stub columns was considerable larger than that of the reinforced

concrete columns which were predicted using strength theory, because the concrete core is confined laterally by the steel tube (see Figure 1.15). Tomii and his colleagues conducted 268 concentrically loaded column tests, where 148 columns were made from circular tubes, 60 were square and 60 octagonal. dimensional properties of all steel tubes are shown in Table 1.3. The major conclusions from these tests were as follows:

(1) Failure modes consisted either of general buckling for longer columns, or crushing in shorter columns.

(2) CFTs which failed in the crushing mode, had a degrading type of failure in which rapid deterioration of axial load was observed in its load-deformation relationship. This relationship was found to be remarkably affected by the cross-sectional shape, width-to-wall thickness ratio, and concrete strength.

(3) It was found that there was actually no increase in axial strength due to triaxial effects (e.g. confinement of concrete by steel tube), although the ultimate loads of most of the CFTs with quite thin wall thickness reached the nominal squash loads.

(4) Values of yielding strength divided by the nominal squash load were not significantly affected by the width-to-wall thickness ratio of the steel tube and compressive strength of the encased concrete.

(5) There were very little differences in inelastic member behavior due to encasement of expansive concrete.

Research on beam flange to concrete-filled tubular column connections by Kato et al [1992] was conducted at the University of Tokyo. In these tests outer stiffening rings, which are welded to the tube face at the beam flange level, were designed in order to replace interior diaphragms. The yield and ultimate strength of this connection were investigated experimentally and theoretically. The predominant stress acting on the cross section of the stiffening ring, is shear stress, which would be the cause of failure if the beam and weld at the connection were not considered.

A rigid frame subassemblage, approximately one half scale, was tested under simulated seismic action. This prototype subassemblage was designed according to current Japanese design practice, so that the yielding of the beam flange should occur before yielding of the beam-to-column connection [Kato et al., 1992]. The hysteresis loop of the specimen was quite stationary showing excellent energy dissipation (see Figure 1.16). Failure of the connection resulted from the propagation of a crack at the intersection between the ring and the beam flange.

Testing of three dimensional subassemblies consisting of four wide flange beams and a concrete filled steel tubular column under constant axial load was conducted at Mic University in Isu, Japan by Morino et al. [1992]. The beams in

the minor direction of the structure's plan were kept under constant axial load while the beams in the major direction were subject to alternately repeated lateral forces simulating earthquake loading. The test specimens were designed to fail either at the beam to column connection panel (P-series), or from flexural failure of the column (C-series). The measured dimensions of each of the test specimens can be seen in Table 1.4. All the C and P-series specimens subjected to the bi-axial bending showed a doglegged deformation in the column and failed with excessive displacement at the connection. The P-series specimens subjected to the uni-axial bending showed stable symmetrical deformation and could sustain the axial load until the end of the test. It was concluded from this test that the P-series are more stable and exhibit more energy dissipation capacity compared to the C-series. This was found to be associated with the fact that the P-series' connection panel yielded in shear, while the specimen subjected to the bi-axial bending becomes unstable due to excessive column deformation of a doglegged shape in the minor direction.

When a structural steel tube with an inner open diaphragm is filled with concrete, voids may form under the diaphragm plate. In order to understand the influence of these voids, compression and shearing tests were conducted on specimens with artificial voids, where the results were compared to specimens without voids [Kimura et al. 1991]. The test procedure parameters and results can be seen in Table 1.5. The effect of concrete voids on the behavior of the

connection was studied by conducting three short-column compressive and shearing tests, while the effect on frame behavior due to these voids was examined by testing addition cruciform shaped frame test specimens, subjecting them to simulated seismic forces with simultaneous constant axial force. The results of the compression test showed that the effect of the voids on the strength of the column was minimal. The diaphragm developed the same deformation as when no voids existed. The flexural shearing test on the column and beam joint showed no deteriorating force characteristics or localized deformation due to the presence of voids. The cruciform tests results had no effects of the presence of voids, and produced sufficiently stable hysteresis characteristics.

Concrete filled steel tubes with interior diaphragm plates having square openings were analyzed by Yokoyama et al. [1991]. Table 1.6 shows that list of the specimens and their geometric properties. Expressions for the full plastic strength of the beam-end connection were derived based on yield line theory. The expressions were found to predict strengths that were in good agreement with the experimental values. Yokoyama et al. also concluded that the seismic design strength of the panel zone in the AIJ Standard used for design of Japanese composite construction [AIJ, 1987] corresponds closely to the load under which the reduction of stiffness begins due to full yielding of the panel zone.

An experimental study of exterior stiffener rings for tubular columns was conducted by Zhijun and Shanzhang [1991], in order to develop a formula which would predict the design load bearing capacity of the stiffener ring subjected to one or two way tension force, with the column under axial load. The geometric parameters of each of the specimens can be seen in Table 1.7. Pertinent information from these tests concluded, for stiffener rings subjected to two-way tension force (e.g. beams framing from both directions into the prototype column), that greater axial compression ratios lowered the capacity of the stiffener ring. These conclusions mandate the necessity for restricted axial compression ratios of the frame column.

Research on concrete filled tubes with inner ribs designed to increase the bond stress between the concrete and the structural steel tube has been conducted by Matsui et al. [1991]. Throughout these tests the inelastic behavior of CFTs subjected to axially and horizontal loads was considered. The main parameters existing in the test program were the presence of inner ribs, axial vertical load ratio, and the presence of a vacant space at the top of the column. The nominal sizes of width and depth of the steel section and the plate thickness were 13.78 in. and 0.354 in., respectively. The concept of the vacant space was intended to represent the possibility of concrete existing in a steel tube with no direct bearing. From the results of this test the following conclusions were noted: (1) the maximum bond stress for specimens with ribs was 5 times the amount for

the specimen with no ribs; (2) the strength of all specimens with inner ribs exceed the flexural strength M_u based on the superposed AIJ strength method [AIJ, 1987], even if the vacant space exists at the top of the specimen; and (3) all specimens with inner ribs showed large energy dissipation capacity and large ductility, while specimens without ribs showed poor performance if a vacant space existed at the top of the specimen.

Research on the comparison of hollow structural tubes to CFTs under a combined axially and horizontal loading, as well a comparison of limiting values of the width-to-thickness ratio for plate elements in the CFTs, was conducted by Matsui [1991]. New limiting values were derived from the comparison of the post buckling behaviors of concrete filled tubular members with those of hollow tubular members, based on the equivalent energy absorption capacity of the members. The hollow and concrete filled test specimens consisted of the same steel tubular section, which had a width-to-thickness ratio, b/t, of about 47. This parameter was consistent with the current AIJ code [AIJ, 1987] which limits the b/t ratio. The test specimen was 5.9 x 5.9 inches square with a 1/8 inch thickness. The results of testing showed that the restoring force of the hollow tubes decreased rapidly at the occurrence of web local buckling following flange local buckling. The restoring force of CFTs was strengthened due to the concrete, with the behavior in the post local buckling range extremely improved. At the occurrence of local buckling in CFTs the compression force sustained by

the structural steel tube was transferred to the concrete. Numerical results obtained from a plastic limit analysis proposed a new limiting value of the width-to-thickness ratio of plate elements of concrete filled steel tubular columns of about 1.5 times the value used for a hollow tube section.

Matsui [1985] developed a method of design for connections composed of concrete filled tubular members and bare steel H-shapes, which was later adopted in the commentary of the standard for tubular steel-concrete composite structures of the Architectural Institute of Japan [AIJ, 1987]. The design of the beam-to-column connection consists of the strength of the diaphragms and the shear strength of the connection panel. In the case of earthquake loading (short-term loading), the allowable strength of the diaphragm ${}_sP_a$, is expressed in Eqns. 1.25 - 1.27 for two types of diaphragms which are shown, with all relative parameters defined in Figure 1.17.

$$\text{Type I:} \quad {}_sP_a = \frac{4}{\sqrt{3}} * h_s * t_s * \sigma_{ys} + 2(4t + t_s) * t * \sigma_{yt} \tag{1.25}$$

when $\sigma_{yt} \geq \sigma_{ys}$, $\sigma_{yt} = \sigma_{ys}$

Type II: ${}_sP_a$ shall be taken as the smaller value obtained from equations (1.26) or (1.27).

$${}_sP_a = (D + 2h_s - d)^2 * \frac{B * t_s}{d^2} * \sigma_{ys} \tag{1.26}$$

$$_sP_a = (D + 2h_s - d) * t_s{}^*\sigma_{ys} \quad (1.27)$$

where h_s, t_s, t, σ_{ys}, σ_{yt}, B, D, and d are the size of the diaphragm (see Figure 1.17), thickness of diaphragm, thickness of tube, yield stress of stiffener, yield stress of tube, width of beam flange, depth and width of tube, and the diameter of the circular hole in the diaphragm, respectively. Note that criteria per Eqn.1.27 is omitted in the current AIJ provisions [AIJ, 1987], and hence is also for the design of the experimental test specimens (to be discussed in Chapter 2).

Equation 1.25 is expressed as the sum of the plastic strength of a diaphragm, S_1, and that of the web plate of a tube, S_2. S_1 is obtained from plastic analysis using the assumptions that the a-a section in Figure 1.17(a) yields in a state of combined normal and shearing stresses. In calculating S_2, the effective width ($4t + t_s$) of a web plate was determined on the basis of the consideration for the test results which were obtained by tension tests for simple specimens composed of a filled tube and stiffener plates. Eqn. 1.25 is applicable in the range of $30° < \theta \leq 45°$, $20 \leq D/t \leq 50$, $0.75 \leq t_s/t \leq 2.0$, where the minimum size of h_s is 0.15D. However, it also be conservatively used for a diaphragm of $\theta \leq 30°$.

For the case of a type II diaphragm, Eqn 1.26 is obtained from the condition that the section b-b of a diaphragm (see Figure 1.17(b)) begins to yield due to bending moment produced by the distributed load P/B applied from a beam flange. In this analysis, a stiffener is assumed to be a end-fixed beam with span d, depth $(D + 2h_s - d)/2$ and width t_s. Eqn 1.27 is obtained from the

condition that the section c-c in Figure 1.17(b) yields in a state of normal stress under P. Eqs 1.25 through 1.27 are expressed as the allowable strength of a diaphragm, ${}_sP_a$. A value of the allowable moment applied to a connection may be expressed by Eqn 1.27.

$$ {}_sM_a = 2^* {}_sP_a {}^*{}_sj \tag{1.28} $$

where ${}_sj$ is the beam depth between flanges and ${}_sM_a$ is the overturning moment of two beams framing into the joint.

The panel zone of a beam-to-CFT column connection must have enough shear strength so that the connecting beams can reach their ultimate strength. The commentary of AIJ standard recommends an allowable strength ${}_pM_a$ for a CFT where

$$ {}_pM_a = 2\ {}_pP_a {}^*\ {}_sj = ({}_cA^*\frac{5D}{{}_sj} {}^*\ {}_cf_s + \frac{{}_sA}{2} {}^*\frac{\sigma_{yt}}{\sqrt{3}}) {}^*\ {}_sj \tag{1.29} $$

In order to verify the strength formulas of the beam-to-CFT column connections described above, the experimental results of cruciform frame specimens are described below. The test specimens were designed so that initial yielding would occur at the diaphragm. Then the columns and beams were designed to have enough strength in comparison with the strength of the diaphragm or the connection panels. Specimens A and B had outside diaphragms of type I with h_s = 0.787 inch and 1.18 inch, respectively. Specimens C had interior diaphragms of type II with d=4.72 inch. The allowable

beam loads, ${}_sQ_a$ and ${}_pQ_a$, are calculated according to Eqns. 1.28 and 1.29 and correspond to ${}_sP_a$ and ${}_pP_a$. Their values are summarized in Table 1.8. From the load-displacement relations of the specimens, it was recognized that the beam load ${}_sQ_a$ corresponding to ${}_sM_a$ showed fairly good agreement to the yielding load of specimens and the connections had enough spare strength to the final states.

Twelve square CFT column and H shape beam specimens were also tested by Matsui (1985) under constant vertical and varying horizontal loads in order to investigate the strength and behavior of composite frames. Four specimens were designed in order to examine the validity of the strength formulae for the diaphragms. The columns of these specimens were proportioned to have the same allowable bending strength ${}_cM_a$ as that of beam-to-column connections ${}_sM_a$. ${}_cM_a$ is determined by the design formula of the AIJ standard and will be discussed later. Matsui calculated the ultimate strength of the CFT column, ${}_cM_u$, using Eqns. 1.30 through 1.33:

$$ {}_cM_u = {}_sM_{po} + {}_cM_p \quad \text{if } N \le {}_cA^*F_c \tag{1.30} $$

$$ {}_cM_u = {}_sM_{pc} \quad \text{if } N > {}_cA^*F_c \tag{1.31} $$

$$ {}_sM_{pc} = {}_sM_{po} - \frac{(N - {}_cA^*F_c)^2}{8t^*\sigma_{yt}} \tag{1.32} $$

$$ {}_cM_p = \frac{N}{2} * \{(D - 2t) - \frac{N}{(D - 2t)^*F_c}\} \tag{1.33} $$

where ${}_sM_{po}$, N, ${}_cA$, and F_c are the full plastic moment of the tube under pure bending, applied axial force, the cross sectional area of concrete, and concrete compression strength, respectively.

The values of ${}_cM_u/{}_cM_a$ are about 1.5. In the test procedure the beam-to-column connections, designed by Eqns 1.25 to 1.27, were examined to see if they could resist against the increase in column strength from ${}_cM_a$ to ${}_cM_u$ in order to maintain a equilibrium state of moment at the connection. The beams were designed so that the allowable bending moment ${}_bM_a$ and the ultimate moment ${}_bM_u$ corresponded with the yield moment and full plastic moment of the beam cross section, respectively.

The theoretical behavior of the test frames were predicted using the plastic hinge method. The plastic collapse mechanism lines are calculated using Eqn. 1.34.

$$H = \frac{4\,{}_cM_u}{h'} - \frac{2P\Delta}{h'} \qquad (1.34)$$

where ${}_cM_u$, P, Δ, and h' are equal to the column flexural capacity, axial column load, lateral displacement, and height of the column.

Matsui concluded that the CFT frame is very excellent as an earthquake resistant structure when the diaphragms of the beam-to-column connection are designed by the strength formulae, Eqns. 1.25 to 1.27. He also confirmed that the limiting value of width-to-thickness ratio of CFT tubes can be mitigated to

about 1.5 times that of the hollow tubes due to the restricting effect of the filled concrete on local buckling of a tube.

Tests on wide flange beams to hollow structural steel column connections by Blais [1974] on a simple physical model involving monotonic load, have shown that the best method of transferring the flange forces to the tubular column, without deformation of the tube column, is to transfer the flange stress to the tube walls through plates that are in the plane and parallel to the beam web. Continued monotonic load tests on these types of connections were conducted by Picard and Giroux at Laval University in Quebec [1976]. The predominant connection was the one which consisted of coped strap angles around the square tubular column in order to transfer beam flange stress to the panel zone of the column (see Figure 1.18). The details of the specimens are summarized in Table 1.9, and the details of welding of each strap angle is given in Table 1.10. The beam flanges, in this case, were approximately the same width as the steel tube column. This connection was found to have adequate strength to carry the full plastic moment of the connected beams and sufficient rotation capacity to sustain large inelastic rotations while it is considered a 'nearly rigid' connection, it was found to be flexible and thereby cause significant lateral displacement. Use of this type of connection, therefore, requires investigation of P-Δ effects and the possibility of a frame bracing system.

Giroux and Picard conducted subsequent tests [1977] involving monotonic loading in which the beam flange was substantially narrower than the column face (see Figure 1.19). The connection tested here was similar to previous one with the exception that welded double angles were used to transfer flange forces from the wide flange beam to the column. The exact details of the specimens are given in Table 1.11, and the details of the welding of each strap angle given in Table 1.12. The results of this test involving monotonic load, concluded that special attention had to be paid to the geometrical design of the strap angles for the web connection. It was suggested that the strap angles be coped in order to ensure that brittle fracture will not take place. This connection was also found to be flexible and requires the consideration of P-Δ effects on the frame.

While the above tests by Blais, and Picard and Giroux involve no concrete placed inside the tube, the details lend themselves to concepts that could be used in connections between CFT columns and wide flange beams.

1.4 U.S. CFT Column Design Provisions

The results of some of the above mentioned research has lead to U.S. design guidelines. Composite columns can be designed in the U.S. seismic regions by using the criteria found in the newly published NEHRP provisions [NEHRP, 1994] in conjunction with the American Institute of Steel Construction Load Resistance Factor Design Manual (LRFD) [AISC, 1992], the American Concrete Institute Building Code Requirements for Reinforced Concrete (ACI)

[ACI, 1989], the American Institute of Steel Construction Seismic Provisions for Structural Steel Buildings [AISC, 1992], and the American Iron and Steel Institute Load and Resistance Factor Design Specification for Cold-formed Steel Structural Members [AISI, 1991]. The NEHRP provisions define a composite column as a steel column fabricated from rolled or built-up steel shapes and encased in structural concrete, or fabricated from steel pipe or tubing and filled with structural concrete, where the structural steel portion accounts for at least 4 percent of the gross column area. The limitations and design requirements of composite columns for seismic regions of performance categories D and E according to the NEHRP [NEHRP, 1994] will be stated below and will later be compared to the limitations and design requirements of composite columns for non-seismic regions according to both the LRFD and the ACI. The stated limitations and design requirements of the NEHRP for steel tubing filled with structural concrete consist of the following:

(1) The design of composite columns subjected to seismic forces acting alone or in combination with other prescribed loads shall be determined according to the provisions in Chapter I of the LRFD and the following:

(2) Concrete in composite members shall have a specified compressive strength not less than 3 ksi. The compressive strength shall not exceed 10 ksi for normal weight concrete and 4 ksi for lightweight concrete.

(3) The shear strength of the column shall be calculated as the strength of the steel section alone. This conservative limitation is a result of little test evidence to demonstrate whether some portion of the concrete can be used for resisting shear. This approach is consistent with recommendations proposed by Furlong (1988) and the provisions in the latest draft of Eurocode 4 for composite construction.

(4) Seismic design forces in columns shall be calculated using NEHRP Eq. 2.2.6-3 and 2.2.6-4.

(5) Splices of the structural steel tube or pipe shall meet the requirements of AISC Seismic Provisions for Structural Steel Buildings.

(6) The minimum required shear strength of the column shall meet the provisions of Sec. 21.4.5.1 of the ACI, which states that the design force shall be determined from consideration of the maximum forces that can be generated at the faces of the joints at each end of the member. These joint forces shall be determined using the maximum probable moment strengths of the member associated with the range of factored axial loads on the member. The member shears need not exceed those determined from joint strengths based on the probable moment strength of the transverse members framing into the joint.

(7) The strong-column/weak-beam design requirements below must be satisfied to limit plastic hinge formations in the columns. Column bases shall be detailed to sustain inelastic flexural hinging.

(i) the flexural strength of the columns shall meet the requirements of Sec. 21.4.2.2 of the ACI:

$$\Sigma M_e \geq (6/5)\Sigma M_g \tag{1.35}$$

where ΣM_e is the sum of the moment, at the center of the joint, corresponding to the design flexural strength of the columns framing into that joint. Column flexural strength shall be calculated for the factored axial force, consistent with the direction of the lateral forces considered, resulting in the lowest flexural strength. ΣM_g is the sum of moments, at the center of the joint, corresponding to the design flexural strengths of girders framing into that joint. Flexural strengths shall be summed such that the column moments oppose the beam moments. Eqn. 1.35 shall be satisfied for beam moments acting in both directions in the vertical plane of the frame considered.

(ii) the provisions of Sec. 8.6 of the AISC Seismic Provisions for Structural Steel Buildings shall be met

(8) The minimum wall thickness of structural steel tubing filled with concrete shall be equal to $b\sqrt{(F_y/2E_s)}$ for each face of width b. The reduced slenderness criteria, in comparison to that of the LRFD, were imposed as a conservative measure until further research data becomes available on the cyclic response of filled tubes.

The stated limitations and design requirements of the NEHRP [NEHRP] for composite connections consist of the following:

(1) Moment connection design strengths shall meet or exceed the flexural and shear forces associated with plastic hinging of the beams adjacent to the connection

(2) Composite connections shall be demonstrated to have strength, ductility, and toughness at least equal to those for similar structural steel or reinforced concrete connections that meet the provisions of Chapter 5 and Chapter 6 of the NEHRP.

(3) All connections in the structure shall have adequate deformation capacity to resist their critical factored design loads under the design story drifts calculated according to the requirements of Chapter 2.

(4) Calculated connection strengths shall be based on rational models that satisfy equilibrium of internal forces and strength limitations of component materials and elements based on potential failure modes.

(5) Force transfer between structural steel and concrete shall only be considered to occur through direct bearing and/or shear friction. Force transfer shall be calculated based only on direct bearing forces and/or clamping forces provided by reinforcement, shear studs, or other mechanical devices. Bond between steel and concrete is not to be considered as a connection force transfer mechanism.

(6) The design strength of steel components of connections shall not exceed those prescribed in the LRFD or the Seismic Provisions for Structural Steel Buildings.

(7) Ultimate bearing and shear friction design strengths calculated according to Chapters 10 and 11 of the ACI shall be reduced by 25 percent.

(8) The panel zone shear strength may be calculated as the sum of the strengths of the structural steel and reinforced concrete shear elements where each is calculated following the provisions of Sec. 8 of the Seismic Provisions for Structural Steel Buildings and Sec. 21.5 of the ACI.

The LRFD criteria for designing non-seismic composite columns is referenced from the NEHRP quite frequently and will be stated below for the purpose of comparison between the two design specifications. The stated non-seismic limitations of the LRFD for steel tubing filled with structural concrete consist of the following:

(1) The cross-sectional area of the steel tube must comprise at least 4% of the total composite cross section.

(2) Concrete shall have a specified compressive strength f_c' of not less than 3 ksi nor more than 8 ksi for normal weight concrete and not less than 4 ksi for light weight concrete.

(3) The specified minimum yield stress of the structural steel used in calculating the strength of a composite column shall not exceed 55 ksi.

(4) The minimum wall thickness of the rectangular structural tube shall be equal to $b^*\sqrt{(F_y/3E)}$ for each face of width b. This specification is identical to the one found in the 1992 ACI Building Code and its purpose is to prevent local buckling of the steel tube prior to yielding.

The design strength of axially loaded CFT composite columns according to the LRFD is $\phi_c P_n$, where $\phi_c = 0.85$ and the nominal axial compressive strength P_n is determined from the following:

$$P_n = A_s F_{cr} \tag{1.36}$$

For $\lambda \leq 1.5$ $$F_{cr} = (0.658^{\lambda_c^2})F_{my} \tag{1.37a}$$

For $\lambda > 1.5$ $$F_{cr} = \left(\frac{0.887}{\lambda_c^2}\right)F_{my} \tag{1.37b}$$

where: $$\lambda = \left(\frac{Kl}{r\pi}\right) * \sqrt{\left(\frac{F_{my}}{E_m}\right)} \tag{1.38}$$

$$F_{my} = F_y + 0.85f_c'\left(\frac{A_c}{A_s}\right) \tag{1.39}$$

$$E_m = E_s + 0.2E_c\left(\frac{A_c}{A_s}\right) \tag{1.40}$$

where A_c, A_s, E_s, E_c, F_y, and f_c' are the area of concrete (in^2), area of steel tube (in^2), modulus of elasticity of steel (ksi), modulus of elasticity of concrete (ksi),

specified minimum yield stress of steel tube (ksi), and specified compressive strength of concrete (ksi), respectively, of the cross-section.

The design of CFT columns for combined axial compression and flexure according to the LRFD is similar to that specified for steel columns. The interaction of these forces shall be limited by the formulas given in equations H1-1 through H1-6 in chapter H of the LRFD [AISC, 1992]:

for $\frac{P_u}{\Phi P_n} \geq 0.2$

$$\frac{P_u}{\Phi P_n} + \frac{8}{9}\left(\frac{M_{ux}}{\Phi_b M_{nx}} + \frac{M_{uy}}{\Phi_b M_{ny}}\right) \leq 1.0 \qquad (1.41)$$

for $\frac{P_u}{\Phi P_n} < 0.2$

$$\frac{P_u}{2\Phi P_n} + \left(\frac{M_{ux}}{\Phi_b M_{nx}} + \frac{M_{uy}}{\Phi_b M_{ny}}\right) \leq 1.0 \qquad (1.42)$$

$$M_u = B_1 M_{nt} + B_2 M_{lt} \qquad (1.43)$$

$$B_1 = \frac{C_m}{\left(1 - \frac{P_u}{P_e}\right)} \geq 1 \qquad (1.44)$$

$$C_m = 0.6 - 0.4\left(\frac{M_1}{M_2}\right) \qquad (1.45)$$

$$B_2 = \frac{1}{} \qquad (1.46)$$

$$1 - \Sigma P_u\left(\frac{\Delta_{oh}}{\Sigma HL}\right)$$

or $$B_2 = \frac{1}{1 - \frac{\Sigma P_u}{\Sigma P_e}} \qquad (1.47)$$

where:

P_u = required axial strength, kips

P_n = nominal axial strength determined in accordance with Sect. D1, kips

M_u = required flexural strength, kip-in.

Φ = resistance factor for tension

Φ_b = resistance factor for bending

M_{nt} = required flexural strength in member assuming there is no lateral translation of the frame, kip-in.

M_{lt} = required flexural strength in member as a result of lateral translation of the frame only, kip-in.

Δ_{oh} = translation deflection of the story under consideration, in.

ΣH = sum of all story horizontal forces producing Δ_{oh}, kips.

L = story height, in.

The above equations shall be used to determine the interaction of combined axial and flexure forces for composite columns with the following modifications:

M_n = nominal flexural strength determined from plastic stress distribution on the composite cross section except when the axial term in Eqns. 1.41 and 1.42 is less than 0.3. In that case the nominal flexural strength shall be determined by straight line transition between the nominal flexural strength determined from the plastic distribution on the composite cross section at $(P_u/\phi_c P_n) = 0.3$ and the flexural strength at $P_u = 0$.

where

$$M_n = M_p = Z^* F_y \tag{1.48}$$

$$P_e = A_s \left(\frac{F_{my}}{\lambda_c^2}\right) \tag{1.49}$$

ϕ_b = resistance factor for flexure from LRFD Section I3

$\phi_c = 0.85$

where P_e is the elastic buckling load in kips. The resulting moment - axial load interaction diagram is shown in Figure 1.20.

The design specifications for a structural steel tube filled with concrete as stated in the 1992 ACI are as follows:

(1) The strength of a composite member shall be computed for the same limiting conditions applicable to ordinary reinforced concrete members. The same rules used for computing the load-moment interaction strength for reinforced concrete beam columns, utilizing the concept of strain compatibility,

can be applied to composite sections. The ACI moment - axial load interaction surface is shown in Figure 1.21 for a CFT column similar to the test specimens of the current study reported herein.

(2) Any axial load strength assigned to concrete of a composite member shall be transferred to the concrete by members or brackets in direct bearing on the composite member concrete. All axial load strength not assigned to concrete of a composite member shall be developed by direct connection to the structural tube. Direct bearing or direct connection can be developed through lugs, plates, or reinforcing bars welded to the structural tube before concrete is cast.

(3) For evaluation of slenderness effects, the radius of gyration of a composite section shall be not greater than the value given by the following:

$$r = \sqrt{\left(\frac{\frac{E_c I_g}{5} + E_s I_t}{\frac{E_c A_g}{5} + E_s A_t}\right)} \qquad (1.50)$$

where EI may be taken as either of the two following:

$$EI = \frac{\frac{E_c I_g}{2.5}}{1 + \beta_d} \qquad (1.51)$$

$$EI = \frac{\frac{E_c I_g}{5}}{1 + \beta_d} + E_s I_t \qquad (1.52)$$

In the above expressions E_c, E_s, I_g, I_t, A_g, A_t, and β_d are the modulus of elasticity of concrete (psi), modulus of elasticity of steel (psi), gross moment of inertia, moment of inertia of the structural steel tube about the centroidal axis of the composite member cross section, gross area of section (in^2), the area of structural steel tube in the composite section (in^2), and the ratio of the maximum factored axial dead load to the maximum total factored axial load, respectively.

(4) The CFT composite sections should have a steel wall thickness large enough to attain longitudinal yield stress before buckling outward. This is accomplished by setting the minimum wall thickness t for each face of width b of the steel tube to be equal to:

$$t = b\sqrt{\left(\frac{F_y}{3E_s}\right)} \qquad (1.53)$$

1.5 Japanese CFT Column Design Provisions (A.I.J. Specifications)

The Architectural Institute of Japan [AIJ, 1987] contains structural design codes which involve consideration of seismic effects due to the intense

seismicity of the Japanese islands. The provision research noted earlier in Section 1.3 led to a number of the provisions in the AIJ Specification. Typical CFT column to beam connections suggested by the AIJ can be seen in Figure 1.22.

The design specifications for a structural steel tube filled with concrete as stated in the 1987 AIJ are as follows:

(1) The cross-sectional area of longitudinal steel members in a column or a compression member shall be not less than 0.8% of the gross area of concrete.

(2) The width-to-thickness ratio, B/t, for a square or rectangular steel tube, shall be limited to the following:

$$\frac{b}{t} \leq \frac{232}{\sqrt{F}} \tag{1.54}$$

where F is the yield stress in MPa.

(3) Calculation for the allowable axial force and bending moment in columns:

When $0 \leq N \leq {}_cN_c$ or $M \geq {}_sM_o$

$$N = {}_cN \tag{1.55}$$

$$M \leq {}_sM_o + {}_cM \tag{1.56}$$

When $N > {}_cN_c$ or $M < {}_sM_o$

$$N \leq {}_cN_c + {}_sN \tag{1.57}$$

$$M = {}_sM \tag{1.58}$$

When $N < 0$

$$N \geq {}_sN \tag{1.59}$$

$$M = {}_sM \tag{1.60}$$

where N, ${}_cN_c$, ${}_cN$, ${}_sN$, M, ${}_sM_o$, ${}_cM$, and ${}_sM$ are the design compressive force, allowable compressive force of concrete portion subjected to the ultimate compressive strength of concrete portion subjected to compression alone (equal to ${}_cA^*f_c'$), allowable compressive force of concrete portion, allowable compressive force of steel portion, design bending moment, allowable bending moment of steel portion subjected to bending alone, allowable bending moment of concrete portion, and allowable bending moment of steel portion, respectively.

(4) Calculation of allowable forces for a column subjected to combined axial force and bending moment may be made by the following, instead of the above equations:

$$N = {}_sN + {}_cN \tag{1.61}$$

$$M \leq {}_sM + {}_cM \tag{1.62}$$

(5) Calculation of allowable forces for a column which has an effective buckling length exceeding 12 times the depth of the cross section shall conform to the requirements below:

When $N \leq {}_cN_c$ or $M \geq {}_sM_o\,(1 - {}_c\nu^*{}_cN / N_k)$

$$N = {}_cN \tag{1.63}$$

$$M \leq {}_sM_o\left(1 - \frac{{}_cV^* {}_cN}{N_k}\right) + {}_cM \tag{1.64}$$

When $N > {}_cN_c$ or $M < {}_sM_o\,(1 - {}_cV^*{}_cN/\,N_k)$

$$N \leq {}_cN_c + {}_sN \tag{1.65}$$

$$M = {}_sM\left(1 - \frac{{}_cV^* {}_cN_c}{N_k}\right) \tag{1.66}$$

where ${}_cV$ is the factor of safety and shall be taken as 3.0 and 1.5 for the long-term (serviceability) and the short-term (earthquake) stress conditions, respectively. N_k is the buckling strength of the column.

(6) ${}_sN$ is the allowable compressive strength of the steel portion as a long column, and shall be computed according to Design Standard for Steel Structures taking the slenderness effect into consideration.

(7) ${}_cN$ and ${}_cN_c$ are the allowable compressive strengths of the filled concrete portion as a long column, and shall be computed for the cross section subjected to bending moment equal to ${}_cM$ multiplied by ${}_c\delta$ given below and axial compression ${}_cN$. However, end eccentricities not less than 5% of the depth of the concrete section shall be considered in the calculation described above.

$${}_c\delta = \frac{1}{1 - \dfrac{{}_cV^* {}_cN_c}{{}_cN_k}} \tag{1.67}$$

$$\pi^2 {}_cE^* {}_cI$$

where $_cN_k = \dfrac{}{5\ l_k^2}$ (1.68)

(8) Calculation for the allowable shear force of a concrete filled steel tubular column for long term stress condition shall be made by the following:

$$Q \le Q_A \tag{1.69}$$

$$Q_A = (1 + \beta)_rQ_{AL} \tag{1.70}$$

$$_rQ_{AL} = b' * {}_rj * a * f_s \tag{1.71}$$

$$a = \frac{4}{\dfrac{M}{Q*{}_rd} + 1} \quad \text{and } 1 \le a \le 2 \tag{1.72}$$

$$\beta = \frac{7.5*{}_sA}{b' * {}_rj} \tag{1.73}$$

$$_rj = 0.75*D \tag{1.74}$$

where Q, Q_A, β, $_rQ_{AL}$, b', $_rj$, f_s, M, $_rd$, and D are the design shear force, allowable shear force, coefficient related to the type and dimension of the steel web, allowable shear force under long-term stress condition of concrete portion in column, effective width of concrete at steel flange, distance between centroids of tension and compression under flexure, allowable shear stress of concrete, design bending moment, distance between extreme compression fiber and

center of compression reinforcement, and depth of the flexural member, respectively.

(9) Calculation for the allowable shear force of a concrete filled steel tubular column for short term stress condition shall be made by the following:

$$ {}_sQ_A = \frac{{}_sA^* \, {}_sf_s}{2} \tag{1.75} $$

where ${}_sQ_A$, ${}_sA$, and ${}_sf_s$ are the allowable shear force of steel portion, area of steel portion, and the allowable shear stress of steel, respectively.

(10) Bond between steel tube and concrete shall be investigated, where a part of the shear force in a beam is transferred as the compression force in the filled concrete portion of a column.

(11) Calculation for shear force of a connection panel surrounded by columns and beams shall be made according to the following:

$$ 2f_s^* {}_s\beta^* {}_cV + {}_sV^* \, {}_sf_s \geq h'/h * ({}_sM_1 + {}_sM_2) \tag{1.76} $$

$$ {}_cV = {}_cA * {}_{sn}d \tag{1.77} $$

$$ {}_J\beta = 2.5 \, \frac{{}_sD}{{}_{sn}d} \tag{1.78} $$

where ${}_cV$, ${}_sV$, h', h, ${}_sM_1$, ${}_sM_2$, ${}_cA$, ${}_J\beta$, ${}_sD$, and ${}_{sn}d$ are the volume of concrete portion of beam-to-column connection, volume of the steel web of beam-to-column connection, clear height of the column, story height, absolute value of allowable bending moment of steel portion at one end of member under short-

term stress condition, absolute value of allowable bending moment of steel portion at the other end of member under short-term stress condition, area of concrete portion, coefficient related to the shape of the beam-to-column connection with a concrete filled steel tubular column, diameter of steel tube, and the distance between the upper and lower chords or flanges of the steel beam, respectively.

(12) The ultimate axial - flexural strength of a composite concrete and steel tubular member shall be computed as follows:

$$N_u = {}_cN_u + {}_mN_u + {}_sN_u \tag{1.79}$$

$$M_u = {}_cM_u + {}_mM_u + {}_sM_u \tag{1.80}$$

where ${}_sM_u$ shall be computed according to Table 1.13, and ${}_cM_u$ shall be computed according to Table 1.14, where ${}_cr_u = 0.85$. N_u, ${}_cN_u$, ${}_mN_u$, ${}_sN_u$, M_u, ${}_cM_u$, ${}_mM_u$, and ${}_sM_u$ are the ultimate compressive strength of the composite member, ultimate compressive strength of the concrete portion, ultimate compressive strength of the main reinforcement (if any at all), ultimate compressive strength of the steel portion, ultimate flexural strength of the composite member, ultimate flexural strength of filled concrete portion, ultimate flexural strength of the main reinforcement, and the ultimate flexural strength of the steel portion. The superposed axial load - moment interaction strength of a CFT column is presented in Figure 1.23.

(13) The ultimate shear strength of concrete filled steel tubular members shall be computed as shown below:

$$Q_u = {}_cQ_u + {}_sQ_u \tag{1.81}$$

$${}_cQ_u = \Sigma \frac{{}_cM_u}{l'} \tag{1.82}$$

$${}_sQ_u = \min({}_sQ_{su}, {}_sQ_{bu}) \tag{1.83}$$

$${}_sQ_{su} = \frac{{}_sA * {}_s\sigma_r}{2 * \sqrt{3}} \tag{1.84}$$

$${}_sQ_{bu} = \Sigma \frac{{}_sM_u}{l'} \tag{1.85}$$

where ${}_cM_u$ may be computed according to Table 1.15, l' is the clear span length of beam, ${}_cQ_u$ is the ultimate shear strength of the concrete portion, ${}_sQ_u$ is the ultimate shear strength of the steel portion, ${}_sQ_{su}$ is the ultimate shear strength in ${}_sQ_u$ controlled by shear yielding of steel portion, ${}_sQ_{bu}$ is the ultimate shear strength in ${}_sQ_u$ controlled by flexural failure of steel portion, ${}_sA$ is area of steel portion, and ${}_s\sigma_y$ is the yield stress of steel.

(14) The ultimate shear strength of beam-to-column connections can be computed as follows:

$${}_JM_u = {}_cV * {}_JF_s * {}_j\beta + 1.2{}_sV * \frac{{}_s\sigma_y}{\sqrt{3}} \tag{1.86}$$

$$ {}_{J}F_{s} = \min\left(0.12F_{c},\ 18 + \frac{3.6F_{c}}{100}\right) \tag{1.87} $$

$$ {}_{c}V = {}_{c}A^{*}{}_{sB}d \tag{1.88} $$

$$ {}_{s}V = \frac{{}_{s}A}{2} {}^{*}{}_{sB}d \tag{1.89} $$

$$ {}_{j}\beta = 2.5\frac{{}_{s}D}{{}_{sB}d} \tag{1.90} $$

${}_{J}M_{u}$, ${}_{c}V$, ${}_{J}F_{s}$, F_{c}, ${}_{j}\beta$, ${}_{c}A$, ${}_{s}A$, and ${}_{s}V$ are ultimate shear strength of beam-to-column connection converted to bending moment, volume of concrete portion of beam-to-column connection, shear strength of concrete in beam-to-column connection, concrete compressive strength (kg/cm^2), coefficient related to shape of concrete filled steel tubular column, cross sectional area of the concrete, cross sectional area of the steel tube section, and the volume of steel web of beam-to-column connection. The shear capacity of a CFT-to-wide flange beam connection, computed using equations (1.86) through (1.90), increases linearly in relation to the increasing thickness of the structural steel tube, as shown in Figure 1.24. The shear capacity of the connection seems to decrease exponentially with increasing beam depth, as shown in Figure 1.25, while it increases parabolically with increasing column width, as shown in Figure 1.26.

1.7 Objectives

The attributes of the materials and demonstrated performance from previous research indicates that the use of concrete filled steel tube composite columns appears to be a viable option for seismic resistant design. The application of this form of construction for seismic resistant design would be desirable because of its adequate member strength and ductility during seismic cyclic loading and its economic advantages due to the decrease of structural steel weight . Due to the lack of knowledge and data associated with the seismic behavior of the moment connections between a concrete filled steel tube column and wide flange beams, as well as design criteria applicable for U.S. design practice, a research program was conducted to study this topic. The study involved experimentally testing square CFT columns with rigid connections to wide flange beams, such as that which may be used in a perimeter moment resisting frame for a seismic resistant structural system.

The objectives of this research study are:

(1) Experimentally assess the cyclic stiffness, strength and ductility of CFT column-to-beam and beam-to-column connections when subjected to combined axial and flexural loading under seismic conditions.

(2) Experimentally assess the stiffness of CFT columns and beam-to-column connections.

(3) Experimentally assess and analyze the force transfer mechanism and failure mode of the CFT column-to-wide flange beam connections under

seismic loading conditions, and develop recommendations that result in economical connection designs.

1.8 Scope

This report is a summary of a portion of the research program which consisted of an experimental study of CFT column-to-wide flange beam full moment connections subjected to combined loading under seismic conditions. This study reported herein is part of a major ongoing investigation on the seismic connection behavior in CFT column systems. After the introduction given in Chapter 1, Chapter 2 of this report includes the prototype building design and the description of an experimental program which involved the testing of two full scale CFT column-to-wide flange beam subassemblages. The experimental behavior of each test specimen is described in Chapter 3. An analysis of the experimental results for column stiffness, connection strength, stiffness, and ductility, the force state developed with in the joint, and the separate components of interstory drift is presented in Chapter 4. Conclusions and a summary of recommended connection design based on the test program are given in Chapter 5.

Table 1.1 - Axial Load Data For CFT Columns, Furlong Test (1967)

Shape	Tube Size In.	Wall Thickness in.	f_y ksi	A_s in^2	f'_c ksi	A_c in^2	P_o Computed kips	P_u Measured kips	P_o/P_u
Round	4.50	0.125	60.0	1.73	4.20	14.17	163.4	160.0	0.979
Round	4.50	0.125	60.0	1.73	4.20	14.17	163.4	170.0	1.040
Square	5.00	0.189	70.3	3.64	6.50	21.36	393.8	360.0	0.915
Square	4.00	0.084	48.0	1.33	3.40	14.67	110.8	117.8	1.063
Square	4.00	0.084	48.0	1.33	3.40	14.67	110.8	109.8	0.990
Square	4.00	0.125	48.0	1.95	4.18	14.05	149.1	150.0	1.008
Square	4.00	0.125	48.0	1.95	4.18	14.05	149.1	152.0	1.018
Round	6.00	0.061	48.0	1.18	3.05	27.10	134.9	153.4	1.140
Round	6.00	0.061	48.0	1.18	3.75	27.10	152.8	162.2	1.062
Round	6.00	0.061	48.0	1.18	3.75	27.10	152.8	164.8	1.080
Round	5.00	0.095	42.0	1.40	5.10	17.91	142.1	141.0	0.993
Round	5.00	0.095	42.0	1.40	5.10	17.91	142.1	140.0	0.985
Round	5.00	0.095	42.0	1.40	5.10	17.91	142.1	148.0	1.041

Table 1.2 - Bending Plus Axial Load Data For CFT Columns, Furlong Tests (1968)

Shape	Tube Size	Wall Thickness	f_y	A_s	f'_c	A_c	P_o Computed	M_o Computed	P_u Measured	M_u Measured	P_o/P_u	M_o/M_u
	In.	In.	ksi	in^2	ksi	in^2	kips	kip-in	kips	kip-in		
Square	5.00	0.189	70.3	3.64	6.50	21.00	393.8	401.0	200.0	310.0	0.508	0.673
									150.0	365.0	0.381	0.793
									150.0	430.0	0.381	0.935
									100.0	450.0	0.254	0.978
Round	4.50	0.125	60.0	1.73	4.20	14.17	163.4	143.0	100.0	100.0	0.612	0.700
									90.0	106.0	0.551	0.741
									75.0	131.0	0.459	0.917
									50.0	141.0	0.306	0.985
									25.0	144.0	0.153	1.007
Square	4.00	0.084	48.0	1.33	3.40	14.67	110.8	93.2	84.0	44.3	0.759	0.476
									84.0	44.6	0.759	0.479
									54.4	91.7	0.492	0.986
									20.2	104.9	0.182	1.128
									20.10	114.10	0.181	1.229
Round	6.00	0.061	48.00	1.18	3.75	27.10	152.80	100.80	127.60	88.00	0.836	0.874
					3.75		152.80		94.80	157.60	0.606	1.562
					3.75		152.80		64.30	152.70	0.422	1.515
					3.05		134.90		30.60	143.40	0.227	1.420
					3.05		134.90		30.40	133.10	0.226	1.322
Square	4.00	0.125	48.00	1.95	4.18	14.05	149.00	137.00	98.40	119.00	0.661	0.870
									68.80	162.00	0.463	1.180
									67.80	162.00	0.456	1.180
									58.60	190.00	0.394	1.386
									29.00	209.00	0.195	1.526
									28.80	193.00	0.194	1.408
									9.00	165.00	0.065	1.203
									0.00	204.00	0.000	1.489
Round	5.00	0.095	42.00	1.40	5.10	17.90	142.10	96.60	127.80	78.00	0.898	0.821
									120.00	112.00	0.845	1.160
									90.00	141.00	0.634	1.460
									79.00	140.00	0.556	1.450
									78.50	126.40	0.552	1.310
									77.60	140.50	0.546	1.454
									68.80	150.50	0.483	1.560
									60.00	156.00	0.422	1.613
									58.60	155.50	0.412	1.610
									39.30	145.60	0.276	1.507
									20.00	140.80	0.141	1.457
									9.80	130.00	0.069	1.346

Table 1.3 - Dimensional Properties of the Steel Tubes, Tomii et al. (1977)

Shape of Cross Section	Circular		Octagonal	Square
Diameter or Length of Side (in)	3.94	5.91	5.91	5.91
Wall Thickness (in)	0.118, 0.157, 0.213	.79, .126, .169	.79, .126, .169	.79, .126, .169
Diameter to Thickness Ratio	33, 25, 19	75, 47, 35	75, 47, 35	75, 47, 35
Length of Column (in)	3.3, 7.3, 11.2, 15.2, 19.1, 23.0, 27.0	11.8, 17.7, 23.6, 29.5	11.8, 17.7, 23.6, 29.5	11.8, 17.7, 23.6, 29.5
Effective Length of Column (in)	12.8, 16.7, 20.7, 24.6, 28.5, 32.5, 36.4	11.8 17.7, 23.6, 29.5	11.8, 17.7, 23.6, 29.5	11.8, 17.7, 23.6, 29.5
Slenderness Ratio	12.8 to 36.4	7.9 to 19.9	7.7 to 19.5	6.9 to 17.0
Effective Slenderness Ratio	10.6 to 30.3	6.7 to 17.5	6.4 to 17.0	5.6 to 14.8
Total Number of Specimens	70	78	60	60

Table 1.4 - Measured Dimensions of Specimens in Inches, Morino et al. (1992)

Specimen	b_c	t_c	b_p	h_p	t_p	l_b	h	h'
SCP	4.93	0.23	4.92	9.16	0.17	70.87	44.67	39.80
SCP00	4.92	0.23	4.92	9.08	0.17	70.94	44.64	39.74
SCP11	9.25	0.23	4.90	9.09	0.17	70.89	44.63	39.74
SCP20	9.25	0.23	4.90	9.13	0.17	71.04	44.59	39.67
SCP31	4.92	0.23	4.90	9.13	0.17	70.96	44.64	39.72
SCC	4.93	0.23	4.90	9.09	0.37	70.81	44.62	39.72
SCC00	4.92	0.23	4.91	9.12	0.35	70.87	44.62	39.59
SCC11	4.92	0.23	4.91	9.09	0.35	70.87	44.62	39.72
SCC20	4.92	0.23	4.92	9.10	0.35	70.98	44.57	39.67
SCC31	4.92	0.23	4.91	9.07	0.35	70.83	44.59	39.70

b_c : width of column
t_c : thickness of column
b_p : width of panel
h_p : height of panel
t_p : thickness of panel
l_b : half length of beam
h : half length of column
h' : half clear length of column

Table 1.5 - List of Specimens, Kimura et al (1984) Test Matrix

Specimen	Void Ratio %	Thickness in	$_sN_o$ ton	N_o ton
B 1-3	0.0	0.0	337	469
B 4	31.4	6.0	337	469
B 5-6	31.4	6.0	307	439
B 7-9	31.4	13.8	307	439
B 10	56.6	6.0	323	449
B 11	56.6	13.8	323	449
A 1	31.4	6.0	337	469
A 2	0.0	0.0	337	469
A 3	31.4	6.0	307	439
A 4	31.4	13.8	307	439
A 5	56.6	6.0	323	449
A 6	56.6	13.8	323	449

Table 1.6 - Dimensions of Specimens in Inches, Yokoyama et al. (1991) Test Matrix

Specimen	Column	Beam	Inner Ring Stiffener
	${}_cB \times {}_cB \times {}_ct$	${}_bH \times {}_bB \times {}_bt_w \times {}_bt_f \times {}_rt$	$d^B \times d^t$
IS5 - 8 I	11.81 x 11.81 x 0.354	12.60 x 6.30 x 0.236 x 0.748 x 1.28	8.27 x 0.354
IS7 - 13 I	11.81 x 11.81 x 0.354	15.75 x 8.27 x 0.236 x 0.748 x 1.28	6.30 x 0.354
IS7 - 18 IV	11.81 x 11.81 x 0.236	15.75 x 8.27 x 0.236 x 0.748 x 1.43	4.72 x 0.748
IS9 - 12 I	11.81 x 11.81 x 0.354	15.75 x 10.24 x 0.236 x 0.748 x 1.28	8.27 x 0.354

Table 1.7 - Details of Specimens in Inches, Zhijun and Shanzhang (1991) Test Matrix

Loading Manner	Specimen	Type	Steel Tub			Stiffener Ring		
			D	t	H	B_f	h_s	t_s
One-way tension w/o ax. compress.	1,2	I	8.39	0.197	15.74	4.33	1.26	0.315
	3,4	IV	8.39	0.197	15.74	5.51	2.36	0.315
One-way tension with ax. compress.	5	I	8.39	0.118	15.74	4.33	1.26	0.315
	6	I	8.39	0.118	15.74	4.33	1.26	0.315
	7	IV	8.39	0.118	15.74	5.51	1.38	0.315
	8	IV	8.39	0.118	15.74	5.51	1.38	0.315
Two-way tension with axial compression	9	I	8.39	0.118	15.74	4.33	2.36	0.315
	10	I	8.39	0.118	15.74	4.33	2.36	0.315
	11	I	8.39	0.118	15.74	4.33	2.36	0.315
	12	I	8.39	0.118	15.74	4.33	2.36	0.315
	13	IV	8.39	0.118	15.74	5.51	1.38	0.315
	14	IV	8.39	0.118	15.74	5.51	1.38	0.315
Two-way tension with varying axial compress.	15	I	8.35	0.118	15.74	4.33	1.26	0.291
	16	I	8.35	0.118	15.74	4.33	1.26	0.291
	17	I	8.35	0.118	15.74	4.33	1.26	0.291
	18	I	8.35	0.118	15.74	4.33	1.26	0.291
	19	I	8.35	0.118	15.74	4.33	1.26	0.291
	20	I	8.35	0.12	15.74	4.33	1.26	0.291

Table 1.8 - Design Strength and Test Results, Matsui (1985)

Specimen Name	Steel				Concrete	Load	Design Strength		Test	Qmax / sQa	Mode of Failure
	Stiffener Beam		Column								
	Yield Stress (ksi)	Ulitmate Stress (ksi)	Yield Stress (ksi)	Ultimate Stress (ksi)	Fc (psi)	N (kip)	sQa (kip)	pQa (kip)	Qmax (kip)		
A-M*	43.1	59.0	49.8	60.0	4082	172.0	9.50	15.83	16.27	1.71	fracture of
A-C*	43.1	59.0	49.8	60.0	4082	169.8	9.04	15.72	14.84	1.64	stiffener
B-M*	46.1	60.6	49.8	60.2	4082	196.2	11.88	15.90	20.04	1.69	"
B-C*	46.1	60.6	49.8	60.2	4082	169.8	11.64	15.74	17.00	1.46	"
C-M*	46.9	60.4	59.7	67.0	4082	189.6	11.66	17.79	21.38	1.83	local buckling
C-C*	46.9	60.4	59.7	67.0	4082	189.6	12.06	17.88	20.17	1.67	of panel

Table 1.9 - Details of Specimens, Picard and Giroux Tests (1976)

Category	No. of Specimens	Column Size	Beam Size	Strap Angles	Net Area of Strap Angles	Length of Strap Angles Top	Length of Strap Angles Bottom
		[in]	[in]	[in]	[in^2]	[in]	[in]
A	4	8x8x1/4	W8x35	4x3x5/8	2.50	22.50	22.50
B	4	10x10x1/4	W10x49	5x5x1	5.00	28.50	28.50
C	5	8x8x3/8	W8x35	4x4x3/4	3.00	28.00	22.50
D	3	8x8x3/8	W8x35	4x4x5/8	2.50	28.00	22.50
E	3	8x8x3/8	W8x35	4x4x9/16	2.25	28.00	22.50
F	2	8x8x3/8	W8x35	4x4x3/4	3.00	17.50	14.75

Table 1.10 - Details of Welding of Each Strap Angle, Picard and Giroux Tests (1976)

	Welding to the Tube		Welding to One Beam			
			Top Angle		Bottom Angle	
Category	Size of Fillet Weld [in]	Total Length of Weld [in]	Size of Fillet Weld [in]	Total Length of Weld [in]	Size of Fillet Weld [in]	Total Length of Weld [in]
A	0.250	14	0.44	9	0.44	9
B	0.250	18	0.44	13	0.44	13
C,D,E	0.375	14	0.50	8	0.44	10
F*	0.375	18	0.50	8	0.44	10

*One-sided connection.

Table 1.11 - Details of Specimens, Picard and Giroux Tests (1976)

Category	No. of Specimens	Beam Size	Strap Angles	Net Area of Strap Angles	Length of Strap Angles		Web Connection
					Top	Bottom	
		[in]	[in]	[in^2]	[in]	[in]	[in]
G	1	W8X48	4X4X1	4.00	30.5	30.5	plate 5x3 1/2x1/4*
H	5	W12X45	5X5X1/4	3.75	30.5	30.5	plate 5x3 1/2x1/4*
I	1	W12X40	4X4X3/4	3.00	30.5	30.5	plate 5x3 1/2x1/4*
J	1	W12X45	5X5X3/4	3.75	40.0	30.5	plate 5x3 1/2x1/4*
K	1	W12X40	4X4X3/4	3.00	38.0	30.5	plate 5x3 1/2x1/4*
L	3	W12X45	5X5X3/4	3.75	40.0	30.5	2 angles 4x4x1/4[1]
M	1	W12X40	4X4X3/4	3.00	38.0	30.5	2 angles 4x4x1/4[1]

* Plate welded to tubular column and bolted to beam web.

[1] Two angles welded to tubular column and beam web.

Table 1.12 - Details of Welding of Each Strap Angle
Picard and Giroux Tests (1977)

	Welding to One Beam			
	Top Angle		Bottom Angle	
Category	Size of Fillet Weld [in]	Total Length of Weld [in]	Size of Fillet Weld [in]	Total Length of Weld [in]
G	0.625	10.00	0.625	10.00
H	0.438	11.00	0.438	11.00
I	0.438	10.00	0.438	10.00
J, L	0.438	11.00	0.438	11.25
K, M	0.438	10.00	0.438	10.25

Table 1.13 - Ultimate Flexural Strength of Steel Portion [AIJ, 1987]

	Range of axial force	$_sM_U$
Open-web section under strong-axis bending	$0 \leq {}_sN_U \leq {}_sA \cdot {}_s\sigma_Y$	${}_sZ_p \cdot {}_s\sigma_Y - {}_sN_U \cdot {}_sd/2$
	$-{}_sA \cdot {}_s\sigma_Y \leq {}_sN_U \leq 0$	${}_sZ_p \cdot {}_s\sigma_Y + {}_sN_U \cdot {}_sd/2$
Cross-shaped open-web section	${}_sa_m \cdot {}_s\sigma_Y \leq {}_sN_U \leq {}_sA \cdot {}_s\sigma_Y$	${}_sZ_p \cdot {}_s\sigma_Y - \frac{{}_sd}{2}({}_sN_U - {}_sa_m \cdot {}_s\sigma_Y)$
	$-{}_sa_m \cdot {}_s\sigma_Y \leq {}_sN_U \leq {}_sa_m \cdot {}_s\sigma_Y$	${}_sZ_p \cdot {}_s\sigma_Y$
	$-{}_sA \cdot {}_s\sigma_Y \leq {}_sN_U \leq -{}_sa_m \cdot {}_s\sigma_Y$	${}_sZ_p \cdot {}_s\sigma_Y + \frac{{}_sd}{2}\left({}_sN_U + {}_sa_m \cdot {}_s\sigma_Y\right)$
Full-web section under strong-axis bending and rectangular tube	$\frac{{}_sa_w}{2} \cdot {}_s\sigma_Y \leq {}_sN_U \leq {}_sA \cdot {}_s\sigma_Y$	${}_sZ_p \cdot {}_s\sigma_Y - \frac{{}_sd}{2}\left({}_sN_U - \frac{1}{2}{}_sa_w \cdot {}_s\sigma_Y\right)$
	$-\frac{{}_sa_w}{2} \cdot {}_s\sigma_Y \leq {}_sN_U \leq \frac{{}_sa_w}{2} \cdot {}_s\sigma_Y$	${}_sZ_p \cdot {}_s\sigma_Y$
	$-{}_sA \cdot {}_s\sigma_Y \leq {}_sN_U \leq -\frac{{}_sa_w}{2} \cdot {}_s\sigma_Y$	${}_sZ_p \cdot {}_s\sigma_Y + \frac{{}_sd}{2}\left({}_sN_U + \frac{1}{2}{}_sa_w \cdot {}_s\sigma_Y\right)$
Full-web section under weak-axis bending	$({}_sa_f + {}_sa_w) \cdot {}_s\sigma_Y \leq {}_sN_U \leq {}_sA \cdot {}_s\sigma_Y$	${}_sZ_p \cdot {}_s\sigma_Y - \frac{{}_sb}{2}({}_sN_U - {}_sa_w \cdot {}_s\sigma_Y)$
	$-({}_sa_f + {}_sa_w) \cdot {}_s\sigma_Y \leq {}_sN_U \leq ({}_sa_f + {}_sa_w) \cdot {}_s\sigma_Y$	${}_sZ_p \cdot {}_s\sigma_Y$
	$-{}_sA \cdot {}_s\sigma_Y \leq {}_sN_U \leq -({}_sa_f + {}_sa_w) \cdot {}_s\sigma_Y$	${}_sZ_p \cdot {}_s\sigma_Y + \frac{b_f}{2}({}_sN_U + {}_sa_w \cdot {}_s\sigma_Y)$
Cross-shaped full-web section	$\left(2{}_sa_f + \frac{3{}_sa_w}{2}\right) \cdot {}_s\sigma_Y \leq {}_sN_U \leq {}_sA \cdot {}_s\sigma_Y$	${}_sd \cdot \frac{{}_sA}{2} \cdot {}_s\sigma_Y - \frac{{}_sd}{2} \cdot {}_sN_U$
	$\left({}_sa_f + \frac{3}{2}{}_sa_w\right) \cdot {}_s\sigma_Y \leq {}_sN_U \leq \left(2{}_sa_f + \frac{3{}_sa_w}{2}\right) \cdot {}_s\sigma_Y$	${}_sZ_p \cdot {}_s\sigma_Y - \frac{b_f}{2}\left({}_sN_U - \frac{3}{2}{}_sa_w \cdot {}_s\sigma_Y\right)$
	$-\left({}_sa_f + \frac{3}{2}{}_sa_w\right) \cdot {}_s\sigma_Y \leq {}_sN_U \leq \left({}_sa_f + \frac{3}{2}{}_sa_w\right) \cdot {}_s\sigma_Y$	${}_sZ_p \cdot {}_s\sigma_Y$
	$-\left(2{}_sa_f + \frac{3{}_sa_w}{2}\right) \cdot {}_s\sigma_Y \leq {}_sN_U \leq -\left({}_sa_f + \frac{3}{2}{}_sa_w\right) \cdot {}_s\sigma_Y$	${}_sZ_p \cdot {}_s\sigma_Y + \frac{b_f}{2}\left({}_sN_U + \frac{3}{2}{}_sa_w \cdot {}_s\sigma_Y\right)$
	$-{}_sA \cdot {}_s\sigma_Y \leq {}_sN_U \leq -\left(2{}_sa_f + \frac{3{}_sa_w}{2}\right) \cdot {}_s\sigma_Y$	${}_sd\frac{{}_sA}{2} \cdot {}_s\sigma_Y + \frac{{}_sd}{2} \cdot {}_sN_U$
Circular tube	$0.2{}_sA \cdot {}_s\sigma_Y \leq {}_sN_U \leq {}_sA \cdot {}_s\sigma_Y$	$1.25\left(1 - \frac{{}_sN_U}{{}_sA \cdot {}_s\sigma_Y}\right){}_sZ_p \cdot {}_s\sigma_Y$
	$-0.2{}_sA \cdot {}_s\sigma_Y \leq {}_sN_U \leq 0.2{}_sA \cdot {}_s\sigma_Y$	${}_sZ_p \cdot {}_s\sigma_Y$
	$-{}_sA \cdot {}_s\sigma_Y \leq {}_sN_U \leq -0.2{}_sA \cdot {}_s\sigma_Y$	$1.25\left(1 + \frac{{}_sN_U}{{}_sA \cdot {}_s\sigma_Y}\right){}_sZ_p \cdot {}_s\sigma_Y$

Table 1.14 - Ultimate Flexural Strength of Symmetrical Hollow Concrete Section [AIJ, 1987]

	x_{n1}	${}_cN_U/(bD\cdot F_c)$	${}_cM_U/(bD^2\cdot F_c)$
Square-hollow rectangular section	$0\leqq x_{n1}\leqq {}_cd_1$	—	$\frac{1}{2}\frac{{}_cN_U}{bD\cdot F_c}\left(1-\frac{1}{{}_cr_U}\frac{{}_cN_U}{bD\cdot F_c}\right)$
	${}_cd_1\leqq x_{n1}\leqq 1-{}_cd_1$	${}_cr_U\left\{x_{n1}-\frac{D}{b}(1-2{}_cd_1)\times(x_{n1}-{}_cd_1)\right\}$	${}_cr_U\left\{\frac{x_{n1}(1-x_{n1})}{2}-\frac{D}{b}\times\frac{(1-2{}_cd_1)(x_{n1}-{}_cd_1)(1-x_{n1}-{}_cd_1)}{2}\right\}$
	$1-{}_cd_1\leqq x_{n1}\leqq 1$	${}_cr_U\left\{x_{n1}-\frac{D}{b}(1-2{}_cd_1)^2\right\}$	${}_cr_U\frac{x_{n1}(1-x_{n1})}{2}$
Circular-hollow rectangular section	$0\leqq x_{n1}\leqq {}_cd_1$	—	$\frac{1}{2}\frac{{}_cN_U}{bD\cdot F_c}\left(1-\frac{1}{{}_cr_U}\frac{{}_cN_U}{bD\cdot F_c}\right)$
	${}_cd_1\leqq x_{n1}\leqq 1-{}_cd_1$	${}_cr_U\left\{x_{n1}-\frac{D}{b}\frac{(1-{}_cd_1)^2}{4}\cdot\times(\theta_n-\sin\theta_n\cdot\cos\theta_n)\right\}$	${}_cr_U\left\{\frac{x_{n1}(1-x_{n1})}{2}-\frac{D}{b}\frac{(1-2{}_cd_1)^3}{12}\sin^3\theta_n\right\}$
	$1-{}_cd_1\leqq x_{n1}\leqq 1$	${}_cr_U\left\{x_{n1}-\frac{D}{b}\frac{\pi(1-2{}_cd_1)^2}{4}\right\}$	${}_cr_U\frac{x_{n1}(1-x_{n1})}{2}$

$$\theta_n=\cos^{-1}\left(\frac{1-2x_{n1}}{1-2{}_cd_1}\right)$$

Table 1.15 - Ultimate Flexural Strength of Members [AIJ, 1987]

Rectangular section	${}_cM_U/(bD^2\cdot F_c)$	
	$\frac{1}{2}\frac{{}_cN_U}{bD\cdot F_c}\left(1-\frac{1}{{}_cr_U}\frac{{}_cN_U}{bD\cdot F_c}\right)$	
Circular section	${}_cN_U/({}_cD^2\cdot F_c)$	${}_cM_U/({}_cD^3\cdot F_c)$
	$\frac{{}_cr_U}{4}(\theta_n-\sin\theta_n\cdot\cos\theta_n)$	$\frac{{}_cr_U}{12}\sin^3\theta_n$

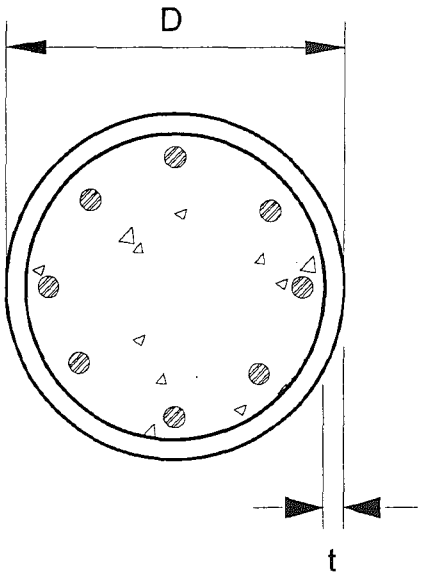

(i.) Circular steel tube filled with concrete

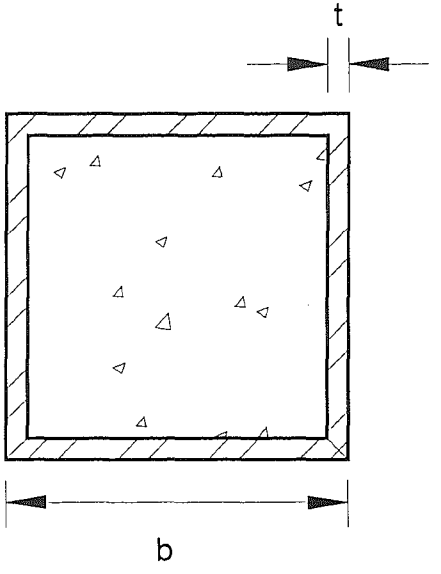

(ii.) Square steel tube filled with concrete

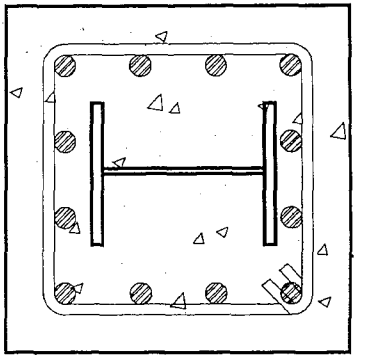

(iii.) Structural steel shape encased in reinforced concrete

Figure 1.1 Typical Forms of Composite Columns

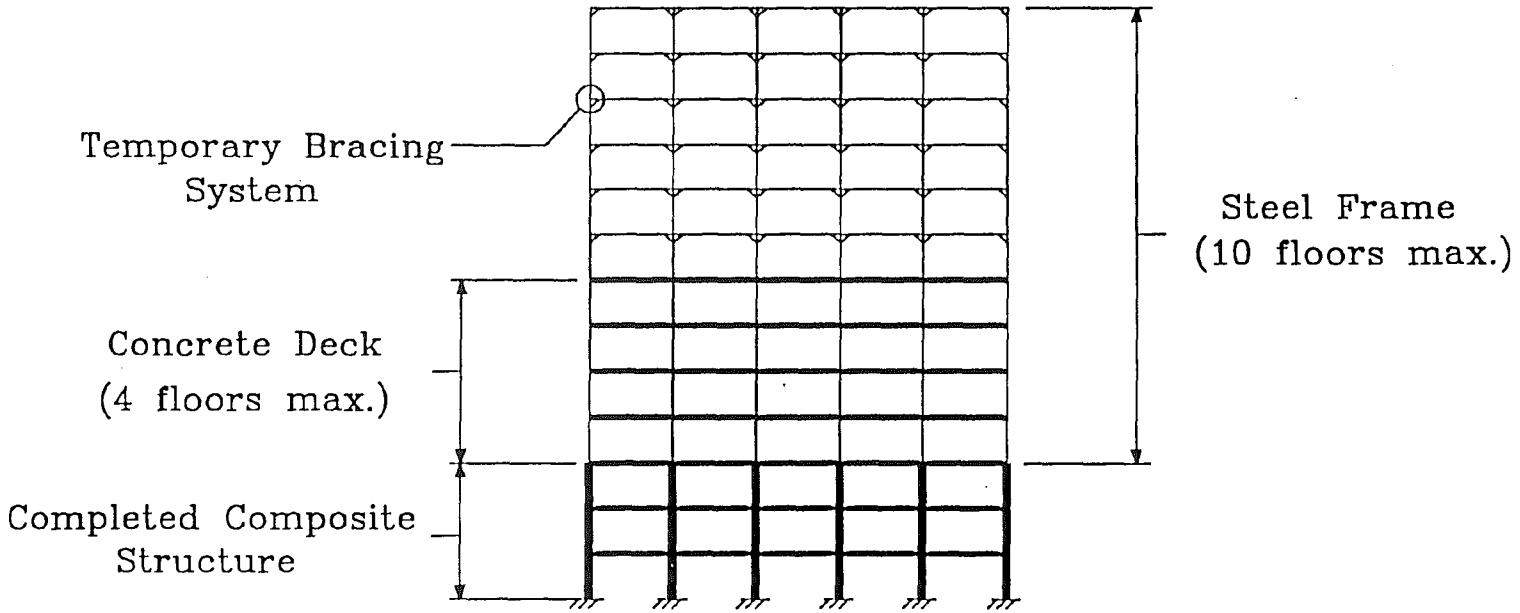

Figure 1.2 Construction Sequence of Building with SRC Composite Columns

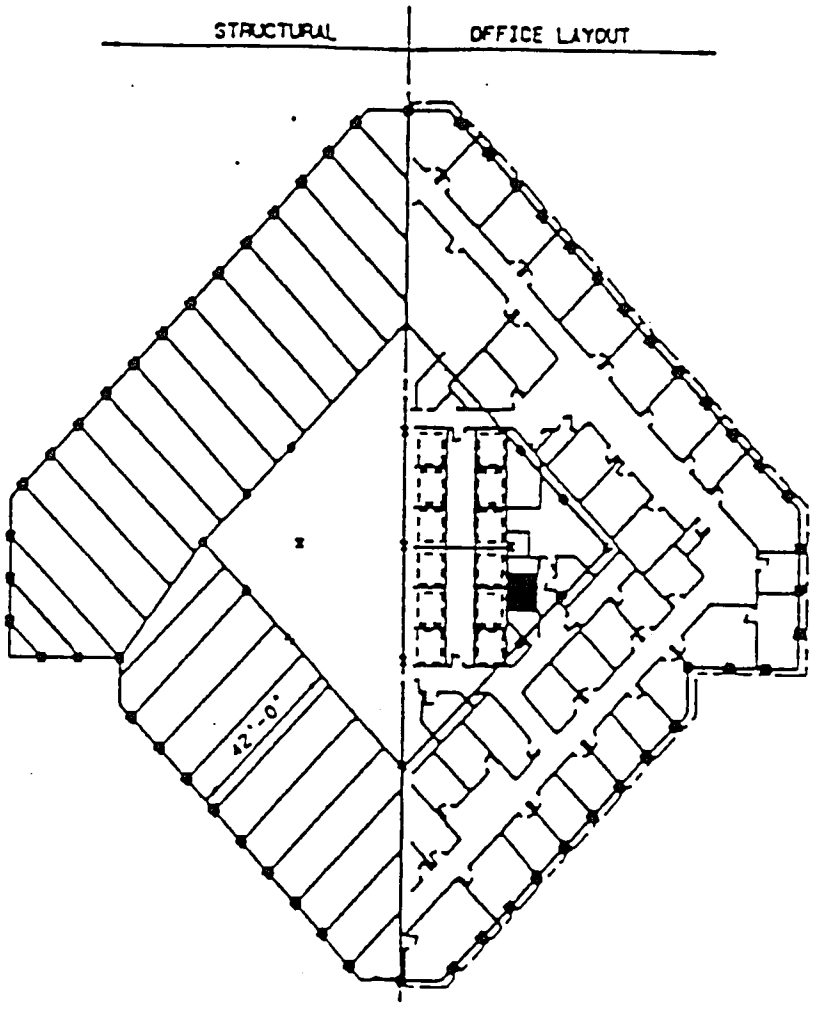

Figure 1.3 Three Houston Center Gulf Tower,
Composite Tube Frame [Griffis, 1987]

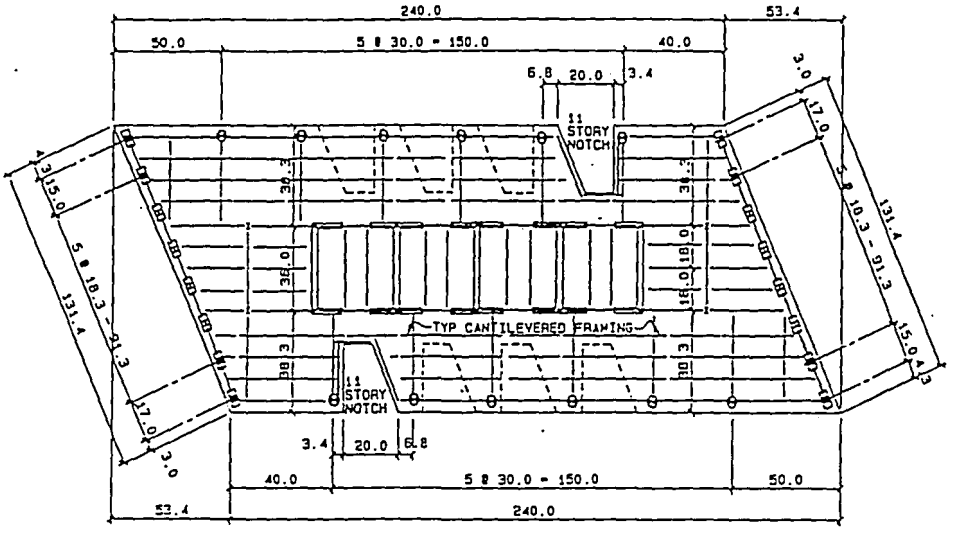

Floor Plan

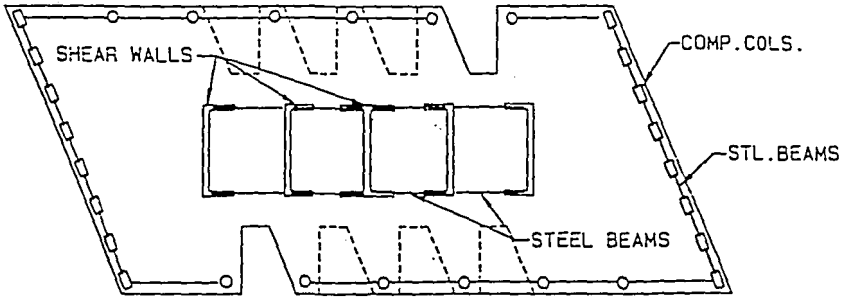

Composite Shear Wall and Perimeter Frame

Figure 1.4 First City Tower Composite Shear Wall and Composite Perimeter Frame [Griffis, 1987]

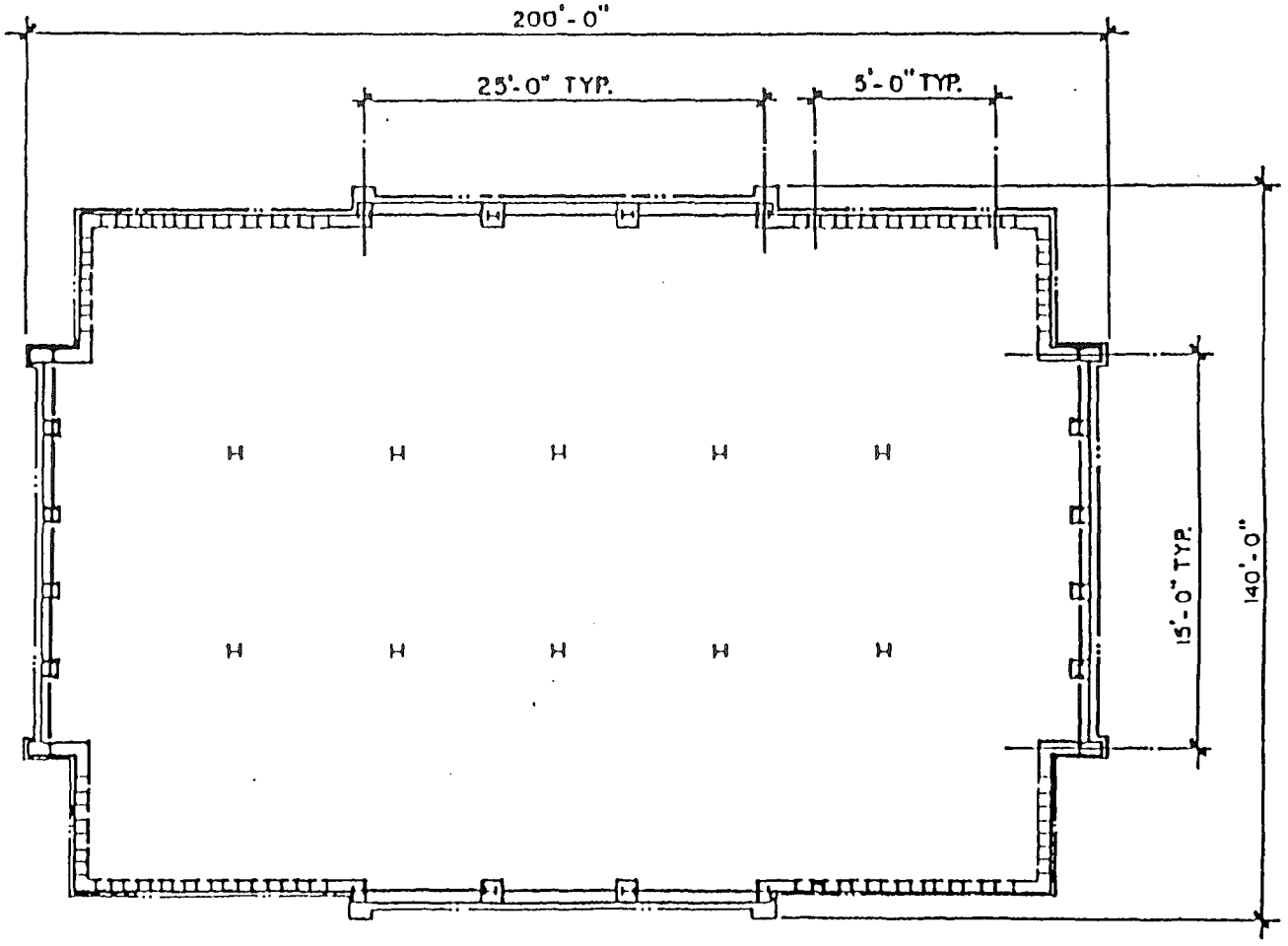

Figure 1.5 Momentum Place, System D-Punched Concrete Walls at Building Corners with Composite Column/Steel Spandrel Infills [Griffis, 1987]

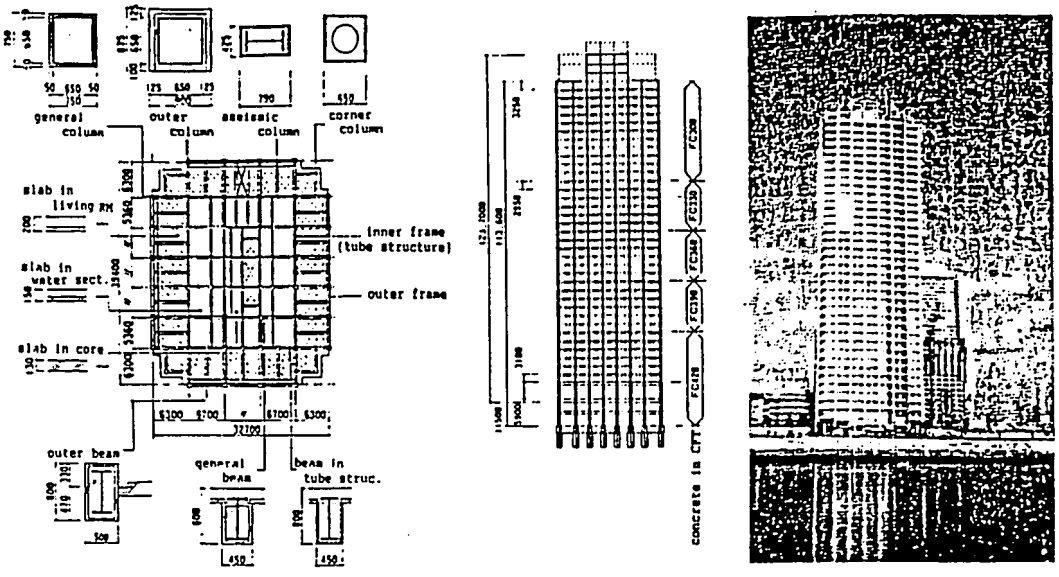

Figure 1.6 CFT Column High Rise Condominium, Tokyo [Endoh et al., 1991]

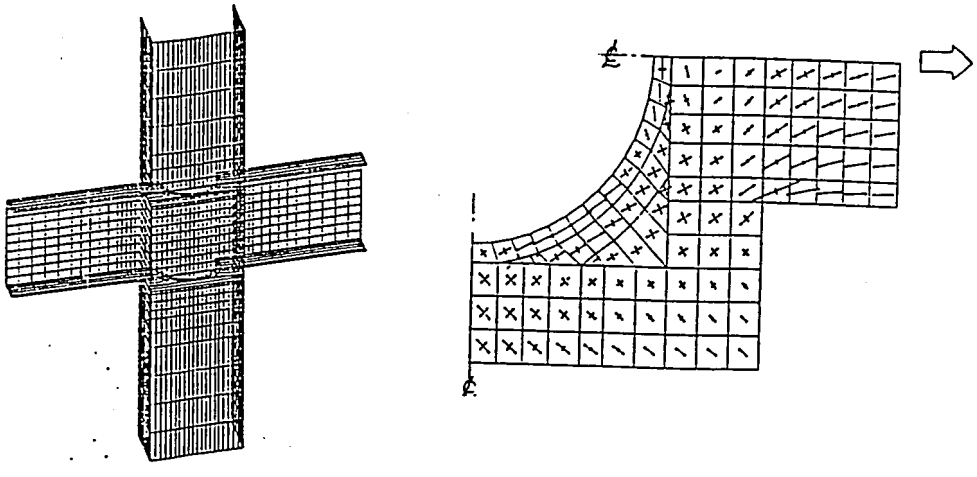

Figure 1.7 FEM Analytical Model of Connection and Stress Flow in Diaphragm [Endoh et al., 1991]

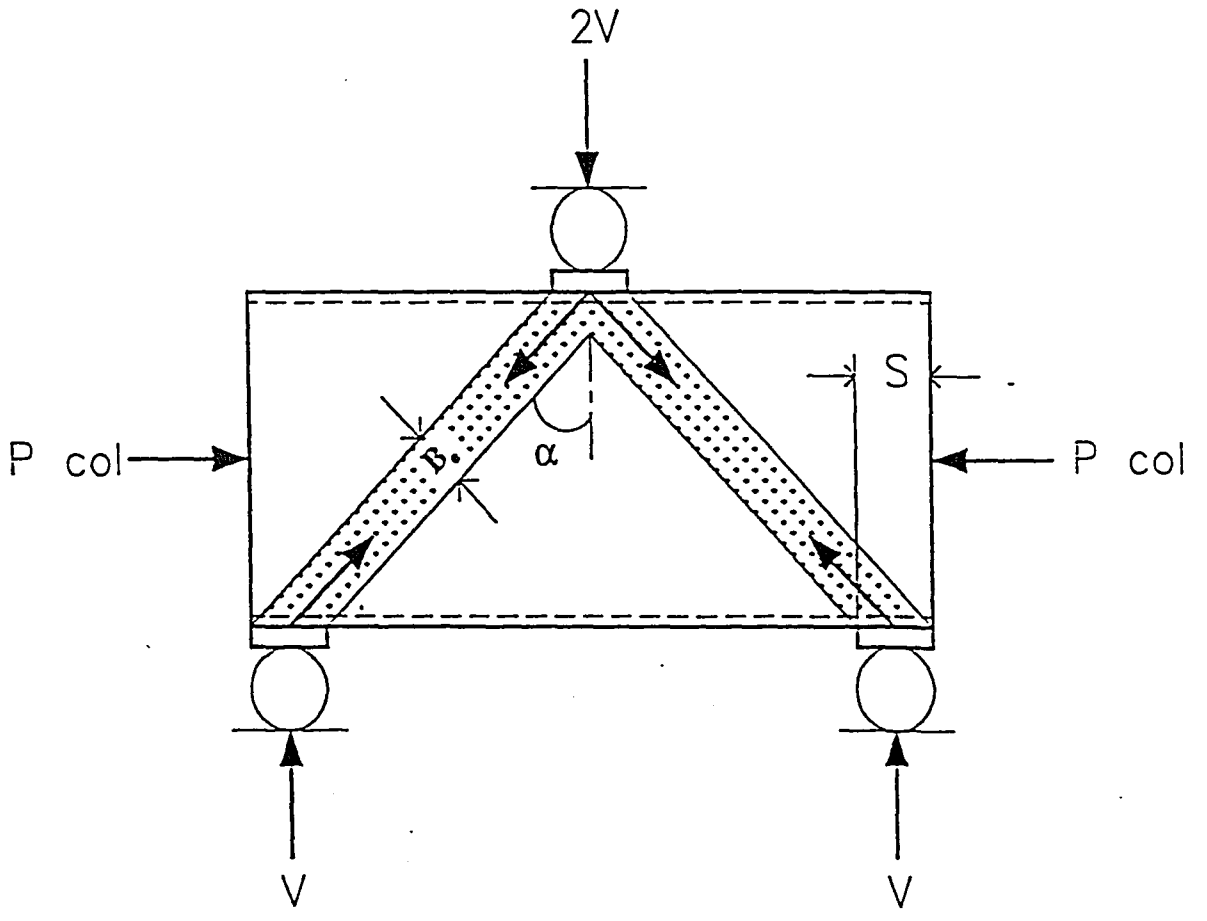

α = compression strut angle

S = bearing width

B_e = compression strut width

Figure 1.8 Schematic of Panel Zone Shear Test Set-Up

CFT PANEL ZONE SHEAR STRENGTH MODEL

KANATANI MODEL

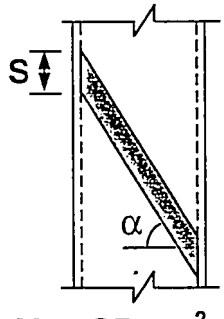

$V_c = SB\cos^2\alpha\, f'_c$

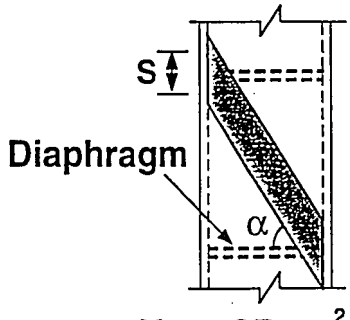

$V_c = 2SB\cos^2\alpha\, f'_c$

MODIFIED STRUT MODEL

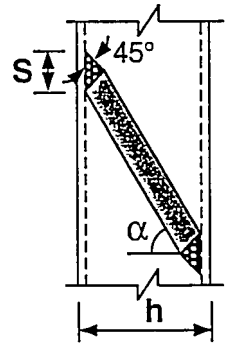

$V_c = SB\cos45°\cos\alpha\ 0.85\, f'_c$

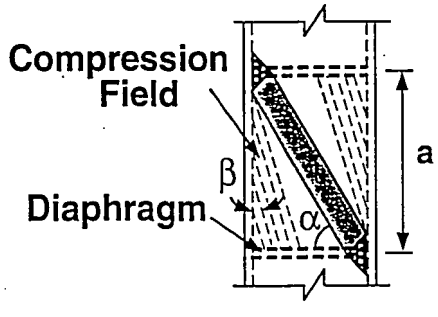

$V_c = SB\cos45°\cos\alpha\ 0.85f'_c + aB\sin^2\beta\ 0.85f'_c$

ACI

$V_c = Bh15\sqrt{f'_c}$ (No Diaphragm)

$V_c = Bh20\sqrt{f'_c}$ (Diaphragm)

Figure 1.9 CFT Panel Zone Shear Capacity Models

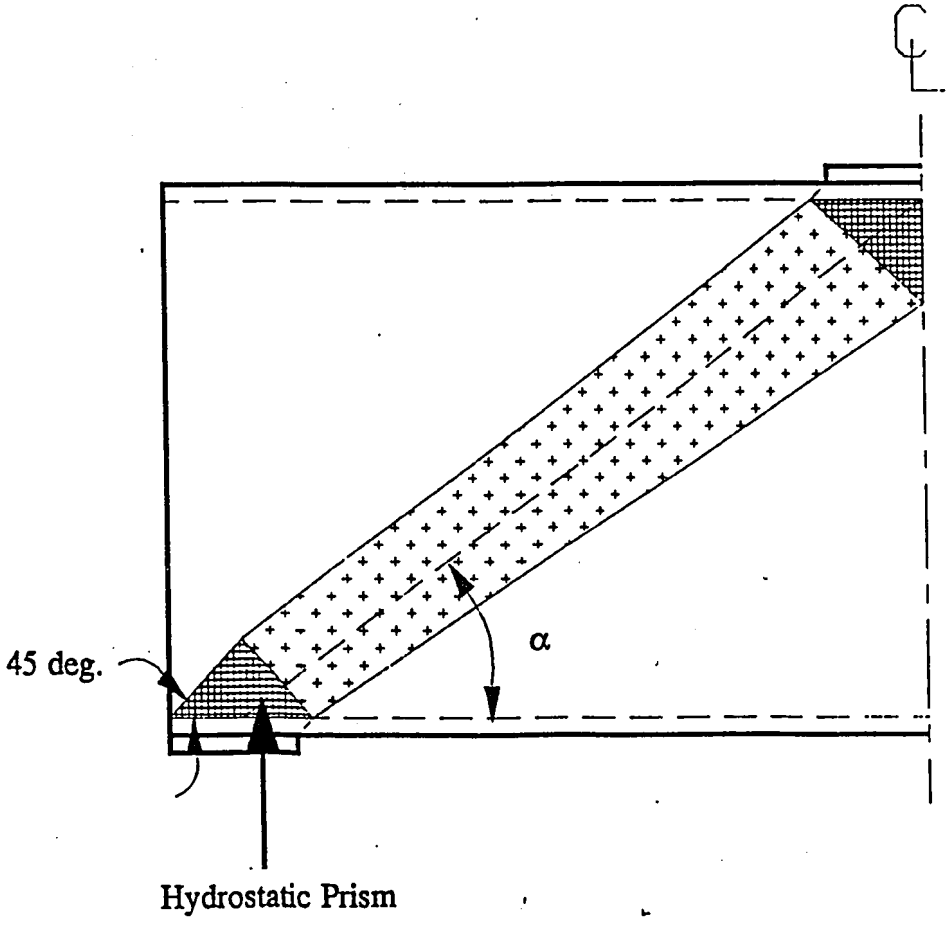

Figure 1.10 Hydrostatic Prism Formed Along Primary Compression Strut

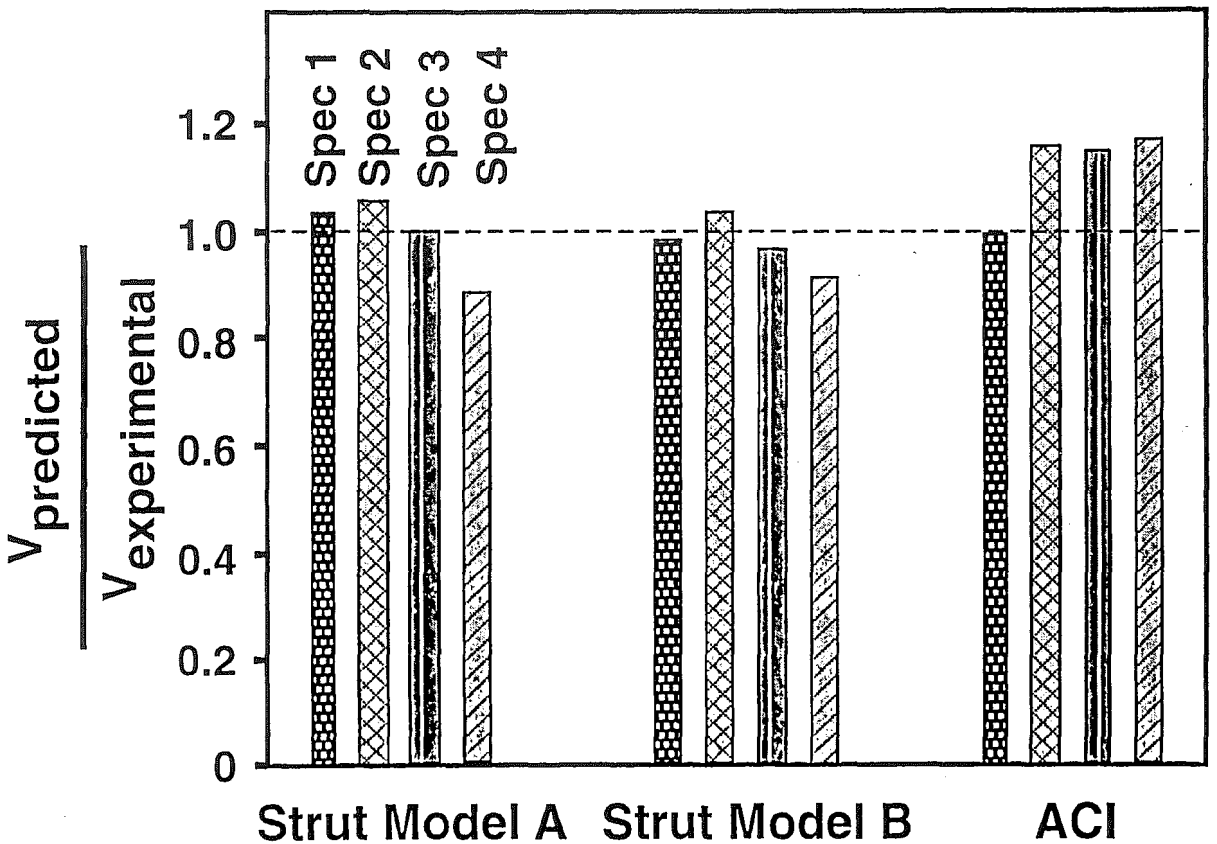

Figure 1.11 Comparison Between Predicted and Experimental Shear Capacity

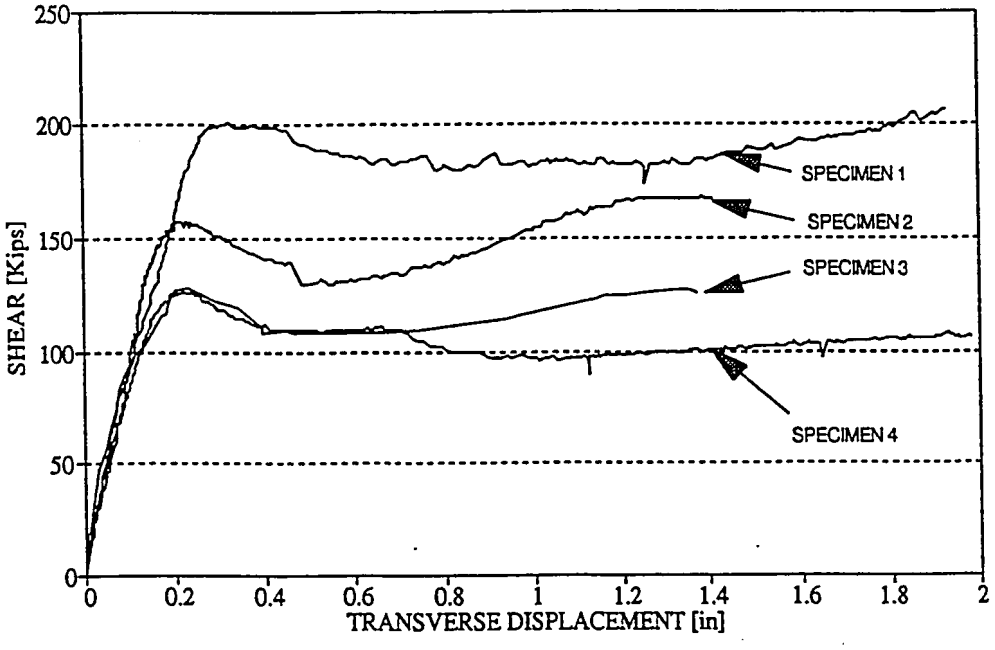

Figure 1.12 Load versus Transverse Displacement of CFT Panel Zone Test Specimens

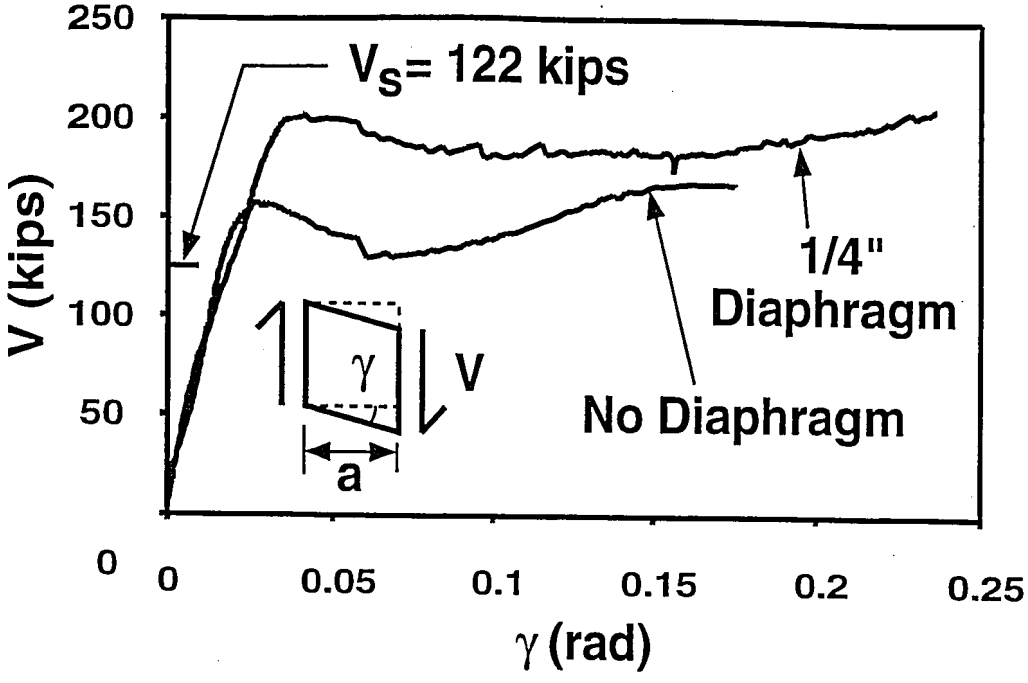

Figure 1.13 Effect of Diaphragm on Experimental Shear-Deformation Response

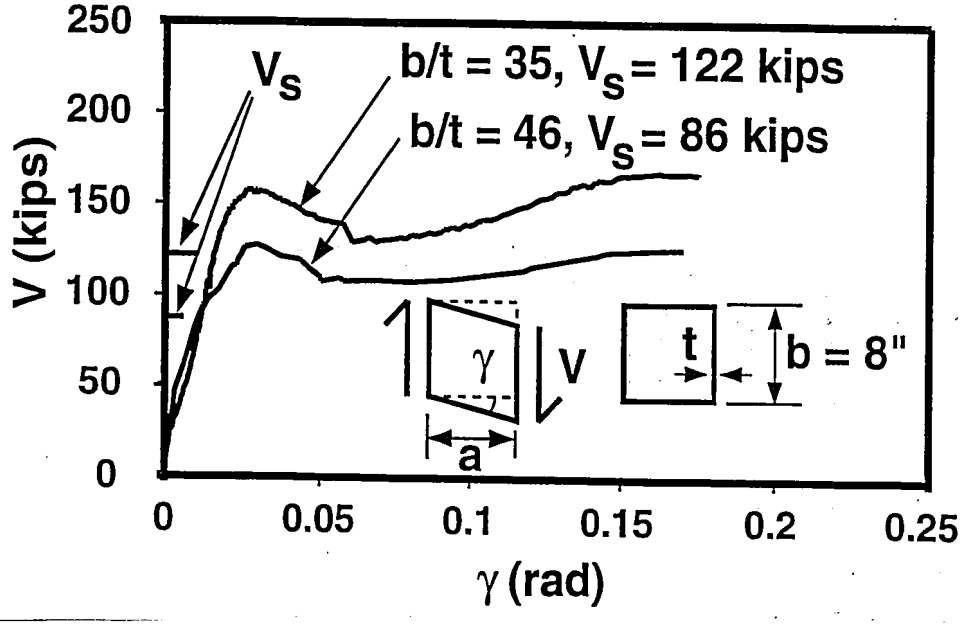

Figure 1.14 Effect of Tube Width-to-Thickness Ratio (b/t) on Experimental Shear-Deformation Response

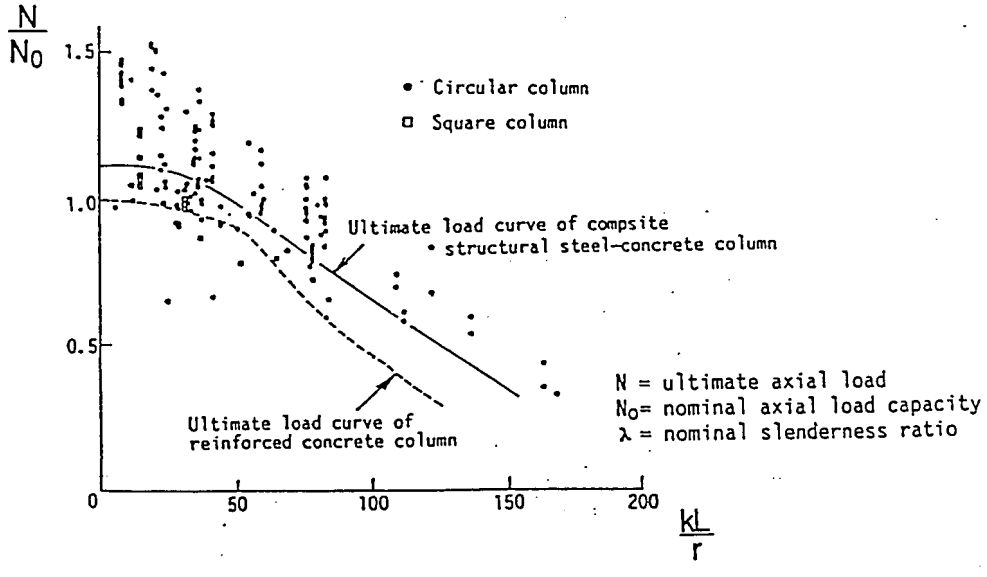

Figure 1.15 Ultimate Capacity of CFT Columns Subjected to Concentric Axial Load [Tomi, 1991]

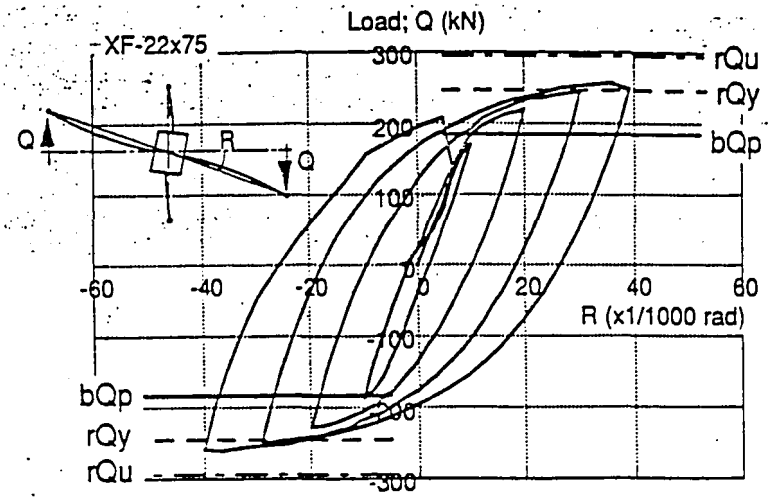

Figure 1.16 Load - Rotation Angle Correlation [Kato et al., 1992]

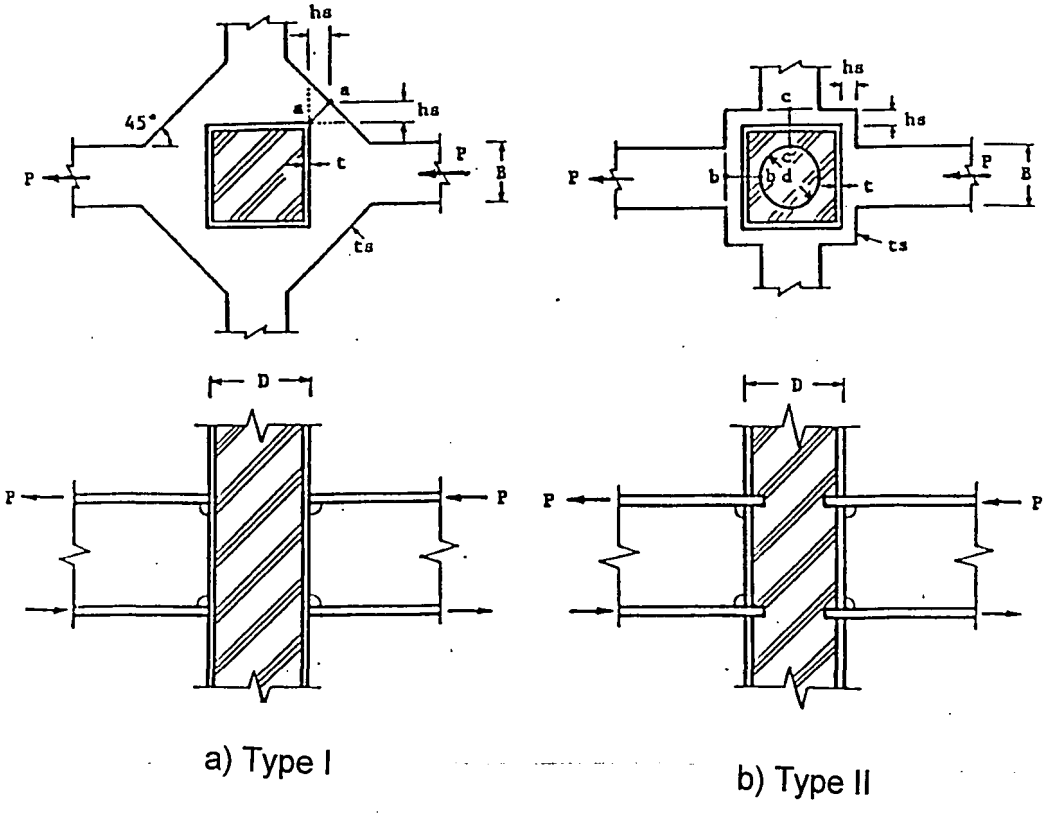

a) Type I

b) Type II

Figure 1.17 Beam-to-Column Connections [Matsui, 1985]

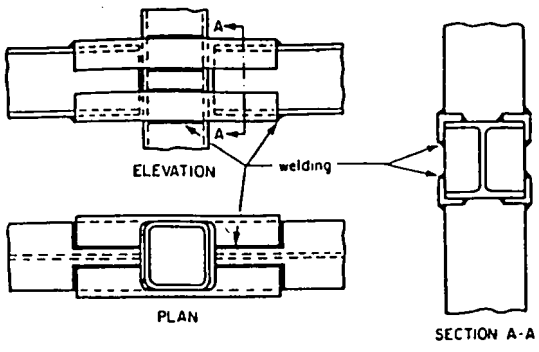

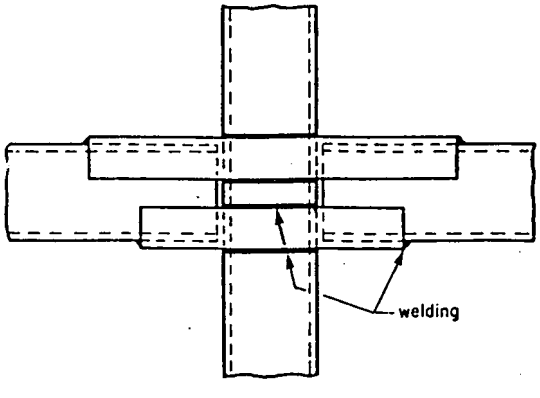

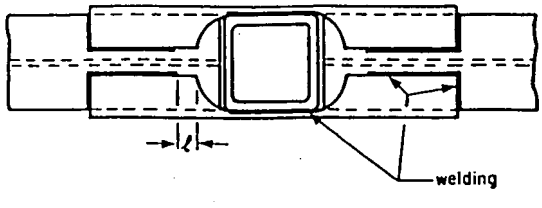

PLAN VIEW OF TOP STRAP ANGLES

Figure 1.18 Strap Angle Beam-to-CFT Moment Connections [Picard and Giroux, 1976]

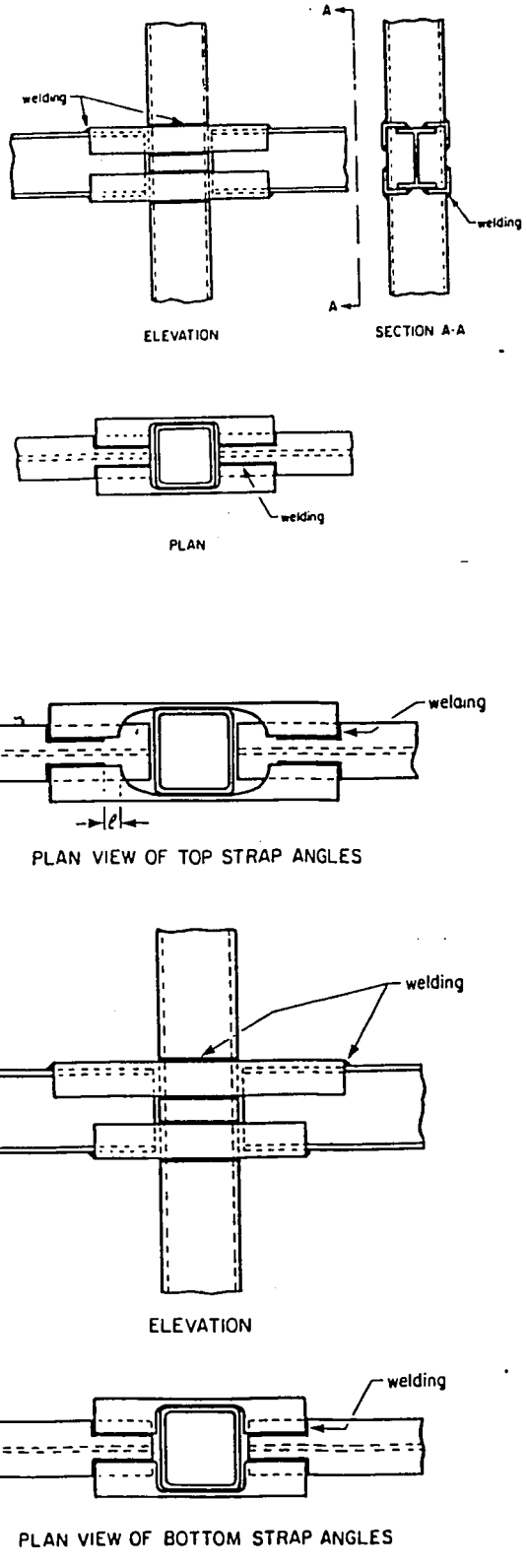

Figure 1.19 Revised Strap Angle Beam-to-CFT Moment Connections [Picard and Giroux, 1977]

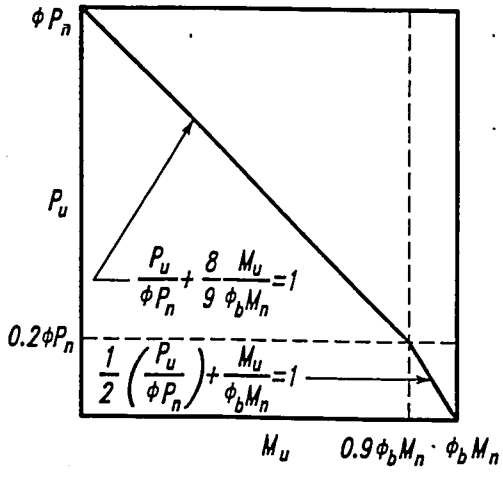

Figure 1.20 LRFD Beam-Column Interaction Equations [AISC, 1992]

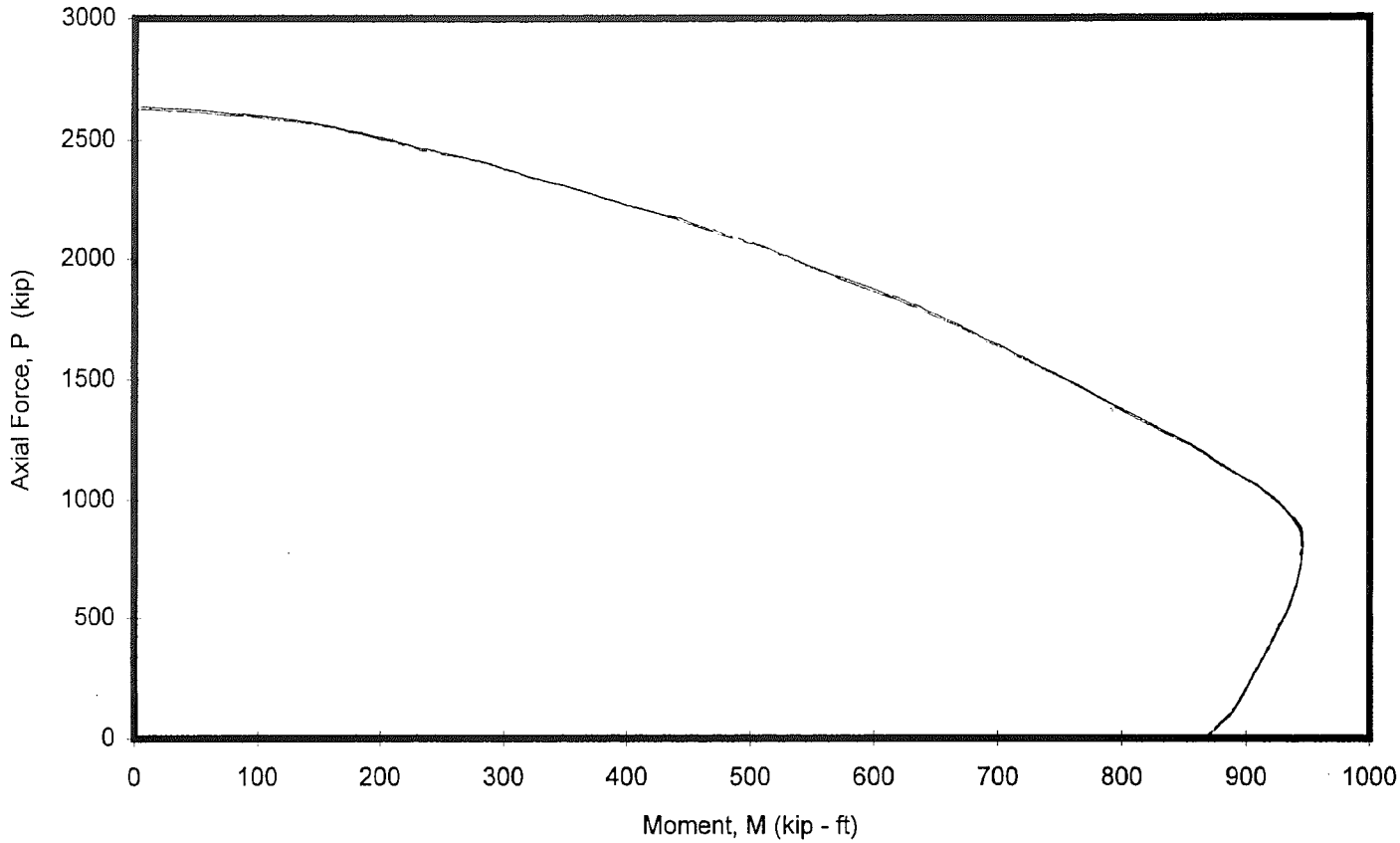

Figure 1.21 - CFT Interaction Curve, ACI Criteria with No Material Reduction Factors or Axial Strength Limitations

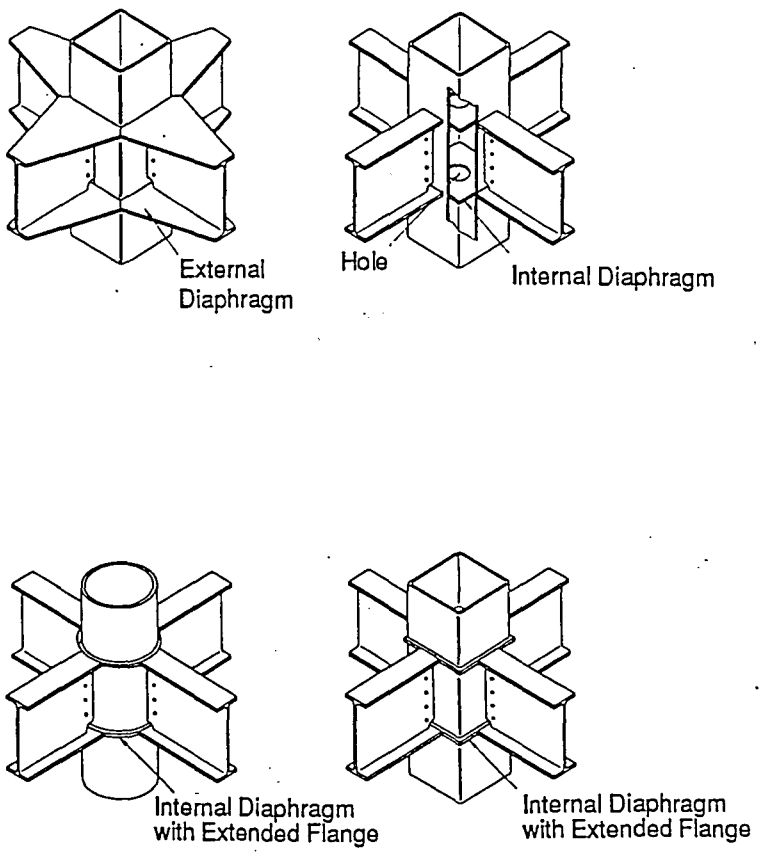

Figure 1.22 Typical CFT Column-to-Beam Connections [AIJ, 1987]

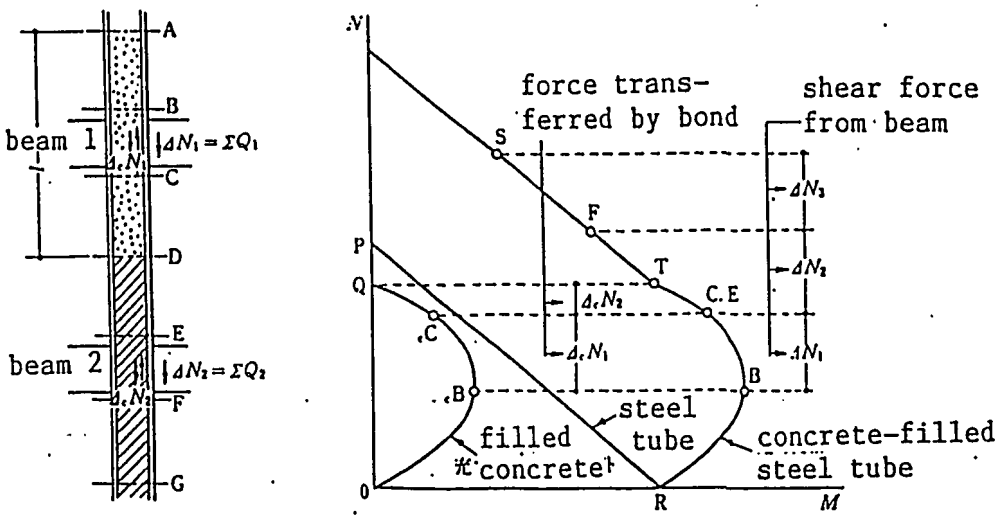

Figure 1.23 AIJ Beam-Column Interaction for CFT Columns [AIJ, 1987]

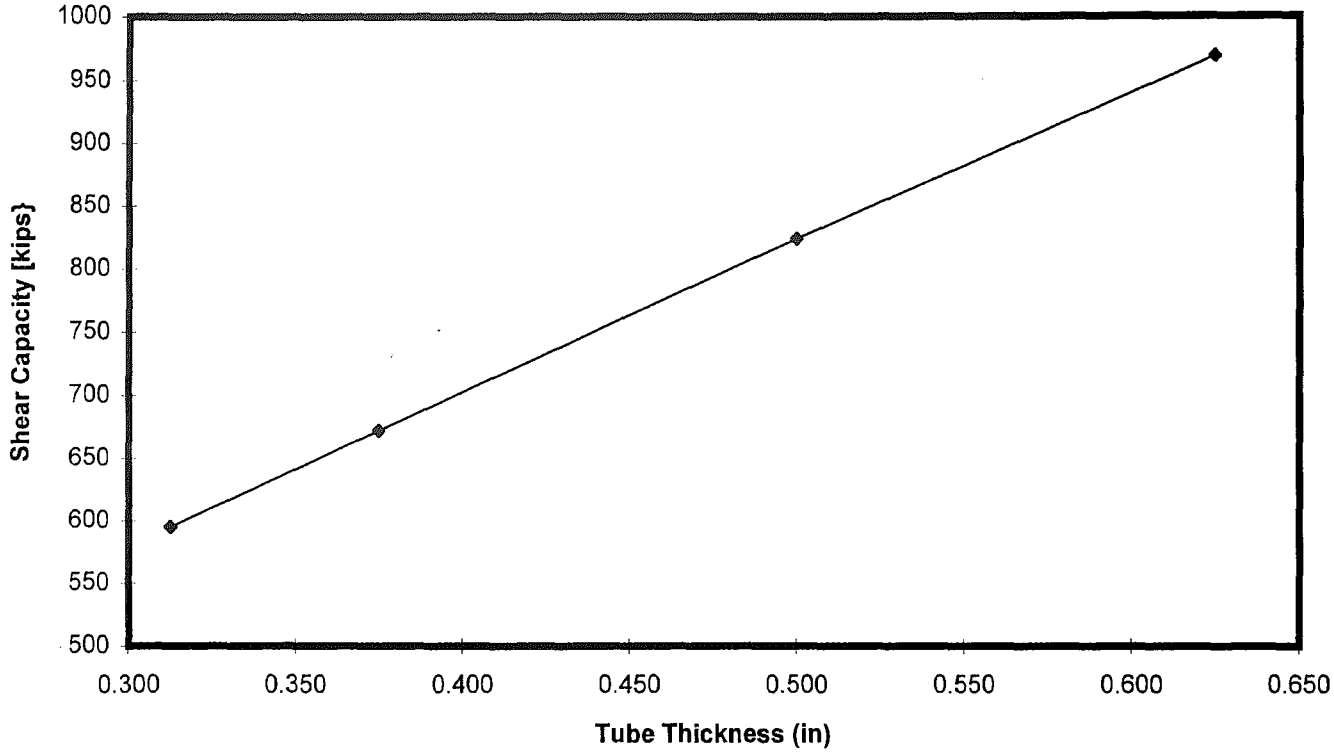

Figure 1.24 - Connection Shear Capacity per AIJ (1987) as a Function of CFT Wall Thickness

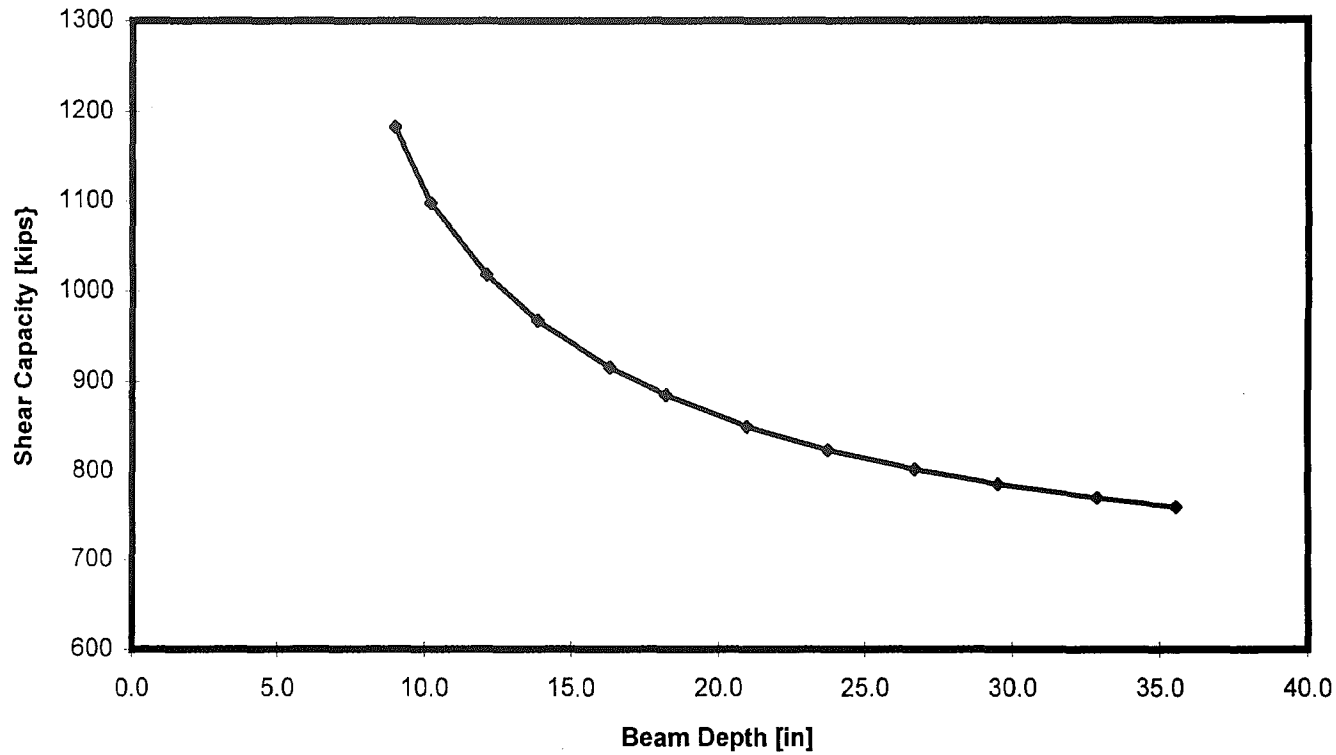

Figure 1.25 - Connection Shear Capacity per AIJ [1987] as a Function of Beam Depth

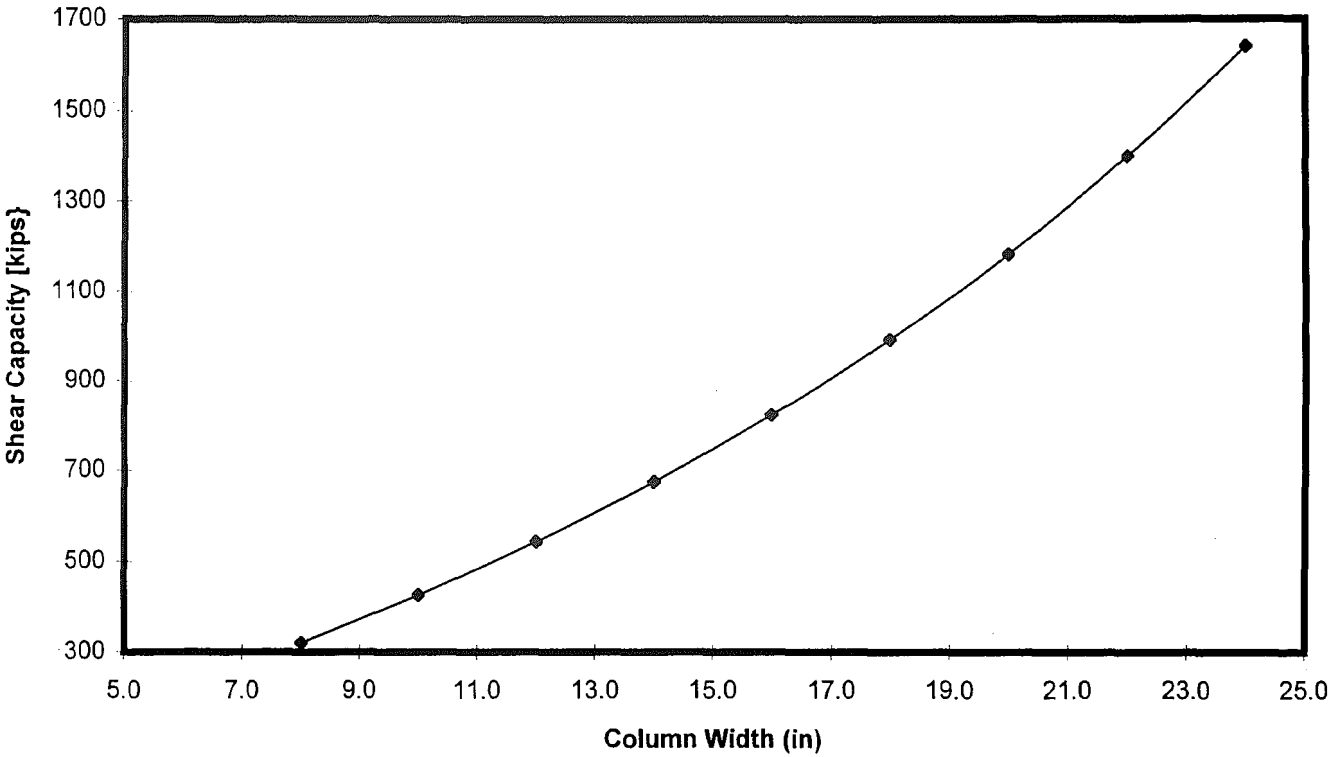

Figure 1.26 - Connection Shear Capacity per AIJ [1987] as a Function of Column Width.

Chapter 2

Experimental Program

2.1 General

The area of major interest in the experimental study reported herein was the connection between the wide flange beam sections and the concrete filled tube column (CFT) which governed the strength, stiffness, and capacity of the subassemblage. The design of the experimental setup had the requirement that each test specimen simulate as accurately as possible the forces which act on the connection in a multistory composite moment resisting frame (see Figure 2.1). This required that the boundary conditions and the force state in the vicinity of the connection of a test specimen must resemble those of a connection in the prototype building subjected to gravity and lateral seismic loading conditions. Furthermore, the proportions among the members of the material properties of the test specimen had to resemble closely that of the members in prototype structure. To meet these requirements, a subassembly was designed consisting of two wide flange beams attached to a CFT column by a rigid connection for a special moment resisting frame. The prototype building adopted for the study was designed in accordance with the NEHRP (1991), ACI, and LRFD [AISC, 1994] provisions. The NEHRP provision was used to determine the seismic design loads. The ACI and LRFD provisions were used to design the CFT column and wide flange steel beams, respectively. Each test specimen

represented a full scale model of the connection and adjacent beam and column members of an interior joint at the ninth floor of a perimeter moment resisting frame.

The design of each test specimen connection focused on providing strength, stiffness, and ductility for cyclic loading. The force transfer mechanism was studied in order to evaluate the effectiveness of the steel panel zone, encased concrete, and the connection's diaphragm plates on member performance. The diaphragm plates used in the CFT connections transferred beam flange forces through the connection, and were either internal (Specimen 1) or external (Specimen 3).

2.2 Prototype Building Frames

The prototype building consisted of a 20 story office building structure (Seismic Hazards Exposure Group 2), located in a seismic zone where the effective peak ground acceleration (A_a) and effective peak velocity - related acceleration (A_v) were both equal to 0.4 g's. The assumed soil profile was Type S_2 - consisting of a deep cohessionless or stiff clay conditions of depth greater than 200 feet.

The prototype building is shown in Figure 2.2. The story height of the structure's first floor was 15'-0" with the remaining floors at 12'-0", resulting in a total height 243 feet. The building had 5 bays at 20'-0", for a total structural width

of 100 feet. The prototype structure was designed as a perimeter moment resisting frame, with an interior concrete shear wall which doubled as the elevator shaft. The plan of the structure (see Figure 2.3) depended on no interior columns, with eight large composite floor girders extending from the perimeter moment resisting frame to the concrete shear wall. These floor girders, in conjunction with floor stringers, supported a composite concrete-metal deck floor system. The design tributary area of each exterior frame in one direction was 30 feet wide by 100 feet long (the full length of the frame), while the concrete shear wall maintained a tributary area that consisted of its own 20' width plus 10' on each side for a total of 40' wide by 100' long. The design dead load for each perimeter frame was calculated from a 20' width by 100' length.

The seismic design loads for the prototype structure were based the NEHRP Equivalent Lateral Force Procedure [NEHRP, 1991] (the 1994 edition was not published when the prototype structure was designed). In this procedure the fundamental period of the building (T) in the direction under consideration is first calculated by the following approximation:

$$T_a = C_t h_n^{3/4} \qquad (2.1)$$

where the fundamental period T based on substantiated structural analysis shall be :

$$T \leq 1.2T_a \qquad (2.2)$$

In Equation 2.1 $C_t = 0.035$ for moment resisting frame systems of steel which resist 100 percent of the required seismic force, and h_n is the height in feet above the base to the highest level of the building. For the prototype frame, the period T was determined to be equal to 2.585 seconds.

The seismic base shear, V, is equal to the seismic design coefficient (C_s) multiplied by the total dead load and applicable portions of other gravity loads (W) according to Section 4.2 of the NEHRP, where

$$V = C_s W \tag{2.3}$$

For the prototype perimeter MRF, W was equal to 4740 kips.

The seismic design coefficient (C_s) was determined according to the following:

$$C_s = \frac{1.2A_vS}{RT^{2/3}} \tag{2.4}$$

where A_v is the coefficient representing effective peak velocity acceleration, S is the coefficient for the soil profile characteristics of the site, and R is the response modification factor, respectively. The values used for A_v, S, and R for the prototype design were 0.4, 1.2, and, respectively 8, where the value of R is stipulated by NEHRP for special (ductile) moment resisting frames. The calculated value of C_s using the above values was 0.0382 resulting in a base shear V of 174 kips for the MRF frame.

The lateral force (F_x) induced at any level representing the seismic forces, is computed per NEHRP from the following expressions:

$$F_x = C_{vx}V \tag{2.5}$$

where

$$C_{vx} = \frac{w_x h_x^{\,k}}{\Sigma^{n}_{i=1} w_i h_i^{\,k}} \tag{2.6}$$

in which C_{vx} is the vertical distribution factor, w_i and w_x are the portion of the total gravity load (W) of the building located or assigned to level i or x, and h_x and h_i are the heights in feet from the base to level i or x, respectively. In Equation 2.6 the exponent k is related to the building period. The value of 2.0 was used for k in designing a perimeter MRF for the prototype.

The static lateral loads calculated above were combined with the standard dead and live loads in order to analyze the MRF for combined load effects. The roof dead and live loads were 60 psf and 30 psf, while the floor dead and live loads were both 80 psf. A live load reduction factor of 20% was applied to the floor live loading.

The AISC LRFD load combinations [AISC - LRFD 1994] were checked in conjunction with additional cases recommended by NEHRP (1991), which are

$$(1.1 + 0.5\,A_v)\,DL + 1.0\,LL + 1.0\,E \tag{2.7}$$

$$(0.9 - 0.5\,A_v)\,DL + 1.0\,E \tag{2.8}$$

The load combination controlling the design of most members was one recommended by AISC which is

$$1.2\ DL + 0.5\ LL + 1.0\ E \qquad (2.9)$$

In the above expressions, DL, LL and E are the dead load, live load, and seismic loading, respectively, with A_v equal to the NEHRP effective peak velocity - related acceleration coefficient.

For the purpose of comparison, two separate prototype frames were designed for the above loads. The first frame was designed utilizing standard wide flange column and beam steel sections in accordance with the LRFD Specifications (AISC, 1994). This resulting design is shown in Figure 2.4. The columns supporting the first eight stories were all W14x176 steel sections, while the columns supporting the ninth through twelfth floor levels were W14x159, and the columns supporting the remaining thirteenth through twentieth stories were W14x109. The girders of the first ten floor levels were W24x62 steel sections, the girders at the eleventh through nineteenth stores were W24x55, while the roof beams were W18x46. The second frame was a concrete filled tube composite column frame designed according to the LRFD specifications discussed in Section 1.3 of Chapter 1. The columns of this prototype frame supporting the first eight stories were each 16x16x5/8 steel tubes, the columns supporting the ninth through eleventh floor levels were 16x16x1/2 steel tubes, with the remaining columns supporting the eleventh though twentieth floor levels

16x16x3/8 steel sections. All of these steel tubes were designed to be filled with an 8000 psi strength concrete. The girders of this frame were identical to those of the wide flange column frame.

The design of both frames was found to be controlled by interstory drift criteria per NEHRP [1991], where the drift δ_x is based on the elastic displacement δ_{xe} from an equivalent lateral load analysis, which are multiplied by the factor C_D:

$$\delta_x = C_D \delta_{xe} \tag{2.10}$$

A value of C_D equal to 5.5 was used, where the interstory drift limit of 1.5% was required in accordance with NEHRP [1991]. The equivalent lateral loads for the strength design and drift control checks based on NEHRP criteria are shown in Figures 2.5 and 2.6, respectively. The loads associated with the drift check are smaller because the structural period T is not required to satisfy Equation 2.2. Both frames were checked to ensure that a weak beam - strong column design existed in accordance with NEHRP provision [NEHRP, 1991], where the beams are designed to yield during extreme lateral seismic loading, with the columns remaining essentially elastic.

An economical comparison of the two separate frames was conducted in reference to steel weight of each frame, and summarized in Table 2.1. It was found that the composite CFT column frame offered a substantial steel weight

advantage if all other relative costs, such as the cost of connections, could be kept relatively equal.

The experimental subassemblage was taken from the ninth floor at an interior beam - column of the CFT system, where the columns above and below this floor were 16x16x1/2 steel sections with 8000 psi concrete and the floor girders were W24x62 sections. The column design was based on the interaction curve relating the member's capacity to uniaxial bending and axial load for the calculated prototype seismic and gravity loads, in accordance with the LRFD and ACI provisions for composite columns, discussed in Section 1.3 of Chapter 1. The prototype column had a gravity load of approximately 500 kips, at which the flexural capacity per ACI was 12,394 kip-in accounting for material reduction factors.

2.3 Experimental Setup

The experimental setup was based on the force state developed at the CFT to wide flange connection when the frame was subjected to gravity and lateral seismic loading (see Figure 2.7). The member forces include axial (P), shear (V), and flexural forces (M). At column mid height between floors at the eighth and ninth level, and at midspan of the east and west beams of the prototype building, inflection points were assumed. The experimental setup subassembly resembled the column and beams between these inflection points,

having a specimen column height of 12 feet and a beam length of 10 feet to each side of the center of the column. The combined force state was introduced into the specimen by subjecting it simultaneously to axial load (P) and lateral load (H). The diagrams for axial load (P), shear (V), and flexural force (M) for the test specimen, which represent those of the prototype subassembly, are shown in Figure 2.7(b).

A schematic of the experimental setup is given in Figure 2.8, with a photograph of the actual experimental setup appearing in Figure 2.9. Under the applied axial load P and the horizontal load H, the subassembly had the requirement that it displace as shown in Figure 2.10(b) where the ends of all the members were free to rotate. The base of the column specimen in the experimental setup was bolted through a base plate to a clevis fixture attached to the laboratory floor. The clevis acted as a cylindrical bearing and was post tensioned to the laboratory's reaction floor in order to allow rotational movement yet restrict lateral displacement at the column base. The ends of both the east and west wide flange beams were attached to rigid links through a clevis (e.g. cylindrical bearing) each located 10 feet from the center of the column, as shown in Figure 2.8. The lower end of each rigid link was fastened to a clevis, which was post-tensioned to the floor. The rigid links and clevises arrangement enabled the beams to move freely in the east and west directions, while restricting only the movement at the ends of the beam in the vertical direction,

thus simulating a roller support as shown in Figure 2.10b. The axial load (P) was applied to the specimen using a loading beam and a pair of three inch diameter tension rods, which were connected to a pair of clevis fixtures and post-tensioned to the floor. Each rod was constrained at the load beam by a nut and washer placed on top of a calibrated load cell, which rest upon a hydraulic hollow core ram that reacted against the load beam, to create a tension load of 0.5P in the rod. This axial load setup enabled a constant load of P to be applied to the column using a pressure regulator in the hydraulic system for the hollow core jacks to maintain a constant axial load. A hydraulic actuator was mounted between the reaction wall and the specimen column, at a height of 12 feet above the center of the clevis at the base of the column. The actuator, secured in place by post-tensioning rods, was used to impose the lateral load (H) to cause lateral displacement (Δ) to the test specimen.

The column of the test specimen was braced for out-of-plane displacement in the north-south direction utilizing a Watts bracing mechanism [Yura,1967]. The Watts mechanism devices were essentially rigid links with spherical bearing at each end, which were attached to the specimen at the top and two feet above the base of the column. This scheme permitted displacement in the east-west direction of 11 inches, and in the vertical direction of up to 9 inches, while restricting movement in the north-south direction with minimal friction forces developing. The beams were each braced at five foot

intervals along their lengths, using channels to prevent out-of-plane movement (see Figure 2.11). This permitted movement in the East-West and vertical directions. Frictional forces between the beams and the channel flanges were minimized by greasing their surfaces.

2.4 Specimen Details

A total of two specimens were designed and tested to date, and are noted as Specimens 1 and 3, respectively. The connection details for both specimens are given in Figures 2.12 and 2.13. The connection details and panel zone were designed to resist the maximum expected beam forces that would develop, and which were based on a flexural moment of 1.25 M_p, where M_p is the beam flexural capacity that existed at the end of the cover plates (Specimen 1) or at the end of the structural tees (Specimen 3). Both specimens were constructed from 12'-0" long steel tubes of the same heat and filled with concrete batched on the same date. The concrete was placed after all welding was completed. Twelve foot long W24x62 beams were each framed into opposite sides of the column specimen at a height of 6'-0" above the center of the clevis' pin at the base of the column. Each specimen was mounted on a 21" x 21" x 1" base plate that was fillet welded to the base of the column, utilizing eight-one inch A325 bolts which were post tensioned to secure the column base plate to the clevis fixture to minimize slippage. Although the distance from center line of the

column to the inflection point on the beam was 10 feet in the prototype and experimental models, 12 foot beams were acquired, leaving a two foot overhang. This permitted the beams to be reused in subsequent tests by removing them and turning their respective ends around.

Both specimens were equipped with six 4 1/2" x 5/8" shear studs mounted on the reverse side of the shear tabs at a 3" spacing. A typical shear stud was mounted by drilling a 5/8" diameter hole on the outer face of the steel tube, inserting from inside the tube the stud approximately one half of the depth into the hole, and welding the stud to the steel tube using E70x18 welding material and the self shielded submerged metal arc welding (SMAW) process. Shear tabs on both specimens consisted of 4 1/2" x 15" x 1/2" plates, which were welded to the face of the tube using E70x18 welding material and a double bevel groove weld placed by the SMAW process. Each tab consisted of A36 material with five drilled 1 1/16" diameter holes for the five - one inch diameter A325 bolts necessary to resist the shear on the beam due to gravity and seismic loading. The access holes on the four beams were designed according to the LRFD seismic provisions, in order to prevent any notch effect from occurring.

Specimen 1 was considered the base case for the experiment. This specimen was fabricated with two 5/8" thick diaphragm plates, each with a 6" diameter hole located at the center of the plate. The LRFD, ACI and NEHRP provisions offered little to no direction for the design of the diaphragm plates.

Consequently the design was based on the previous work of Matsui [1985] using Eqns. 1.79 and 1.80, along with the requirement that the diaphragm plate had to be at least as thick as the flange of the connecting beam flange [AIJ, 1987]. The design force ${}_sP_a$ in Matsui's approach was equated to resist the maximum beam flange tensile force where

$$T_{max} = \frac{M_{max}}{d_b} \tag{2.11}$$

in which d_b is the beam's depth. In Eqn. 2.11 the moment M_{max} is that at the face of the column and is based on extrapolating the maximum expected beam flexural capacity of 1.25 M_p from the end of the connection region at the column face. These plates were welded to the inner face of the structural tubing using the flux core arc welding process in conjunction with E71T-1 electrodes and an argon - carbon dioxide 75-25 shielding gas to create a single bevel groove weld with R=1/4" and α=45°, where R and α are the root opening and groove angle, respectively. The structural steel tube was cut at two locations, one foot from both the top and bottom diaphragm positions, in order to weld the diaphragm plates to the inside of the tube. The tube was then welded shut using a single bevel full penetration groove weld. The flanges of the beams connected to the column of Specimen 1 were fastened, using field welding techniques. Each beam flange was beveled at a 45° angle and were welded to the specimen with a single bevel groove weld (R=1/4") using the self shielded flux core arc welding

(FCAW) process with NR311Ni electrodes. All of the backing bars were removed, the exposed weld back-gouged, and using NR232 electrodes and the self shielded FCAW process a 1/4 inch fillet weld was placed. The shear tabs on both sides of the CFT column were welded to the web of the beam using E70x18 electrodes and SMAW over a 3 1/2" length on the top and bottom of the tab and a total of 8" in the vertical direction. These welds were required for a W24X62 and designed for a capacity of 20% of the web's moment capacity in accordance with the AISC - LRFD seismic provisions (AISC 1994). Coverplates for each beam flange were attached to the face of the structural tube by full penetration welds using NR-311Ni electrodes and the self-shielded FCAW process. The plates were welded to the beam flanges using 1/2 inch fillet welds. The coverplate stubs consisted of 7/8" x 3 1/2" x 6 3/4" plates for the top flanges and 7/8" x 3 1/2" x 7 1/4" plates for the bottom flanges.

Specimen 3 was designed with external diaphragms. These diaphragms were fabricated from ST7.5x25 structural tee sections, and are shown in Figure 2.13. The tees were designed to transfer to the panel zone the beam's maximum tensile flange force T_{max}, which was calculated using Eqn (2.11)

A section passing through the tee at an angle of $\theta = 19.29°$ from the face of the column, as shown in Figure 2.14, was assumed to resist one half of this flange force T_{max} by yielding the tee's area A_s. Thus, on this basis to resist the flange force T_{max}, it was required that:

$$2\phi A_s \sigma_y * \cos\theta \geq T_{max} \quad (2.12)$$

in which σ_y is the tee's yield stress and ϕ the LRFD material reduction factor of 0.9. The tee sections were welded to the flange of the beam, as was the beam flanges welded to the column, using the same full penetration welding specification as in Specimen 1 for the beam flange to column weld. The edge of the beam flange and the cut web of the tees also were welded to the outer face of the column using this same full penetration weld as for the beam's flange with the NR-311 Ni electrodes. All welds were single bevel groove welds where α=45° and R varied slightly. Only the backing bars of the beam flanges were removed, the exposed material and debris backgouged, and 1/4 inch fillet weld placed. The vertical edge of the tee flanges were welded to the edge of the structural tube using E70-18 electrodes. A 1/4 inch E70-18 fillet weld was then placed on the backside of the tees' flanges as shown in Figure 2.13. The shear tabs of specimen 3 were welded to the web of the beams in the same manner as Specimen 1.

The panel zone shear capacity of both specimens was checked using the modified panel zone strength model (Eqns. 1.65 through 1.73), to ensure that it could resist the panel shear force caused by the flexural beam moments developed at the face of the column. These moments were based on extrapolating the flexural capacity of 1.25 M_p at the end of the coverplates (Specimen 1) or structural tees (Specimen 3) to the face of the column.

Measured dimensions of the cross-sections of the wide-flange beams, columns, and critical connection details are given in Tables 2.2 through 2.5. Included in Tables 2.2 and 2.3 are calculated area (A), moments of inertia (I_x), and plastic section modulus (Z_x) based on measured dimensions for the beams and column's steel tube.

2.5 Material Properties

The design strengths for the structural tubing, fabricated from A500 Grade B material, were based upon a nominal yield strength of 46 ksi, with the nominal design strengths for the W24x62 beams based on A36 steel. The structural steel tubes were manufactured by a cold formed process, and were from all the same plate material produced in a single heat. The wide flange sections for Specimen 1 and Specimen 2 came from two separate heats. Material properties for the steel shapes and the interior diaphragms were determined from uniaxial tension tests in accordance with ASTM standard test methods for tension testing of metallic materials [ASTM, 1991]. The properties are presented in Tables 2.6 through 2.8, where E, F_y, and F_u are Young's modulus, the yield and the ultimate stress, respectively. The W24x62s used in Specimen 1 had an average measured yield stress of 49.6 ksi and 42.5 ksi in the web and flange, respectively, where Specimen 3 had 50.5 ksi and 43.3 ksi. Typical stress-strain curves for a beam's web and flange of Specimen 1 are shown in Figure 2.15.

The average yield stresses for the top and bottom diaphragm plates of Specimen 1 were 41.0 ksi and 40.4 ksi, respectively, where the average yield stress for the structural tees for Specimen 3 were 40 ksi. The concrete's nominal 28 day design strength was 8000 psi for both specimens, as noted previously. Actual concrete compressive strengths, f'_c, for the different specimens were determined from compression tests on six by twelve inch cylinders on the day of each test, as per ASTM standard test methods for compressive strength of cylindrical concrete specimens [ASTM, 1991]. Young's modulus, E, for each of the specimen cylinder tests were calculated according to the ACI code [ACI 1992], where:

$$E = 57000\sqrt{f'_c} \quad (f'_c \text{ in psi}) \tag{2.13}$$

The results of these tests are presented in Table 2.9. It was found that the average measured concrete compression strength of 6300 psi was below the specified nominal value of 8000 ksi.

2.6 Instrumentation

The instrumentation used for each of the CFT column specimens was designed to measure response which was judged to be critical in determining the test specimen's performance under cyclic loading. These measurements included: lateral and vertical movement of the subassembly; axial, lateral, and rigid link loads; panel zone deformations; strains in the flanges of the W24x62

beams and steel tube of the column; as well as rotations of the column and beams. Except for minor strain gage location changes, the instrumentation plan for Specimens 1 and 3 was essentially consistent.

Sting potentiometers were placed along the height of each test specimen in order to measure the lateral displacements of the column under cyclic lateral loading. The position of these instruments is shown in Figure 2.16. As shown in this figure, lateral displacement measurements were taken at height locations corresponding to: the bottom of the column, 4 inches below the bottom of a beam, 4 inches above the top of a beam, and the top of the column (actuator height). An exception to these locations is where in Specimen 1 the lateral displacement above the beam was taken at 11.25 inches at this location. A linear variable differential transformer (LVDT) was placed at the bottom of the clevis fixture at the base of the column in order to measure any lateral movement between this fixture and the floor. An LVDT was also place between this same clevis and the specimen to measure any relative movement between the two. Two string potentiometers were placed at the end of each beam in order to measure vertical and torsional movement of the beams at the rigid link locations. Typically, each string potentiometer was located at approximately 10 inches to the north and south sides from the centerline of the beam.

To measure the deformation of the panel zone, two separate methods were used. In the first method two LVDTs were placed at each face of the CFT

panel zone. These instruments extended diagonally across the panel zone from the far corners, at elevations where the beam flanges intersected with the column (see Figure 2.17). These LVDTs were effective in measuring the deformation Δ along each diagonal, where the panel zone shear deformation (γ) is calculated by:

$$\gamma = \left(\frac{\Delta_1 - \Delta_2}{2}\right)*\left(\frac{d}{b*h}\right) \qquad (2.14)$$

where Δ_1, Δ_2, h, b, and d are the change in length of one diagonal LVDT, the change in length of the other diagonal LVDT, the vertical distance between LVDT mounting ends, horizontal distance between LVDT mounting ends, and the gage length of the diagonal LVDT mounting system.

Three rosettes were also placed on the outside surface at the center height of each face of the panel zone (Figure 2.18). The shear deformation γ was determined using the strain information collected from these gauges from the following relationship:

$$\gamma = 2\varepsilon_{45} - (\varepsilon_0 + \varepsilon_{90}) \qquad (2.15)$$

In Eqn. 2.15, ε_0, ε_{90}, and ε_{45} are the recorded horizontal, vertical, and diagonal (45°) strains, respectively, of a rosette.

The rotations of the CFT were measured at four locations along the height of the column on the north face using inclinometers. Each inclinometer was mounted to a metal plate bracket which, in turn, was fastened to the specimen

by a 1/4 inch by 1/2 inch long hex nut that had been tack welded to the steel tube. Rotations of both the east and west beams were measured using two inclinometers located on the web at center height of each beam adjacent to the shear tab. The position of all inclinometers are shown in Figure 2.16.

Strains in the steel tube and the W24X62 beams were measured using strain gauges. Pairs of strain gauges were placed on both the east and west outside surfaces of the structural tube at 2.875 and 24 inches above and below the beam flange at a distance of 7 inches apart (see Figure 2.19), resulting in a total of 16 column gauges. A pair of strain gauges were also placed on the top and bottom flange of each beam, each gage spaced 4 inches apart. For Specimen 1, these gauges were located 2 inches from the edge of the cover plate stub, resulting in a distance of 5 1/2" from the east and west face of the CFT column. An additional pair were located at 4 feet from the CFT column face. A typical layout for the beam strain gages is given in Figure 2.20. Strain gauges were also placed on the top and bottom interior diaphragms of Specimen 1 in order to observe force transfer through the diaphragm plates. The layout for the diaphragm plates is given in Figure 2.21 and 2.22.

For Specimen 3 the beam flange gauges were located at 5 1/2" and 4 feet from the east face of the column, on both the top and bottom flanges (see Figure 2.23). On the west beam of Specimen 3, two gauges were placed 4" apart on the beam flanges, at 2" and 4 feet from the face of the column. At the 2"

distance from the column face the west external diaphragm was gauged by placing strain gages on the web and flange of the structural tees (see Figure 2.23 and 2.24). Two strain gauges were also placed 4 inches apart on the flanges of both beams of Specimen 3, at 1 inch from the edge of the external diaphragm in order to detect beam yielding outside of the external diaphragm (see Figure 2.23). The east and west beams had their respective flanges gauged identically.

Calibrated load cells were used to monitor the applied axial load P and lateral load H, as well as the reaction axial force developed in each rigid link.

2.6 Test Procedure

Prior to testing, each specimen was white washed in the vicinity of the connection in order to visually detect any signs of the steel yielding. Each specimen was tested under cyclic lateral displacement control with respect to the top of the column. The displacement history is shown in Figure 2.25, and is in accordance with ATC-24 [1992]. The displacement history was imposed by the horizontal hydraulic actuator, using proportions of the yield displacement Δ_y as a basis. A test proceeded with cycles of displacement amplitude of $0.25\Delta_y$, $0.5\Delta_y$, $0.75\Delta_y$, Δ_y, $1.5\Delta_y$, $2\Delta_y$, $3\Delta_y$... . Prior to imposing lateral displacement, a targeted axial load of P=450 kips was applied to the column. Each cycle of displacement involved imposing symmetric displacements in the east and west direction with

respect to the initial plumb position of the column. The yield displacement Δ_y was associated with the flexural capacity of the beams, and was determined from extrapolating from the displacements at first yield moment M_y in the beams to the displacements corresponding to beam flexural capacity M_p. A test was terminated when either a specimen reached a displacement ductility of $\mu = 6\Delta_y$, or its capacity deteriorated below 80% of its peak resistance.

Prior to conducting the above test, each specimen was subjected to a set of elastic cycles of displacement (e.g. Δ less than Δ_y) to investigate the column's elastic lateral stiffness under different levels of axial force P. These initial sets of tests involved axial loads of 0 and 225 kips, respectively.

TABLE 2.1 ECONOMICAL COMPARISON OF CFT AND WF MOMENT RESISTING FRAMES (Complete Building)

Frame	Total Steel Weight [lbs]	Concrete [cy]	Approx. Steel Cost [$]	Approx. Concrete Cost [$]	Total Cost [$]	Maximum Factored Inter-story Drift (%)
CFT Column Frame	1043500	340	2087000	30500	2117500	0.01488
WF Column Frame	1330700	---	2661400	---	2661400	0.01489
Cost Difference					544000	

Table 2.2 Average Beam Dimensions and Properties for Specimens 1 and 3

	depth in	t_w in	b_f in	t_f in	Area in^2	I_x in^4	Z_x in^3
Specimen 1							
Measured - East Beam	23.860	0.438	7.090	0.601	18.446	1577.419	155.323
Measured - West Beam	23.760	0.432	7.000	0.583	17.923	1511.557	159.718
Nominal (W24x62)	23.740	0.430	7.040	0.590	18.200	1550.000	153.000
Specimen 3							
Measured - East Beam	23.760	0.437	7.100	0.602	18.405	1564.283	154.565
Measured - West Beam	23.840	0.443	7.080	0.602	18.552	1579.226	155.791
Nominal (W24x62)	23.740	0.430	7.040	0.590	18.200	1550.000	153.000

Table 2.3 Average Column Dimensions and Properties for Steel Tubes of Specimens 1 and 3

	Outer Dimens. in	Wall Thickness in	Area in^2	I in^4	Z in^3
Specimen #1					
Measured	16.08	0.462	28.90	1174.00	169.00
Nominal (16x16x1/2)	16.00	0.500	30.40	1200.00	175.00
Specimen #2					
Measured	16.09	0.463	28.90	1179.00	170.00
Nominal (16x16x1/2)	16.00	0.500	30.40	1200.00	175.00

Table 2.4 - Average Measured Diaphragm Dimensions, Specimen 1

	Hole Diameter [in]	Plate Thickness [in]
Top Diaphragm	6.08	0.64
Bottom Diaphragm	6.15	0.66

Table 2.5 - Average Measured Dimesions for Specimen 3 Exterior Diaphragm

	l_t [in.]	t_f [in.]	b_f [in.]	b_t [in.]	t_1 [in.]	t_w [in.]	t_2 [in.]	α [rad]
East Side Connection								
North Top	9.820	0.491	5.627	7.250	1.294	0.510	0.610	0.636
South Top	9.800	0.490	5.801	7.750	1.515	0.510	0.625	0.669
North Bottom	9.850	0.473	5.654	7.250	1.958	0.513	0.587	0.635
South Bottom	9.880	0.435	5.805	7.875	1.266	0.513	0.556	0.673
Average	9.838	0.472	5.722	7.531	1.508	0.512	0.595	0.653
West Side Connection								
North Top	9.720	0.499	5.614	7.325	1.740	0.509	0.625	0.646
South Top	9.780	0.500	5.814	7.775	1.220	0.509	0.639	0.672
North Bottom	9.800	0.552	5.676	7.250	1.540	0.511	0.687	0.637
South Bottom	9.880	0.563	5.819	8.000	1.830	0.511	0.724	0.681
Average	9.795	0.529	5.731	7.588	1.583	0.510	0.669	0.659
Combined Average	9.816	0.500	5.726	7.559	1.545	0.511	0.632	0.656

Note: l_t = the length of the tees along the beam
t_f = thickness of the tee flange
b_f = width of tee flange
b_t = depth of tee along CFT measured from the edge of the beam flange to the outer tee flange
t_1 = thickness of tee flange measured along beam flange
t_w = thickness of tee web
t_2 = thickness of tee flange measured along CFT
α = angle between beam flange and tee flange

Table 2.6 Measured Beam and Column Material Properties

	F_y ksi	F_u ksi	E ksi
Specimen #1			
Beam Flanges*	42.5	66.1	32255
Beam Web*	49.6	68.9	32051
Nominal	36.0	58.0	29000
Columns**	46.0		
Specimen #2			
Beam Flanges**	43.3	68.9	30480
Beam Web**	50.5	71.8	30480
Nominal	36.0	58.0	29000
Columns**	46.0		

*Based on Tensile Tests

**Based on Mill Report

Table 2.7 Measured Diaphragm Plate Material Properties

	F_y ksi	F_u ksi	E ksi
Specimen #1			
Top Diaphragm Plate*	41.0	67.4	30400
Bottom Diaphragm Plate*	40.4	67.0	30200
Nominal	36.0	58.0	29000

*Based on Tensile Tests

Table 2.8 Structural Tee Material Properties

	F_y ksi	F_u ksi	E ksi
Specimen #1			
Top Diaphragm Plate**	40.0	65.0	29000
Bottom Diaphragm Plate**	40.0	65.0	29000
Nominal	36.0	58.0	29000

**Based on Mill Report

Table 2.9 Measured Concrete Material Properties

	f'c psi	E_{ACI} ksi
28 Day Strength	6000	4415
Strength at Day of Test 1	6300	4524
Strength at Day of Test 2	6300	4524

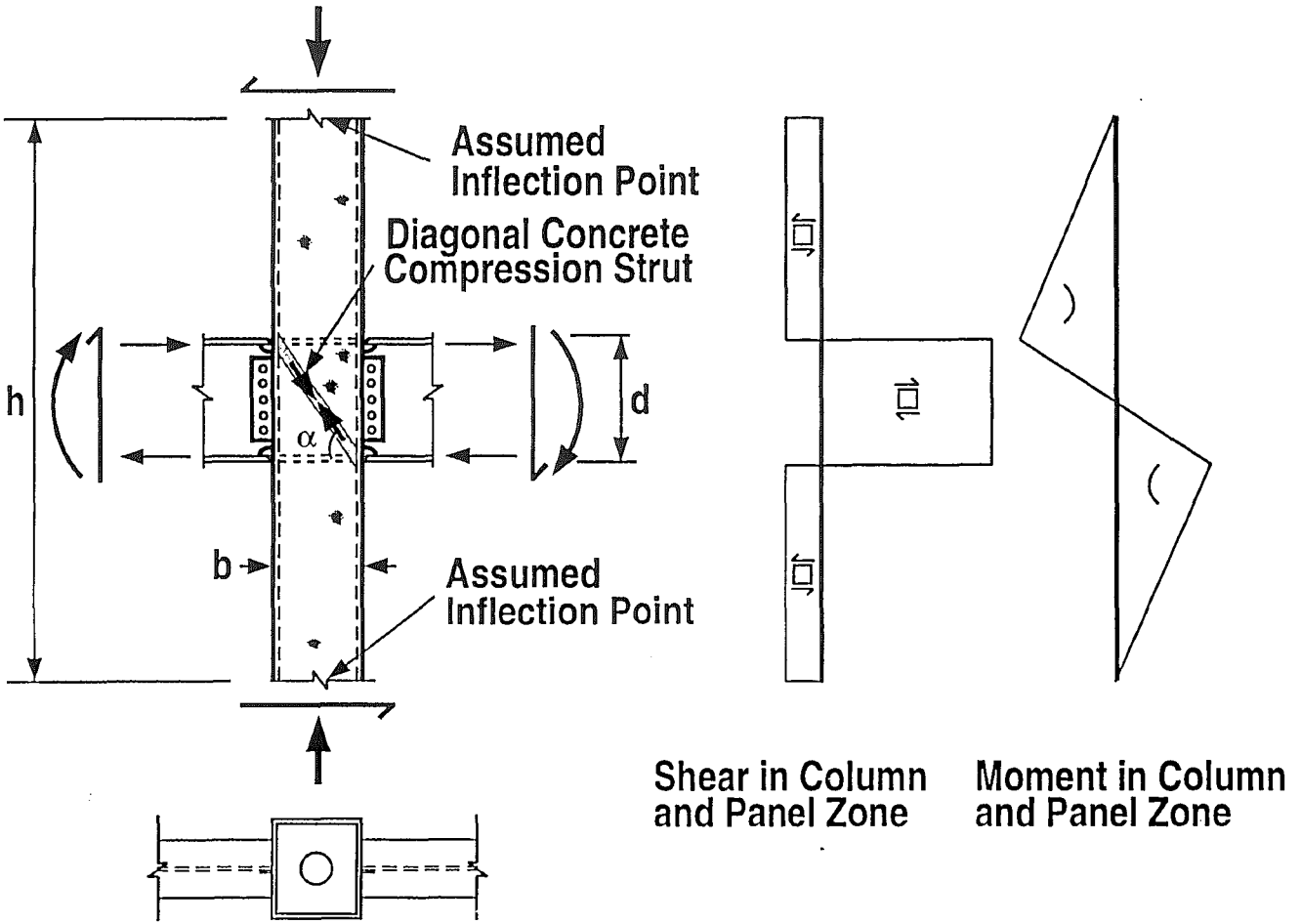

Figure 2.1 - Shear and Moment in Panel Zone Due to Seismic Lateral Loading

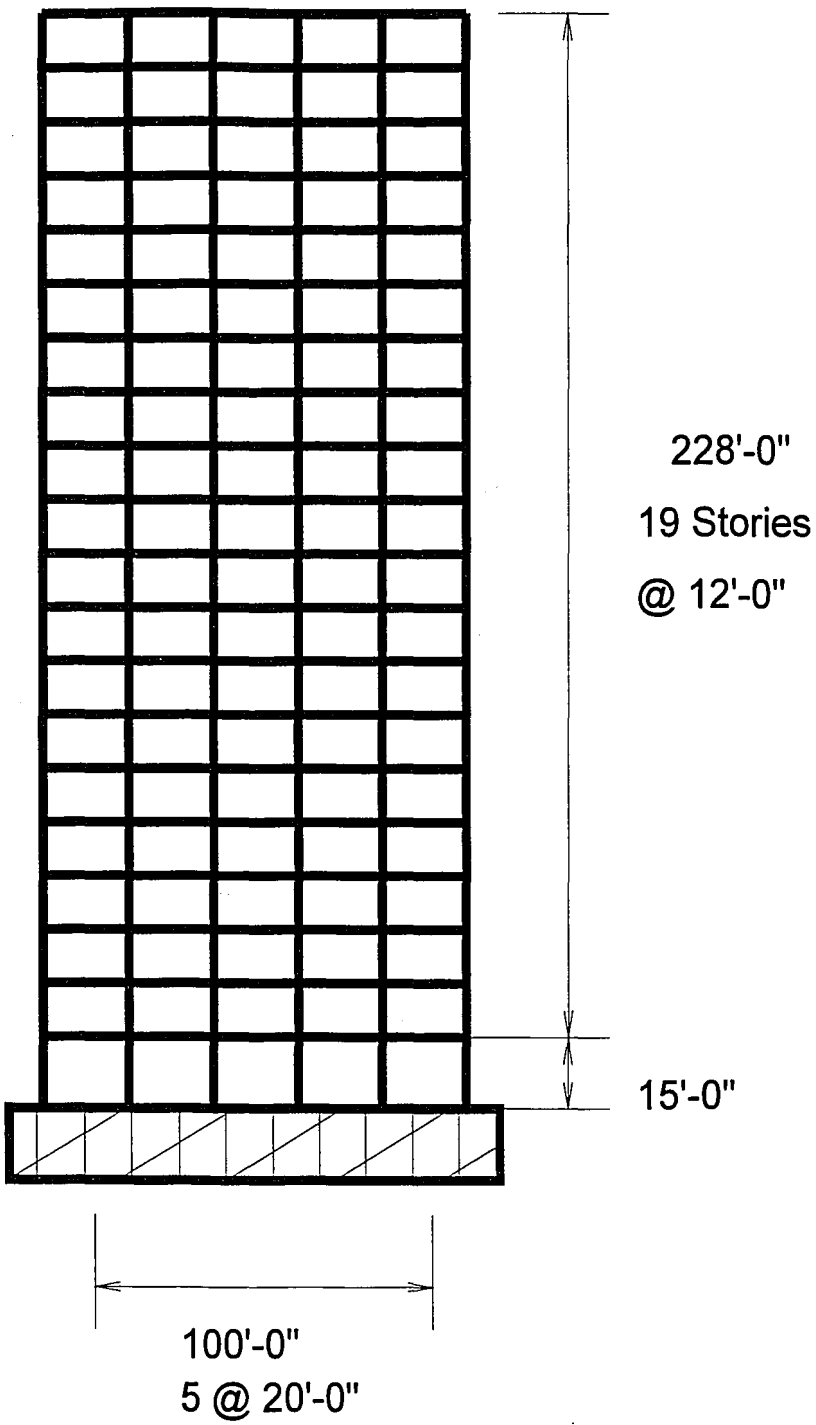

Figure 2.2 Prototype Building Elevation

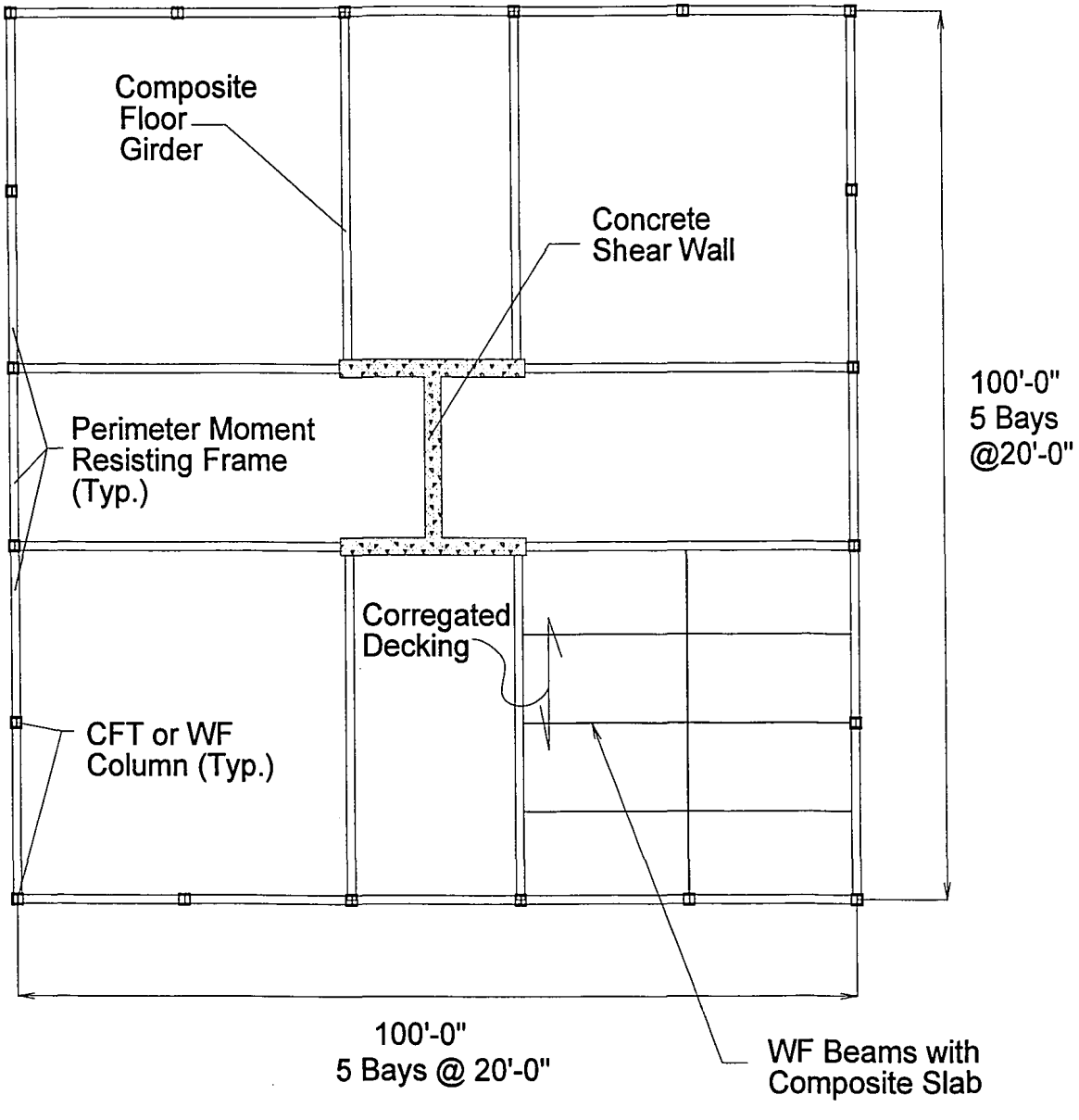

Figure 2.3 - Prototype Typical Floor Plan

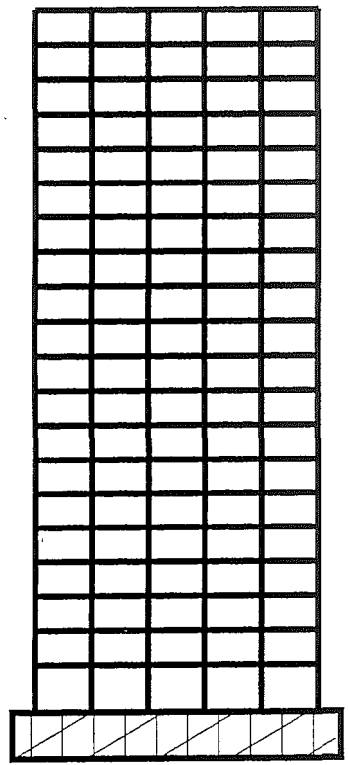

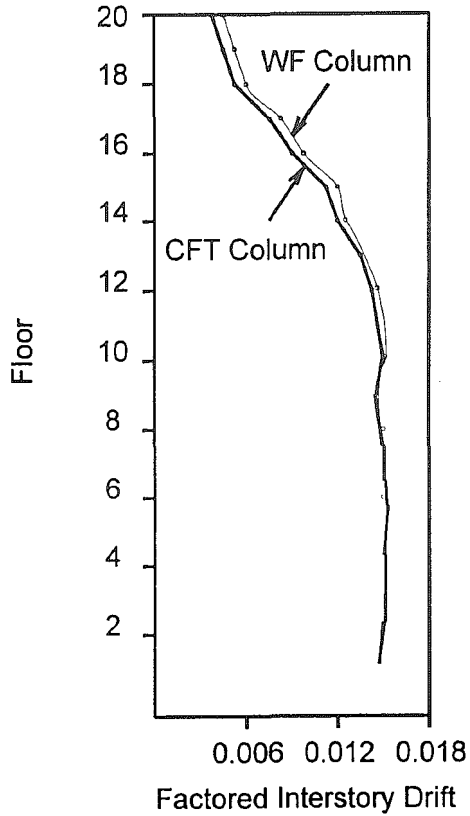

Floor	Beams	Columns	
20	W18x46	W14x109	16x16x3/8
19	W24X55	W14x109	16x16x3/8
18	W24X55	W14x109	16x16x3/8
17	W24X55	W14x109	16x16x3/8
16	W24X55	W14x109	16x16x3/8
15	W24X55	W14x109	16x16x3/8
14	W24X55	W14x109	16x16x3/8
13	W24X55	W14x109	16x16x3/8
12	W24X55	W14x159	16x16x3/8
11	W24X55	W14x159	16x16x3/8
10	W24X62	W14x159	16x16x1/2
9	W24X62	W14x159	16x16x1/2
8	W24X62	W14x176	16x16x5/8
7	W24X62	W14x176	16x16x5/8
6	W24X62	W14x176	16x16x5/8
5	W24X62	W14x176	16x16x5/8
4	W24X62	W14x176	16x16x5/8
3	W24X62	W14x176	16x16x5/8
2	W24X62	W14x176	16x16x5/8
1	W24X62	W14x176	16x16x5/8

Figure 2.4 Prototype Perimeter Moment Resisting Frame for CFT and WF Column Systems

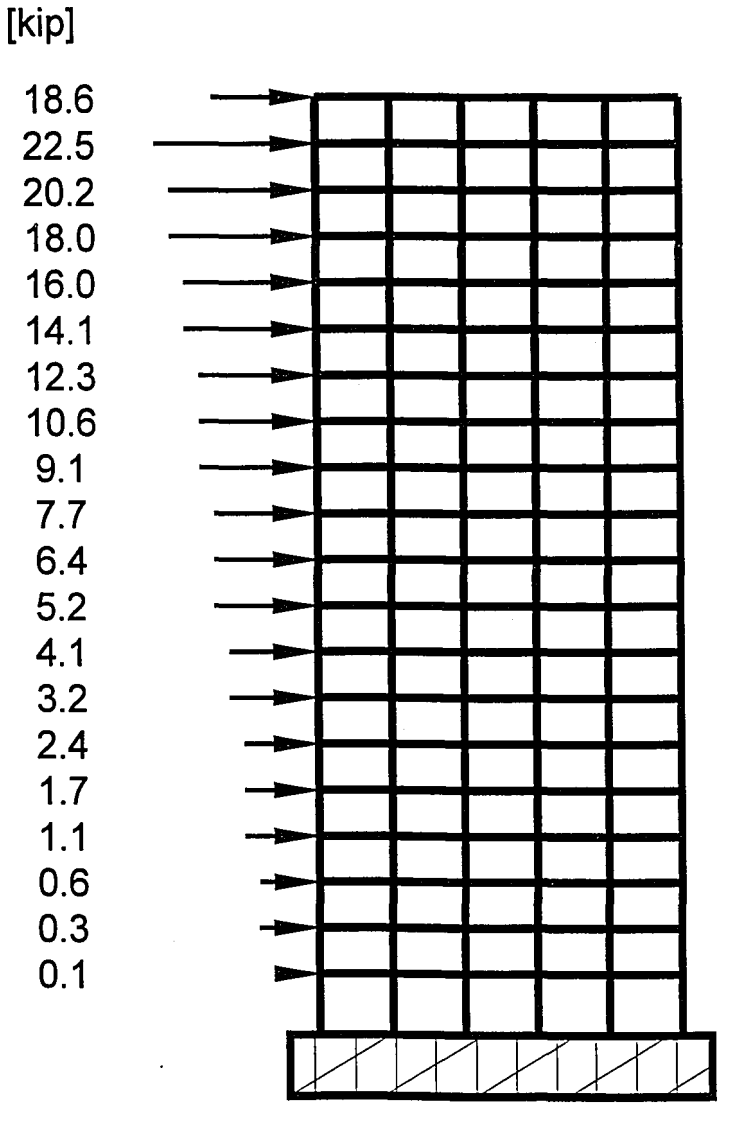

Figure 2.5 NEHRP Equivilent Lateral Loads For Strength Design - CFT and WF Column MRF Frames

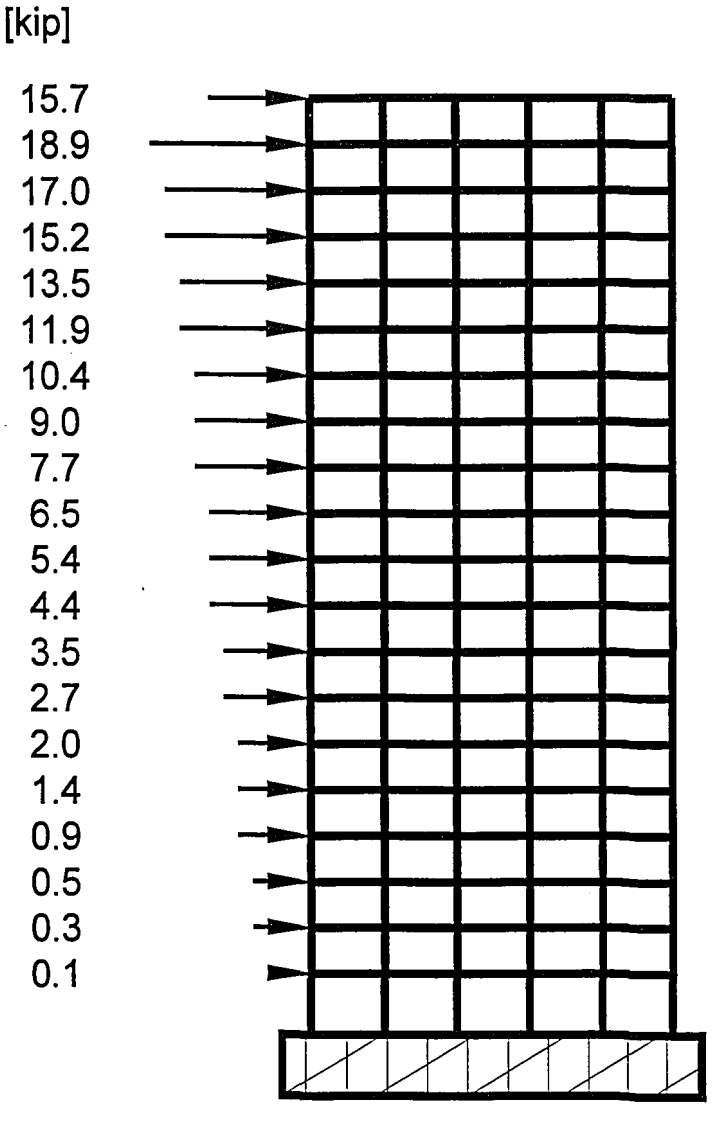

Figure 2.6 NEHRP Equivale Lateral Loads for Inter-story Drift Design - CFT and WF Column MRF Frames

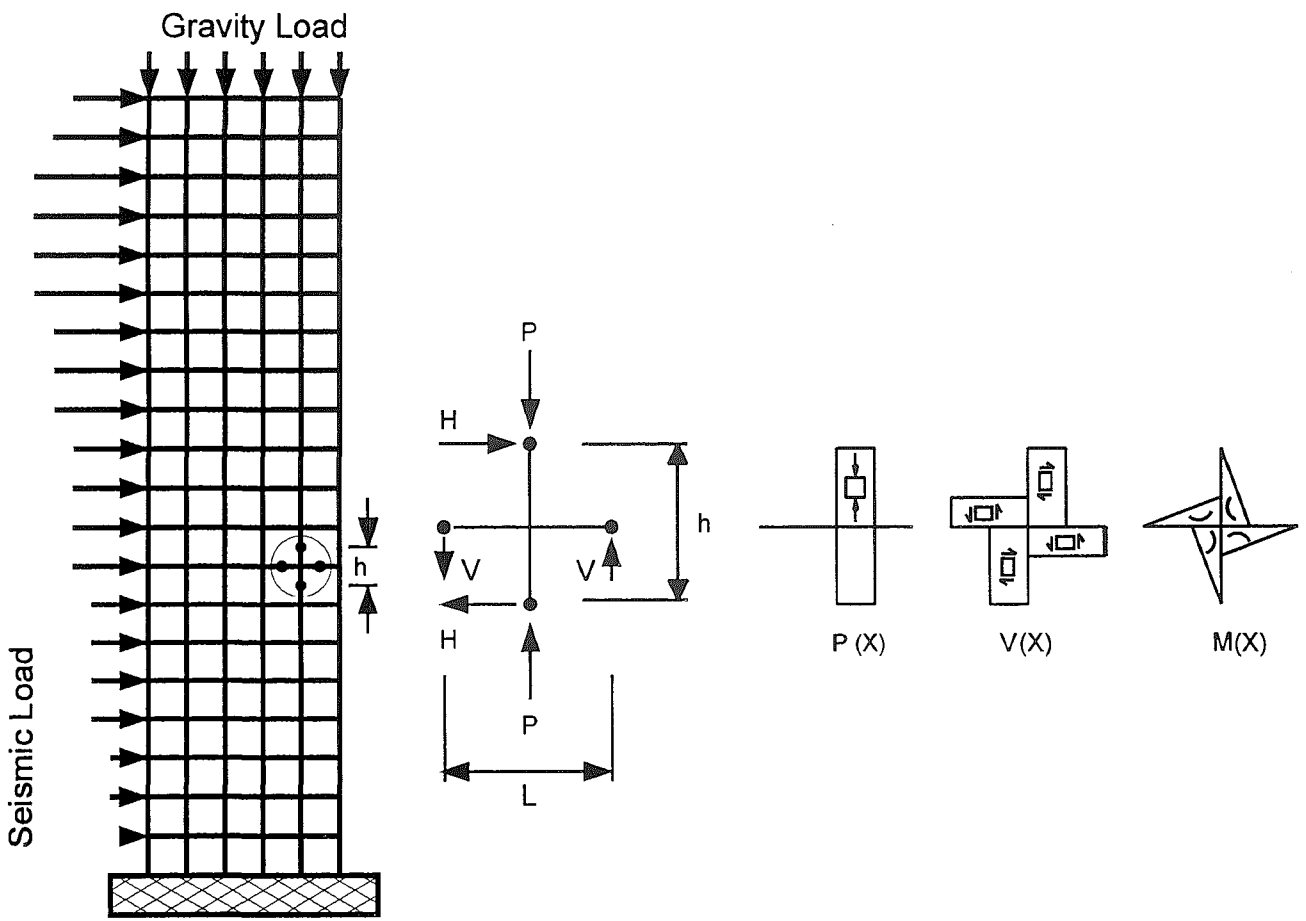

(a.) Prototype Structure (b.) Experimental Subassembly and Member Forces

Figure 2.7 Test Configuration

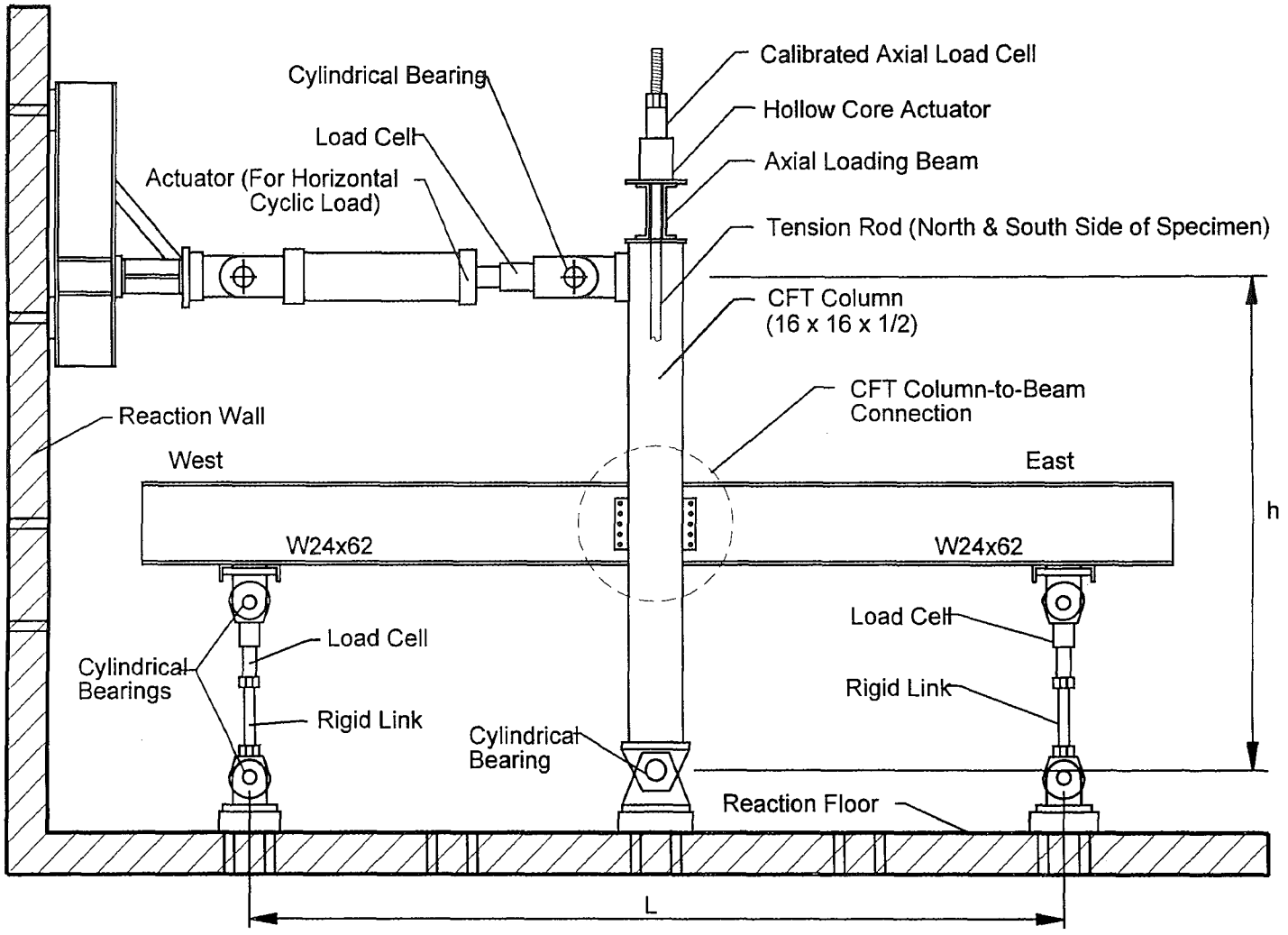

Figure 2.8 CFT Connection Structural Subassembly Test Setup

Figure 2.9 - Photograph of Test Setup

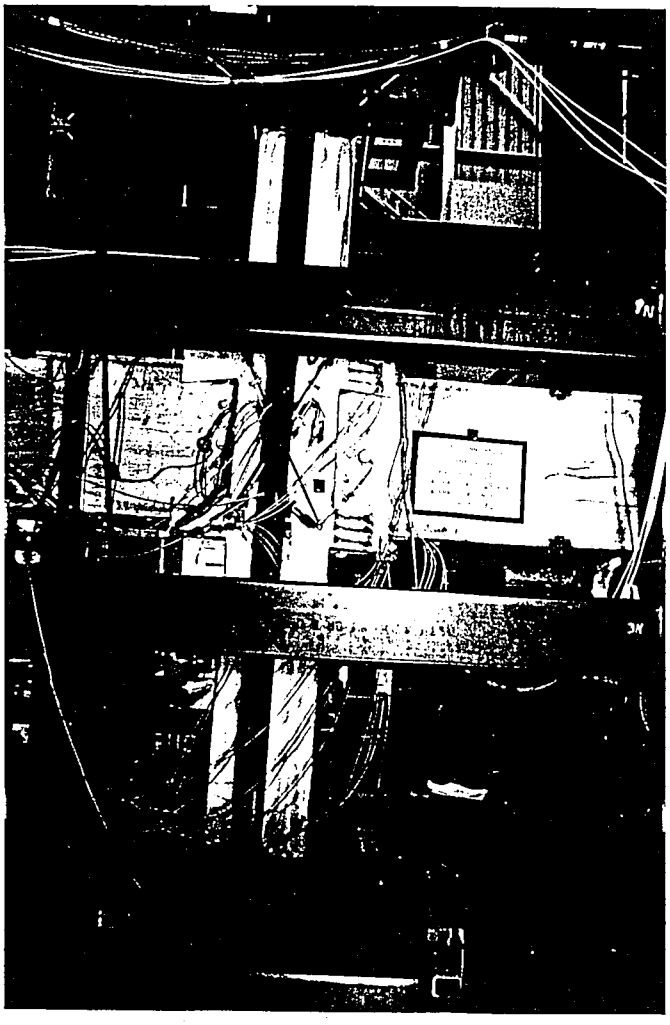

Figure 2.9 - Photograph of Test Setup

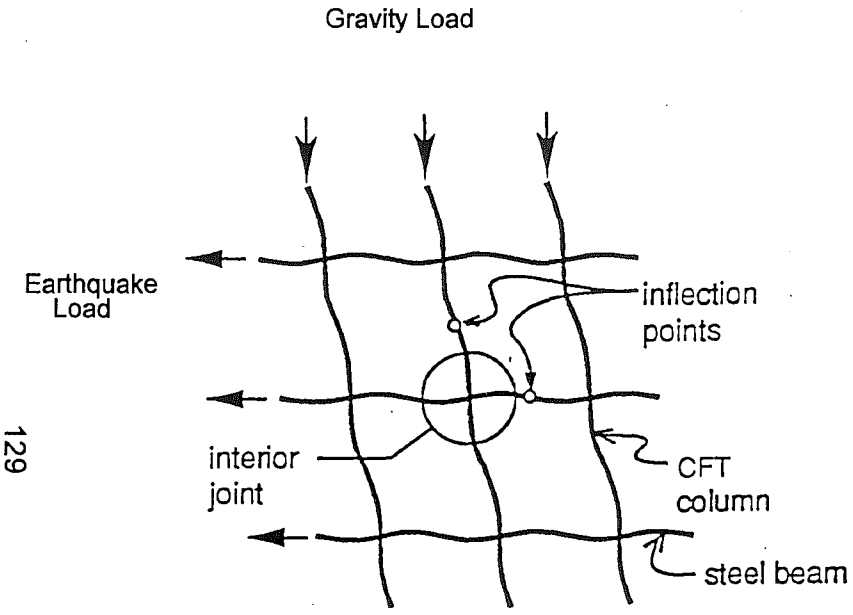

(a) Prototype Composite CFT Joint

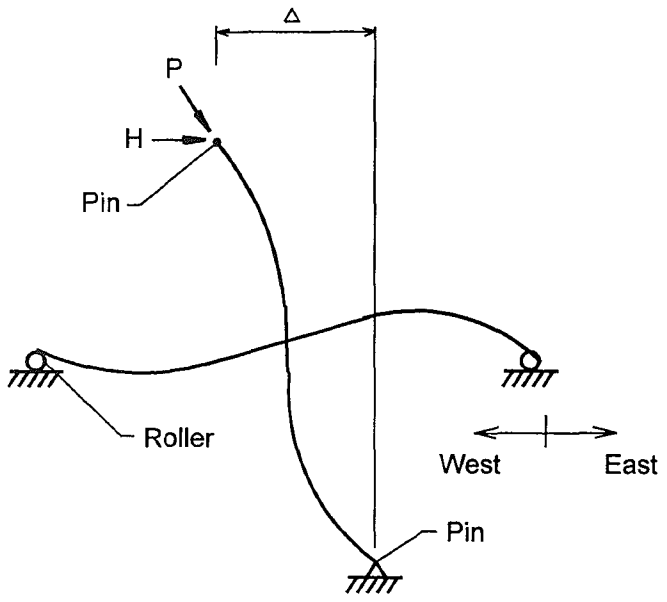

(b) Experimental Setup

Figure 2.10 Kinematics of (a) Prototype Structure in Connection Region, and (b) Experimental Setup

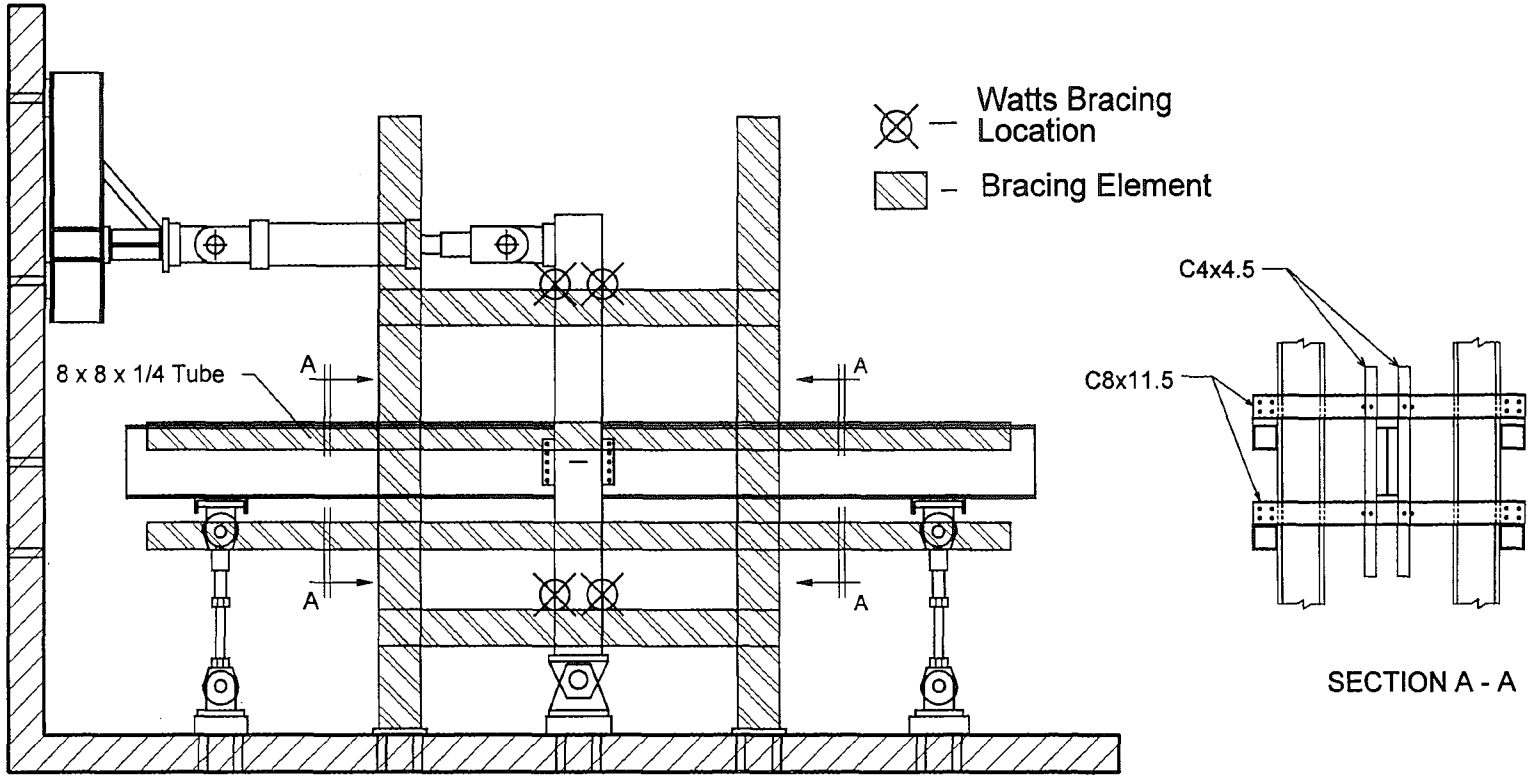

Figure 2.11 Elevation of Lateral Bracing

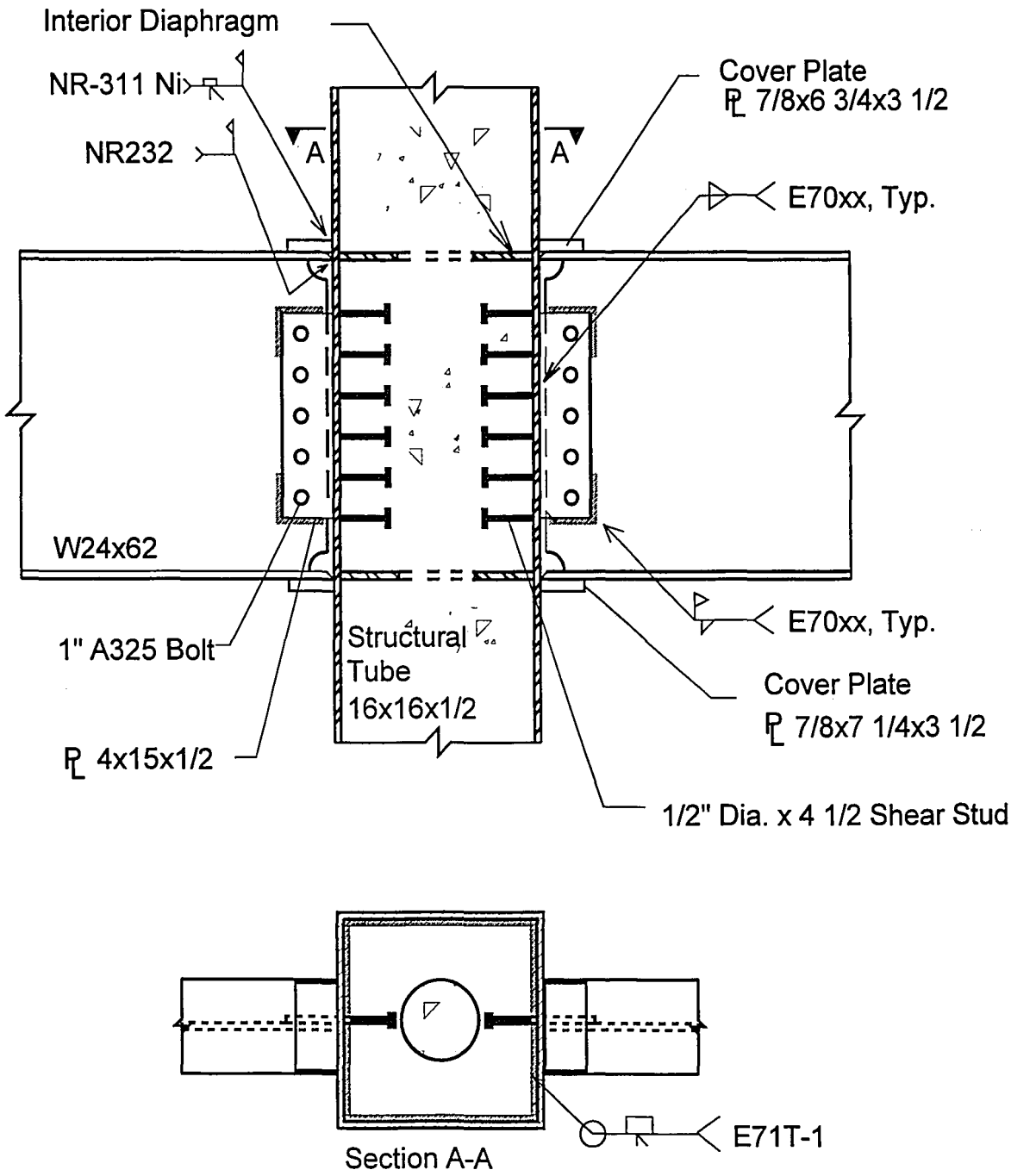

Figure 2.12 Connection 1

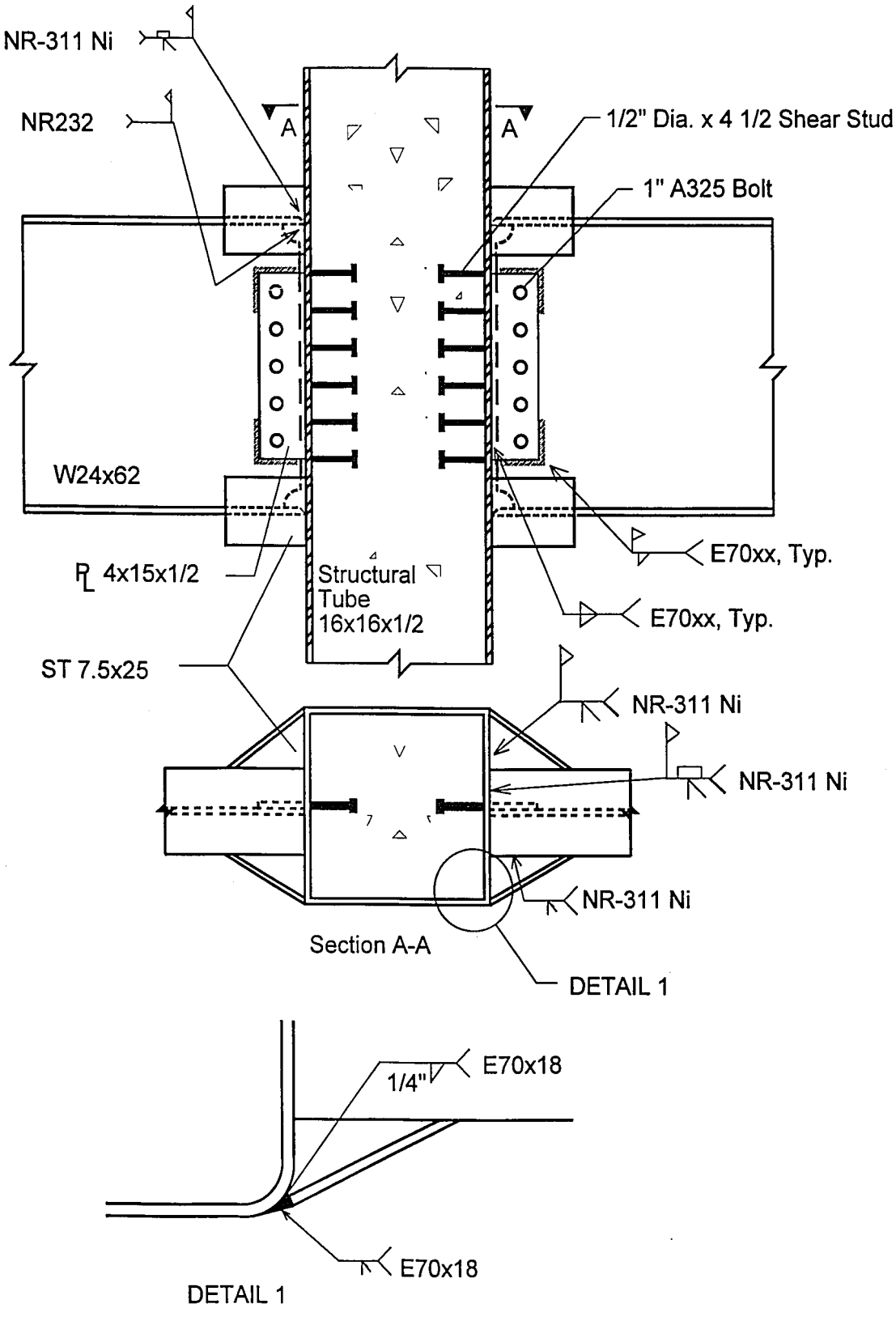

Figure 2.13 Connection 3

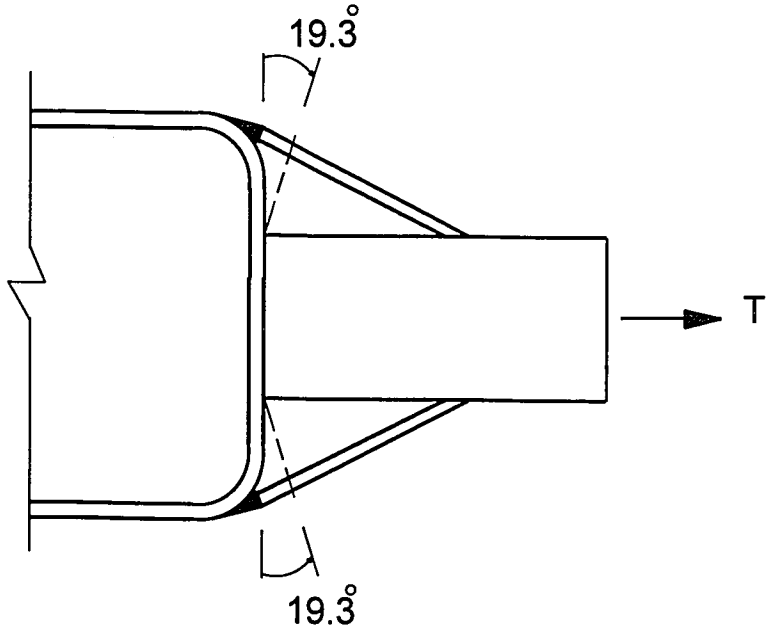

Figure 2.14 - Section Resisting One Half of Flange Force, Specimen 3

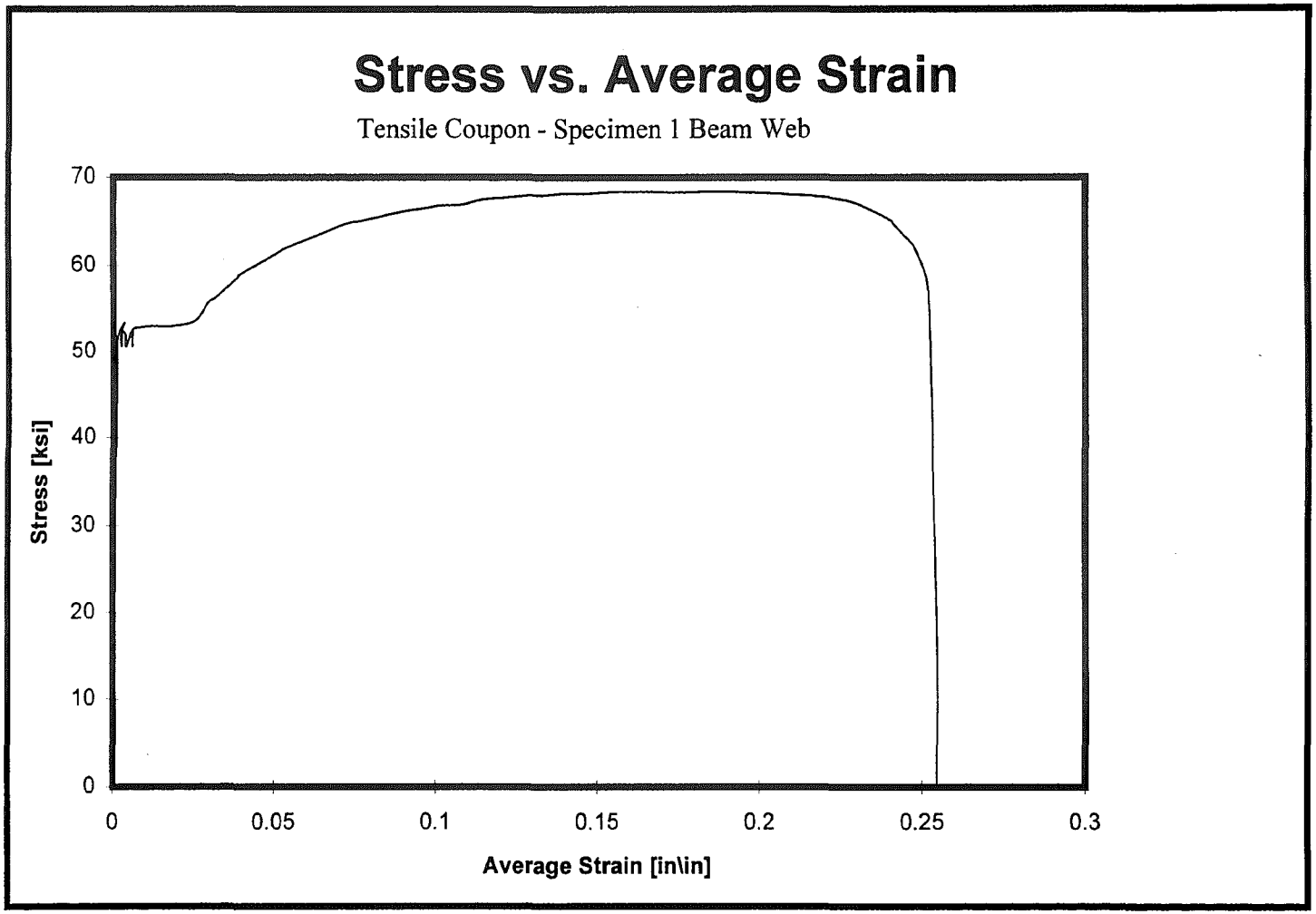

Figure 2.15(a) - Typical Stress-Strain Curve for Beam Web of Specimen 1

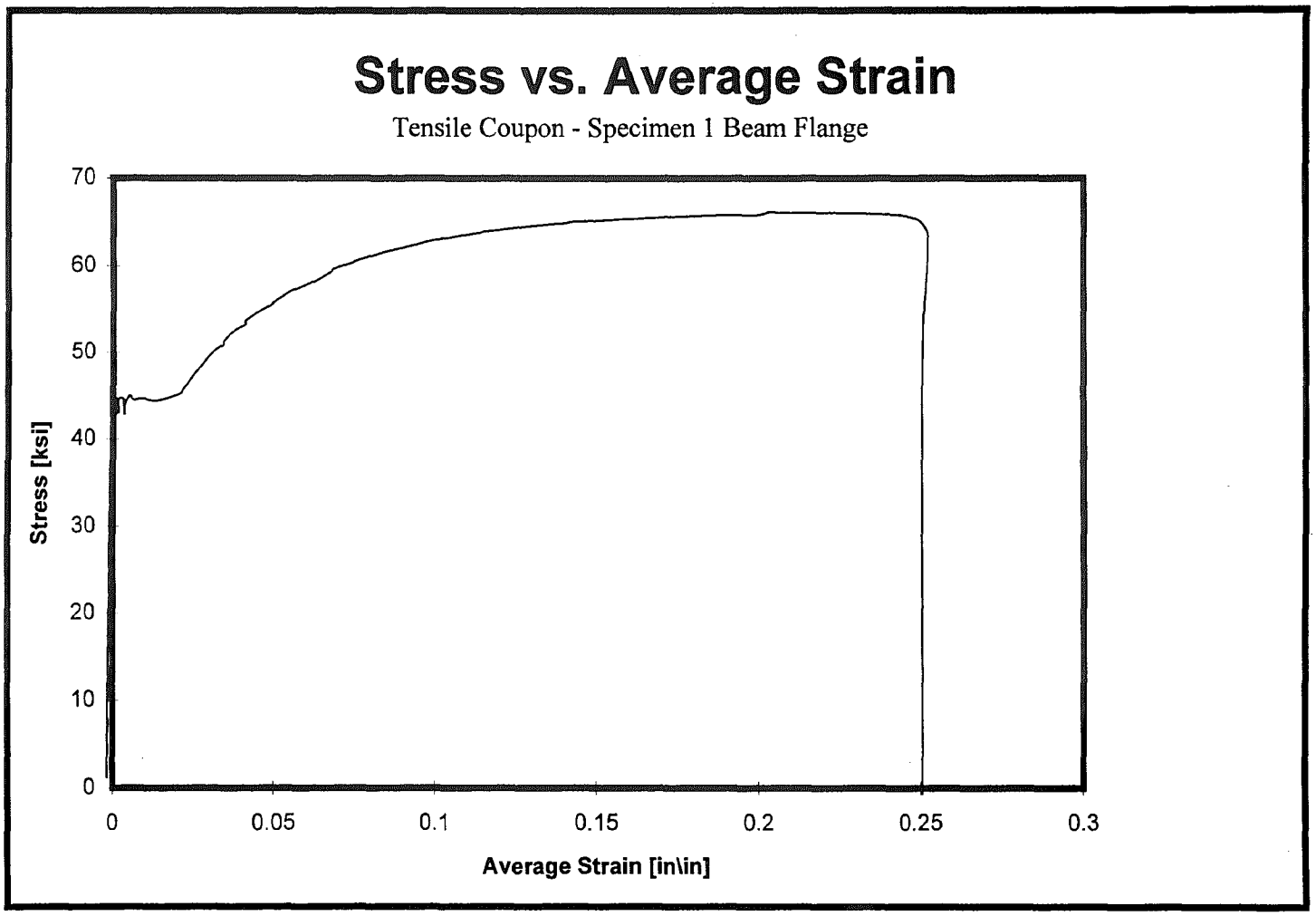

Figure 2.15(b) - Typical Stress-Strain Curve for Beam Flange of Specimen 1

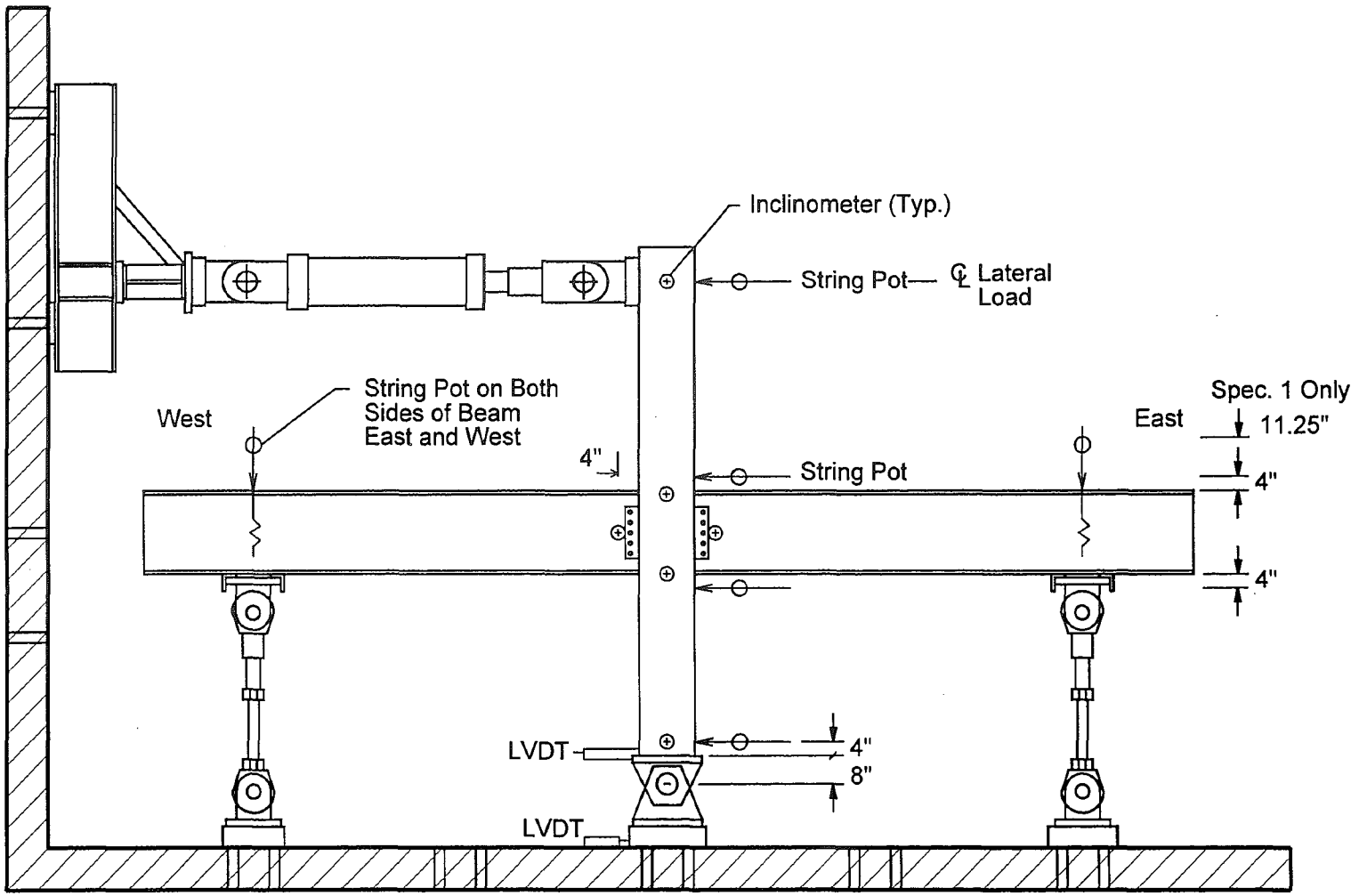

Figure 2.16 - Lateral, Rotational, and Beam Displacement Transducer Instrumentation

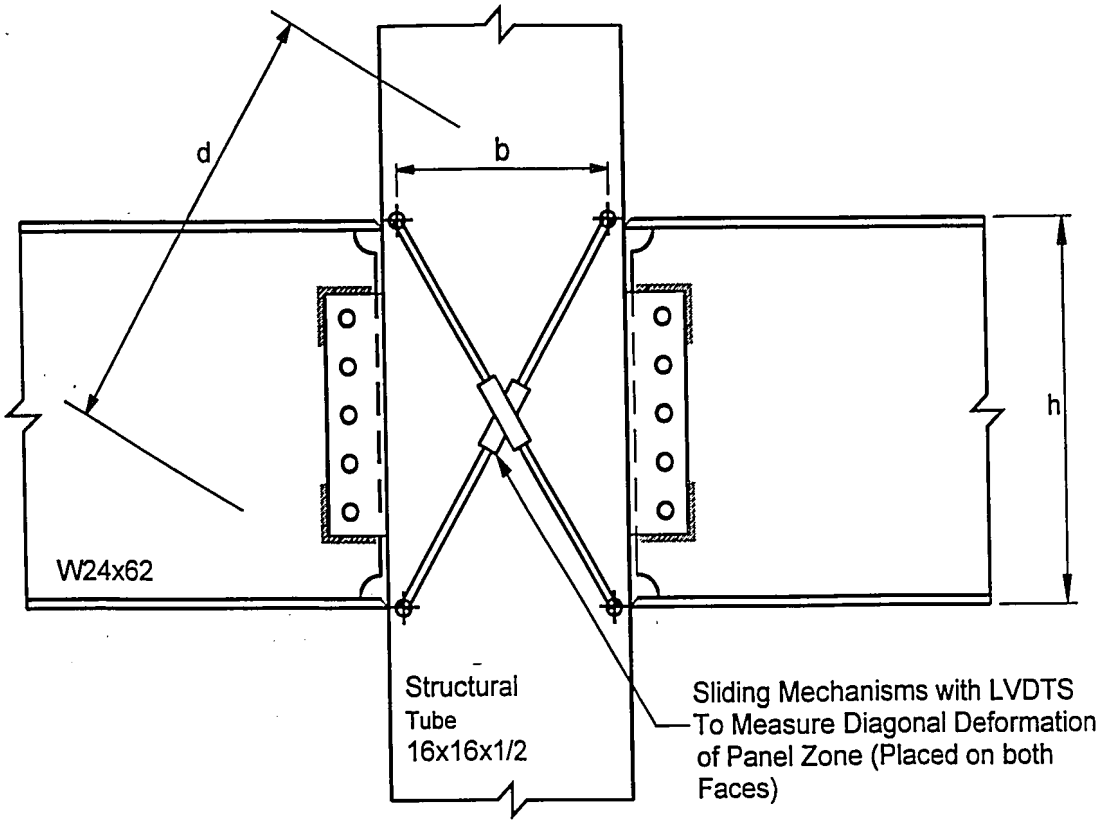

	h in	b in	d in
Specimen 1			
North Face	23.25	13.50	26.85
South Face	23.25	13.25	26.75
Specimen 2			
North Face	23.75	13.50	27.30
South Face	23.75	13.75	27.50

Figure 2.17 - Panel Zone Displacement Transducer Instrumentation

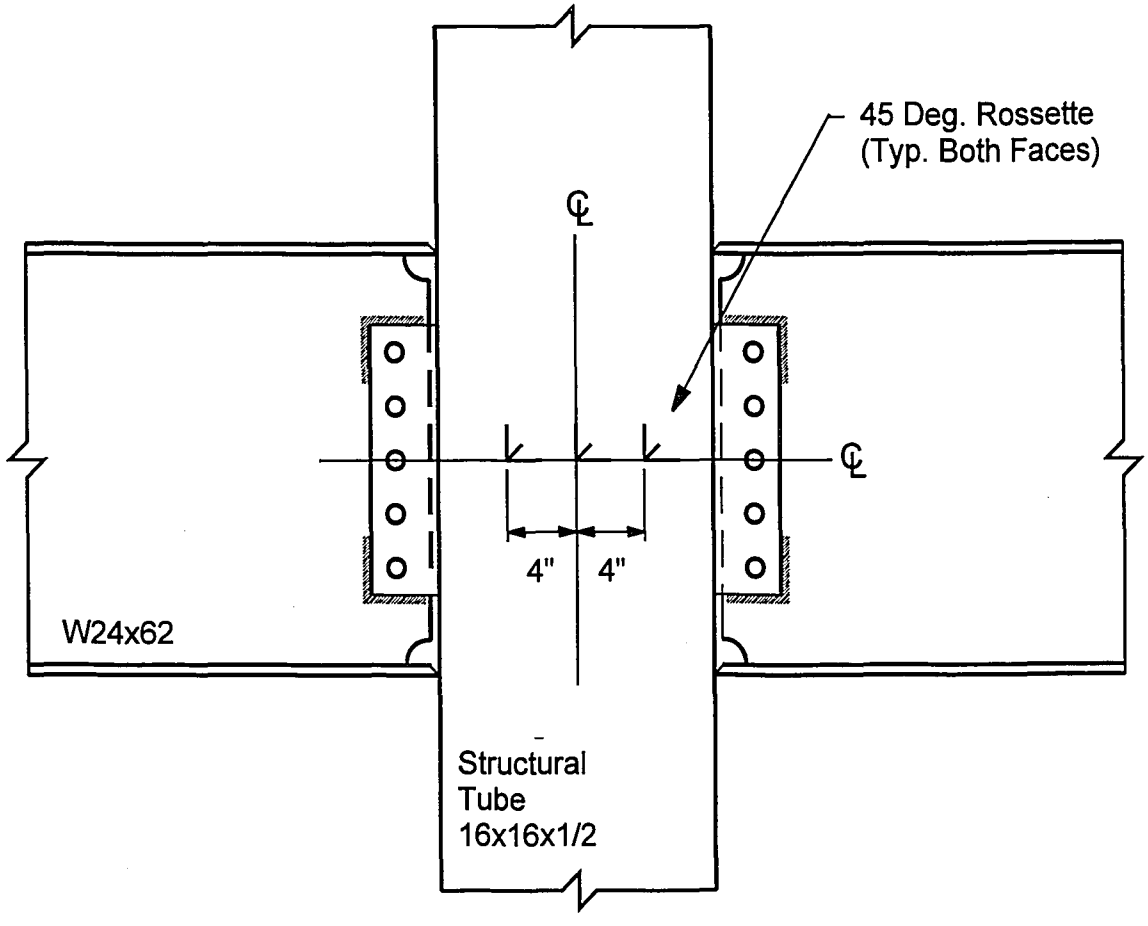

Figure 2.18 - Panel Zone Strain Gage Instrumentation

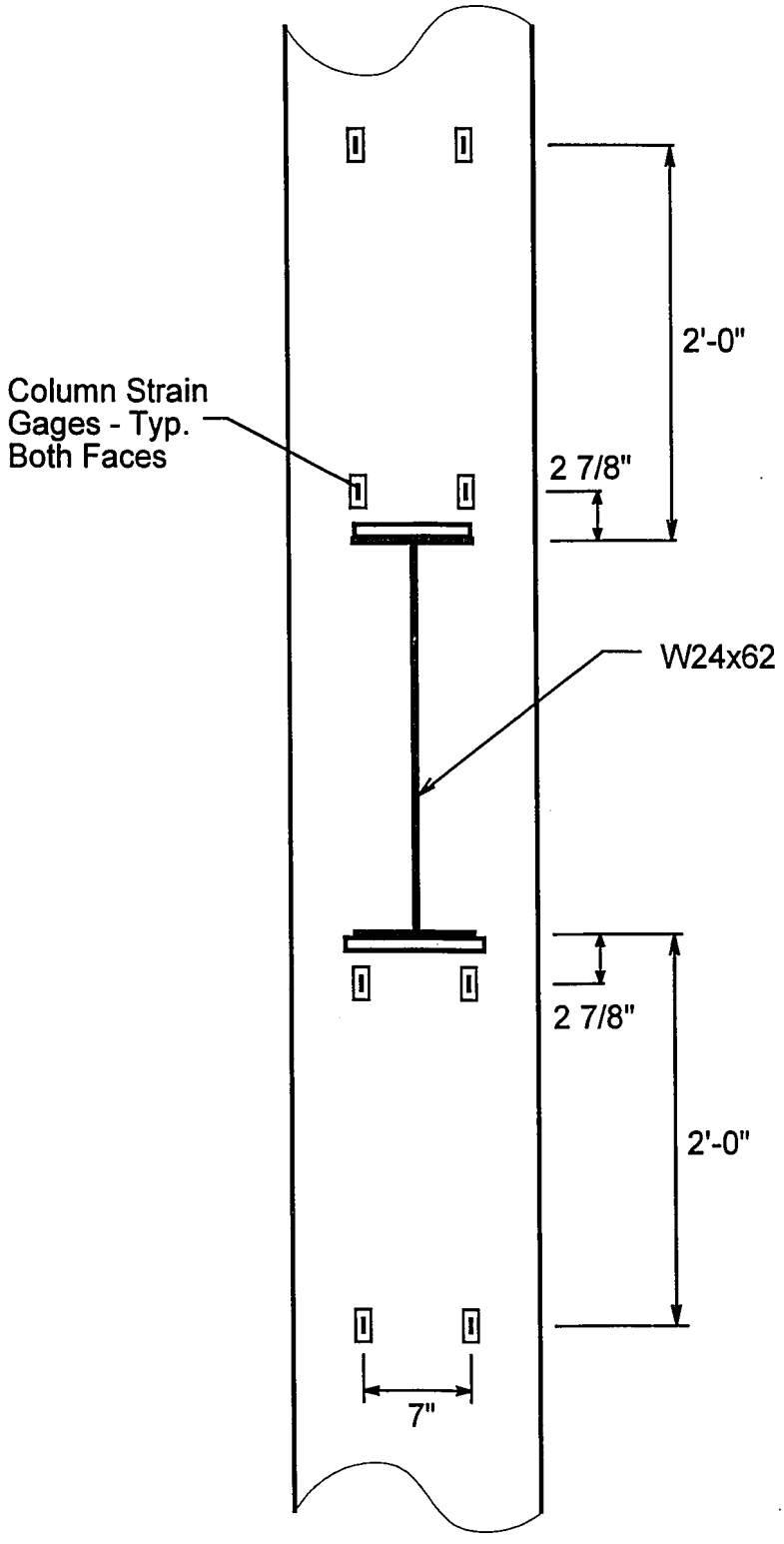

Figure 2.19 - Column Strain Gage Instrumentation
(East and West Faces)

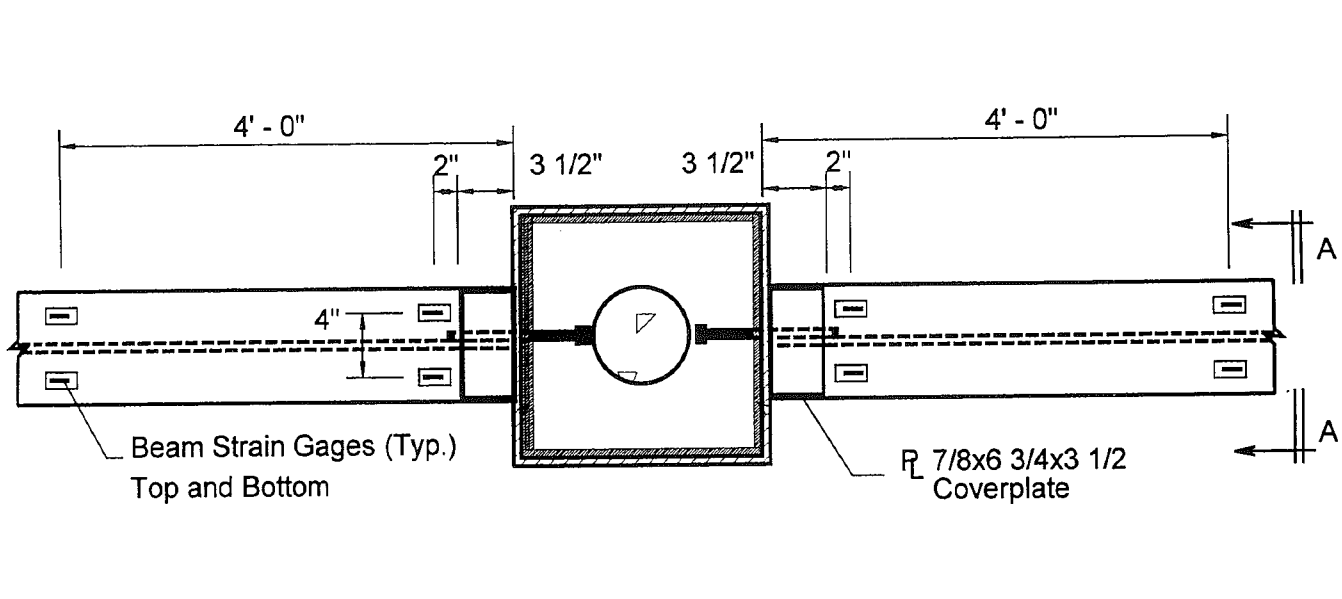

Figure 2.20 - Specimen 1 Beam Strain Gage Instrumentation

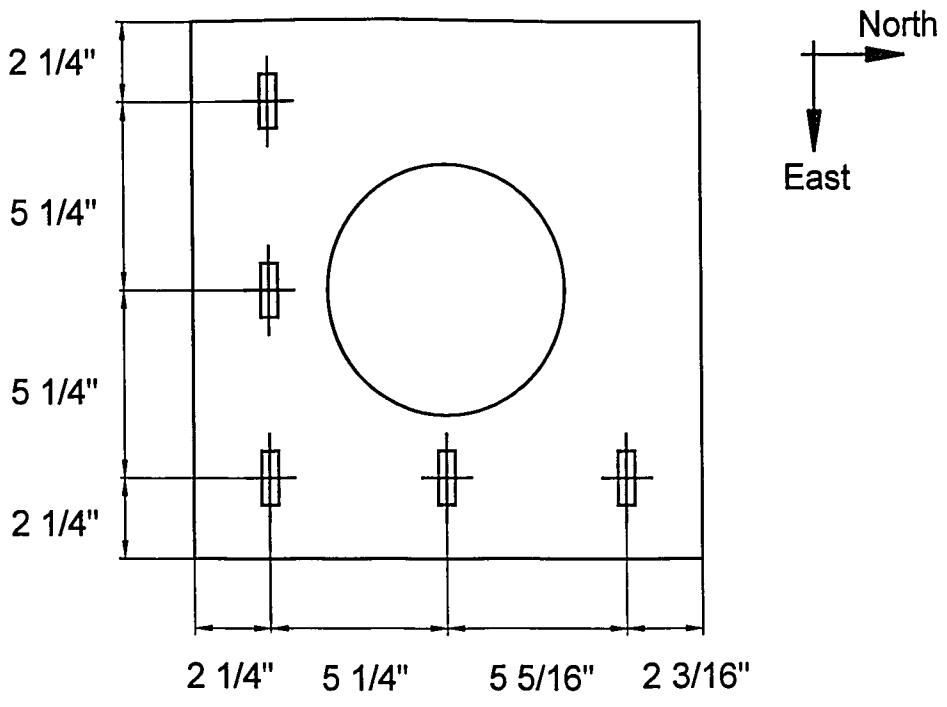

Figure 2.21 - Specimen 1 Top Diaphragm Strain Gage Location (Top View)

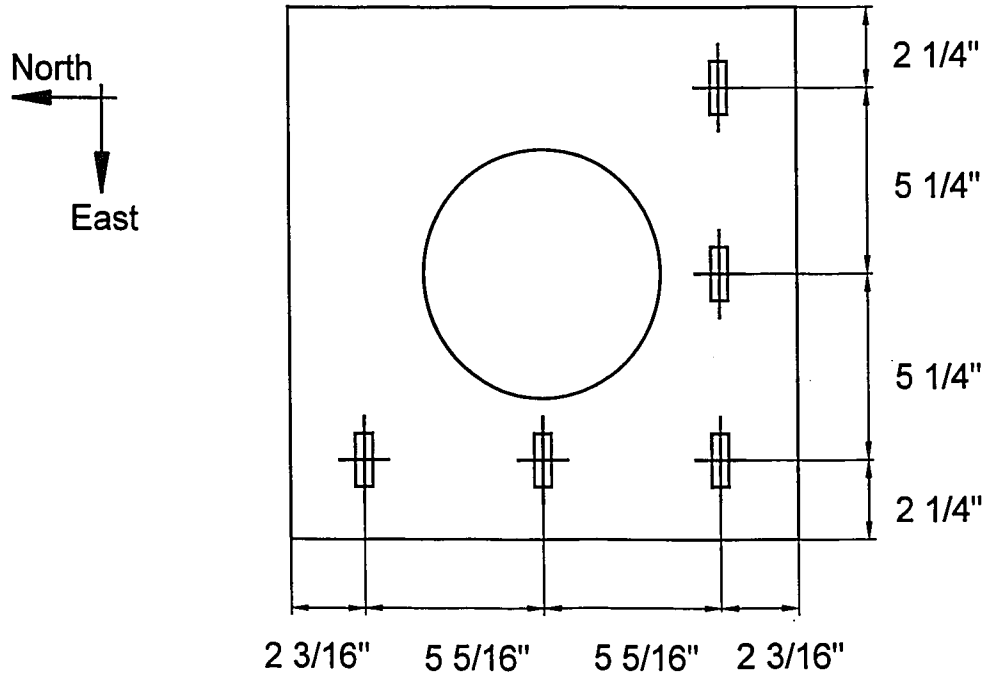

Figure 2.22 - Specimen 1 Bottom Diaphragm Strain Gage Location (Bottom View)

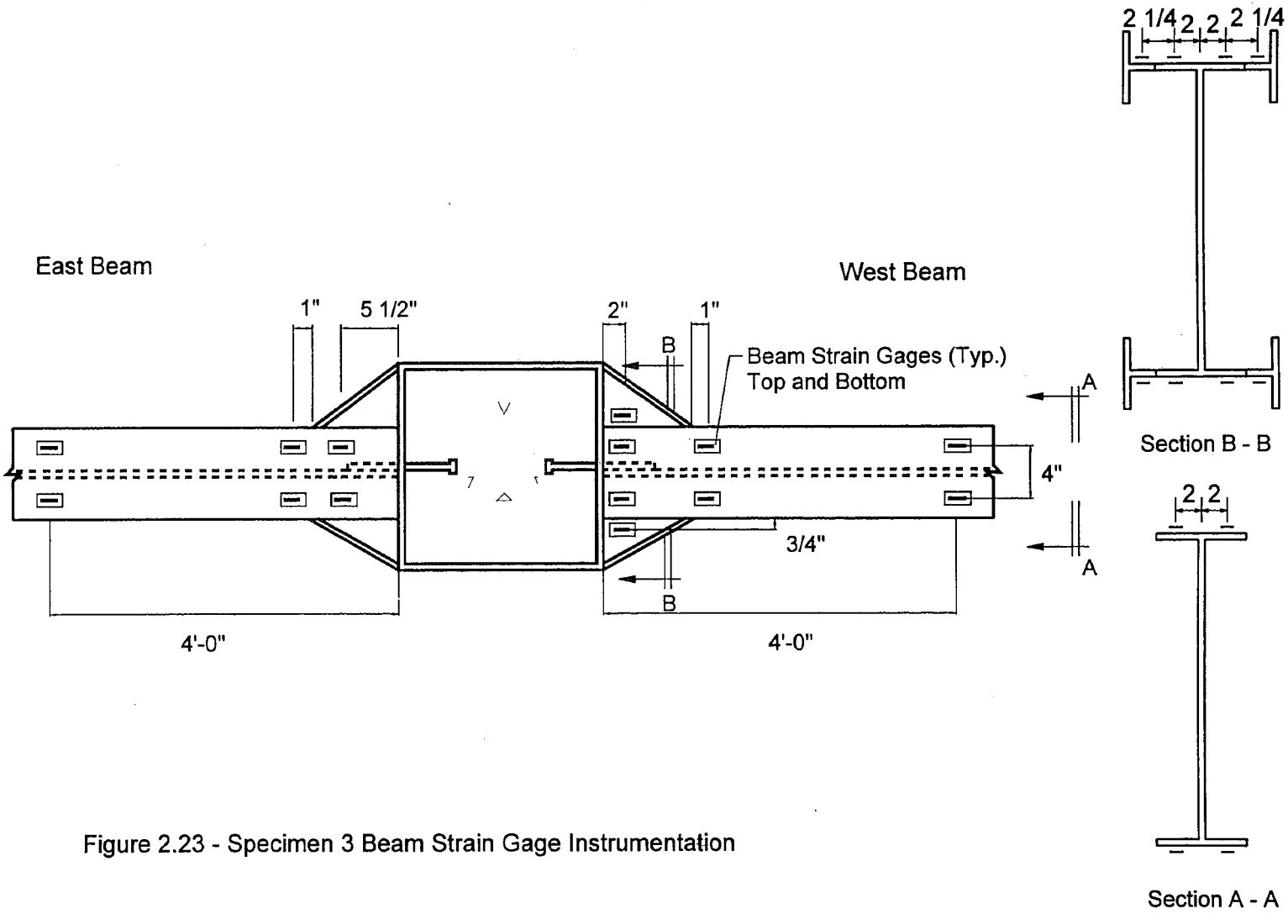

Figure 2.23 - Specimen 3 Beam Strain Gage Instrumentation

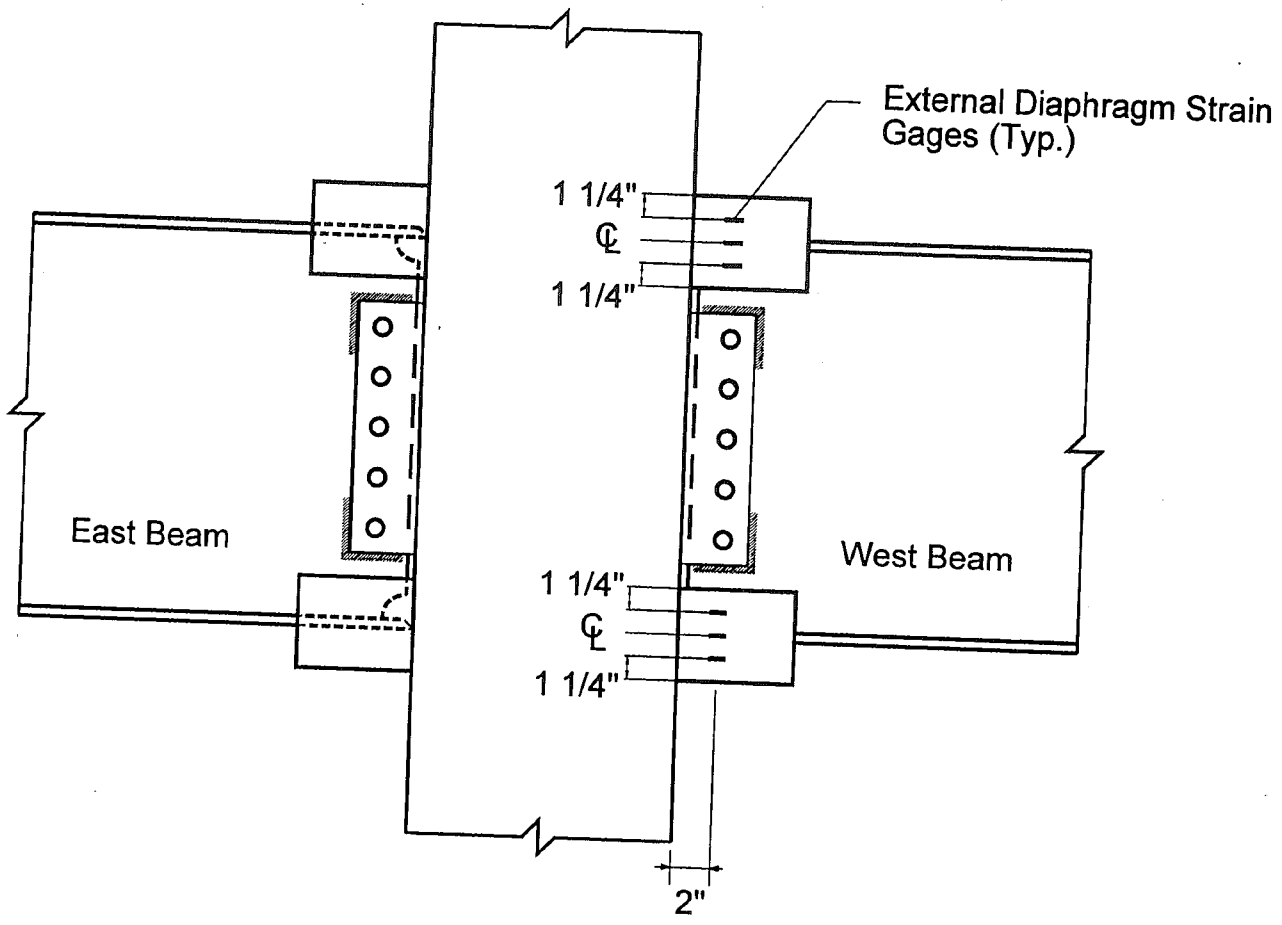

Figure 2.24 - External Diaphragm Strain Instrumentation

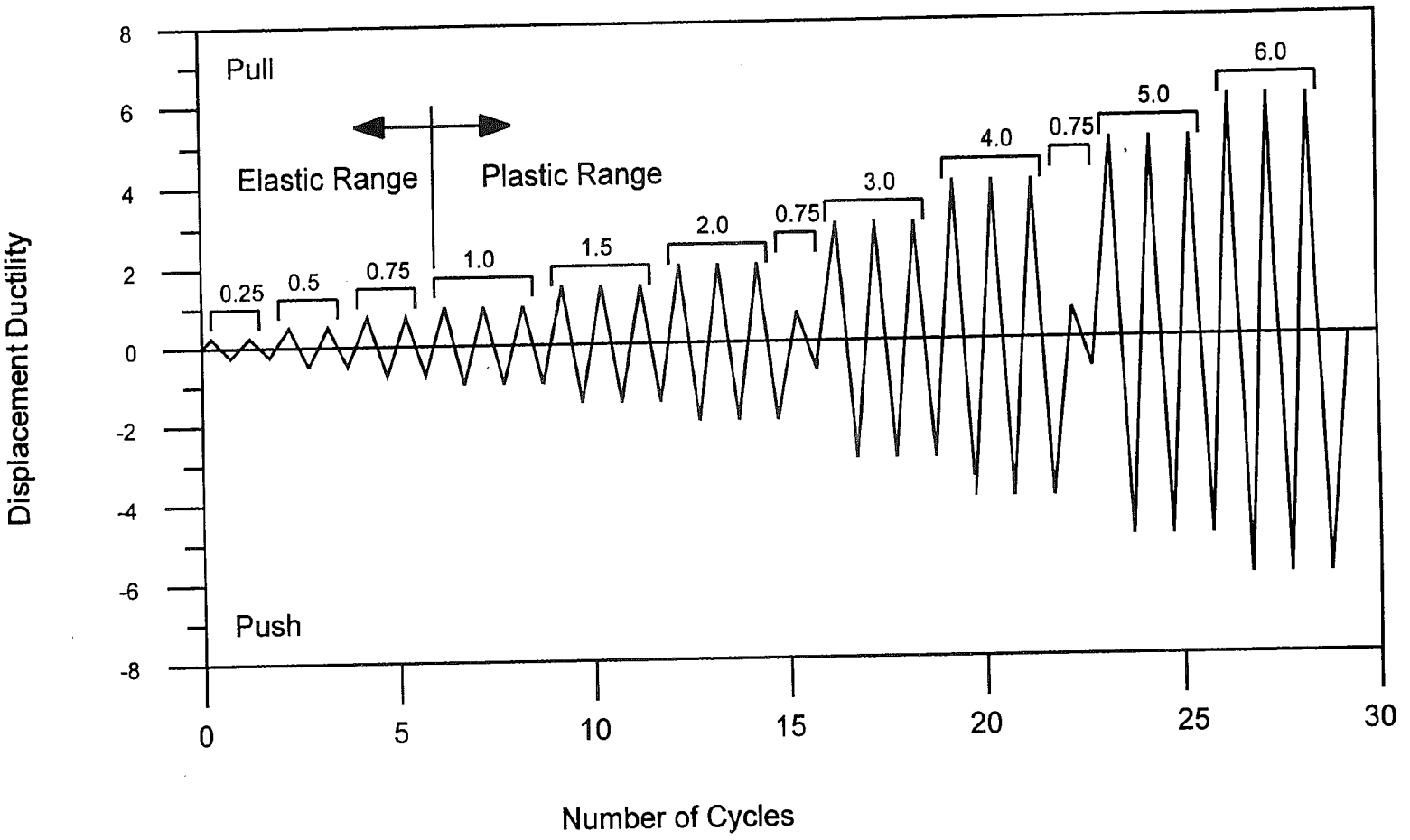

Figure 2.25 - Lateral Displacement History

Chapter 3
Experimental Behavior

3.1 Specimen 1

The lateral load-displacement (H-Δ) hysteretic response for Specimen 1 is shown in Figure 3.1. Before testing Specimen 1, an accidental lateral overloading occurred, causing the specimen to develop inelastic deformation in its beams as it was pushed in the east direction. It was observed that the compression beam flanges had developed minor local buckling over approximately a 9 inch length with an amplitude of 1/16 inch. This inelastic deformation amounted to a residual displacement of 2 inches in the east direction from the vertical plumb position at the top of the column. The lateral displacement history for Specimen 1 was subsequently modified to include six initial elastic cycles before subjecting it to inelastic deformation in the west (pull) direction, in order to straighten out the column to the vertical position. Following the straightening of the column, the displacement history based on ATC-24 was imposed to the test specimen. The modified displacement history for Specimen 1 is shown in Figure 3.2. Shown in Figure 3.3 is a photograph of Specimen 1 taken at the onset of testing.

Prior to imposing the modified displacement history, Specimen 1 was subjected to two cycles of elastic lateral displacements with a column axial load,

P, of 0 and 228 kips, respectively. The purpose of these four cycles of displacement was to verify the operation of the test setup and instrumentation, as well as acquire data that would enable a determination of specimen behavior to be made. In particular, the column's lateral stiffness under different levels of axial load could be evaluated. It was found that the lateral stiffness in the test specimen remained at approximately 55.5 kips/in during these four cycles.

Following the application of these four cycles, the column axial load was increased to 461 kips and the application of the displacement history begun. During the initial six cycles (Cycles 1 through 6) the specimen's lateral stiffness was approximately 58 kips/in. The specimen remained elastic during these cycles, where the strains during Cycle 6 in the beam flanges at 2 inches from the end of the cover plates were equal to the steel's yield strain. The lateral displacement Δ at the end of Cycle 6, referenced from the beginning of Cycle 1 where $\Delta=0$ (e.g. columns out-of-plumb position), was 1.05 inches. The corresponding lateral load H was 61.5 kips. Based on the peak displacement of 1.05 inches at the end of Cycle 6, it was determined that a lateral displacement ductility of $\mu=1$ corresponded to a lateral displacement of 1.64 inches at the top of the column. During Cycle 7, the specimen was subjected to 4 inches of lateral displacement in the west (pull) direction in order that the top of the column was plumb after the elastic unloading. During Cycle 7 yielding developed in the beam flanges over a length of 14 inches (corresponding to 58% of the beam's depth),

as shown in Figure 3.4. Some yielding was also observed in the beam's web adjacent to the yielded beam flanges.

The remaining portion of the test involved subjecting the specimen to the ATC-24 displacement history, which resulted in 17 additional cycles before failure occurred. Cycles 8 though 13 involved the application of the six cycles of elastic displacement. During cycles 14 through 16, Specimen 1 was subjected to a lateral displacement ductility of μ=1.0 that was referenced from the column's plumb position. During these cycles no signs of further yielding were observed.

The next three cycles of displacement (Cycles 17, 18, and 19) involved a displacement ductility of μ=1.5 from the column's plumb position. This resulted in some slight local buckling being observed in the beams' compression flanges. However, no increase in yielding relative to Cycle 7 was observed. At μ=1.5 the corresponding displacements referenced from the position of the column at the onset of testing (e.g. at 2 inches out-of-plumb in the east direction), were 4.45 inches and 0.45 inches in the west (pull) and east (push) directions. The lateral load was 118 and 92.5 kips when these displacements were achieved. Cycles 20 through 22 involved subjecting the top of the column to a displacement ductility of μ=2.0 relative to its plumb position. The lateral load H corresponding to the peak west and east direction displacements was 120 and 106 kips, where these displacements were 5.27 and 1.27 inches from the initial column's out of plumb position. During these displacement cycles the yielding and local buckling

in the beam flanges had become more pronounced. Flange yielding was observed to develop over a length of 21 inches (corresponding to 88% of the beam depth) from the face of the column. An increase in web yielding of the beams was also observed. The hysteretic response indicated that a significant reduction in lateral stiffness relative to the initial elastic stiffness occurred during these cycles at displacements beyond μ=1.5 (see Figure 3.1), which corresponded to Δ equal to 4.45 and 0.45 inches in the west and east directions from the column's initial out-of-plane position. This was due to pronounced inelastic deformations that developed in the beams. The hysteretic behavior however remained stable, as the specimen retained its capacity at the peak displacements of these cycles. The plastic beam rotation, Θ_p, corresponding to the maximum displacements in the west and east directions, was approximately 0.025 and 0 radians. Figure 3.5 shows a photograph of the connection region of Specimen 1 at a displacement of μ=2.0.

During the next two cycles (Cycles 23 and 24) Specimen 1 was subjected to a displacement ductility of μ=3.0, resulting in 6.91 inches and 2.91 inches of lateral displacement in the west and east directions from the column's initial out-of-plumb position, respectively. Theses displacements corresponded to an interstory drift of 4.8 and 2% from the column's out-of-plumb position, and 3.4% from the plumb position. The horizontal load H at Δ equal to 6.91 and 2.91 inches was 124 and 118 kips, respectively. Upon developing the peak

displacement in Cycle 23, a crack initiated in the west beam's tension flange, near the toe of the cover plate's transverse weld (see Figure 3.6). This crack attenuated about 0.75 inches across the flange over the next cycle (e.g. Cycle 24). Necking was observed in the beam flange at the crack, indicating the development of a significant amount of strain. Although an increase in flange and web yielding, as well as local flange buckling, occurred in the beams, the hysteretic response of Specimen 1 during Cycles 23 and 24 remained stable (see Figure 3.1). The beam flange yielding was found to attenuate over a length of approximately one beam depth (e.g. 24 inches). A local slight distortion was observed to develop in the wall of the column between the diaphragm plates in the connection region, to which the beam was attached. This distortion consisted of an outward bulging of the column face, as shown in Figure 3.6, and was associated with a prying action from the beam tension flanges and shear tab. The distortions remained after unloading between displacement cycles, indicating inelastic deformations had occurred. The remaining portions of the column outside of the connection region remained elastic.

Upon achieving the displacement ductility of μ=3.0 at the end of Cycle 24 the test was stopped. While the specimen's behavior had remained hysteretically stable, and a greater lateral displacement could have been imposed, the test was terminated to mitigate further damage in order that the specimen could be retrofitted and a new test conducted in the future.

A photograph of Specimen 1 at the end of Cycle 24 is shown in Figure 3.7, where beam flange and web yielding is evident, as well as fracture in the upper beam flanges. The maximum plastic rotations that developed in the beams at the peak displacements in the west and east directions were 0.0375 and 0.0125 radians. Upon removing the cover plates from the top flanges of the beams following the test, minor cracks were detected in the east wall of the steel tube column. This cracking was located in the material of the tube wall that was between the interior diaphragm and beam flange, and appeared to have developed under the tension force exerted by the beam flange. A photograph of this crack is shown in Figure 3.8. Ultrasound tests were conducted before fabrication and indicated that no discontinuities or flaw existed in the through thickness direction of the steel tube.

3.2 Specimen 3

The lateral load-displacement (H-Δ) hysteretic response for Specimen 3 is shown in figure 3.9. A photograph of Specimen 3 taken at the onset of testing is shown in Figure 3.10.

Prior to imposing the ATC-24 displacement history, Specimen 2 was subjected to six cycles of elastic deformation with a column axial load, P, of 0 kips and seven cycles of elastic deformation with a column axial load, P, of 255 kips. The purpose of these thirteen cycles of displacement was to verify the

operation of the test setup and instrumentation, as well as, acquire data in order to evaluate the column's lateral stiffness under different levels of axial load. It was found that the average lateral stiffness in the test specimen for the first six cycles remained at approximately 68 kips/in. The average lateral stiffness in Specimen 3, when subjected to an axial load of 255 kips, was found to be 70 kips/in.

The remaining portion of the test involved subjecting the specimen to the ATC-24 displacement history with a column axial load of 499.5 kips, which resulted in 17 additional cycles before failure had occurred. Cycles 1 through 6 involved the application of the six elastic displacement cycles, while during Cycle 6 the displacement ductility μ was 0.75, which corresponded to 0.93 inches of lateral displacement and 71.2 kips of lateral load. The elastic lateral stiffness associated with the lateral displacement at the top of the column of the subassembly averaged 72 kips/in. Based on the measured displacement for Cycle 6, it was determined that the lateral displacement Δ corresponding to μ = 1.0 was 1.4 inches. During Cycles 7 through 9, Specimen 3 was subjected to the lateral displacement ductility of μ=1.0, which required a horizontal load of H equal to 93.6 kips to achieve the displacement of Δ=1.4 inches. During these cycles yielding was observed to occur in the top and bottom flanges of the beams. The yielding extended to a distance of 40 inches from the face of the column where flaking of the whitewash were observed. The strain gauges,

which were located on the beam flanges at one inch outside of the tees, indicated that the beam flanges had yielded. According to the data which was collected during the experiment and analyzed after the completion of the test, the strain gauges on the web and flanges of the tees indicated that no yielding had yet developed in these elements. This was consistent with the fact that no cracks or flaking were observed in the whitewash placed on these elements. Also, at this load flaking in the whitewash that covered the beam's web below the yielded flanges was observed, indicating yielding in the region of the beams. No local flange buckling in either the beams or the tees was observed. A photograph showing the beam flange yielding in the connection region is given in Figure 3.11.

The next three cycles of displacement (Cycles 10, 11, and 12) involved a displacement ductility of μ=1.5, which corresponded to Δ equal to 2.1 inches. During Cycle 10 yielding occurred in the web of both beams next to the shear tab, as well as in the flanges of the four tee sections. This yielding, as well as that in the beam flanges continued during Cycles 11 and 12. No yielding was observed in the webs of the tee sections. The lateral load - displacement response (H-Δ) remained stable, with a reduction in stiffness occurring at displacements in the east and west directions beyond Δ equal to 1.4 inches due to beam yielding (see Figure 3.9). The applied lateral load was 112 and 115 kips when the west (pull) and east (push) displacements of Δ equal to 2.1 inches

were achieved. At the completion of a ductility level of μ=1.5 no local buckling in the beam flanges was observed.

Cycles 13, 14, and 15 involved subjecting the top of the column to a displacement ductility of μ=2.0, which corresponded to a displacement and interstory drift of 2.79 inches and 2%, respectively. The lateral load H corresponding to the peak west and east direction displacements was 124 and 121 kips. During these displacement cycles the yielding in the beams and the flanges of the tees became more pronounced, with yielding also occurring in the web of the tees. The onset of local flange buckling was observed in the beams, occurring just outside the connection region where the tees were located. The strain gages indicated that the flanges of the tees which corresponded to the tension flange of the beam developed significantly greater strain that the tees attached to the beam compression flanges. Figure 3.12 shows a photograph of the connection region of Specimen 3 corresponding to a displacement of μ=2.0. Cycle 16 involved a displacement amplitude of 0.5 inches, and therefore only elastic specimen deformations.

During the first half of cycle 17, where the top of the column was subjected to a displacement ductility of μ=3.0, a noticeable fracture developed at the edge of the east beam's top flange. This fracture initiated near the toe of the weld at the end of the tee, see Figure 3.13. As the peak displacement Δ of 4.35 inches was achieved, corresponding to μ=3.0 and requiring a lateral load of H

equal to 129 kips, the crack had propagated about 1.5 inches across the beam's flange towards the web. Similar, but only minor fractures were also observed in the other beam flanges. The strain gauges located 1 inch from the flange fractures measured tensile strains between 10 to 12 times the yield strain, indicating that a strain concentration existed at the flanges where cracks occurred. This provided evidence that the fractures were caused by strain concentrations in the flanges. The tensile strain in the tee section webs, according to the strain gauges, had just approached yield, with the tensile strain in the flange of the tees showing 8 times yield. A photograph of Specimen 3 at the end of Cycle 17 is shown in Figure 3.13 and 3.14, where beam flange yielding is evident. The maximum plastic rotations, Θ_p, that developed in the beams was 0.022 radians, which occurred at the peak displacement of Δ equal to 4.35 inches in the east direction.

Upon completing the first half of Cycle 17 the test was terminated. Although the hysteretic response was stable and showed no signs of deterioration, it was decided to avoid further fracture by stopping the test in order that the specimen be rehabilitated to reduce strain concentrations. The repaired specimen would be then be tested at a later date.

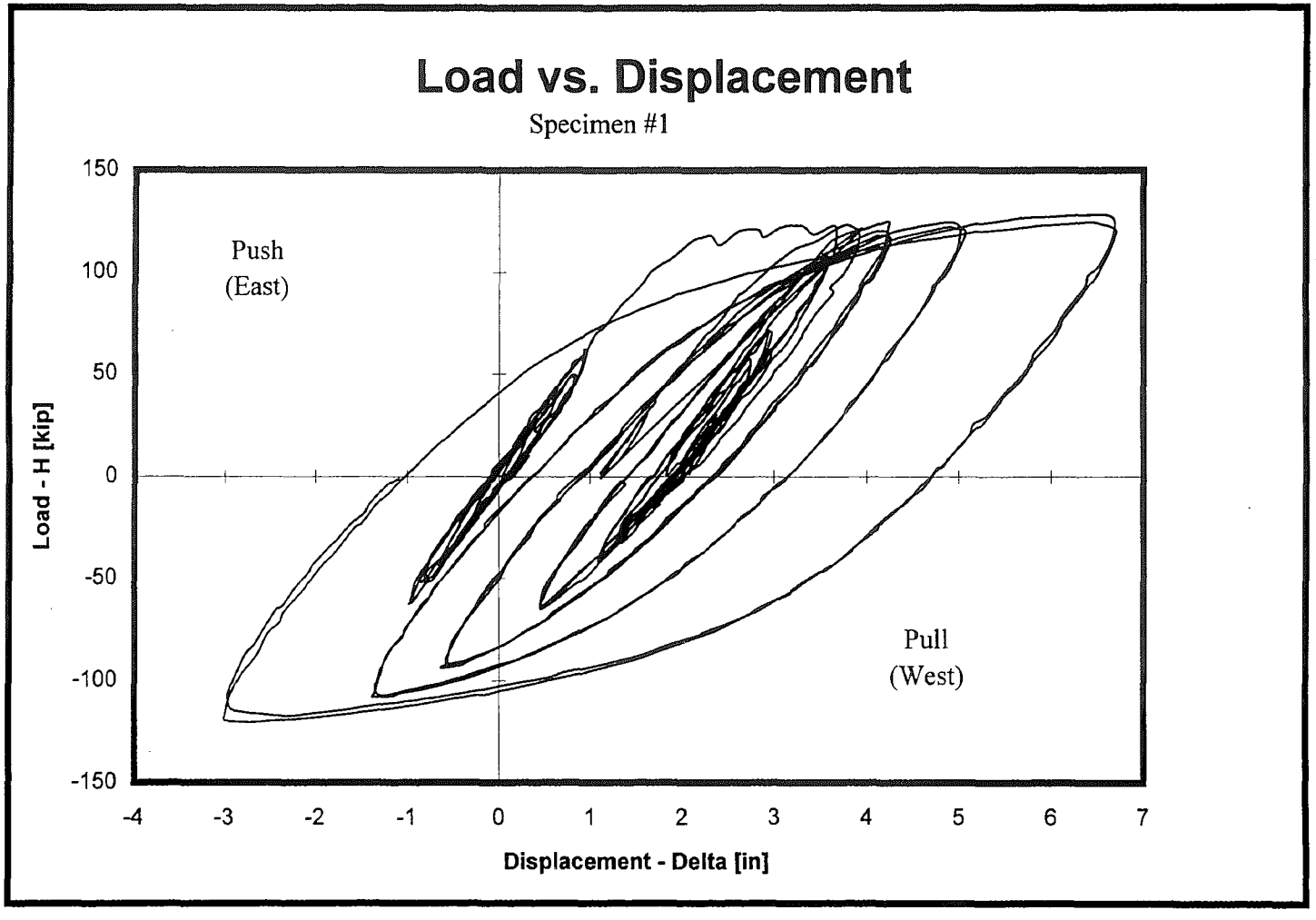

Figure 3.1 Lateral Load - Displacement Response, Specimen 1.

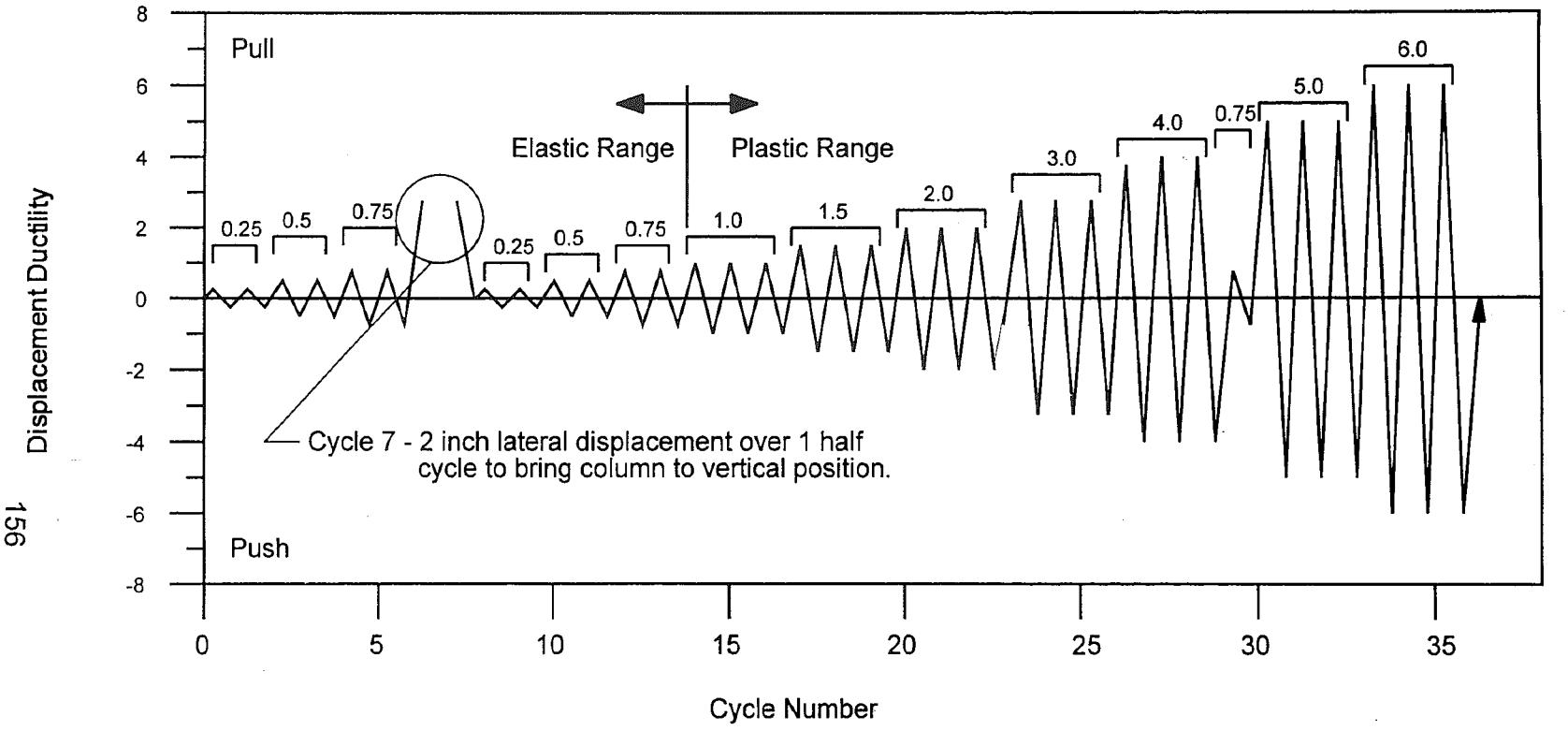

Figure 3.2 Modified Displacement History Involving Seven Initial Cycles, Followed by ATC-24, Specimen 1

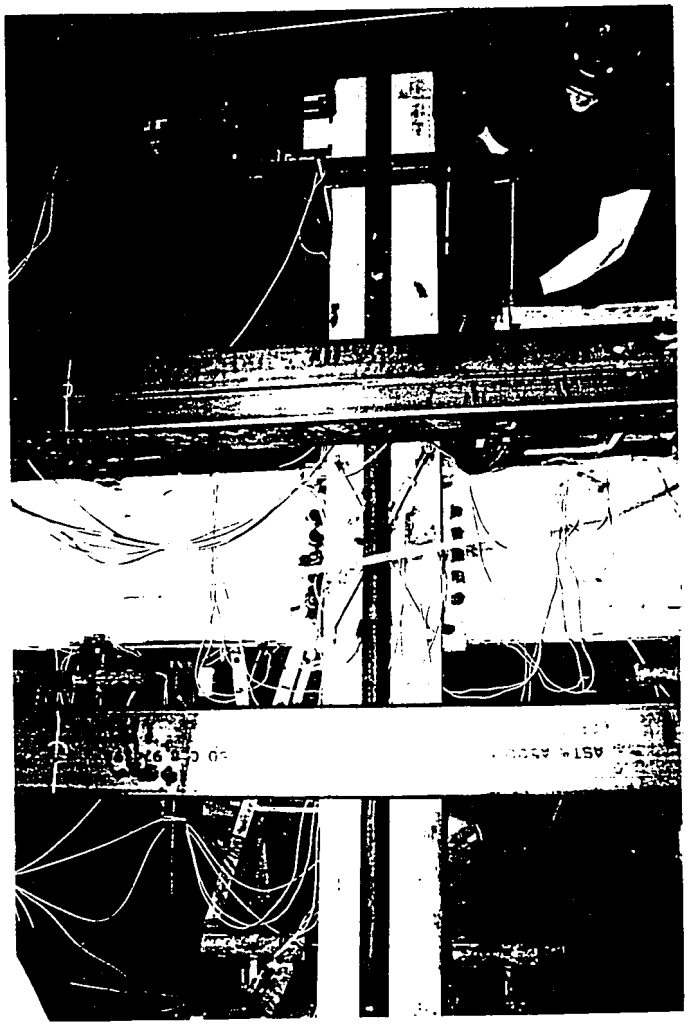

Figure 3.3 - Specimen 1 Before Testing

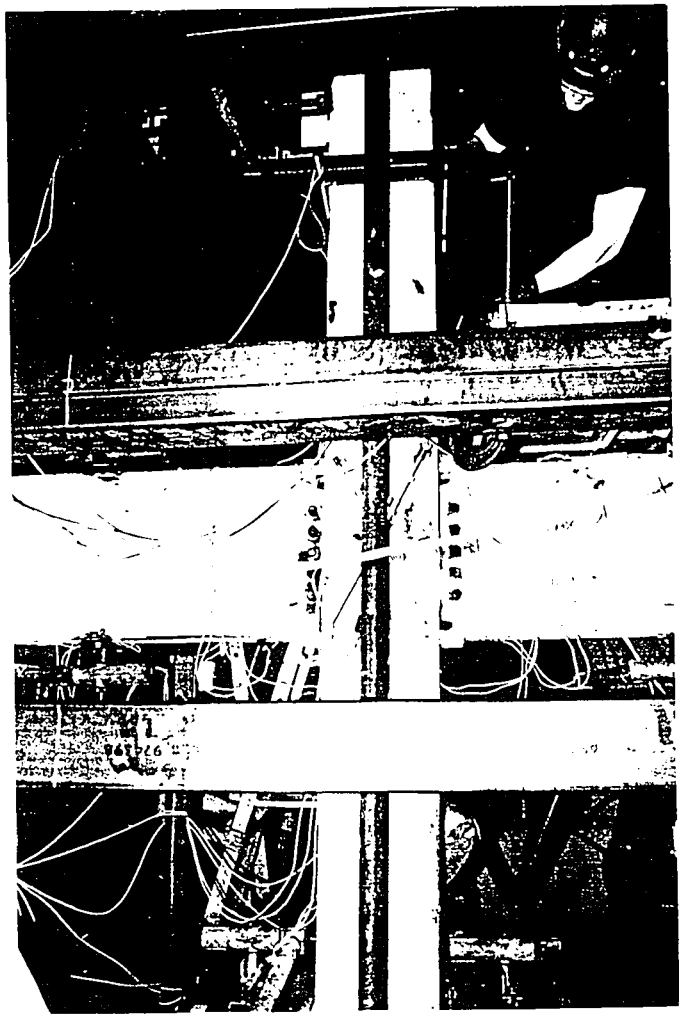

Figure 3.3 - Specimen 1 Before Testing

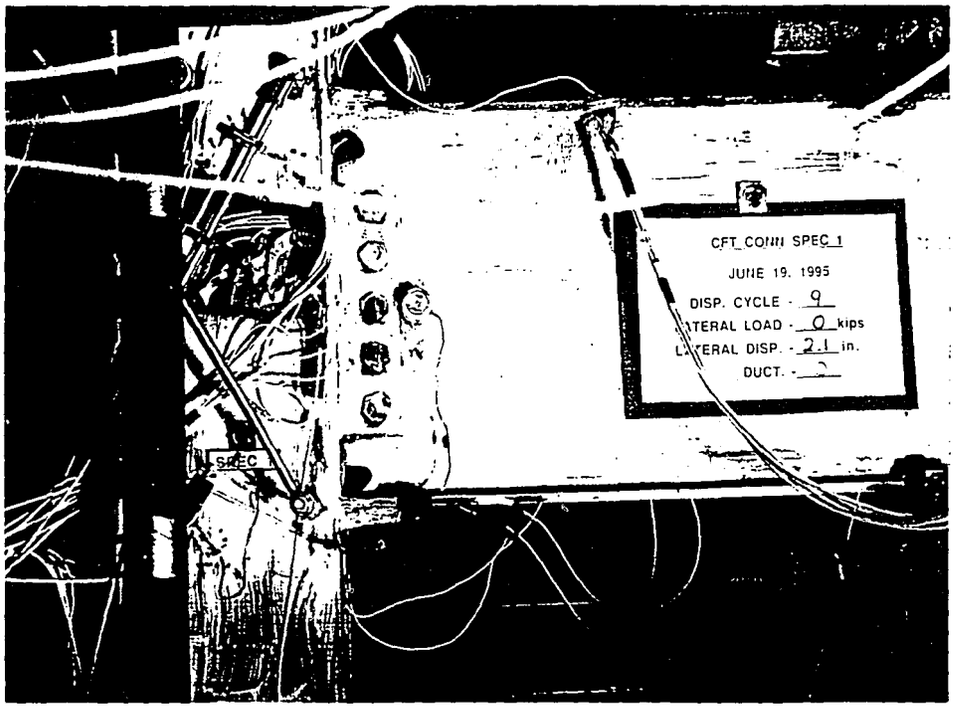

Figure 3.4 - Specimen 1 - Cycle 7

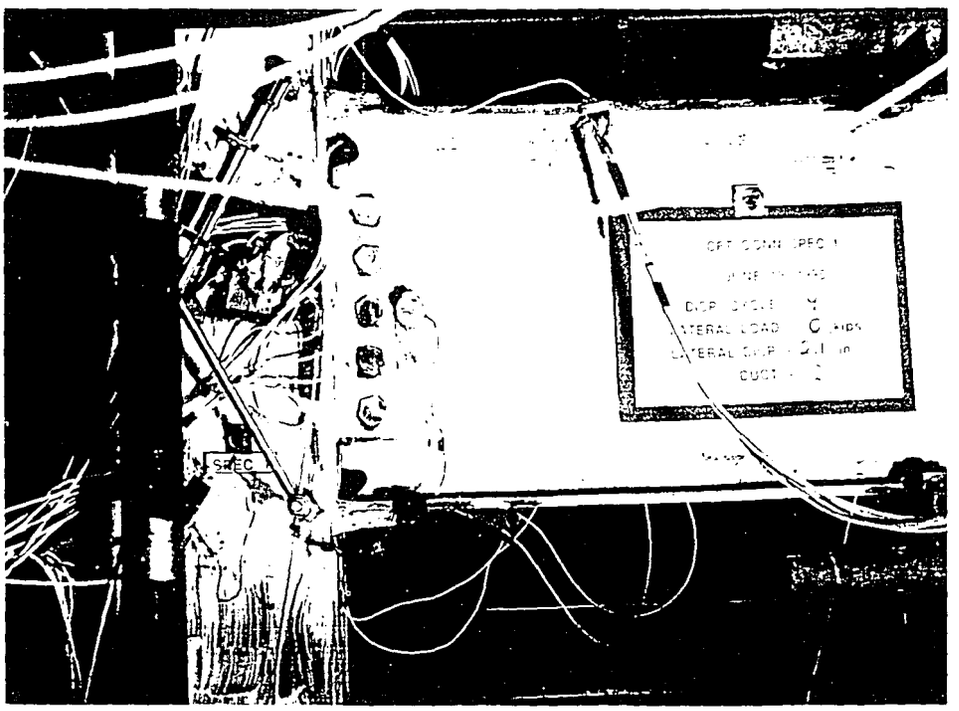

Figure 3.4 - Specimen 1 - Cycle 7

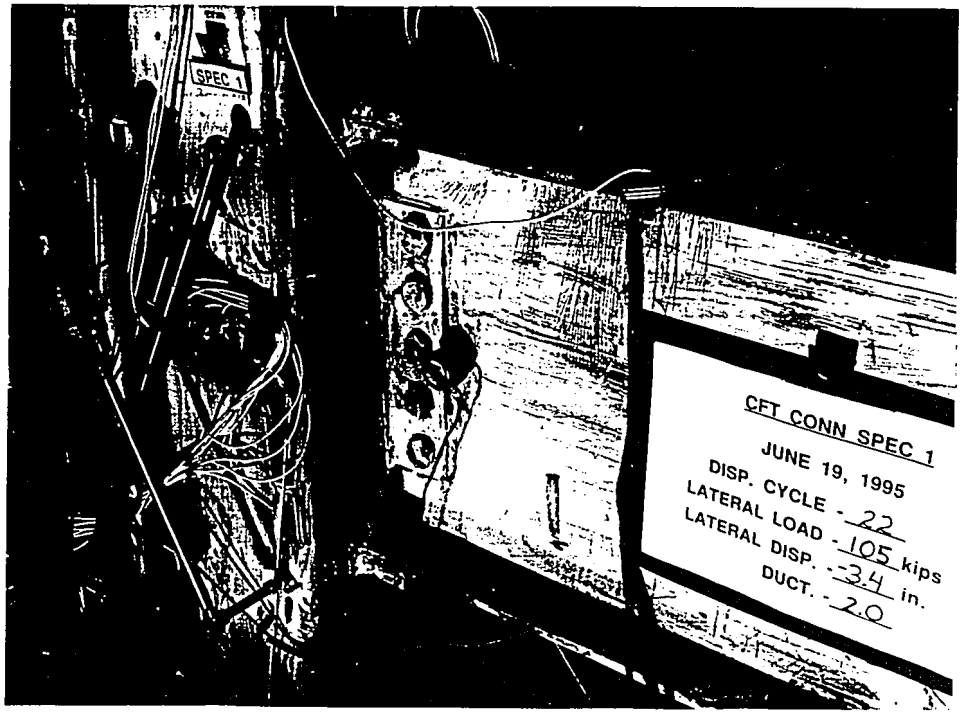

Figure 3.5 - Specimen 1 - Cycle 22 (μ = 2.0)

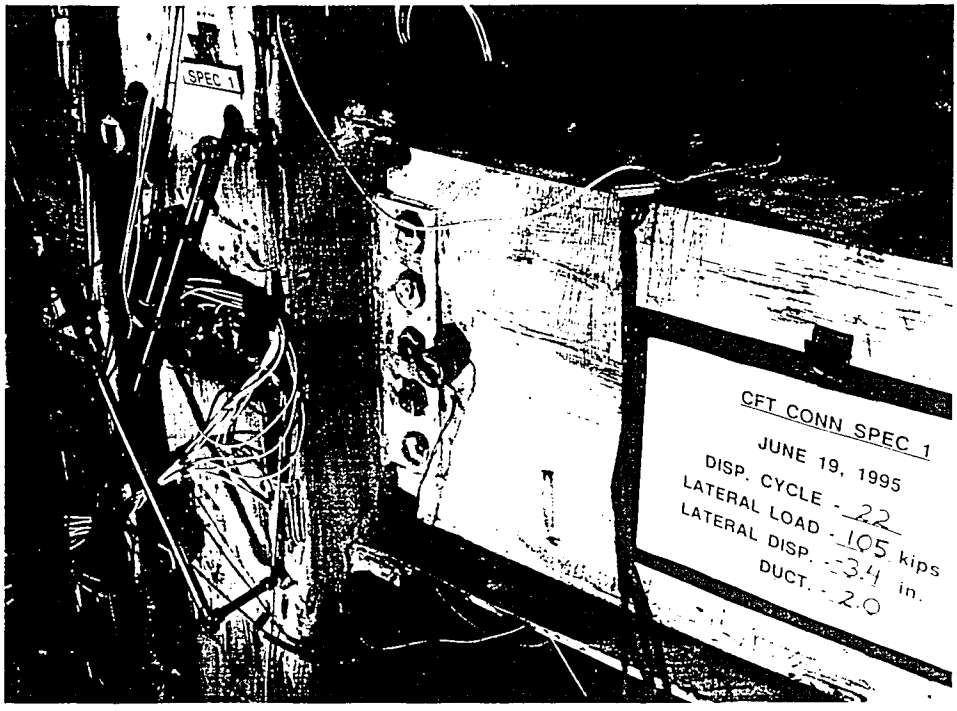

Figure 3.5 - Specimen 1 - Cycle 22 (μ = 2.0)

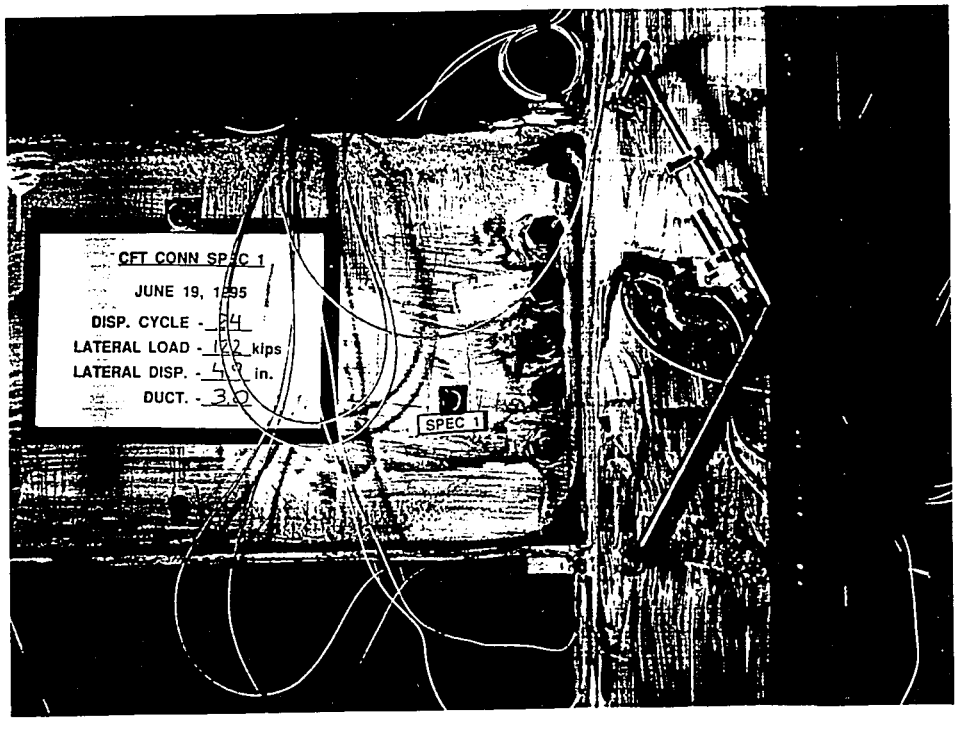

Figure 3.6 - Specimen 1 - Cycle 24 (μ = 3.0)

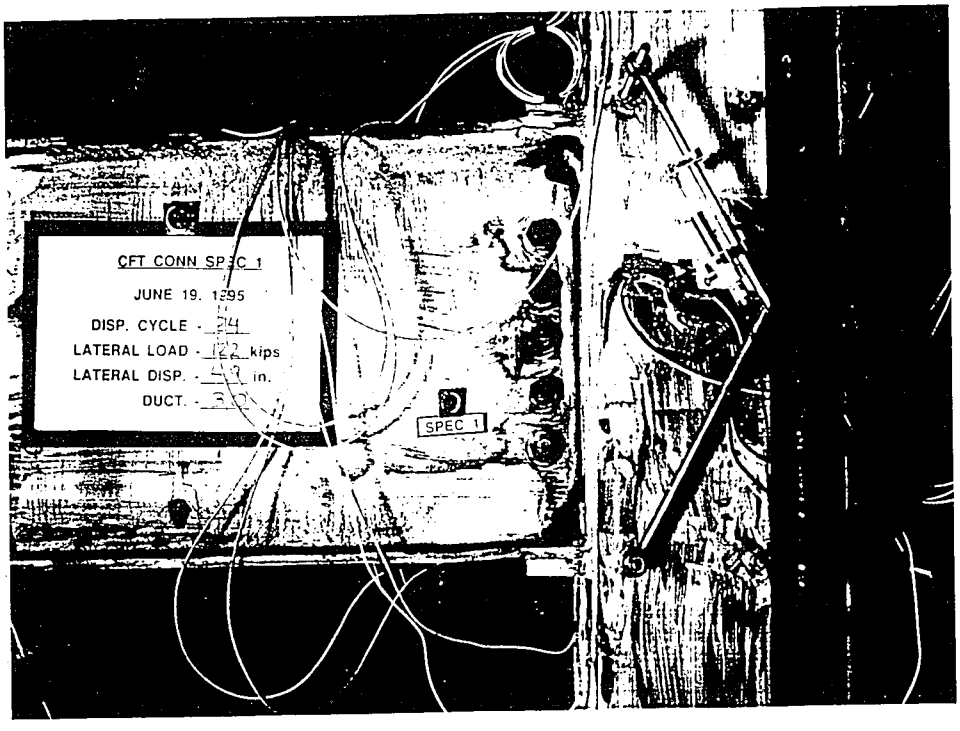

Figure 3.6 - Specimen 1 - Cycle 24 (μ = 3.0)

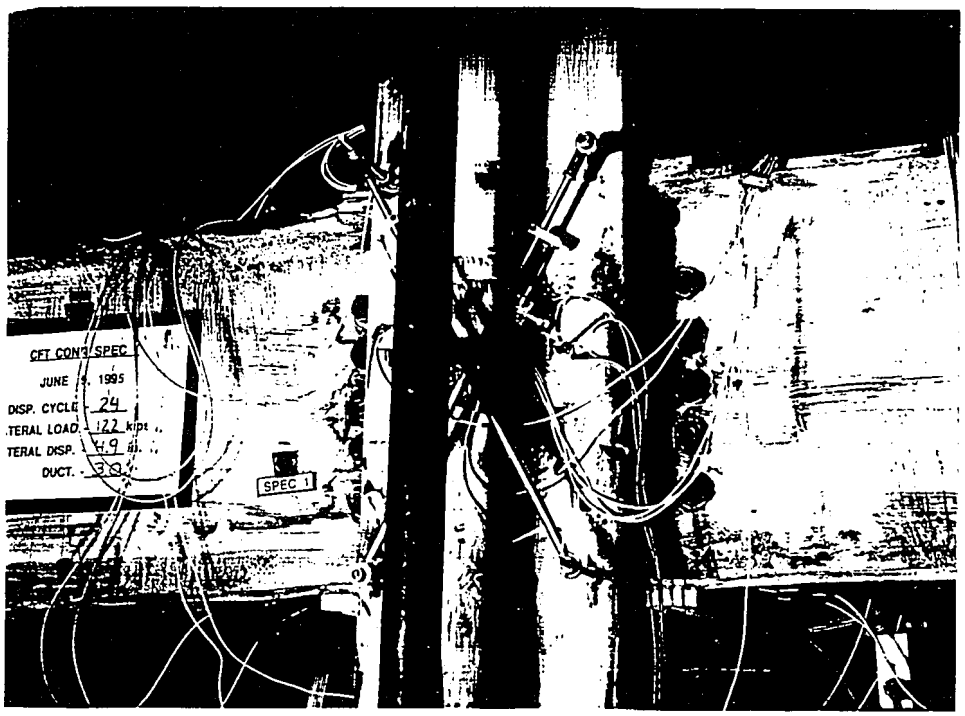

Figure 3.7 - Specimen 1 - End of Cycle 24 (μ = 3.0)

Figure 3.7 - Specimen 1 - End of Cycle 24 (μ = 3.0)

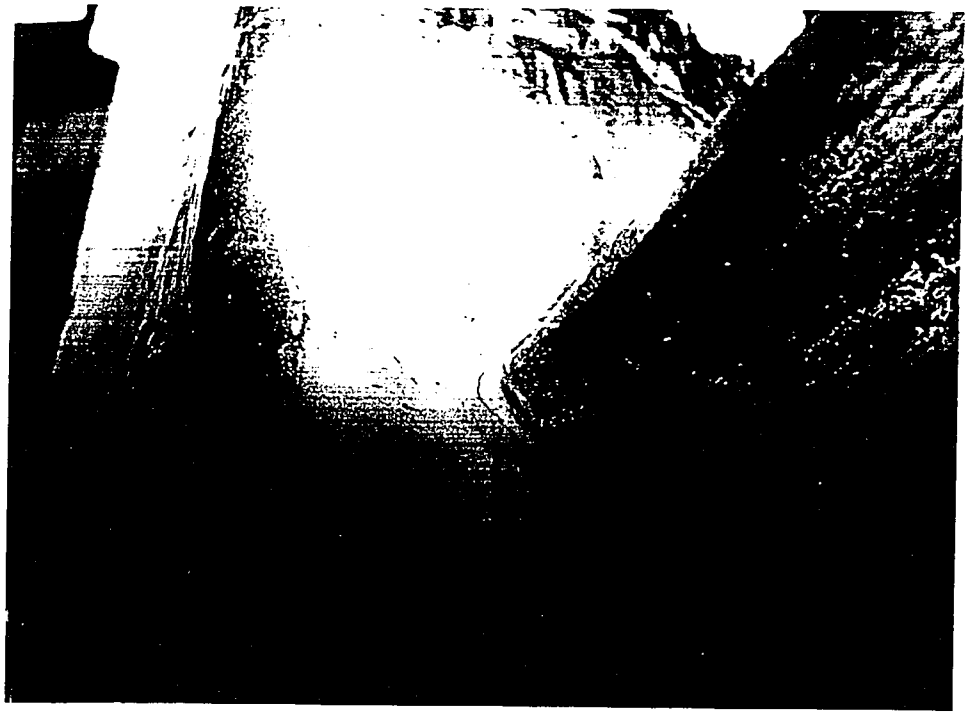

Figure 3.8 - Photograph of Crack in Wall of Column Adjacent to Beam Flange, Specimen 1

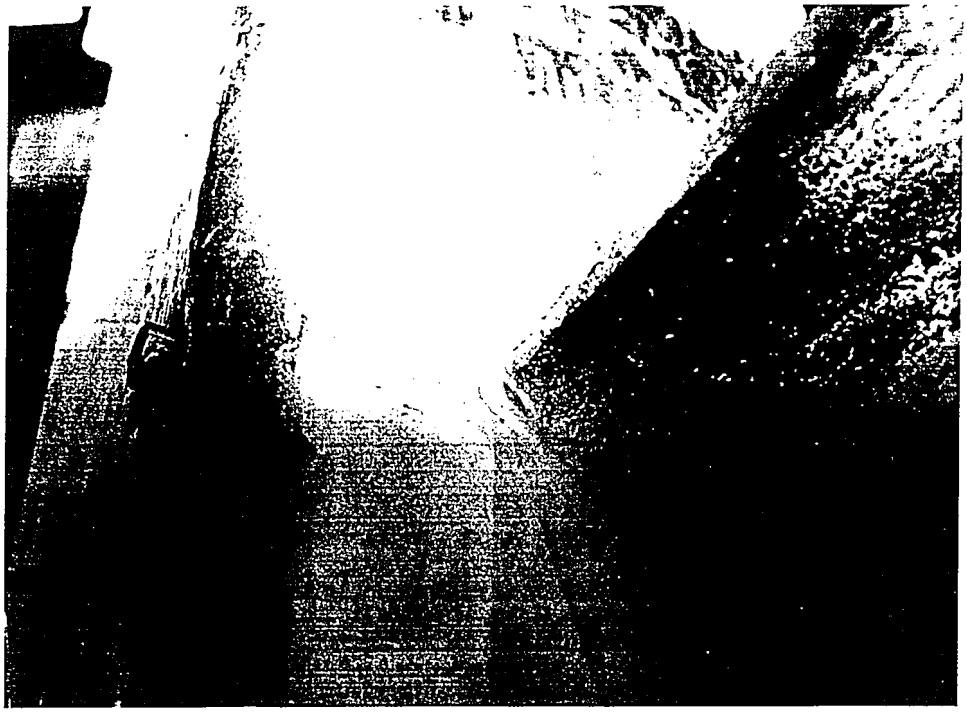

Figure 3.8 - Photograph of Crack in Wall of Column Adjacent to Beam Flange, Specimen 1

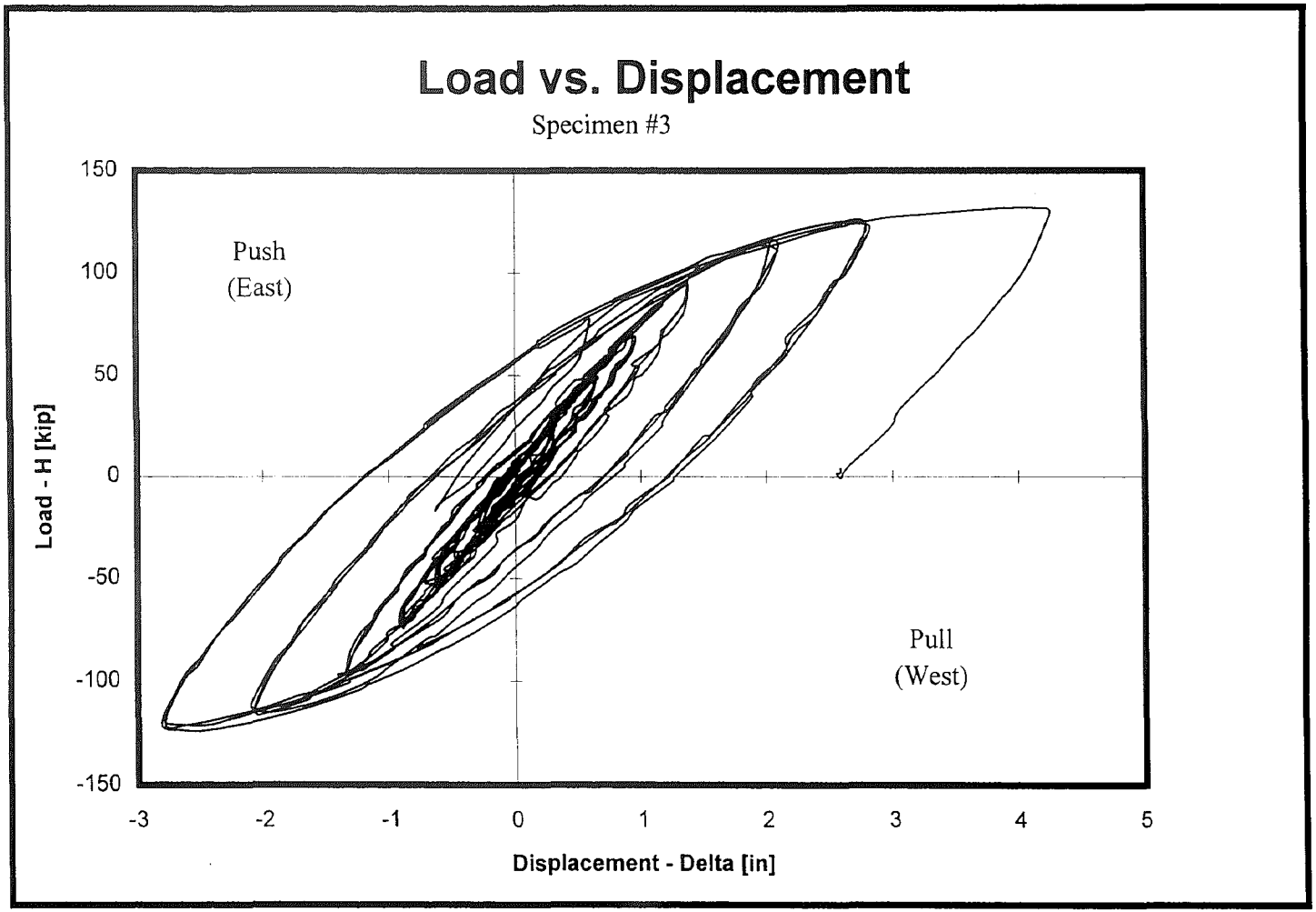

Figure 3.9 Lateral Load - Displacement Response, Specimen 3.

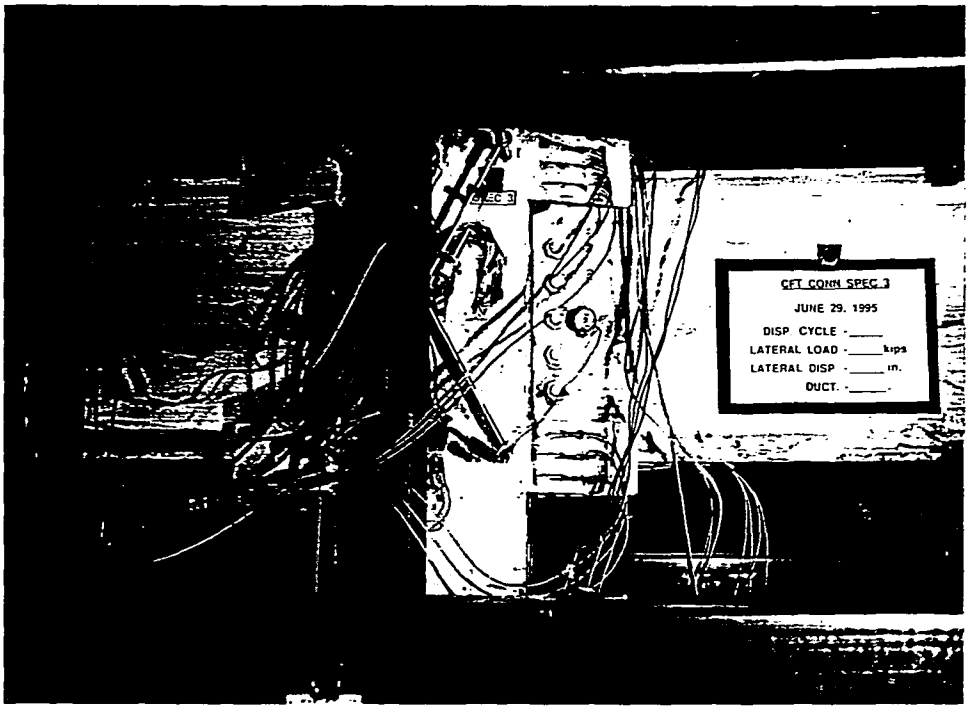

Figure 3.10 - Specimen 3 Before Testing

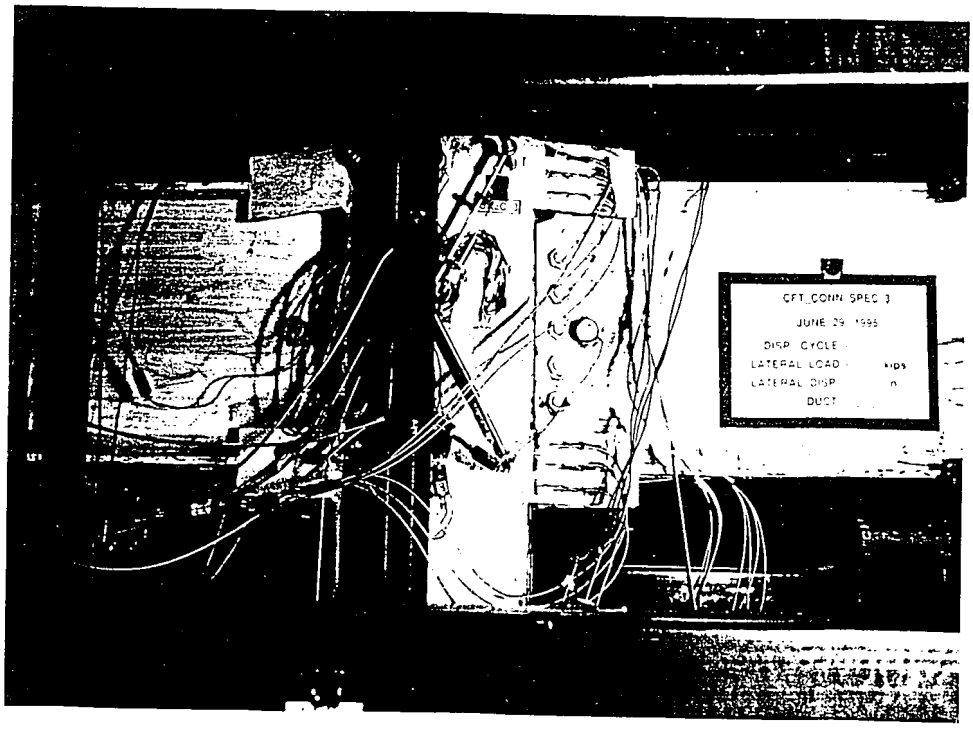

Figure 3.10 - Specimen 3 Before Testing

Figure 3.11 - Specimen 3, Cycle 7 (μ = 1.0)

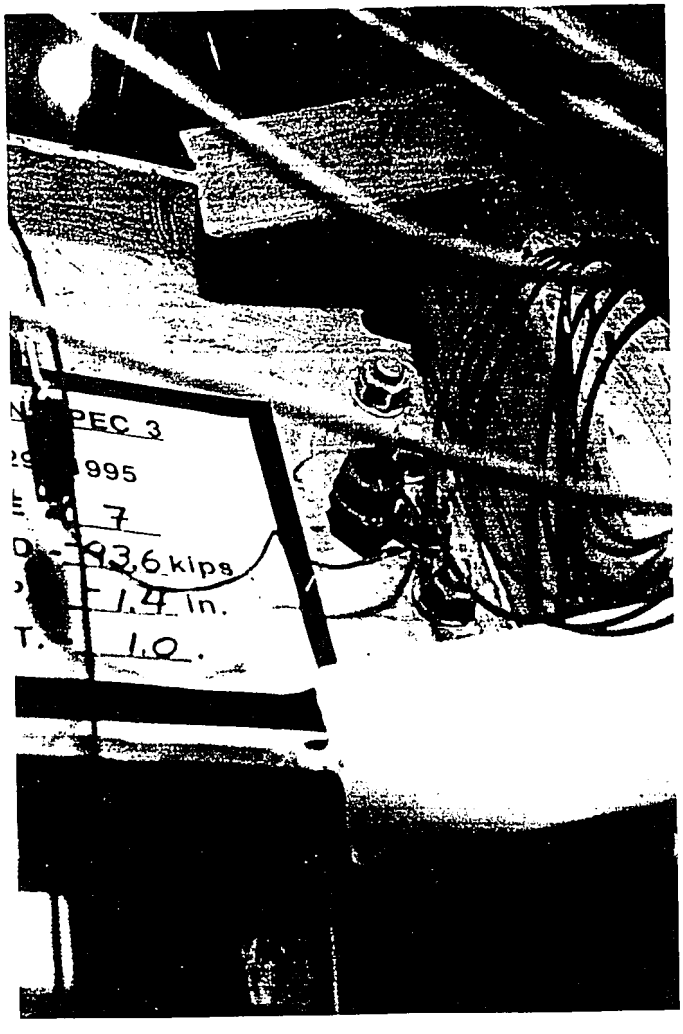

Figure 3.11 - Specimen 3, Cycle 7 (μ = 1.0)

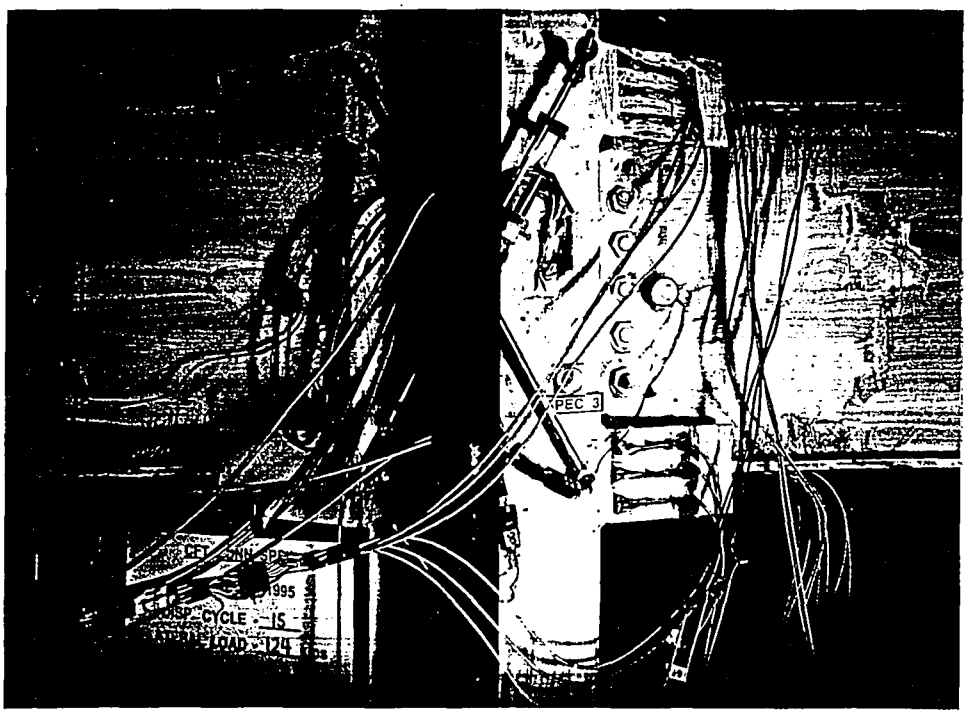

Figure 3.12 - Specimen 3, Cycle 15 (μ = 2.0)

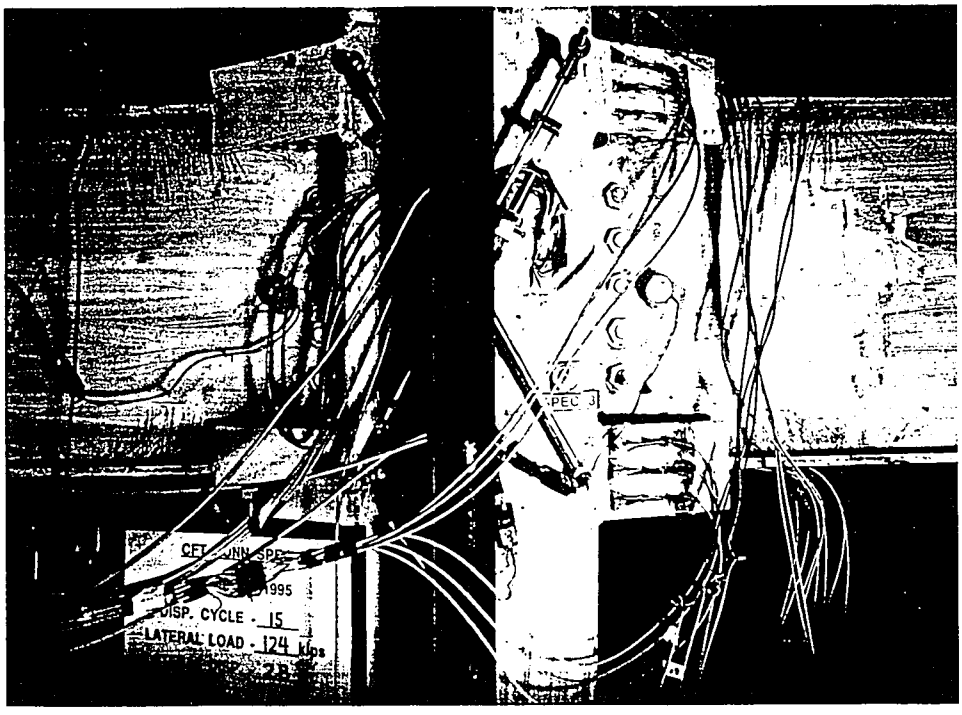

Figure 3.12 - Specimen 3, Cycle 15 (μ = 2.0)

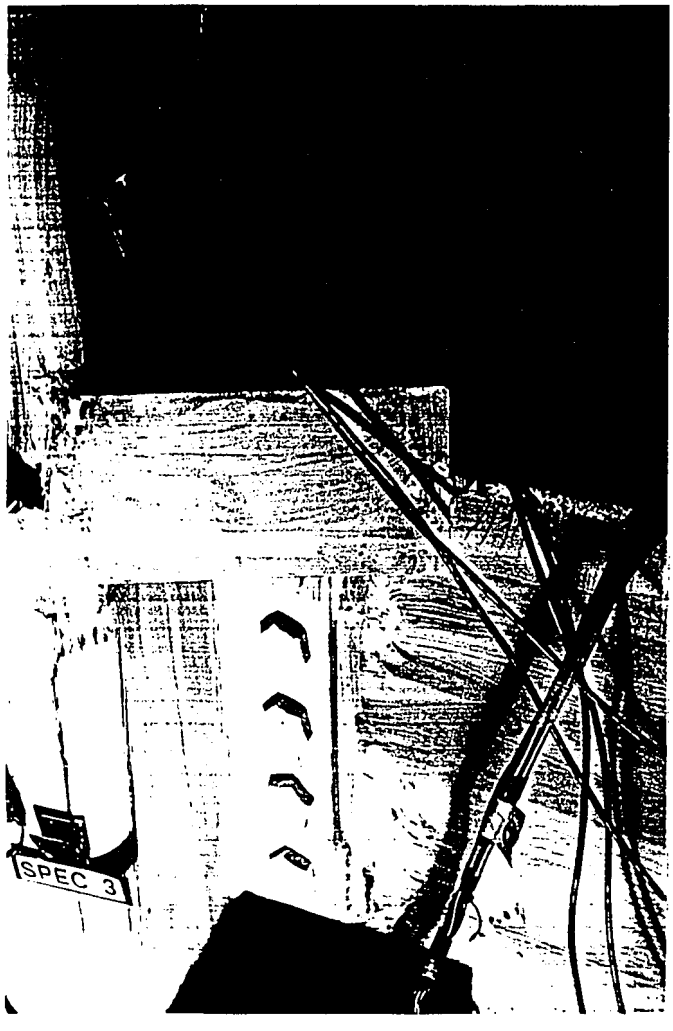

Figure 3.13 - Fracture in Beam Flange During Cycle 17
(μ = 2.0) - Specimen 3

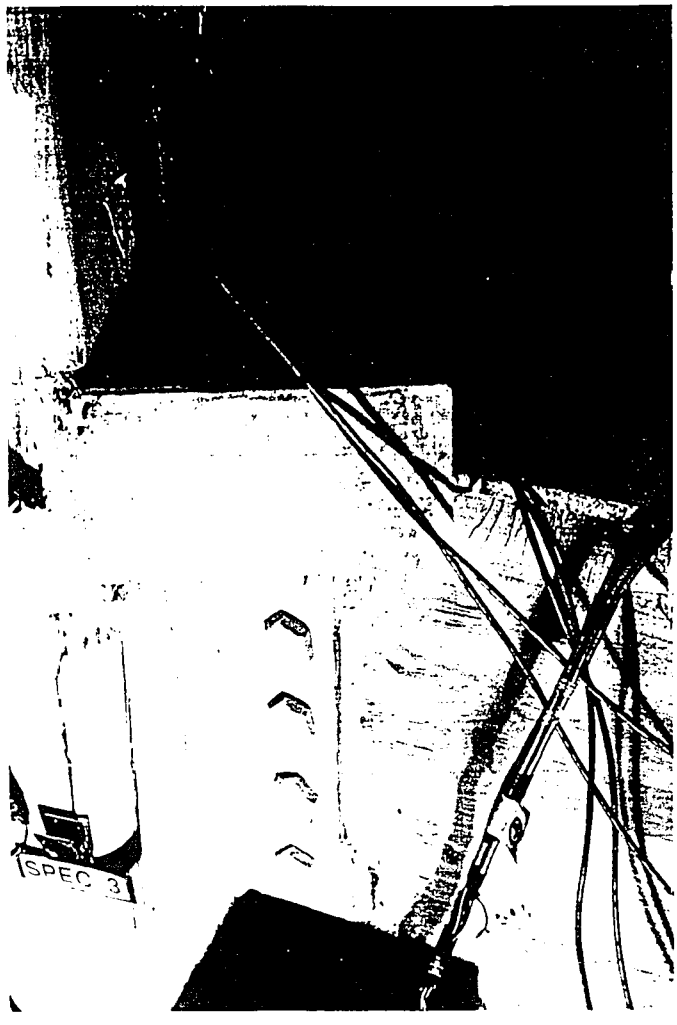

Figure 3.13 - Fracture in Beam Flange During Cycle 17
(μ = 2.0) - Specimen 3

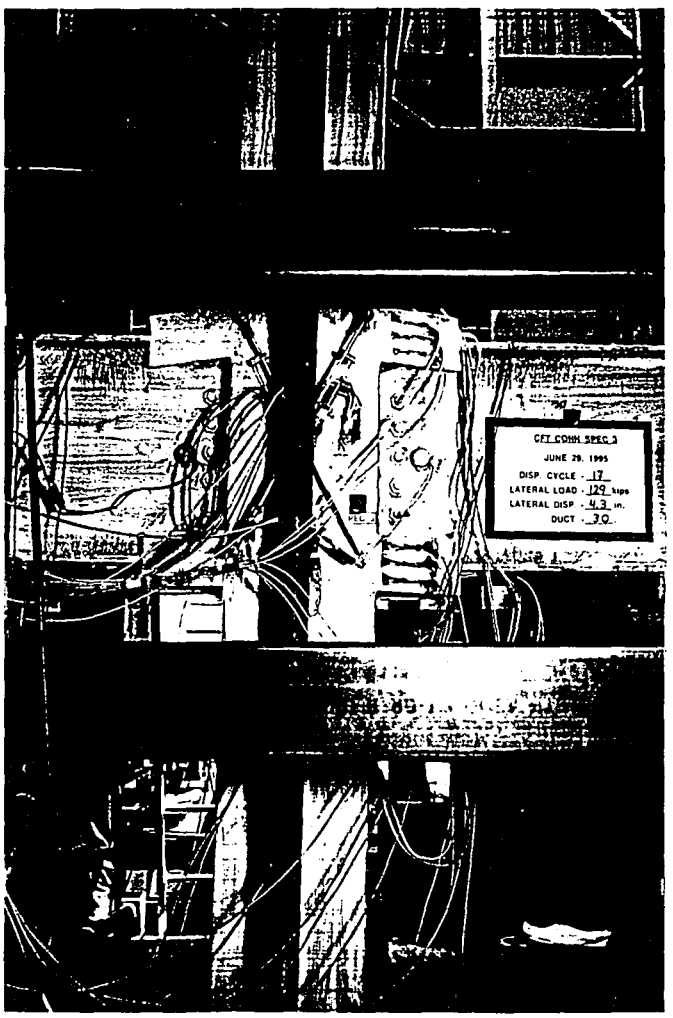

Figure 3.14 - Specimen 3 - End of Cycle 17 (μ = 3.0)

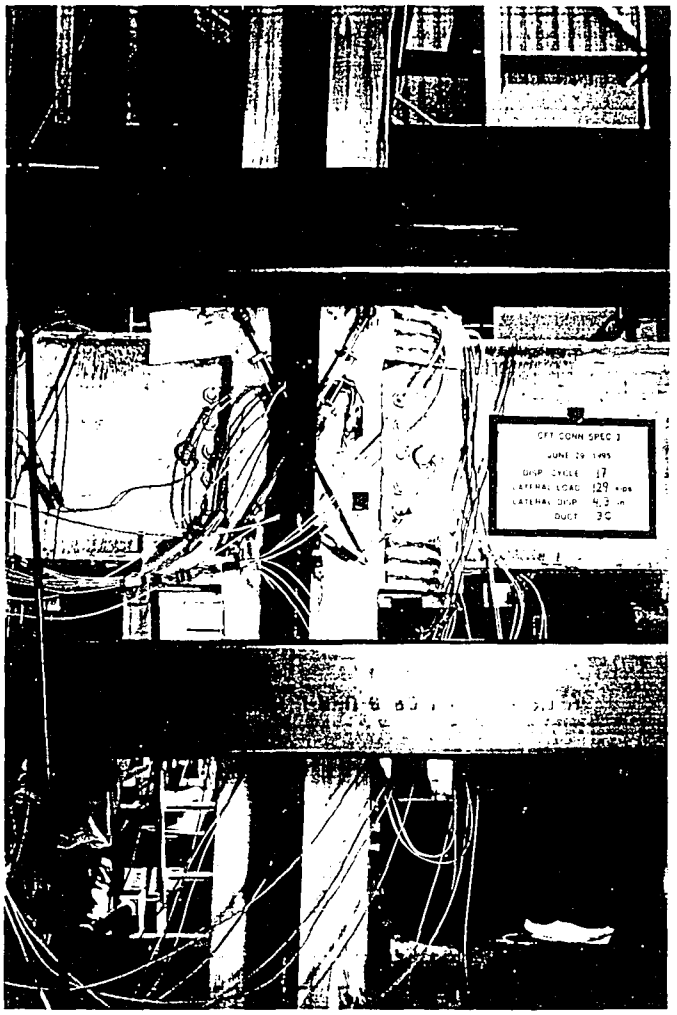

Figure 3.14 - Specimen 3 - End of Cycle 17 (μ = 3.0)

Chapter 4

Analysis of Experimental Results

4.1 General

A synthesis of the measured response of the experimental test specimens is presented in Chapter 4. This includes evaluating the elastic stiffness of the subassemblage and composite column under the cyclically imposed displacements, the deformations developed in each element of the subassemblage and their contribution to interstory drift, in addition to the maximum forces and ductility developed in the components of the test specimens. The behavior and above evaluations are compared with the assumptions adopted in the design of the test specimens, in order to evaluate the design criteria. This involved comparing the maximum forces developed in the elements of the connection, the beams, and column with their assumed force state and member capacity per the design criteria.

4.2 Elastic Behavior

In the design of the prototype high rise building (discussed in Section 2.2) subjected to axial and earthquake lateral loads, it was found that the inter-story drift criteria controlled. In order to design for specific inter-story drift requirements, such as the ones stated by the NEHRP, it is necessary for the

engineer to have an accurate value of the flexural section stiffness EI for the composite column. The design engineer must also know the effect the connection detail has on lateral drift, and the amount of elastic stiffness deterioration of the column, if any at all.

The subassembly elastic stiffness, k_{el}, was obtained from the lateral load - displacement responses for Specimen 1 (see Figure 4.1) and Specimen 3 (see Figure 4.2) by evaluating specimen behavior during the elastic cycles, as well as during elastic unloading from the inelastic force state. It is observed in Figures 4.3 and 4.4 that the initial elastic stiffness k_{el} was 65 kip/in for Specimens 1 and 3, respectively, and that it remained relatively constant during testing. The stiffness k_{el} of Specimen 3 is greater that that of Specimen 1 because of the increase in moment of inertia in the beams where the structural tees exist when compared to that of the former specimen.

The elastic stiffness of the column for each specimen was investigated by evaluating the contribution of column displacement δ_c to the subassemblage's interstory drift δ. In general the interstory drift, δ, is composed of three separate components, namely : (1) the column component, δ_c; (2) beam component, δ_r; and (3) panel zone component, δ_p. Each of these components is illustrated in Figure 4.5. The column component of the inter-story drift was calculated using the measured response in conjunction with the following expression:

$$\delta_c = 2(\Delta_{bm} - 60\Theta_{bpz}) \qquad (4.1)$$

where Δ_{bm}, 60, and Θ_{bpz} are the measured lateral displacement of the lower beam flange (inches), the distance between the pin of the clevis fixture at the base of the column and the inclinometer located at the bottom of the panel zone (inches), and the measured rotation of the column just below the panel zone (rad). The column component, δ_c, for Specimens 1 and 3 is shown plotted in Figures 4.6 and 4.7 against the corresponding horizontal lateral load for the initial excursion to each ductility level achieved in the tests. It is apparent in Figures 4.6 and 4.7 that the stiffness of the column degrades as greater magnitudes of ductility are imposed to the subassembly. This deterioration is associated with minor yielding in the steel tube section, which was found to occur at strain gages located in the column near the joint, as well as cracking of the concrete inside the tube at higher lateral load levels. Although not measured, the reduction in stiffness could also be attributed to speculated slippage that may have occurred between the concrete and steel tubes of the column.

To compare the stiffness of the column with computational design predictions, the deflection of an equivalent column of stiffness EI were computed. Computations were based on several different values of EI, including that considering: (1) uncracked transformed section modulus (EI_{tr}); (2) ACI provision [ACI, 1992] for column stiffness EI_{ACI} used in stability limit state calculations; and, (3) the stiffness of the column (EI_s) considering only the steel tube section of the CFT column. These three stiffness values for EI are Computed as follows:

$$EI_{tr} = E_s \left(I_s + \frac{I_g}{n}\right) \tag{4.2}$$

$$EI_s = E_s * I_s \tag{4.3}$$

$$EI_{ACI} = \frac{E_c * I_g}{5} + E_s * I_s \tag{4.4}$$

where E_s, E_c, I_s, I_g, and n are the modulus of elasticity for steel, modulus of elasticity for concrete based on ACI criteria - Eqn. 2.13, the moment of inertia of the structural steel tube, the moment of inertia of the gross area of the concrete, and the ratio of the steel modulus to the concrete modulus, respectively. The elastic theoretical column displacement based on each of these separate values of EI was calculated at lateral loads of H= ±150 kips using the relationship:

$$\delta_c = \frac{H(h-d_b)^3}{24EI} \tag{4.5}$$

where h is the height of the column (144 inches) as shown in Figure 2.8, and d_b is the depth of the W24x62 beams.

The predictions for column deformation δ_c based on the three separate values for EI are compared with the experimental column deformation envelopes in Figures 4.6 and 4.7. The average of the experimental values (EI_{exp}) of EI up to ductility levels of μ = 0.75 are compared with respect to the theoretical values in Table 4.1. It is observed from Table 4.1 and from that the initial elastic column

lateral stiffness for Specimens 1 and 3 is predicted reasonably well when the inter-story drift is less than 0.3% (Specimen 1) or 0.5% (Specimen 3) for the story height h and when EI in Eqn. 4.5 is based on transformed section modulus (Eqn. 4.2). The steel alone model is shown to be a conservative prediction for the specimens' initial elastic stiffness, and overestimate the deflection.

4.3 Subassemblage Component Deformations

The response of the subassemblage to lateral loading is dependent on the behavior of the column, panel zone, as well as the beams and their connection elements. The inter-story drift consists of the three separate components shown previously in Figure 4.5. The column deformation component has been discussed above and can be calculated according to Eqn. 4.5. The inter-story drift components which are the result of the deformation of the panel zone, δ_p, and the deformation δ_r of the beams and connecting elements (e.g. diaphragms, shear tabs, bolts) framing into the column can be computed as follows:

$$\delta_p = \gamma * (144 - d_b) \tag{4.6}$$

$$\delta_r = \Theta_{bpz} * 144 \tag{4.7}$$

where 144, γ, and d_b are the measured column height in inches, the measured shear deformation of the panel zone, and the measured beam depth in inches.

The panel zone deformation γ is based on Eqn. 2.14, where the measured diagonal displacements Δ_1 and Δ_2 are used to compute γ:

$$\gamma = \frac{(\Delta_1 - \Delta_2)}{2} * \frac{d}{bh} \tag{2.14}$$

A plot of the north panel zone inter-story drift component with respect to the applied lateral load, H, is shown in Figures 4.8(a) and 4.11(a) for Specimens 1 and 3, respectively. The same relationships for the south panel zone inter-story drift components can be observed in Figures 4.8b and 4.11b for Specimens 1 and 3, respectively. The column component of inter-story drift for Specimens 1 and 3 is given in Figures 4.9 and Figures 4.12 for Specimens 1 and 3, respectively, where the H -δ_c relationship for the two specimens are shown. The beam component of inter-story drift for Specimens 1 and 3, are shown in Figures 4.10 and 4.13, where the H - δ_r relationships have been plotted.

The envelop of the δ_p, δ_c, and δ_r components associated with the maximum response during the first half cycle to each ductility level is shown plotted in Figures 4.14 and 4.15 for Specimens 1 and 3, respectively, It is apparent in these figures that the beam and connector deformations δ_r accounted for a majority of the inter-story drift δ of the subassemblage. At a displacement ductility of $\mu = 3$, corresponding to the peak lateral displacements in both specimens, the contribution of δ_p, δ_c, and δ_r to δ was 6.7%, 11.3%, 82.0% for Specimen 1, and 9.4%,13.8%, 76.8% for Specimen 3. The fact that the

beam contributes the most is consistent with the design approach taken for both specimens, where the subassemblages were designed to respond as weak beam - strong column systems. Under this approach the beams are expected to develop significant yielding with the panel zone and column developing, if any, only mild inelastic deformations since they are designed to resist the maximum beam moments based on 1.25 M_p, where M_p is the beam flexural capacity.

The hysteretic response for H - δ_p, H - δ_c, and H - δ_r show that the beams developed significant inelastic deformations and accounted for most of the energy dissipation of each specimen. The panel zone remained relatively elastic throughout the test. The shear strains measured from the strain rosette gages that were placed on the CFT in the panel zone are plotted in Figures 4.16 and 4.17. These results correspond to the peak displacement during the first cycle at each ductility level. The shear strains are shown to be at a maximum magnitude of 0.006 rad. (Specimen 1) and 0.003 rad. (Specimen 2), which are equivalent to 2.1 and 1.05 times the steel tube's shear yield strain. Specimen 1 appears to develop higher shear strain towards the edges of the panel zone, which is probably due to the effect of the interior diaphragm. On the contrary, the distribution of shear strain in the horizontal direction of Specimen 3, which had no interior diaphragm, is more uniform. As noted previously, the strain gages located on the flanges of the steel tube of the column at 2.875 inches above and

below the W24x62 beams (see Figure 2.19) indicated that the steel tube at these locations just reached the yield strain.

4.4 Connection Component Maximum Force - Strength Comparison

In order to design CFT to wide flange connections similar to the ones tested in this experiment, in addition to the deformations developed, it is imperative that the ultimate load and failure condition in each element of the connection be understood. The strength of a particular connection consists of variable mechanisms. Each of these mechanisms could result in a different failure mode.

The components of the joint that could cause failure include: (1) a plastic hinge forming in the girders; (2) a plastic hinge forming in the column; (3) panel zone yielding; and (4) yielding or fracture of the connector elements (e.g. diaphragms, shear tabs, bolts). It has been traditional to have flexural plastic hinges form in the girder, since this mechanism has been shown to provide exceptional cyclic strength and ductility if compact steel sections are used. Plastic hinging in the column is undesirable, and should be avoided for it could lead to instabilities. While in steel wide flange construction, panel zone yielding has been shown to be a ductile mechanism [Tsai & Popov, 19 ; Krawinkler et al, 1971] it has generally been avoided in U.S. design practice. The fracture of a

connector element could be catastrophic, for it could impair the force transfer mechanism into the joint and thereby hinder equilibrium.

To gain further insight into the behavior of the components of the subassemblage connection, some of the force-deformation relationships were examined for each, and the maximum forces developed for each component during the test compared with the design models and criteria discussed in Chapters 1 and 2 for the beam, column, and connection design.

The moments developed in the beams were first examined, where the maximum moment in a beam is calculated by the following:

$$M_{max} = (V_b) * d_l \tag{4.8}$$

where V_b is the maximum measured load in the rigid link or the beam reaction calculated by statics from the horizontal load, and d_l is the distance along the beam from the rigid link location of the beam where M_{max} is to be determined. The maximum moment in the beams were calculated for each specimen at two locations: (1) at the end of the connection where the W24x62 section is not reinforced by any connection details (end of the coverplates for Specimen 1 and end of the structural tees for Specimen 3); and (2) at the face of the column. The maximum moments in the beams at the end of the connection for Specimens 1 and 3, along with the ratios of M_{max} to M_p for each specimen, are summarized in Tables 4.2(a) and 4.3(a). The maximum moments calculated at the face of the column and ratios of M_{max} to M_p at this location for each specimen

are summarized in Tables 4.2(b) and 4.3(b). It can be observed that the ratio of M_{max} to M_p at the end of the connection region ranges from 1.16 to 1.28 verifying the design premise that the panel zone and connection strength should be designed for the beam overstrength of 1.25 M_p. The current design, as stated in Chapter 2, was based on M_{max} equal to 1.25 M_p. The beam moments developed at the end of the connection region during the test are plotted with respect to the beam plastic rotations, for both the east and west beams of Specimens 1 and 3 in Figures 4.18 through 4.21. It is apparent in these figures that the beam developed significant plastic deformations (to be discussed further in Section 4.5), dissipated a pronounced amount of hysteretic energy, while maintaining stable hysteretic behavior and developing moments that exceeded M_p.

The ratio of M_{max} in the beam at the face of the column to the corresponding flexural capacity at this location is summarized in Tables 4.2(b) and 4.3(b). Based on measured beam reactions in the rigid links, the average maximum moments at the face of the column are 0.66 M_p in Specimen 1 and 0.54 M_p in Specimen 3. The ratio M_{max}/ M_p is smaller in Specimen 3 due to the greater flexural capacity M_p of the beam and structural tees that exist at the face of the column. These moments of 0.66 M_p and 0.54 M_p are those that the connection and column must resist. The beam moments developed at the face of the column during each specimen's test are plotted in Figures 4.22 though 4.25 against beam plastic rotations for the east and west beams of Specimens 1

and 3. As in Figures 4.18 to 4.21, the plastic beam rotations plotted in Figures 4.22 to 4.25 are those developed at the end of the connection detail (3.5 inches and 9.75 inches from the face of the column in Specimens 1 and 3, respectively).

The maximum column moments (M_{max}^{col}), which develop to resist the maximum beam moments are summarized in Table 4.4 for Specimens 1 and 3. Considering the size of the joint (16 inches wide by 23.7 inches high), and the beam and column moments and shear acting on the faces of the connection, joint equilibrium at the connection is satisfied. The force state corresponding to the applied axial load and maximum lateral load developed in the column at the face of the connection for Specimens 1 and 3 are plotted and compared to the ACI moment-axial capacity surface in Figure 4.26, where full composite action is assumed. Included in this figure is the AISC Moment - axial load interaction plastic capacity surface in which only the steel section is considered. To develop the ACI and AISC interaction surfaces the measured dimensions and material properties reported in Chapter 2 were utilized. The maximum force state is seen is Figure 4.26 to be well within the M - P interaction surface based on full composite action. If the steel tube were not filled with concrete, it appears that the column is close to failure, stressing the significance of needing to develop some degree of composite action in the column. A comparison of maximum column moments (M_{max}^{col}) with the ACI and AISC capacities (M_{cap}^{ACI} and M_{cap}^{AISC}) is given in Table 4.4 for the applied axial loads of the specimens.

These comparisons indicate a ratio of 0.73 and 0.75 for M_{max}/M_{cap}^{ACI} for Specimens 1 and 3, respectively, and 0.94 and 0.99 for M_{max}/M_{cap}^{AISC} for Specimens 1 and 3, respectively.

The shear force - deformation ($Q - \gamma$) for the panel zones is shown in Figures 4.27 through 4.30 for Specimens 1 and 3, respectively. The shear deformation γ is that based on Eqn. 2.14. The maximum panel zone shear force Q_{max} that developed in Specimens 1 and 3 was 598 kips and 613 kips, respectively. As shown in Figures 4.27 through 4.30, it is apparent that the shear force Q_{max} for both specimens exceeded the plastic shear capacity V_p based on considering only the resistance of the tube section. The ratio of Q_{max}/V_p was 1.26 and 1.29 for Specimens 1 and 3. Since significant yielding was not observed to occur in the panel zone of the connection, this provides evidence that the concrete with in the joint had to contribute to the joint's shear capacity. Also evident in Figures 4.27 through 4.30 is that the maximum shear strain measured by the strain rosette gages in the panel zone and based on Eqn. 2.15 are comparable to those based on the LVDT instrumentation and Eqn 2.14. The maximum shear force Q_{max} for both specimens was compared with the capacity of the composite panel zone, considering the contribution of both the steel tube and concrete. The capacity models discussed in Chapter 1 were utilized, which included: (1) Kanatani's model ($Q_{kanatani}$), Eqn. 1.58 through 1.64; (2) the modified strut model ($Q_{modified}$), Eqns. 1.65 through 1.73; (3) the ACI

provisions (Q_{ACI}), Eqns 1.74 through 1.77; and the AIJ provisions (Q_{AIJ}), Eqns. 1.53 through 1.57. The measured dimensions and material properties were used, which are reported in Chapter 2. For the Kanatani and modified strut models, the strut width S was based on the thickness of the beam flange and any coverplates, considering a 45 degree projection through the steel tube's wall thickness. This resulted in a strut width of S equal to 2.4 inches and 1.5 inches for Specimen 1 and 3, respectively. A summary of the ratio of Q_{max} to the panel zone shear capacity based on the above models is included in Table 4.5. For Specimen 1, all four models predict that the panel zone had sufficient shear capacity to resist Q_{max}, with the Kanatani model providing the smallest estimate of capacity relative to Q_{max} ($Q_{max} = 0.96Q_{Kanatani}$) and the ACI provisions the largest ($Q_{max} = 0.72Q_{ACI}$). On the contrary, for Specimen 3 Q_{max} exceeds both Kanatani's and the modified strut model's capacity prediction ($Q_{max} = 1.17Q_{Kanatani}$; $Q_{max} = 1.17Q_{modified}$), with the ACI and AIJ provisions predicting sufficient specimen panel zone capacity ($Q_{max} = 0.82Q_{ACI}$; $Q_{max} = 0.81Q_{AIJ}$). The strut width of S = 1.5 inches assumed for Specimen 3 in the Kanatani and modified strut models evidently is too small, since the specimen's panel zone was not observed to develop a shear failure. An increase in the strut width to a value of 1.8 inches would have to be assumed to have the capacities $Q_{kanatani}$ and $Q_{modified}$ exceed the maximum panel zone shear Q_{max} in Specimen 3. Thus, the strut width requires further element analysis to refine the models that use a

strut for connections with exterior diaphragms, such as that in Specimen 3. Further such investigation involving interior diaphragms are also warranted.

To avoid failure of the diaphragms, the design of these members was based on their ability to resist the maximum beam tension flange force T_{max}, considering beam overstrength and strain hardening. On this bases the required design force T_{max} is computed from Eqn. 2.11 in Chapter 2, where

$$T_{max} = \frac{M_{max}}{d_b} \qquad (2.11)$$

The force T_{max} is compared in Table 4.6 with the capacity T_{cap} of an interior diaphragm, using Matsui's method to predict T_{cap} for Specimen 1 (Eqn. 1.79). For Specimen 3, T_{cap} is based on Eqn. 2.12, with a material factor value of ϕ = 1.0 since actual material properties and dimensions were used in the computation. The comparison in Table 4.6 indicates that the capacity of the diaphragms of both specimens were adequate to resist the beam's maximum tension flange force. This is consistent with the observations that no failure in the diaphragm occurred.

The measured strains in the interior diaphragm and structural tees and beam flanges are given in Figures 4.31 through 4.36. The strains were plotted at the peak lateral displacements of the first cycle corresponding to each ductility level. The interior diaphragms of Specimen 1 are shown to develop local strains that are at most approximately two times the yield strain of the material. The

strain distribution from the gages indicates that full yielding of the diaphragm did not occur, implying also that its capacity was not developed during the experiment.

The strains plotted in the external tee detail for Specimen 3 (Figure 4.35 and 4.36) show the effect of the stiffness of the tube's wall under normal tension prying forces on the force transfer mechanism. The strains in the compression beam flange and attached tees are more uniform then those of the beam's tension flange and attached structural tees. When the beam flange is in tension, the flexibility of the steel tube's wall results in a majority of the beam's tension force being transferred through the flanges of the structural tees that are welded to the edges of the panel zone. When in compression, the beam flange force acting against the column face is resisting by bearing against the infilled concrete, which stiffens the steel tube's wall and results in a more uniform strain across the connection. Under such action the compression strut in the concrete with in the panel zone is activated. It is observed in Figures 4.35 and 4.36 that the exterior diaphragm configuration was extremely effective in transferring the tension flange force into the panel zone where the peak tee flange tensile strain is approximately nine times the yield strain.

4.5 Connection Ductility

The amount of energy dissipation or ductility which is supplied by a structural system during seismic overloading is a very important property. The maximum displacement ductility μ_{max} and inter-story drift θ_{max} for each specimen are presented in table 4.7. The interstory drift θ is calculated using the following equation:

$$\theta = \frac{\delta}{h} \tag{4.9}$$

where δ is the interstory displacement (displacement at top of column in test specimen) per story and h is the story height. Both Specimen 1 and 3 were able to achieve displacement ductilities of μ equal to 3.0 before terminating the tests following the development of cracks. The corresponding interstory drift for the Specimens 1 and 3 were 3.1% and 3.0%, respectively. Larger displacement ductility values for both specimens may have been achieved, however at the risk of developing too much damage that the specimens could not be repaired and later retested. In addition, the inter-story drift ratio (θ) of both specimens was already equal to or greater than 3%, where drifts greater than this amount in the prototype structure may not be desirable due to stability issues and non-structural damage.

The plastic beam rotation θ_p, which was presented earlier in Figures 4.18 through 4.25, is a measure of a girder to develop ductility and dissipate energy.

The plastic beam rotations were computed from the experimental data at the ends of the connection elements (e.g. where significant plastic hinging occurred), using the following expression:

$$\theta_p = \frac{\Delta - \frac{H}{k_{el}}}{h} * \frac{0.5L}{L_{bm}} \qquad (4.10)$$

where Δ,H, k_{el}, h, L and L_{bm} are equal to the lateral displacement at the top of the column, lateral applied load, elastic lateral stiffness of subassemblage, column height (see Figure 2.8), distance between rigid links providing beam reactions (see Figure 2.8), and the distance along a beam from the rigid link to the location of the plastic hinge where significant yielding occurred (L_{bm} was equal to 108 inches and 102.25 inches for Specimens 1 and 3, respectively).

The maximum plastic beam rotations developed during testing were 0.038 and 0.023 radians in Specimen 1 and 3, respectively. While targeted design capacity values for a specimen's rotation ductility have not been established, and are currently under deliberation in the aftermath of the recent Northridge earthquake, the above plastic rotation developed in the beams of Specimens 1 and 3 are appreciable. These values should be compared with the demand imposed on a CFT moment resisting system during a maximum credible earthquake. The determination of this demand would require conducting several nonlinear time history analyses and a statistical assessment of the result.

To improve the supply of beam plastic rotation, the fractures that occurred in the test specimens would have to be avoided, or a least delayed until greater ductility was imposed on the specimen. To deal with this, the strain concentrations should be minimized in the connection detail (Specimen 3), and the through-thickness stress imposed on the column's steel tube section needs to be reduced (Specimen 1).

Table 4.1 - Comparison of Experimental and Theoretical Values of EI for CFTs

SPECIMEN No.	EI_{EXP} [kip-in^2]	EI_{EXP}/EI_{TRANS}	EI_{EXP}/EI_{ACI}	EI_{EXP}/EI_{STEEL}
1	51077738	0.961	1.349	1.500
3	51603326	0.969	1.358	1.509

Note: EI_{exp} is based on the inital experimental stiffness of the column

Table 4.2(a) - Maximum Beam Moment M_{max}^{bm} at End of Connection Region Calculated by Statics

	H_{max}	Rigid Link Load	M_{max}	Z_{xx}	F_y	M_p	$\frac{M_{max}}{M_p}$
	kip	kip	kip-in	in^3	ksi	kip-in	
Specimen 1							
East Beam	128.2	76.92	8346	155.3	42.5	6601	1.26
West Beam	128.2	76.9	8346	159.7	42.5	6788	1.23
Specimen 3							
East Beam	131.7	79.0	8080	154.6	43.3	6693	1.21
West Beam	131.7	79.0	8080	155.8	43.3	6746	1.20

Table 4.2(b) - Maximum Beam Moments M_{max}^{bm} at Face of Column Calculated by Statics

	H_{max}	Rigid Link Load	M_{max}	Z_{xx}	F_y	M_p	$\frac{M_{max}}{M_p}$
	kip	kip	kip-in	in^3	ksi	kip-in	
Specimen 1							
East Beam	128.2	76.9	8615	297.2	42.5	12631	0.68
West Beam	128.2	76.9	8615	301.6	42.5	12818	0.67
Specimen 2							
East Beam	131.7	79.0	8850	369.0	43.3	15978	0.55
West Beam	131.7	79.0	8850	370.0	43.3	16021	0.55

Table 4.3(a) - Maximum Beam Moment M_{max}^{bm} at End of Connection Region Calculated from Measured Beam Reactions

	Rigid Link Load	M_{max}	Z_{xx}	F_y	M_p	$\frac{M_{max}}{M_p}$
	kip	kip-in	in^3	ksi	kip-in	
Specimen 1						
East Beam	77.8	8441	155.3	42.5	6601	1.28
West Beam	72.5	7866	159.7	42.5	6788	1.16
Specimen 3						
East Beam	76.3	7802	154.6	43.3	6693	1.17
West Beam	78.4	8016	155.8	43.3	6746	1.19

Table 4.3(b) - Maximum Beam Moment M_{max}^{bm} at Face of Column Calculated from Measured Beam Reactions

	Rigid Link Load	M_{max}	Z_{xx}	F_y	M_p	$\frac{M_{max}}{M_p}$
	kip	kip-in	in^3	ksi	kip-in	
Specimen 1						
East Beam	77.8	8714	306.8	42.5	13040	0.67
West Beam	72.5	8120	310.6	42.5	13201	0.62
Specimen 2						
East Beam	76.3	8546	329.2	43.3	14255	0.60
West Beam	78.4	8781	331.0	43.3	14333	0.61

Table 4.4 - Maximum Column Moments M_{max}^{col} at Face of Joint

Specimen	M_{max} [kip-in]	$\frac{M_{max}}{M_{cap,ACI}}$	$\frac{M_{max}}{M_{cap,AISC}}$
1	7692	0.73	0.94
3	7902	0.75	0.99

Table 4.5 - Maximum Experimental Panel Zone Shear Force Q_{max} and Theoretical Panel Zone Shear Strengths

Specimen	Q_{max} kip	$\frac{Q_{max}}{V_p}$	$\frac{Q_{max}}{Q_{Kanatani}}$	$\frac{Q_{max}}{Q_{Modified}}$	$\frac{Q_{max}}{Q_{ACI}}$	$\frac{Q_{max}}{Q_{AIJ}}$
1	598	1.26	0.96	0.84	0.72	0.79
3	613	1.29	1.17	1.17	0.82	0.81

Table 4.6 - Maximum Beam Flange Force

Specimen	T_{max} [kip]	$\frac{T_{max}}{T_{cap}}$
1	362	0.69
3	372	0.94

Table 4.7 - Maximum Displacement Ductility (μ_{max}), Interstrory Drift Ratio (θ_{max}), and Plastic Beam Rotation (θ_{pmax})

Specimen	μ_{max}	θ_{max}	θ_{pmax}
1	3.0*	3.1%	3.8%
3	3.0	3.0%	2.3%

*Note: Specimen 1 referenced from column vertical plumb position

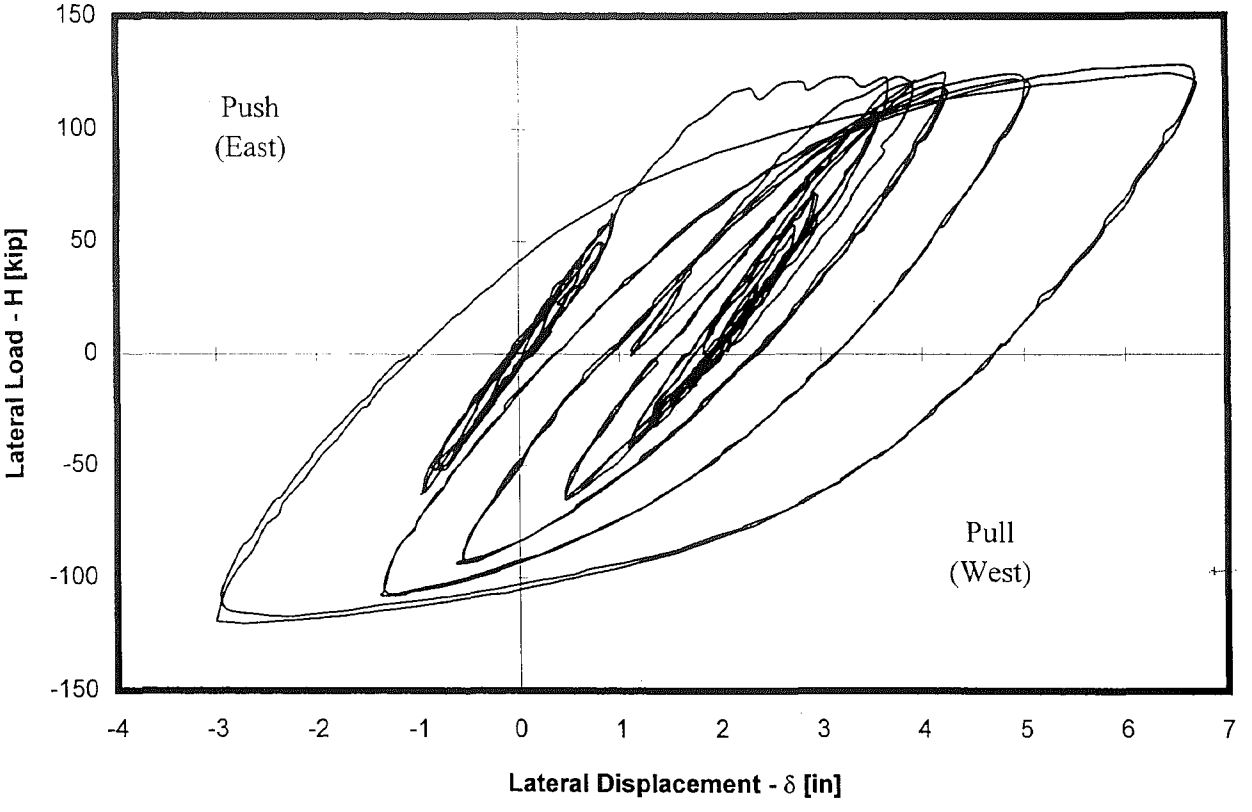

Figure 4.1 Lateral Load - Displacement Response, Specimen 1.

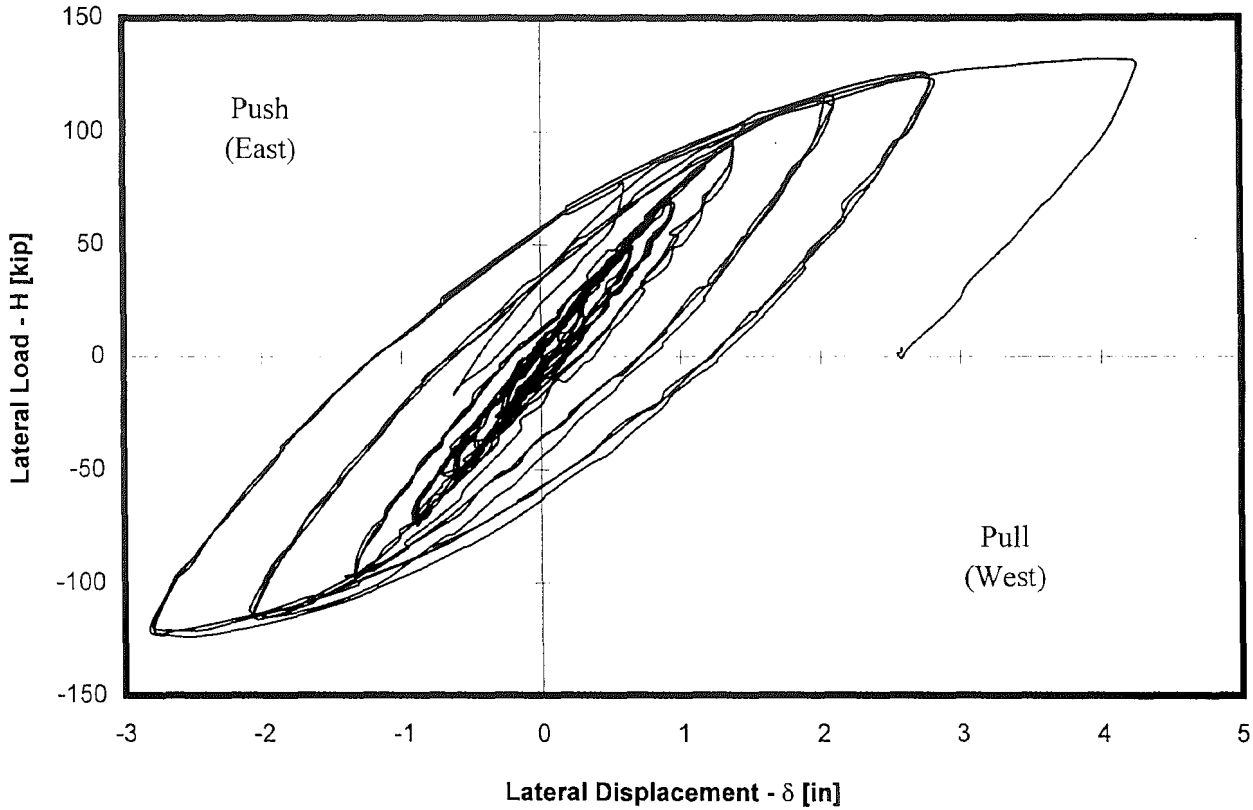

Figure 4.2 Lateral Load - Displacement Response, Specimen 3.

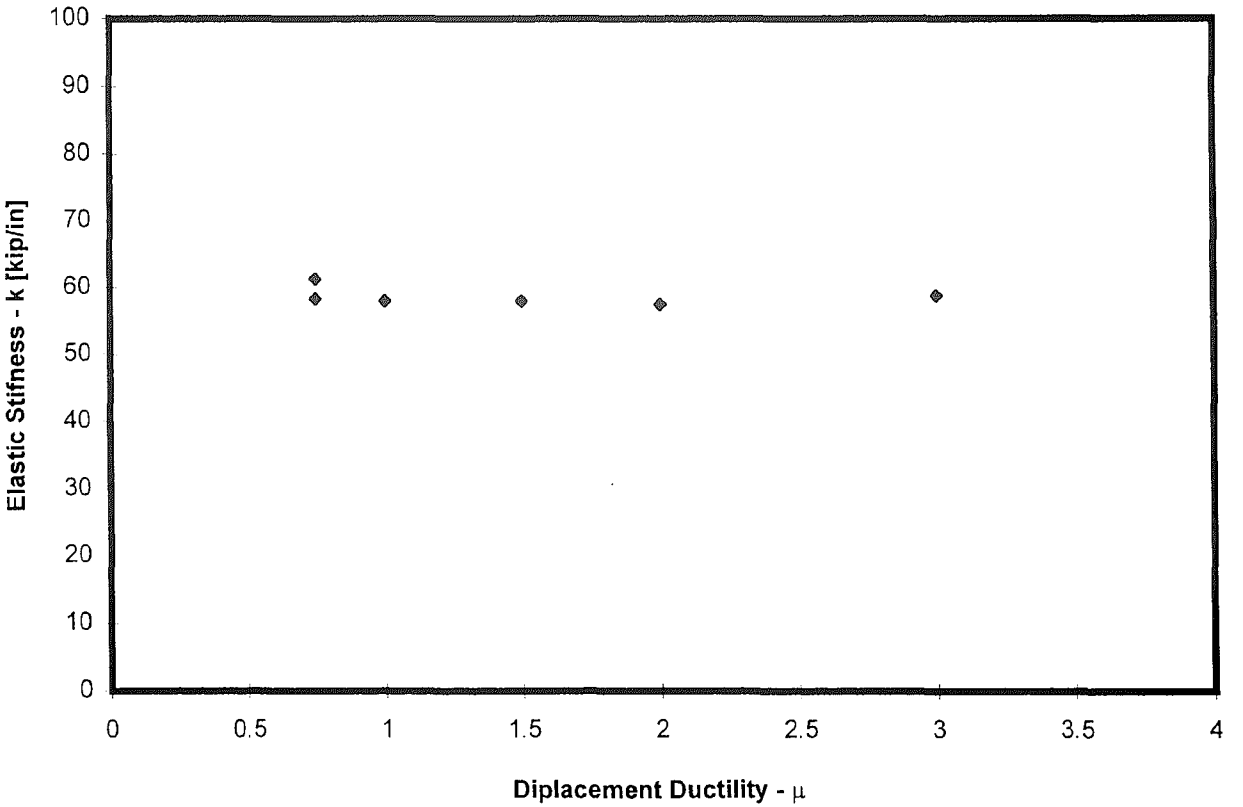

Figure 4.3 - Subassemblage Elastic Stiffness with Respect to Ductility, Specimen 1

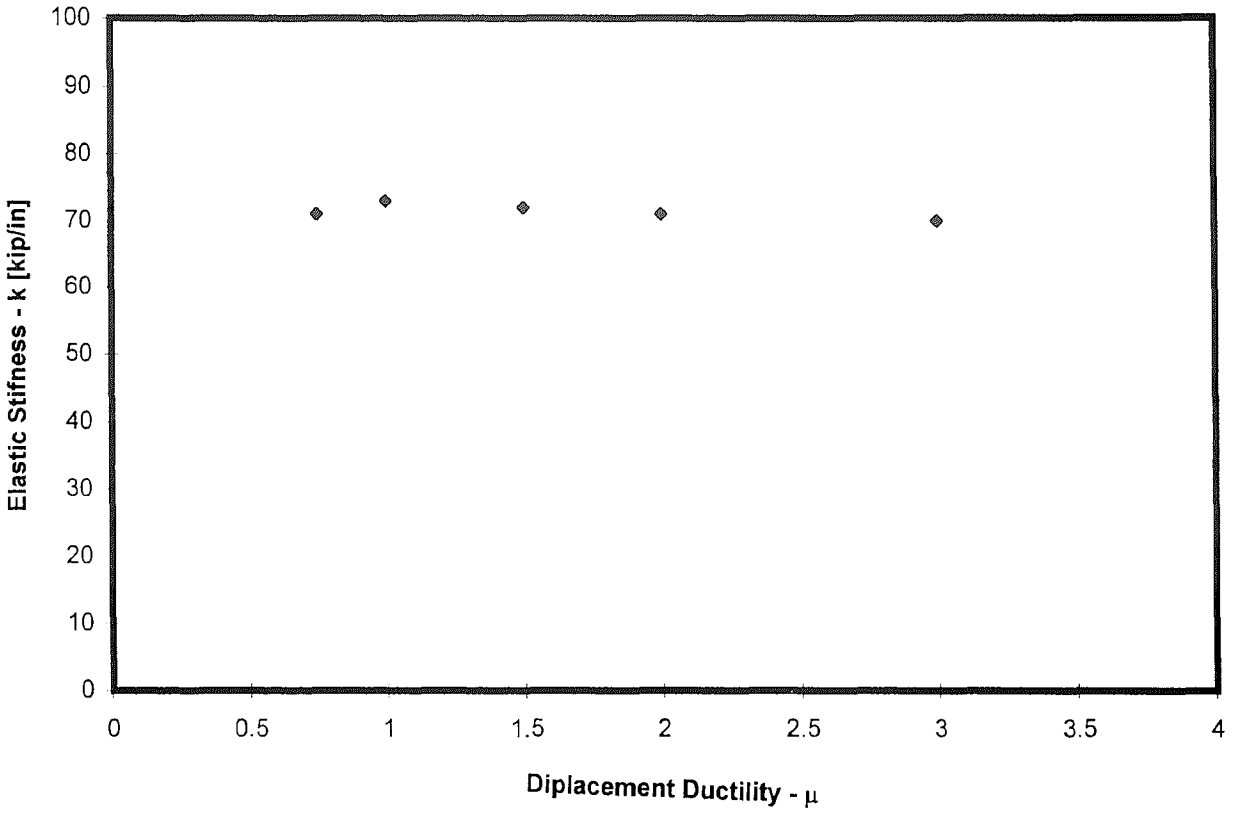

Figure 4.4 - Subassemblage Elastic Stiffness with Respect to Ductility, Specimen 3

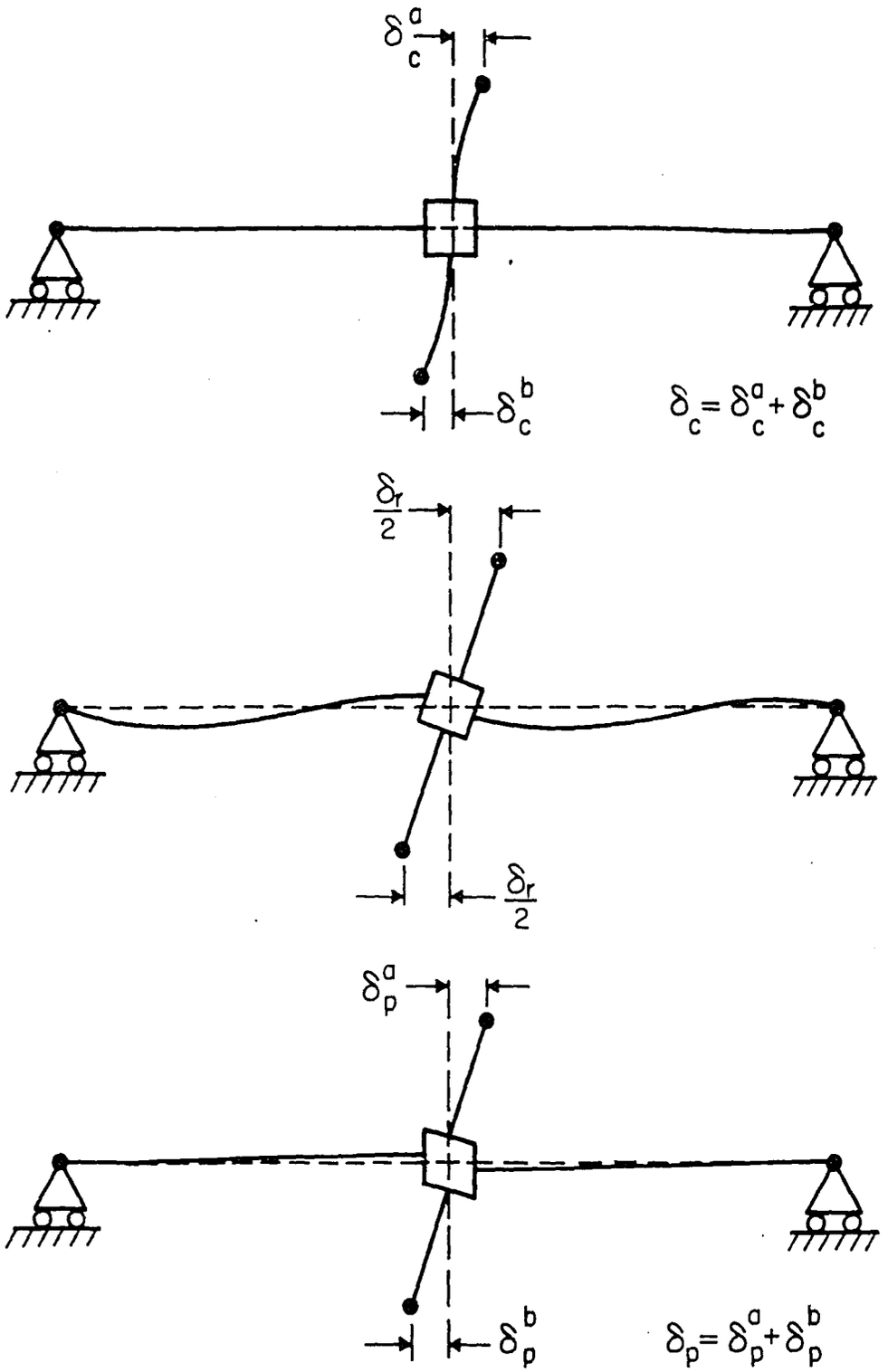

Figure 4.5 - Column Displacement Components [After Krawinkler et al. 1971]

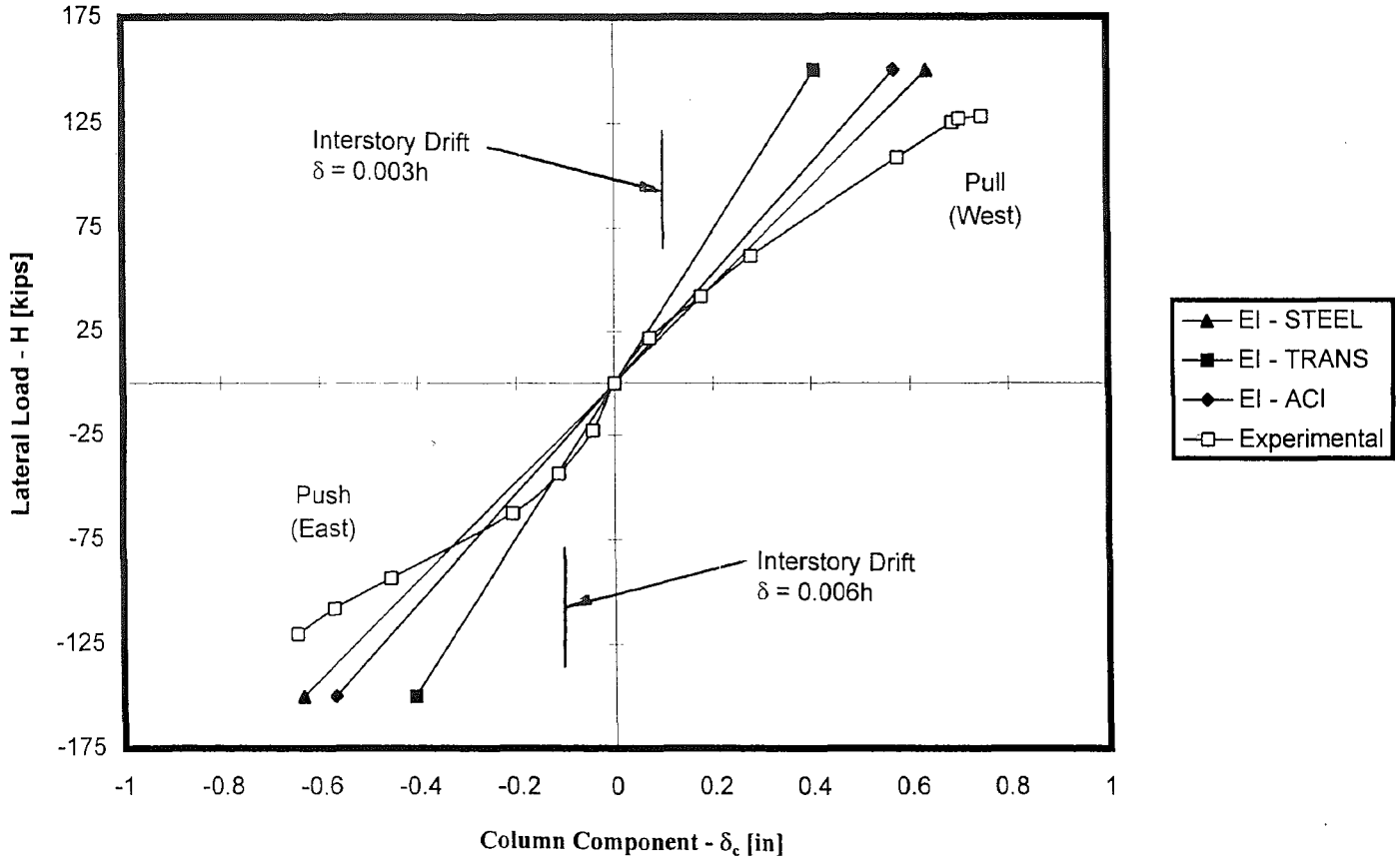

Figure 4.6 - Lateral Load - Column Deformation Envelope Response for Specimen 1

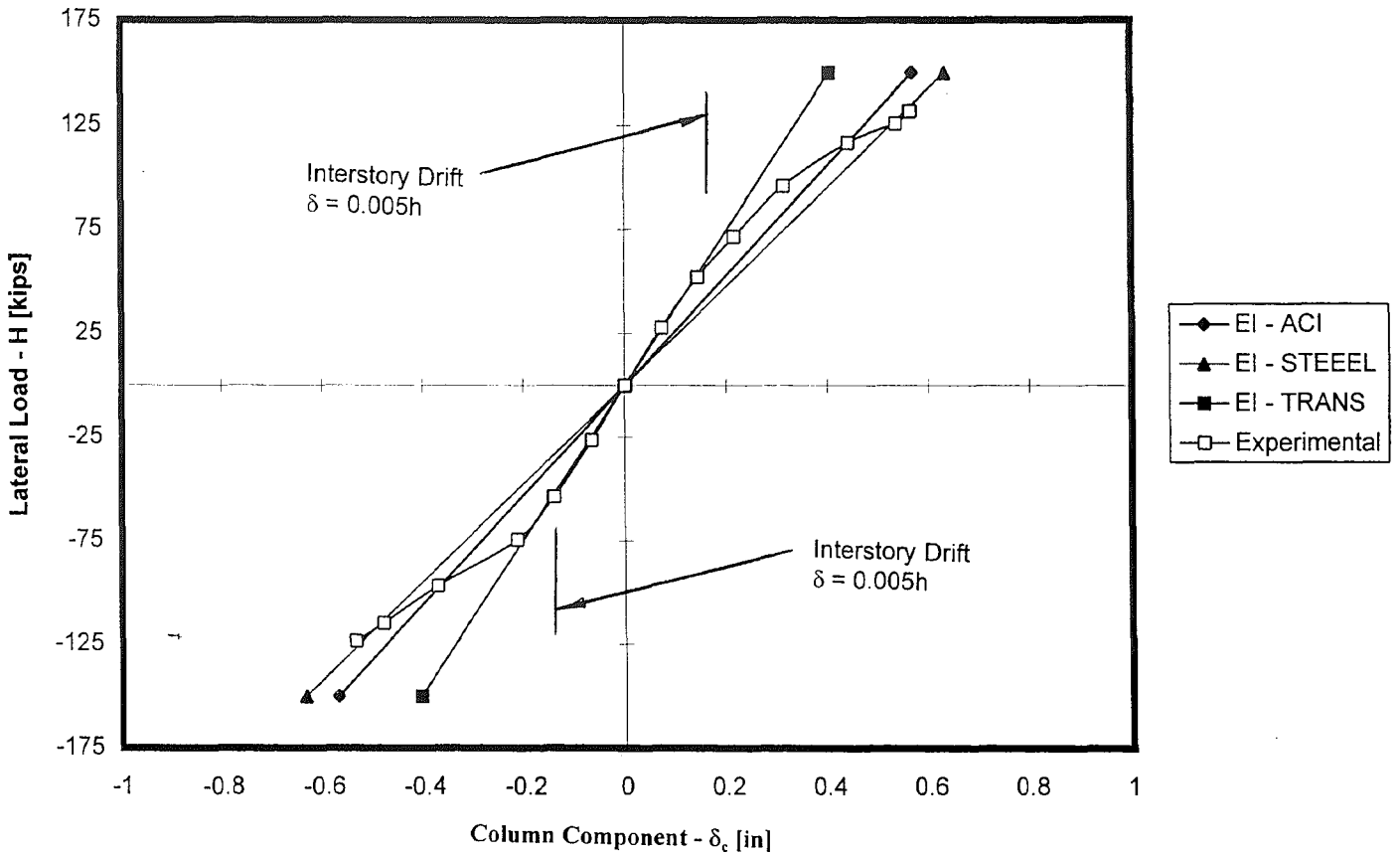

Figure 4.7 - Lateral Load - Column Deformation Envelope Response for Specimen 3

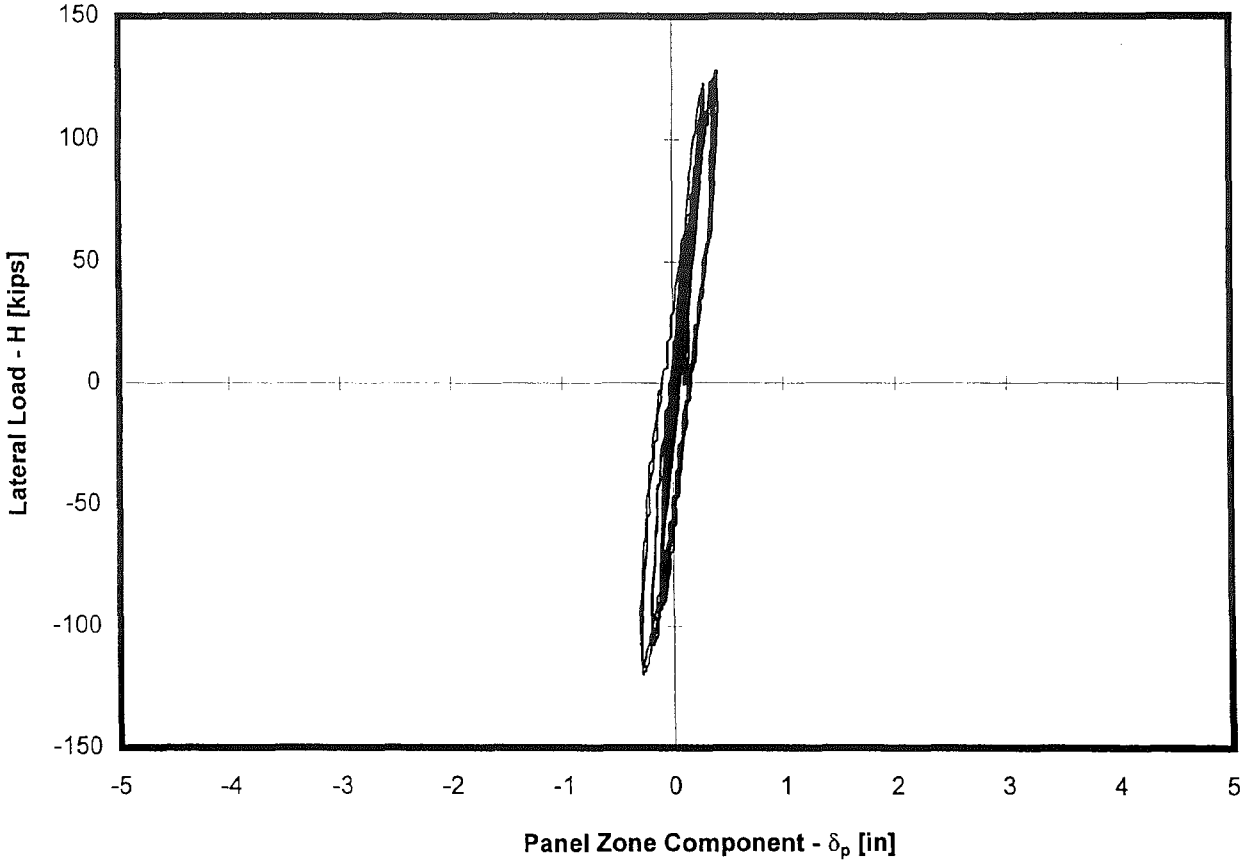

Figure 4.8a - Lateral Load - North Panel Zone Inter-Story Drift Component Relationship, Specimen 1

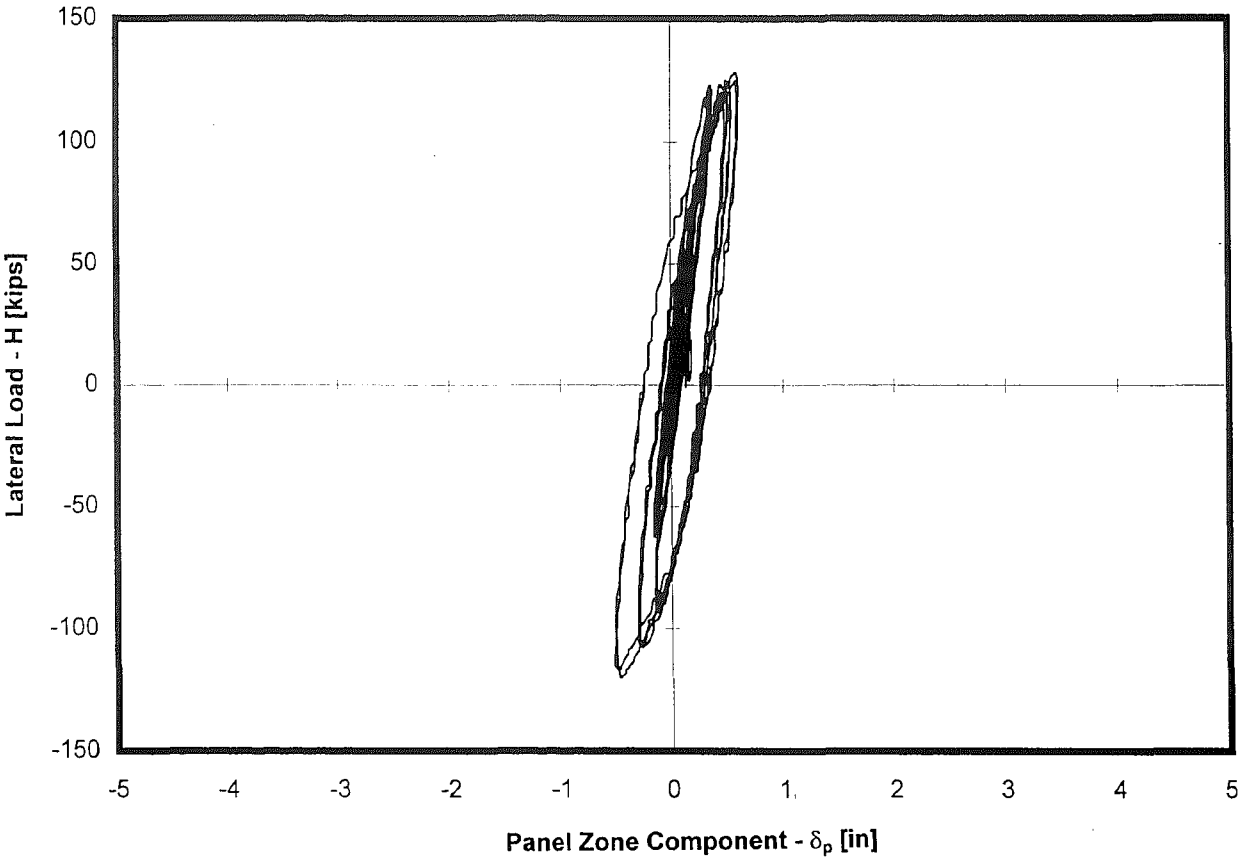

Figure 4.8b - Lateral Load - South Panel Zone Inter-Story Drift Component Relationship, Specimen 1

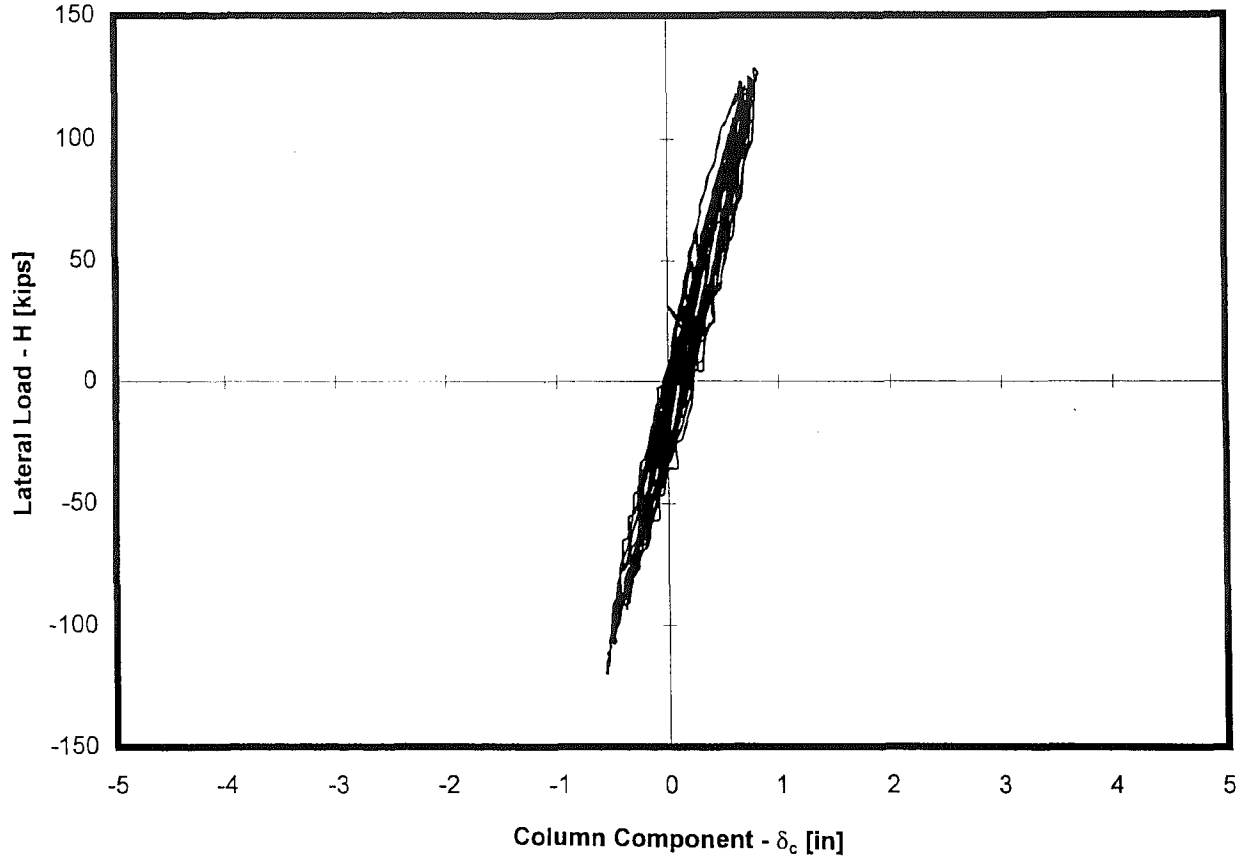

Figure 4.9 - Lateral Load - Column Inter-Story Drift Component Relationship, Specimen 1

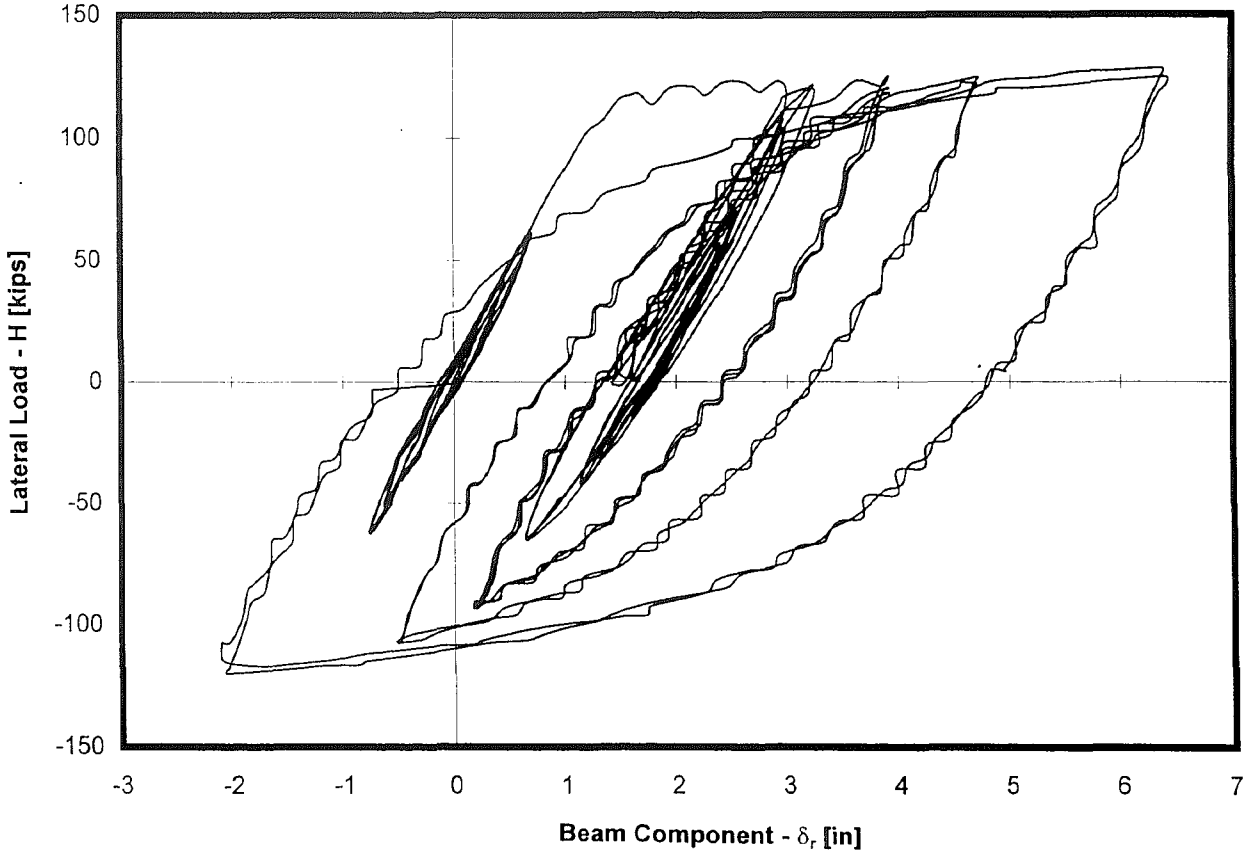

Figure 4.10 - Lateral Load - Beam Inter-Story Drift Component Relationship, Specimen 1

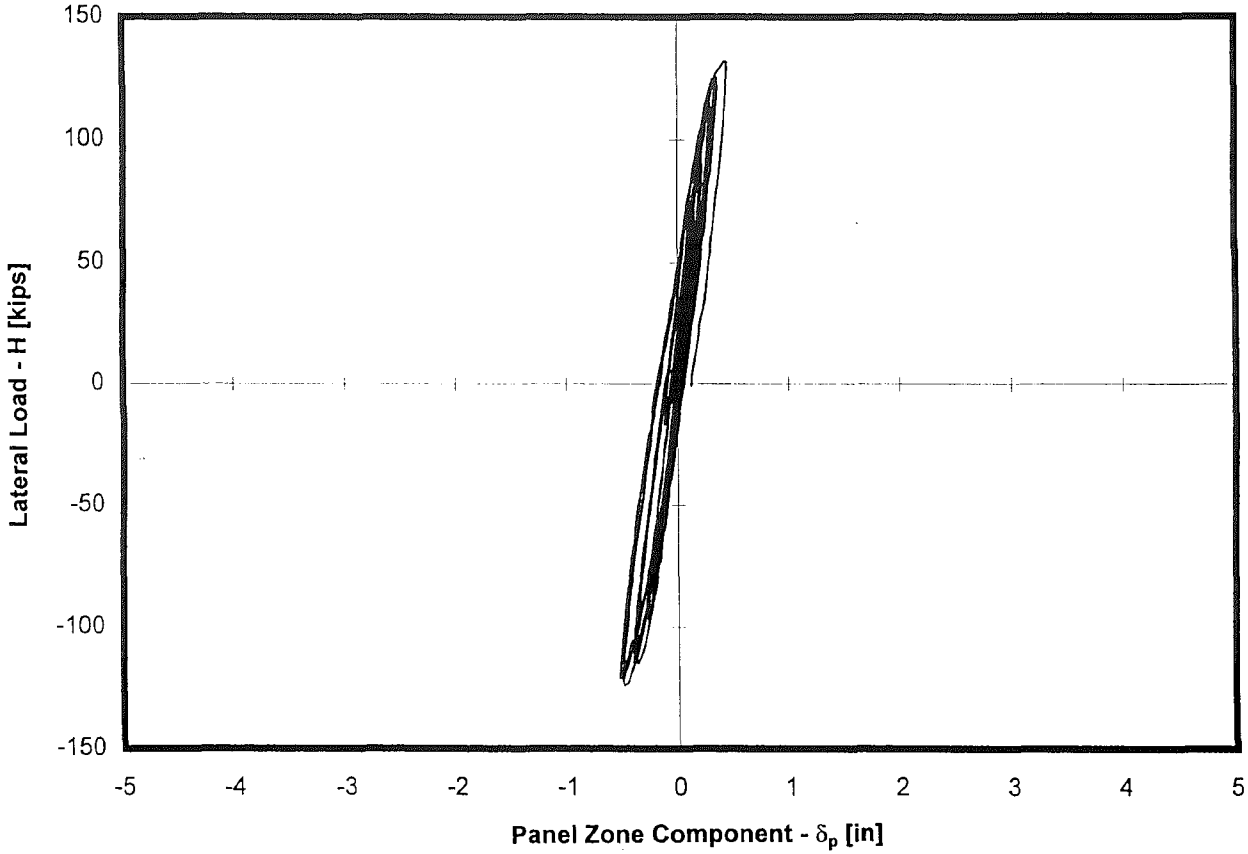

Figure 4.11a - Lateral Load - North Panel Zone Inter-Story Drift Component Relationship, Specimen 3

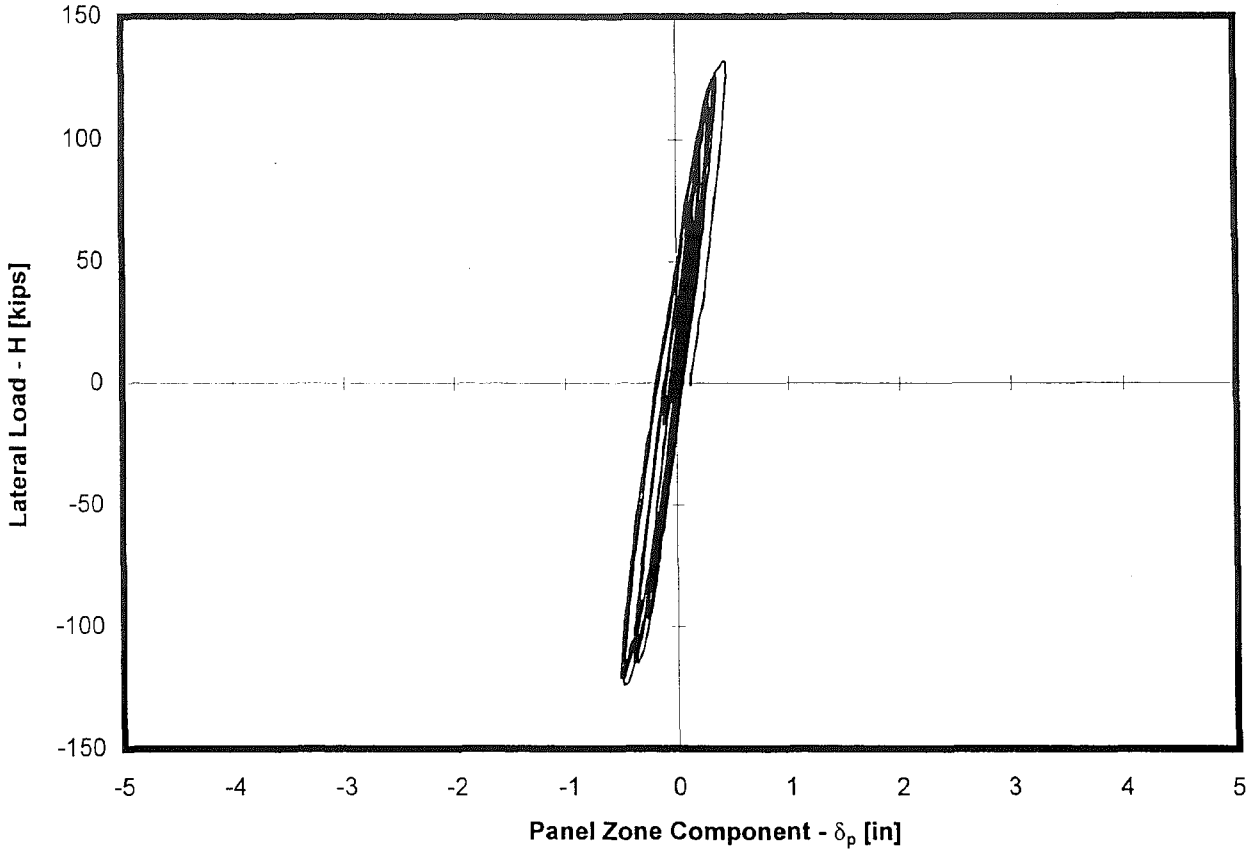

Figure 4.11b - Lateral Load - South Panel Zone Inter-Story Drift Component Relationship, Specimen 3

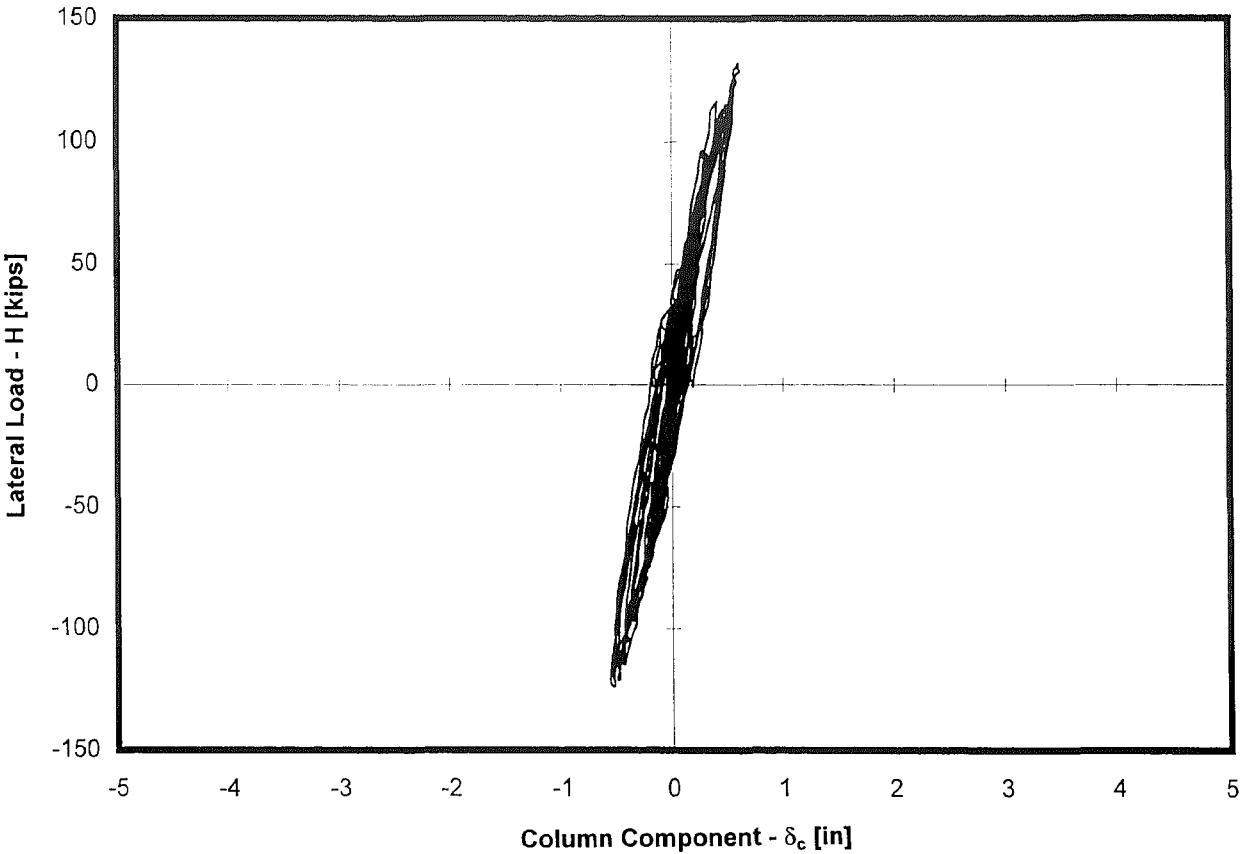

Figure 4.12 - Lateral Load - Column Inter-Story Drift Component Relationship, Specimen 3

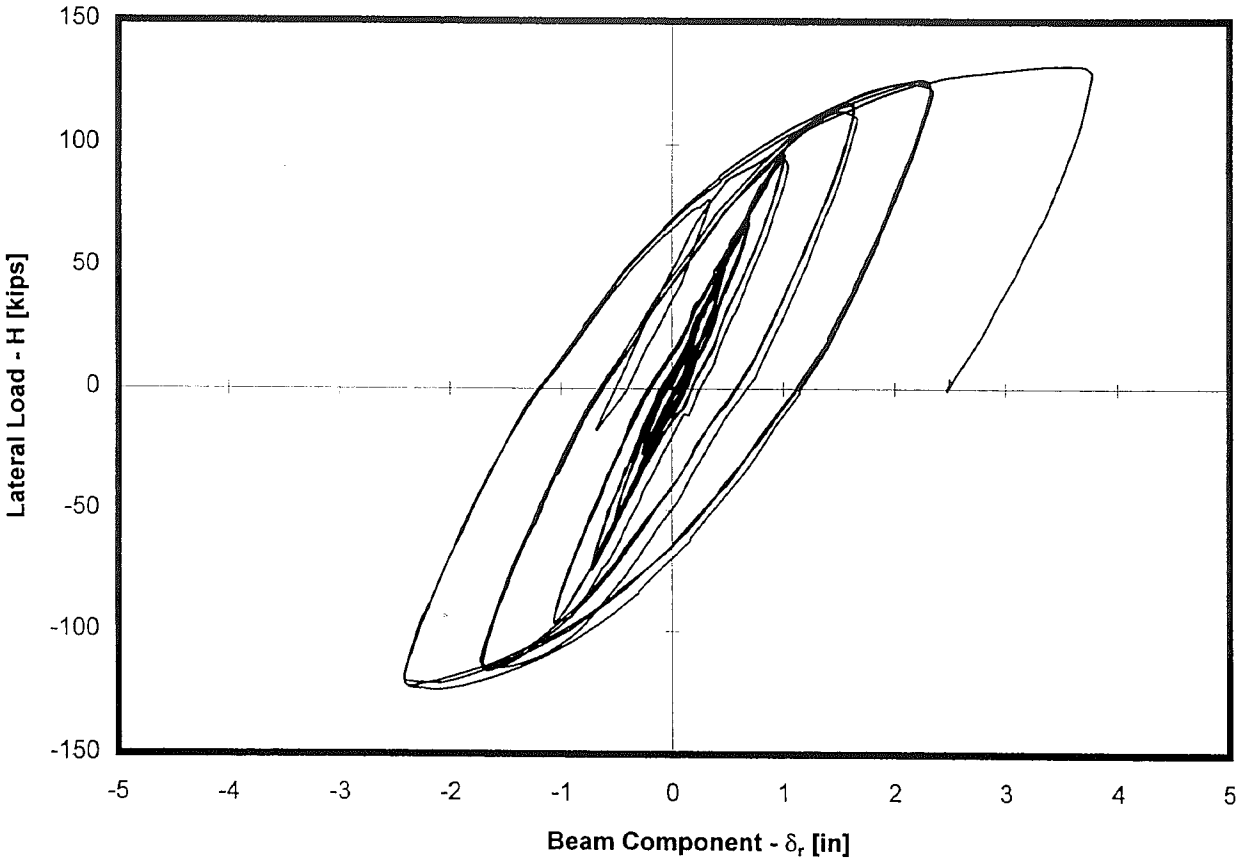

Figure 4.13 - Lateral Load - Beam Inter-Story Drift Component Relationship, Specimen 3

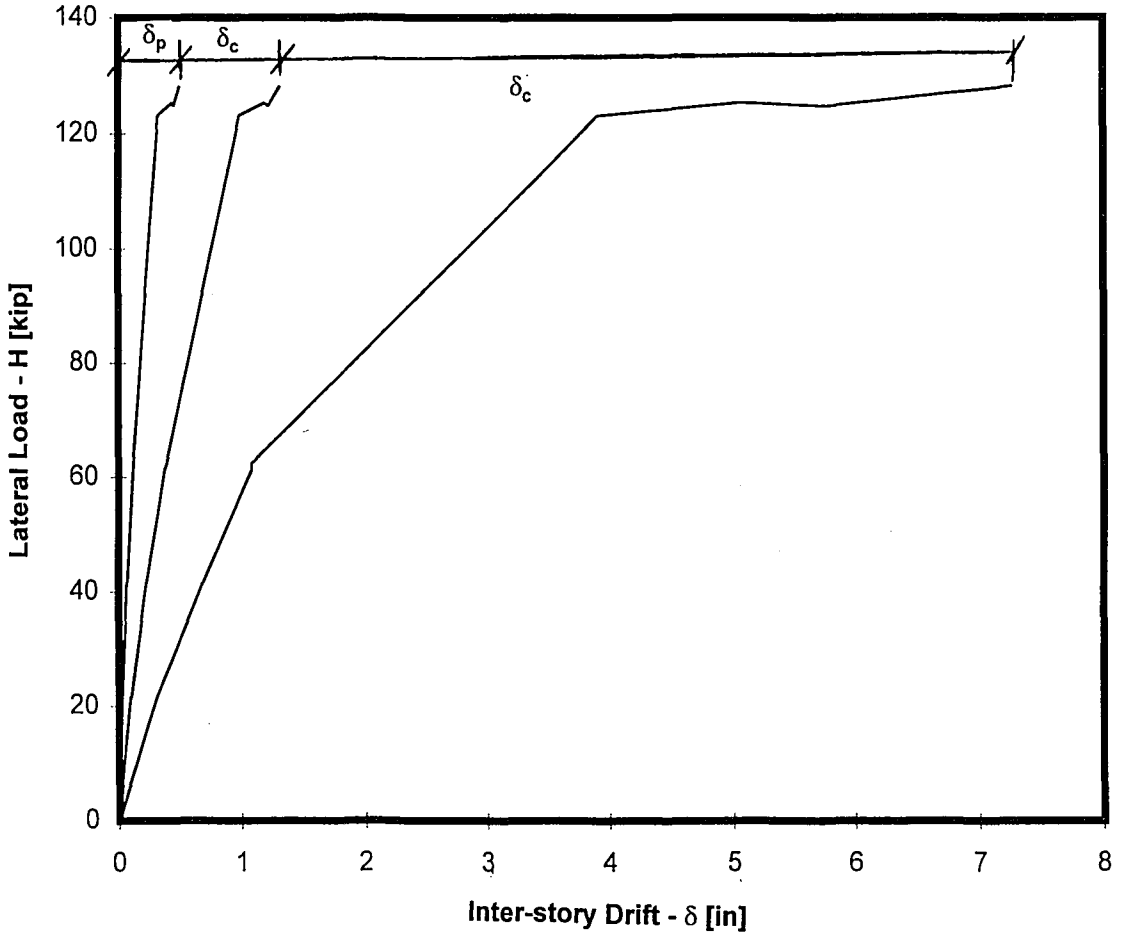

Figure 4.14 - Contribution of Components to Inter-Story Drift, Specimen 1

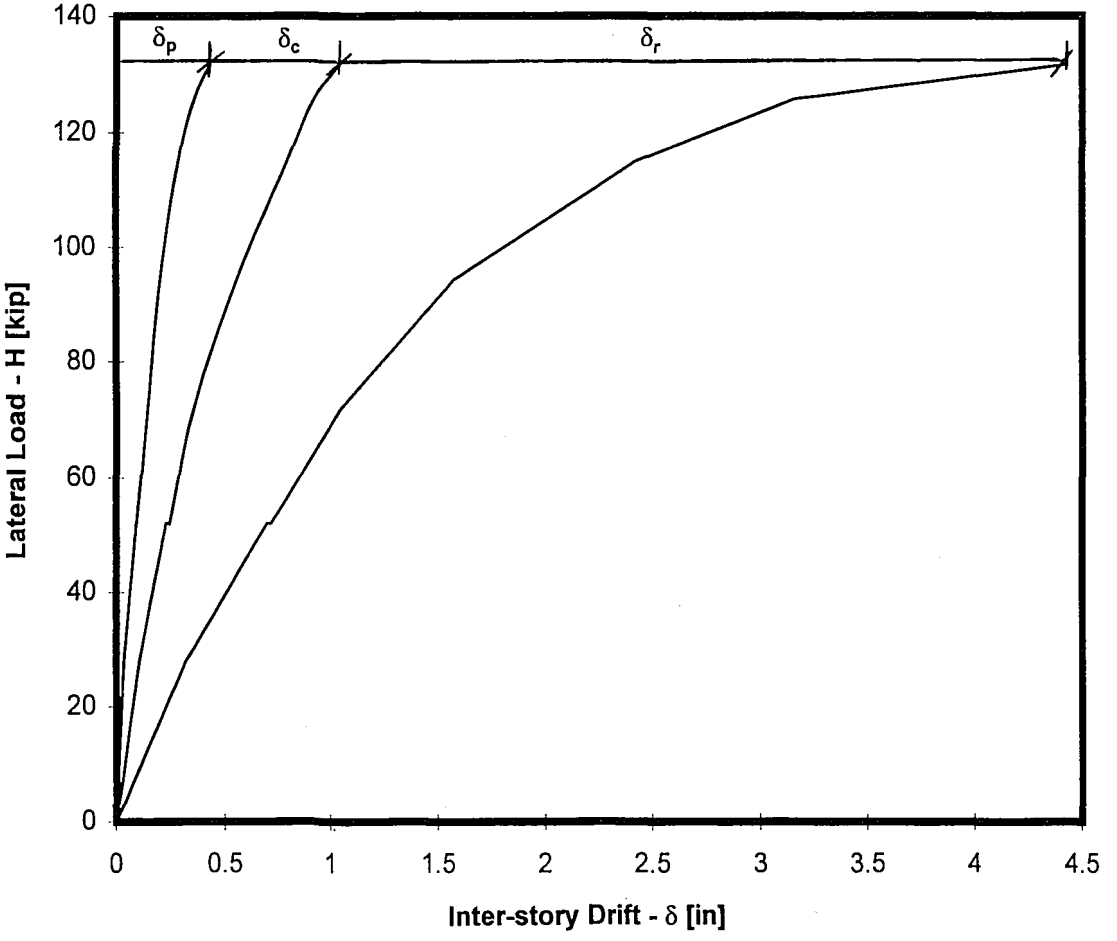

Figure 4.15 - Contribution of Components to Inter-Story Drift, Specimen 3

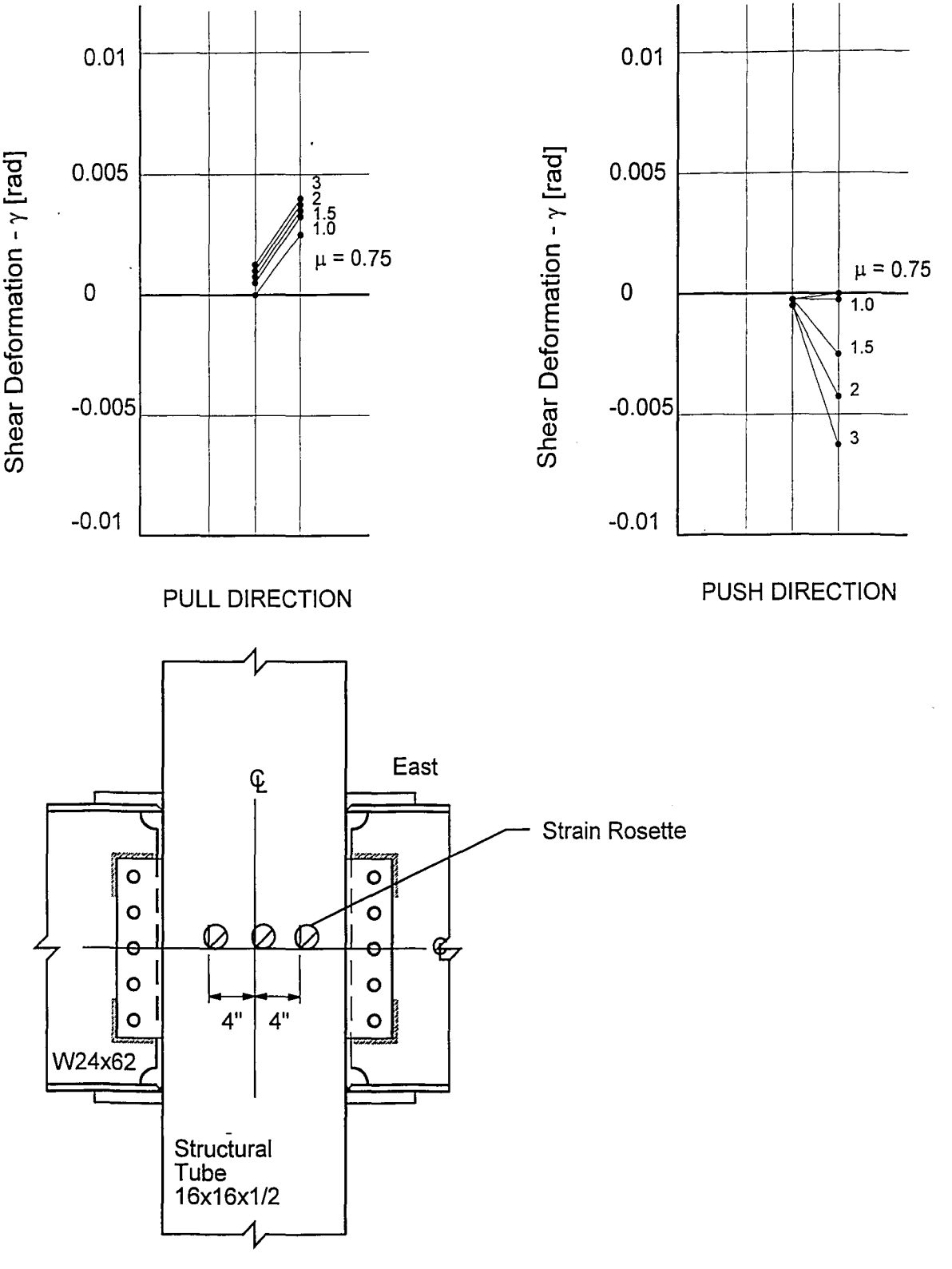

Figure 4.16(a) - South Panel Zone Shear Deformation
Strain Rosettes - Specimen 1

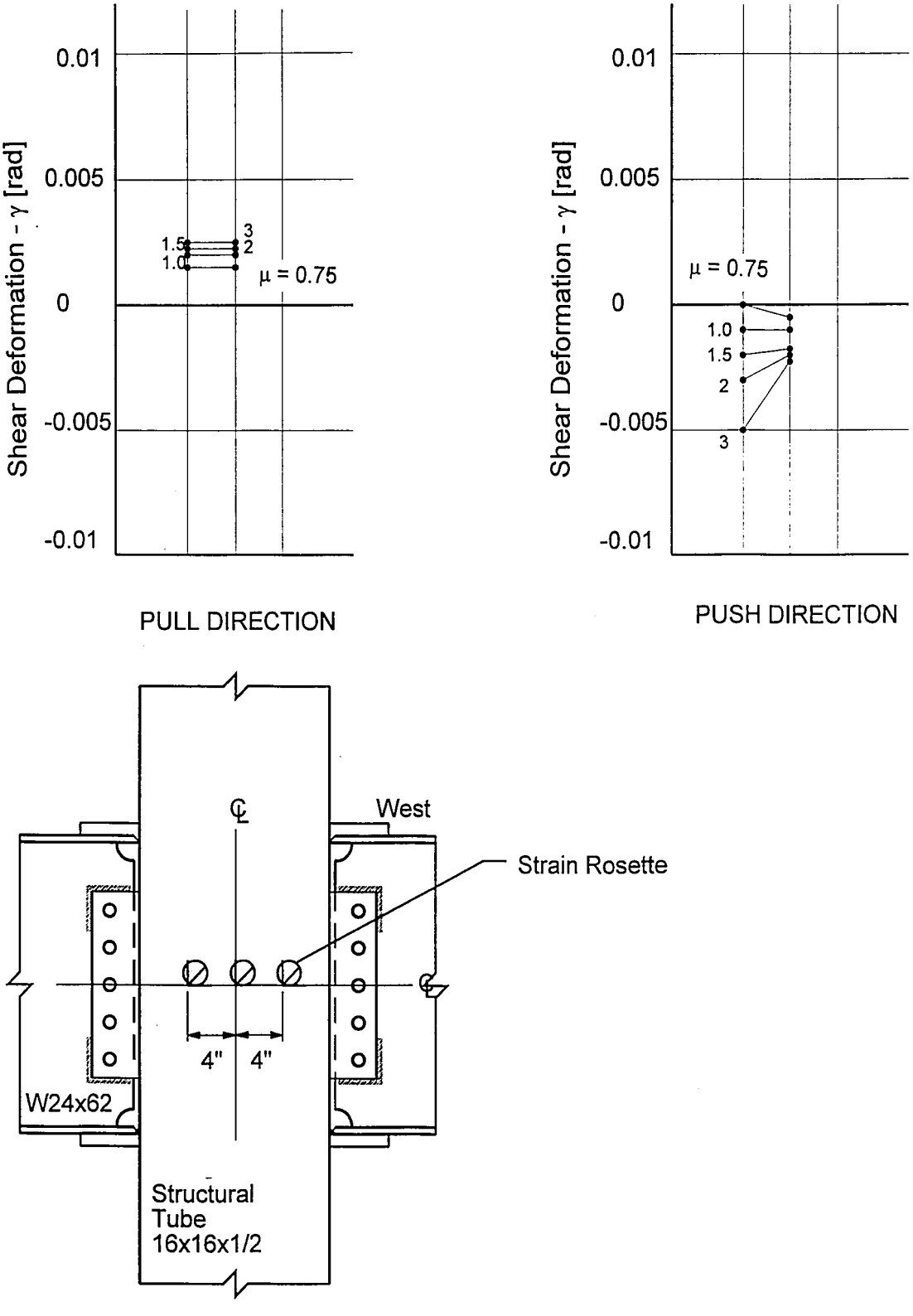

Figure 4.16(b) - North Panel Zone Shear Deformation
Strain Rosettes, Specimen 1

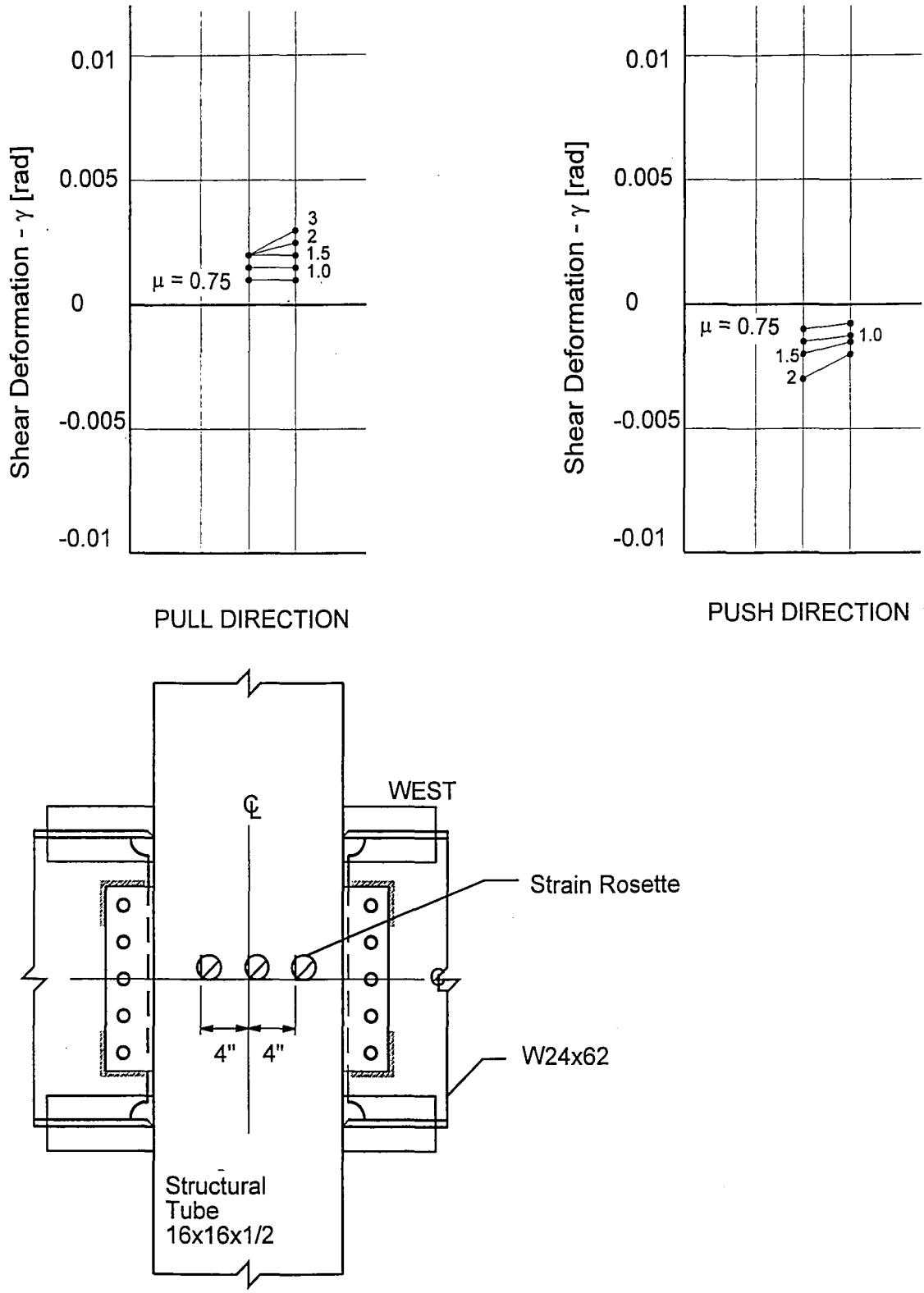

Figure 4.17(a) - South Panel Zone Shear Deformation,
Strain Rosettes - Specimen 3

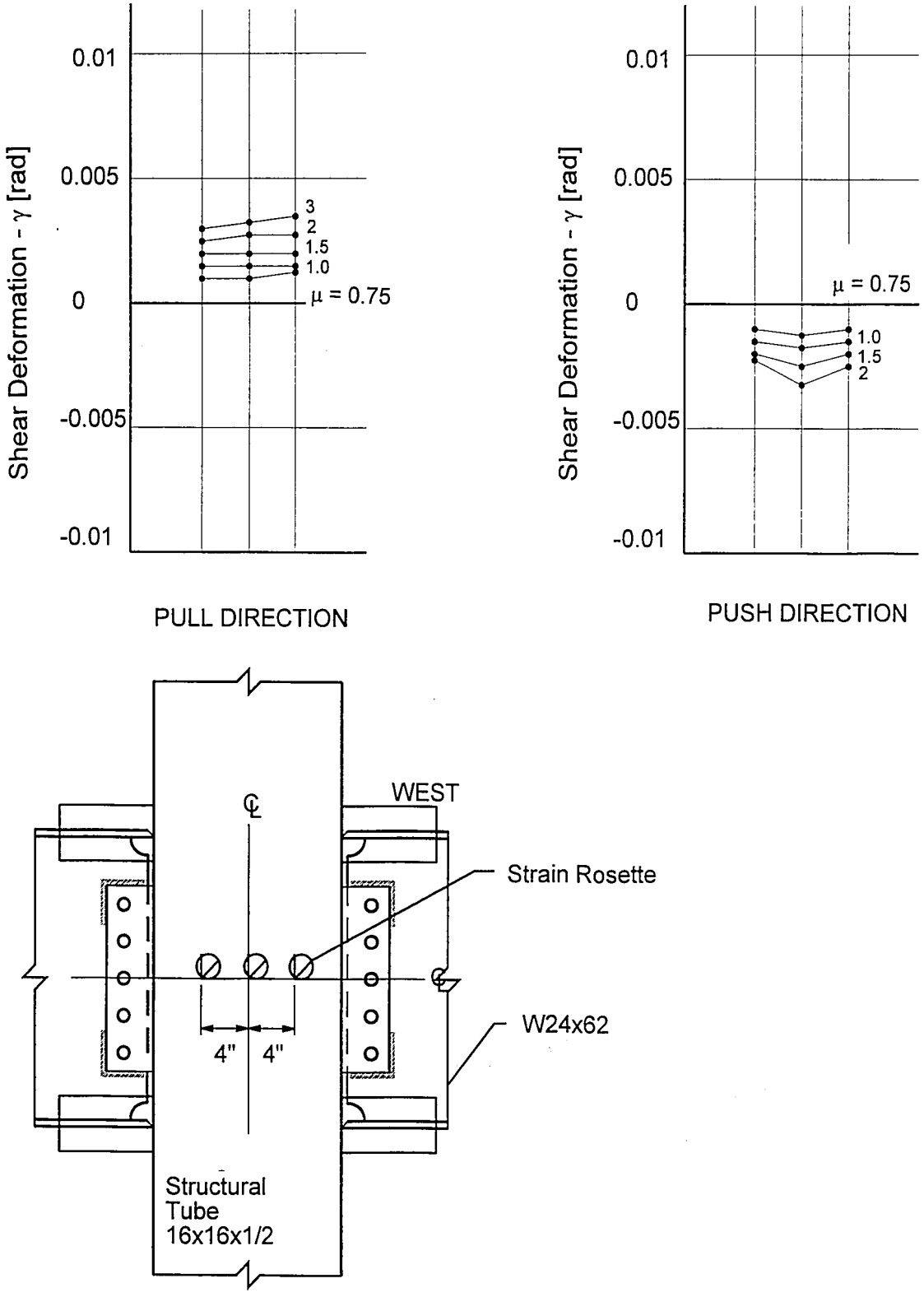

Figure 4.17(b) - North Panel Zone Shear Deformation,
Strain Rosettes - Specimen 3

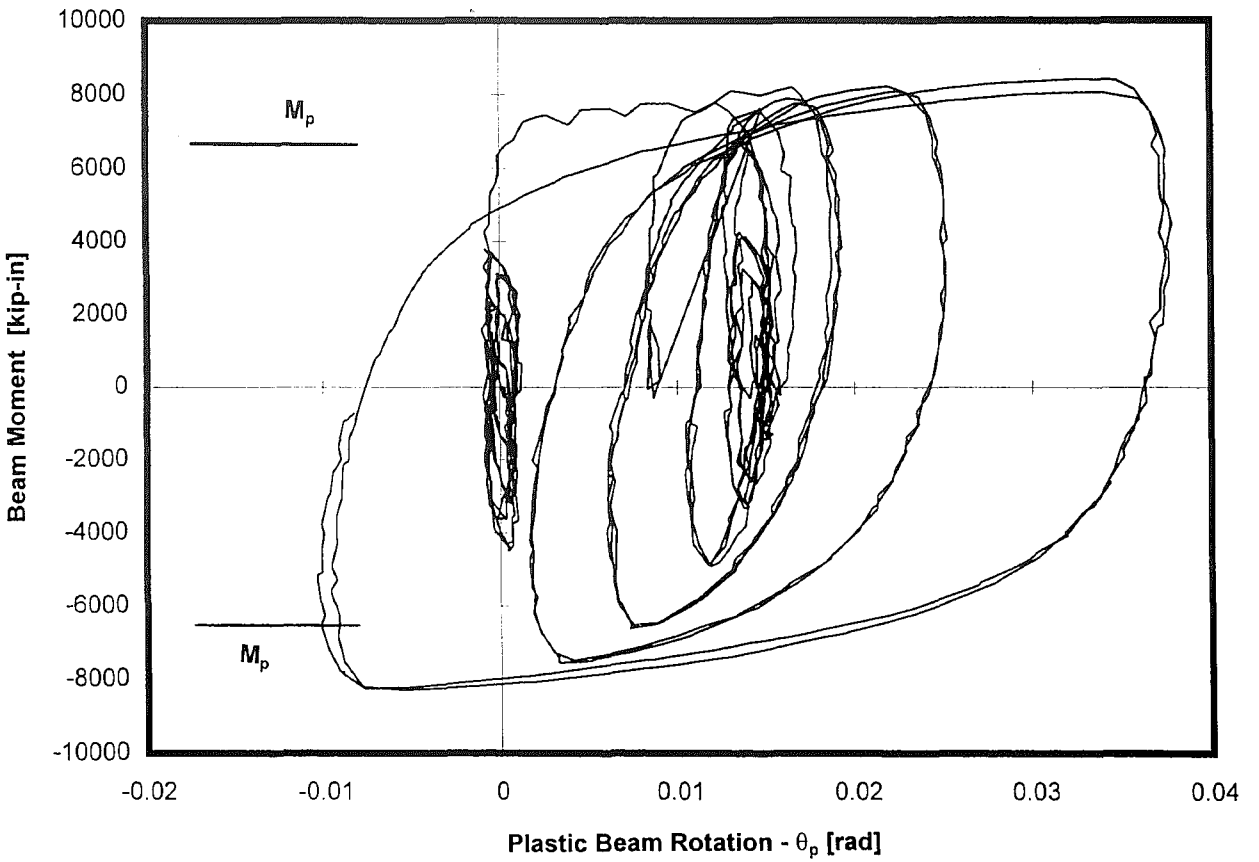

Figure 4.18 - East Beam Moment at Edge of Coverplate vs. Beam Plastic Rotation, Specimen 1

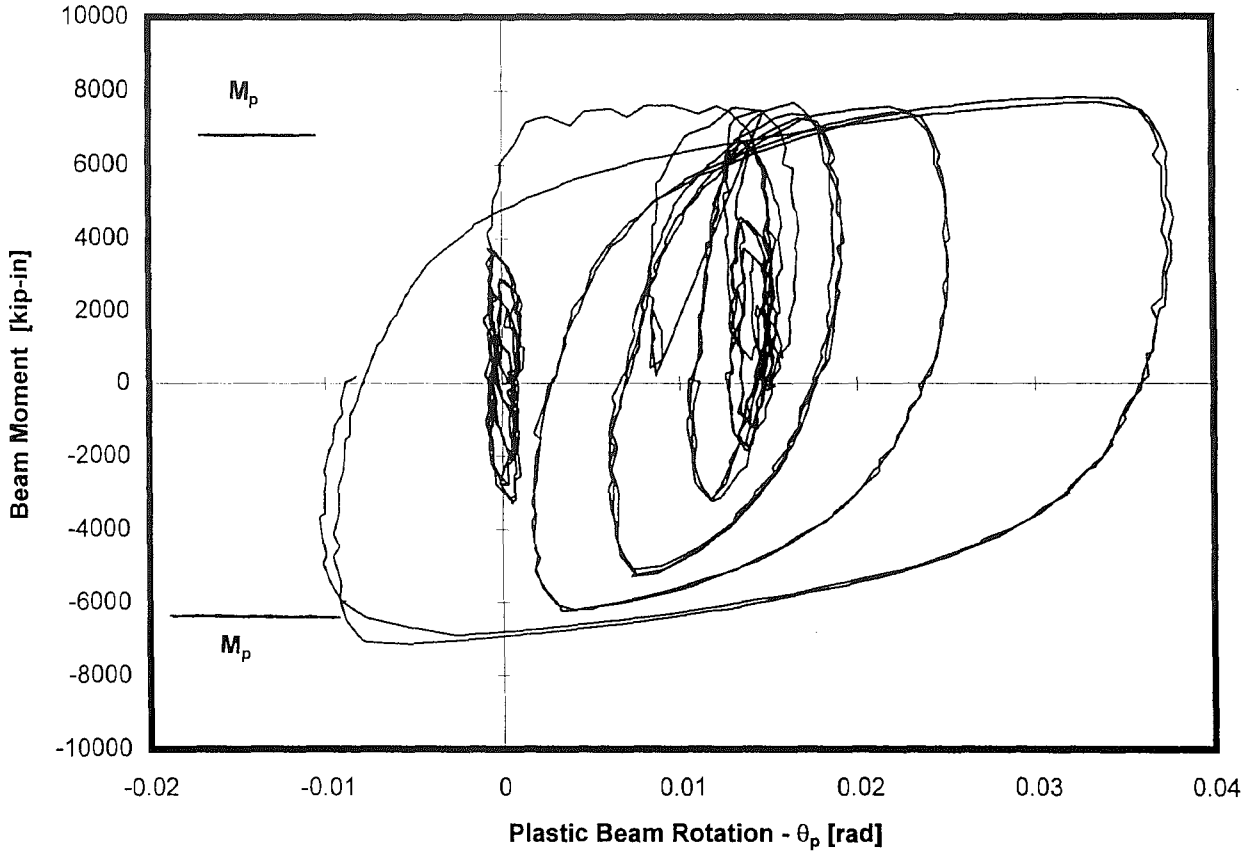

Figure 4.19 - West Beam Moment at Edge of Coverplate vs. Beam Plastic Rotation, Specimen 1

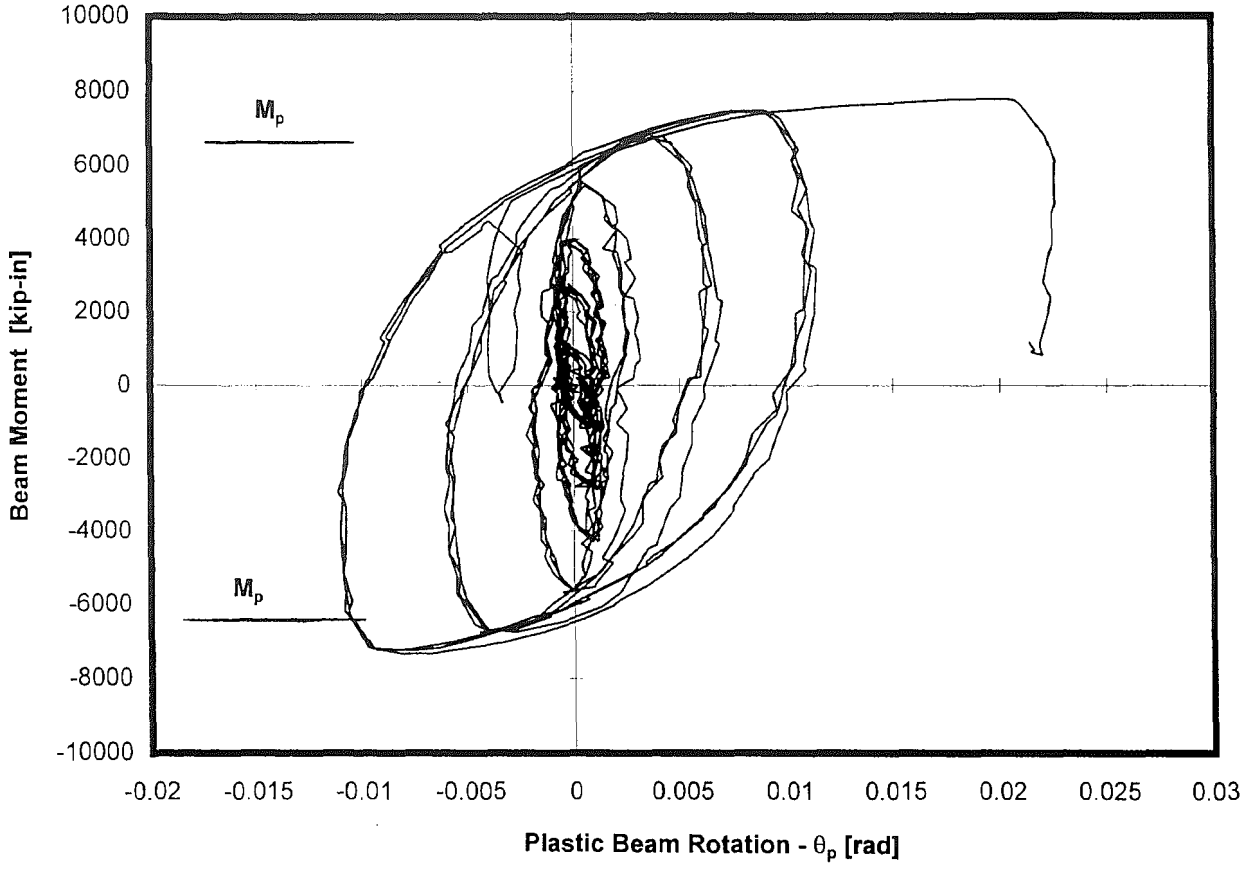

Figure 4.20 - East Beam Moment at Edge of Tees vs. Beam Plastic Rotation, Specimen 3

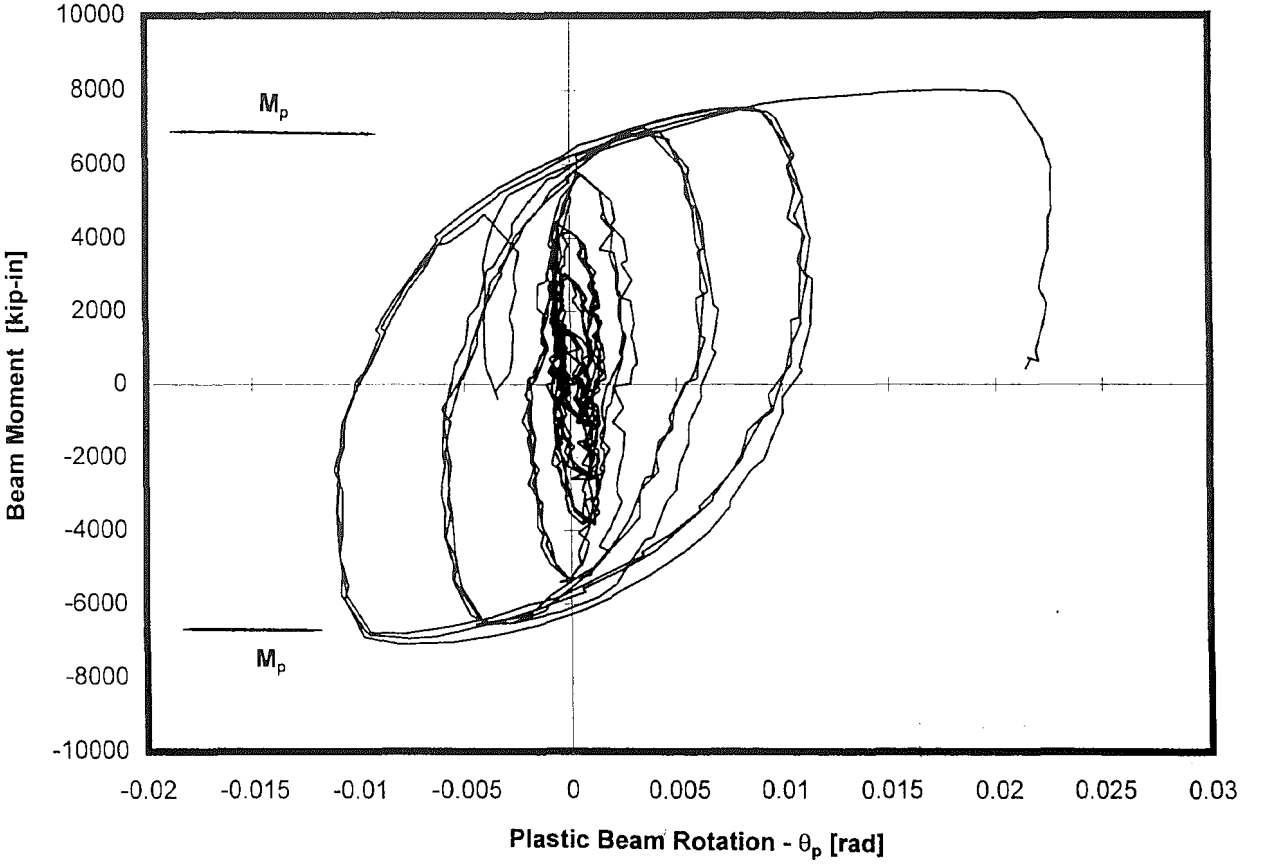

Figure 4.21 - West Beam Moment at Edge of Tees vs. Beam Plastic Rotation, Specimen 3

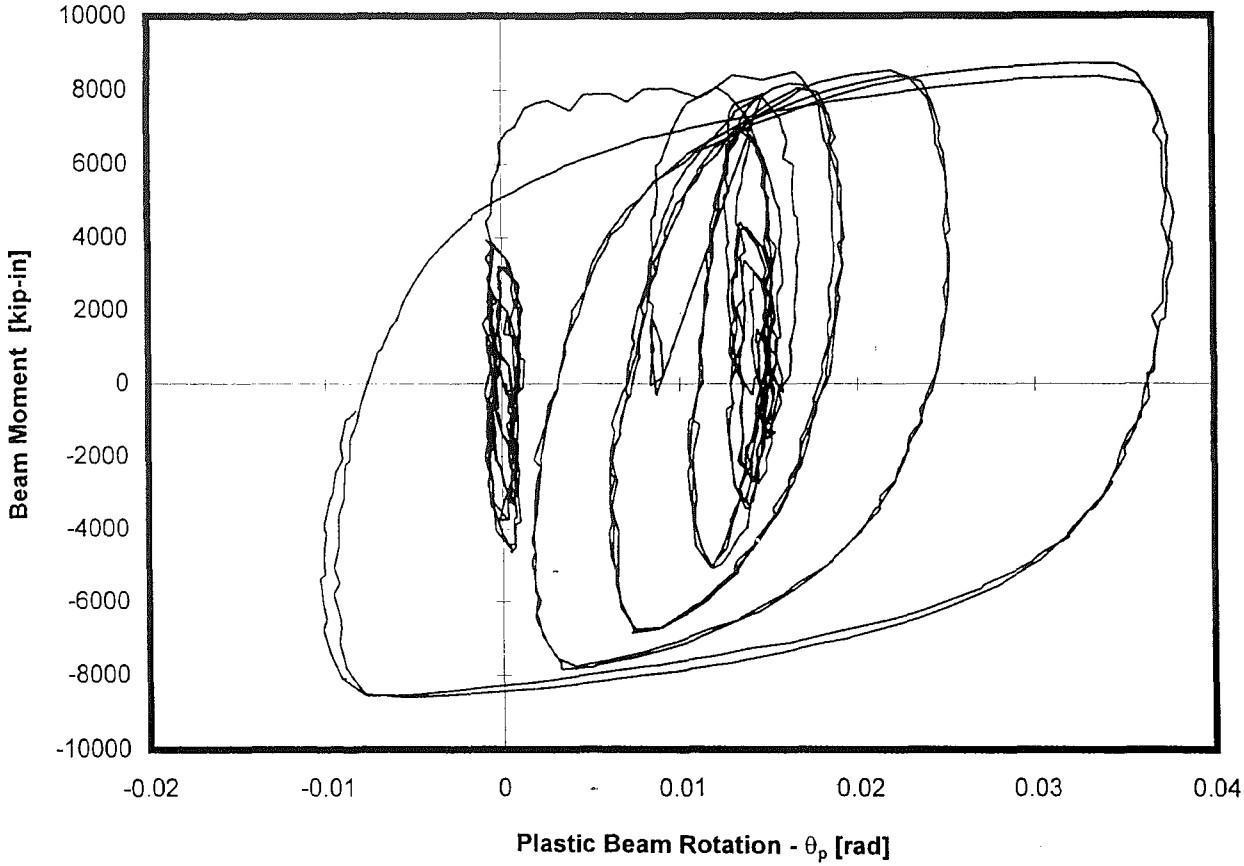

Figure 4.22 - East Beam Moment at Face of Column vs. Beam Plastic Rotation, Specimen 1

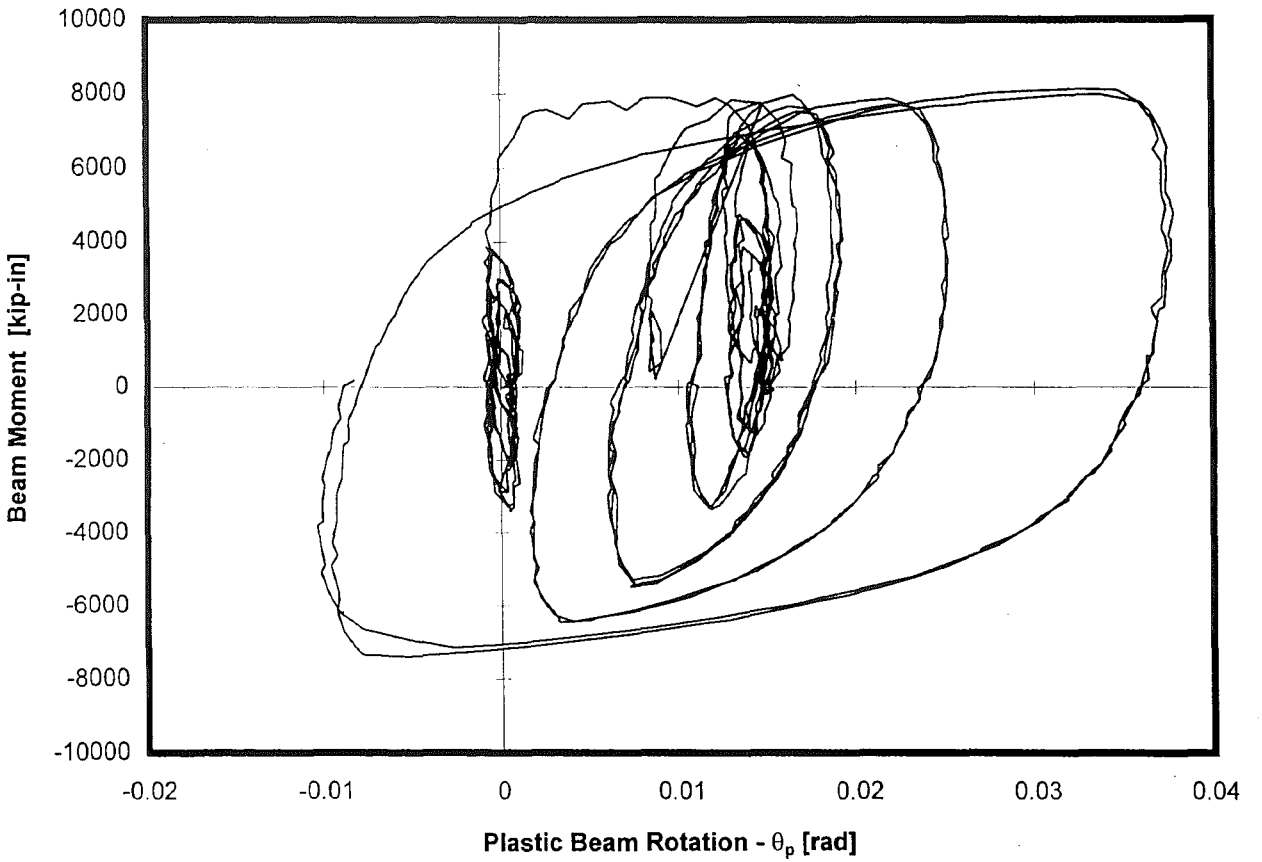

Figure 4.23 - West Beam Moment at Face of Column vs. Beam Plastic Rotation, Specimen 1

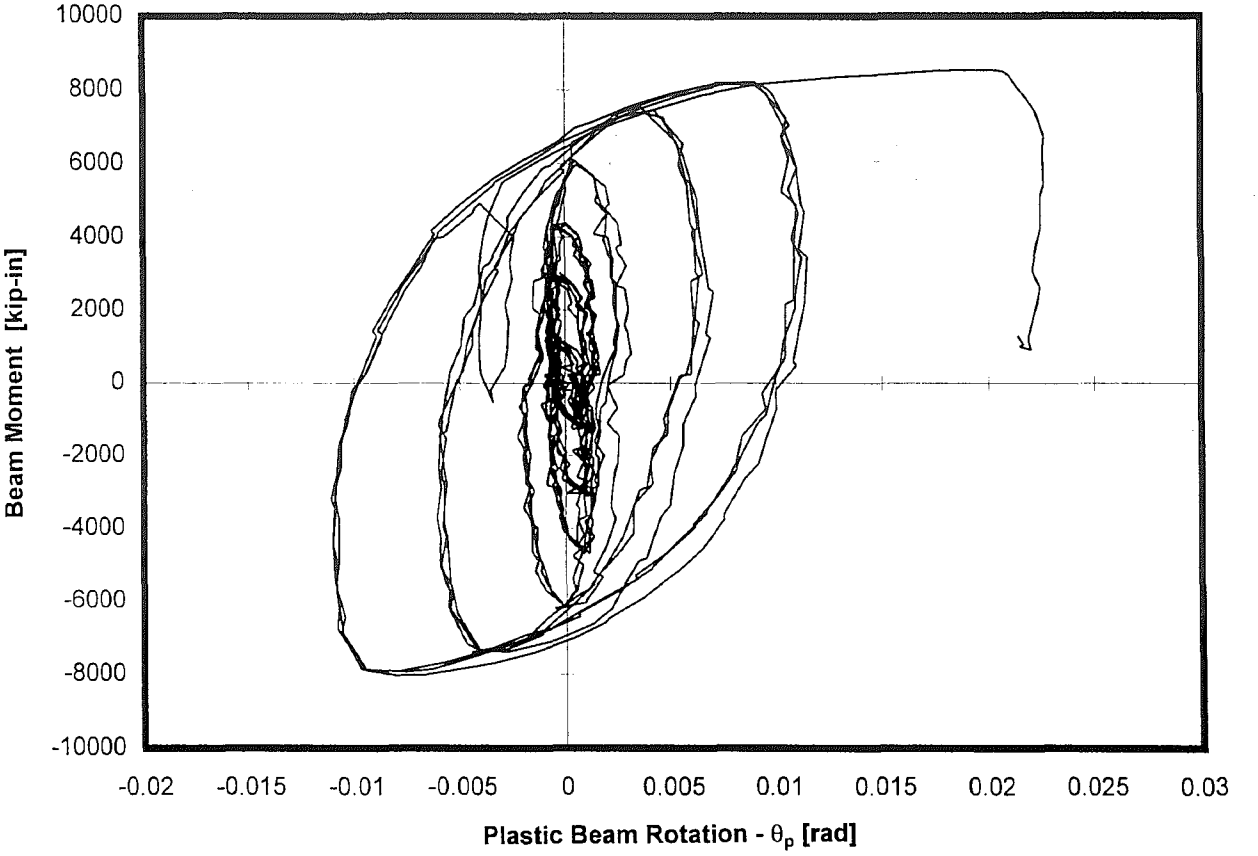

Figure 4.24 - East Beam Moment at Face of Column vs. Beam Plastic Rotation, Specimen 3

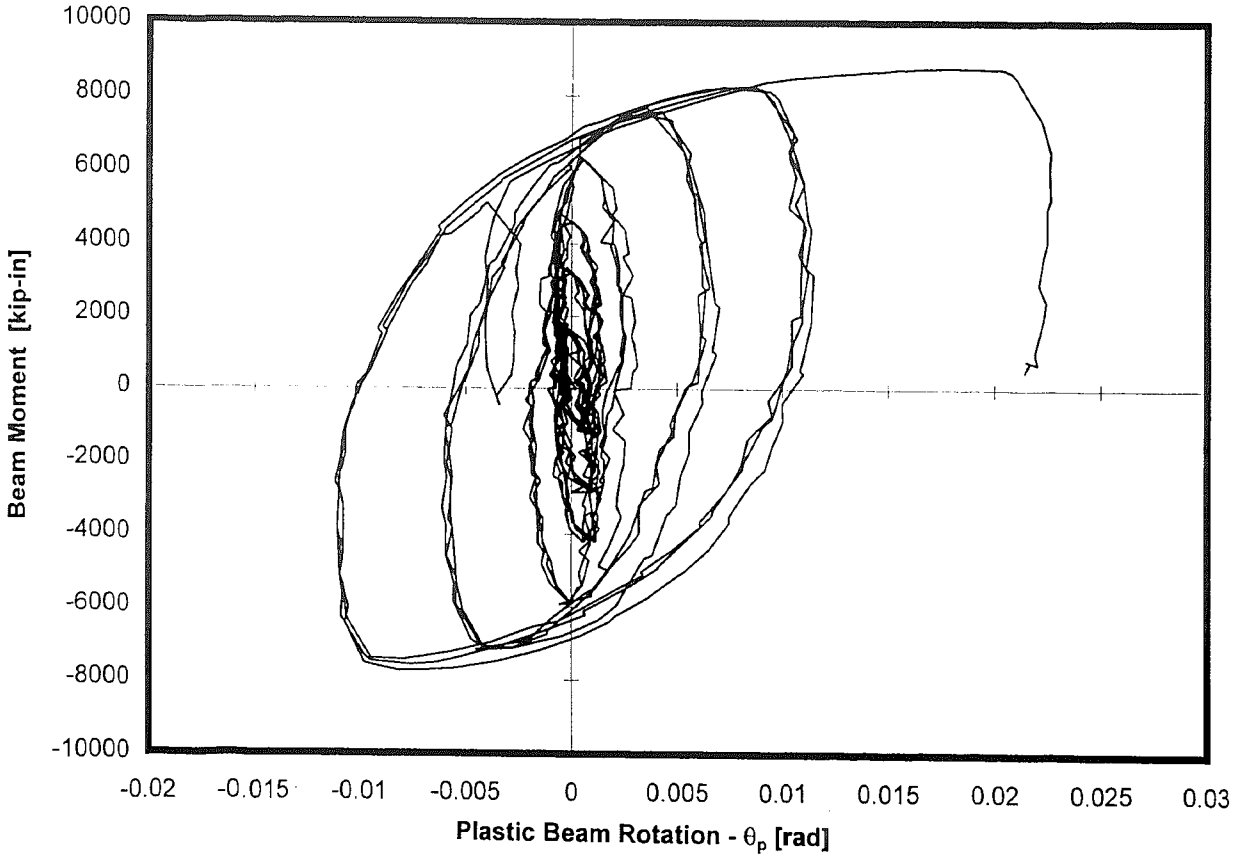

Figure 4.25 - West Beam Moment at Face of Column vs. Beam Plastic Rotation, Specimen 3

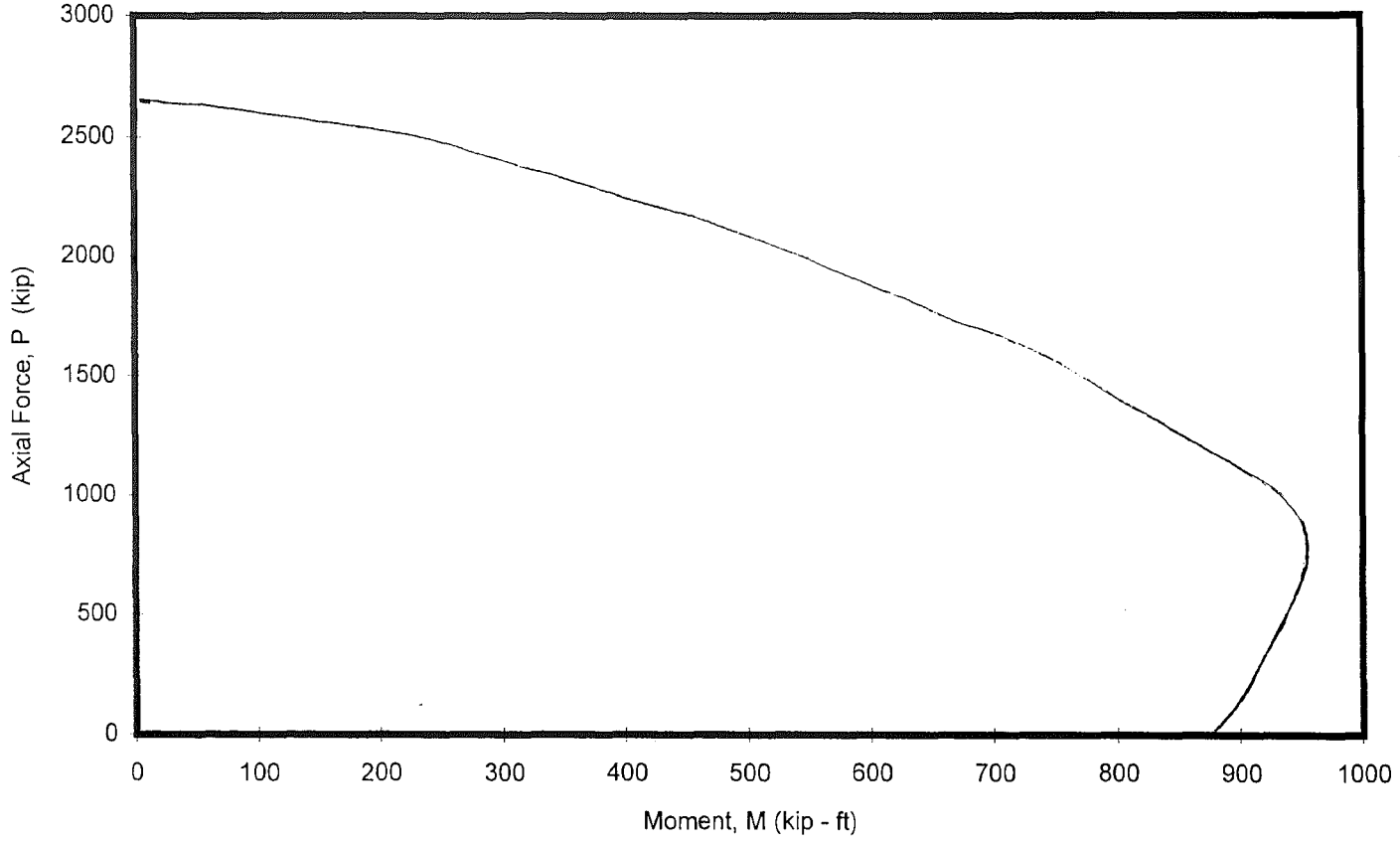

Figure 4.26 - Comparison of Specimen Maximum Force State with ACI and AISC Bare Steel Capacities

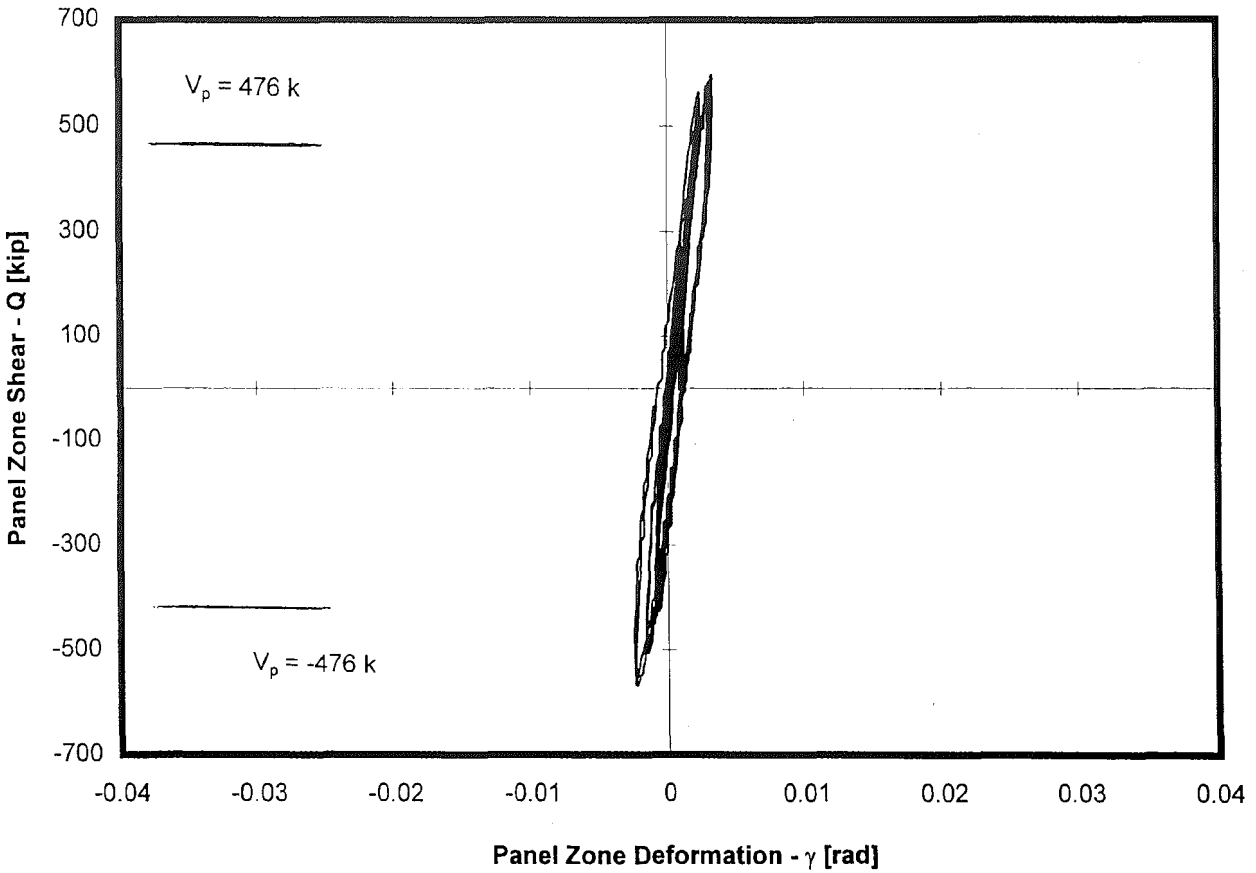

Figure 4.27 - North Panel Zone Shear vs. Panel Zone Deformation, Specimen 1

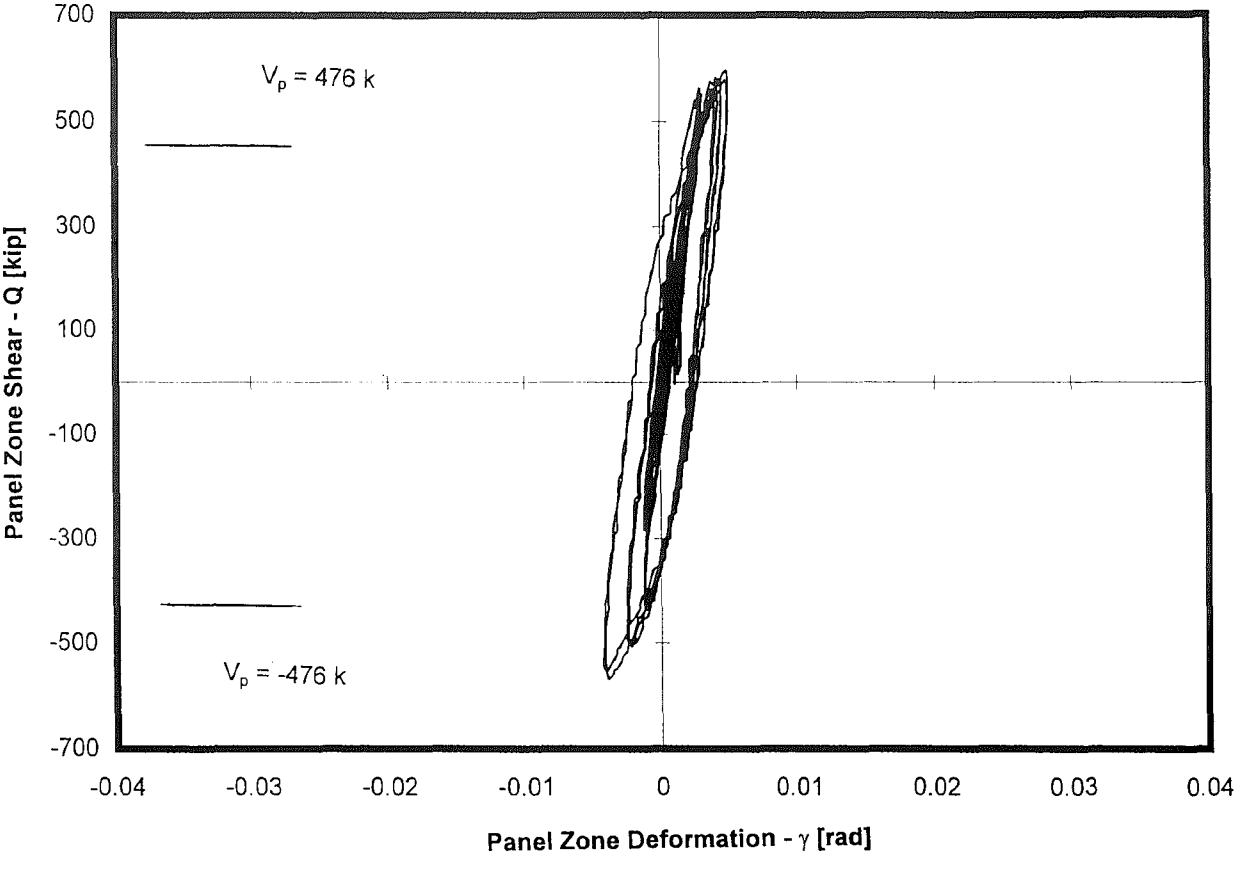

Figure 4.28 - South Panel Zone Shear vs. Panel Zone Deformation, Specimen 1

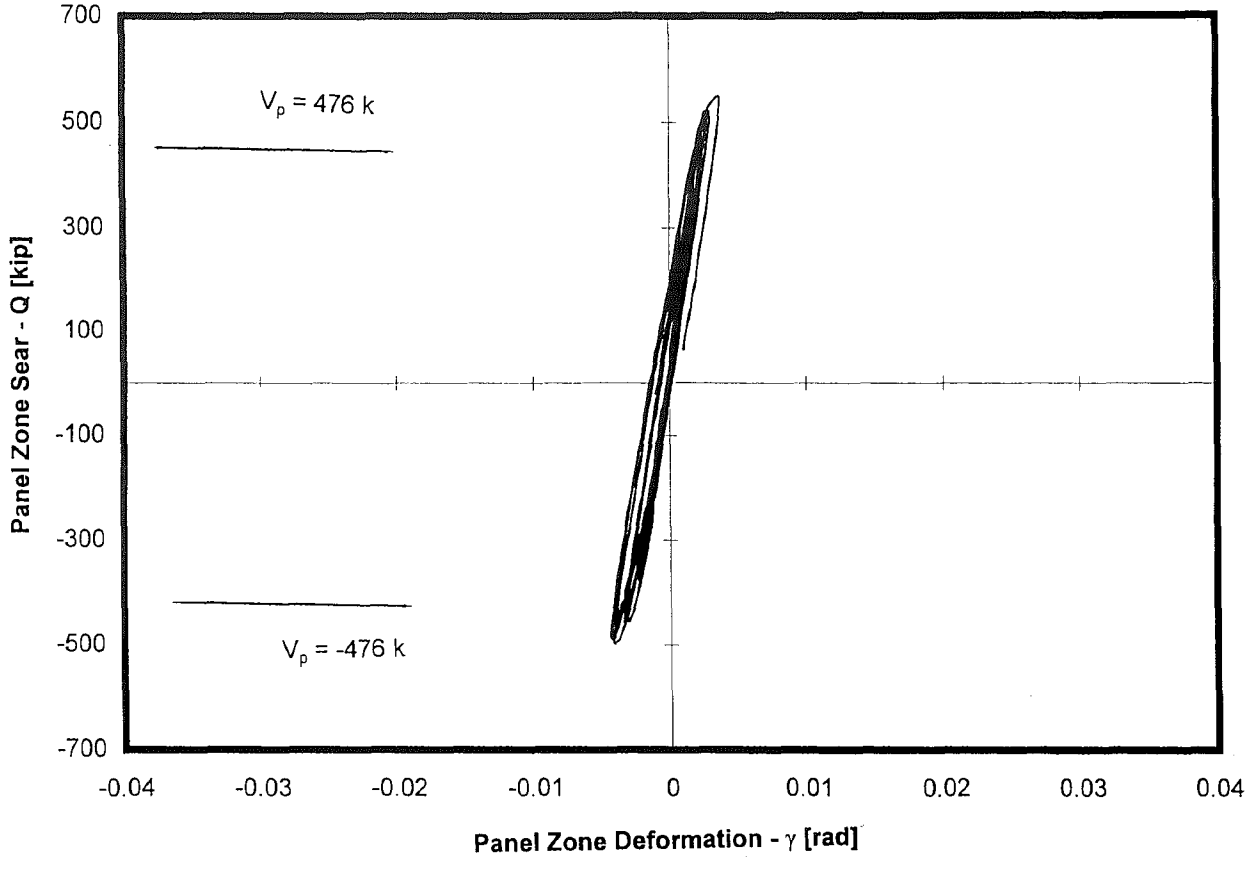

Figure 4.29 - North Panel Zone Shear vs. Panel Zone Deformation, Specimen 3

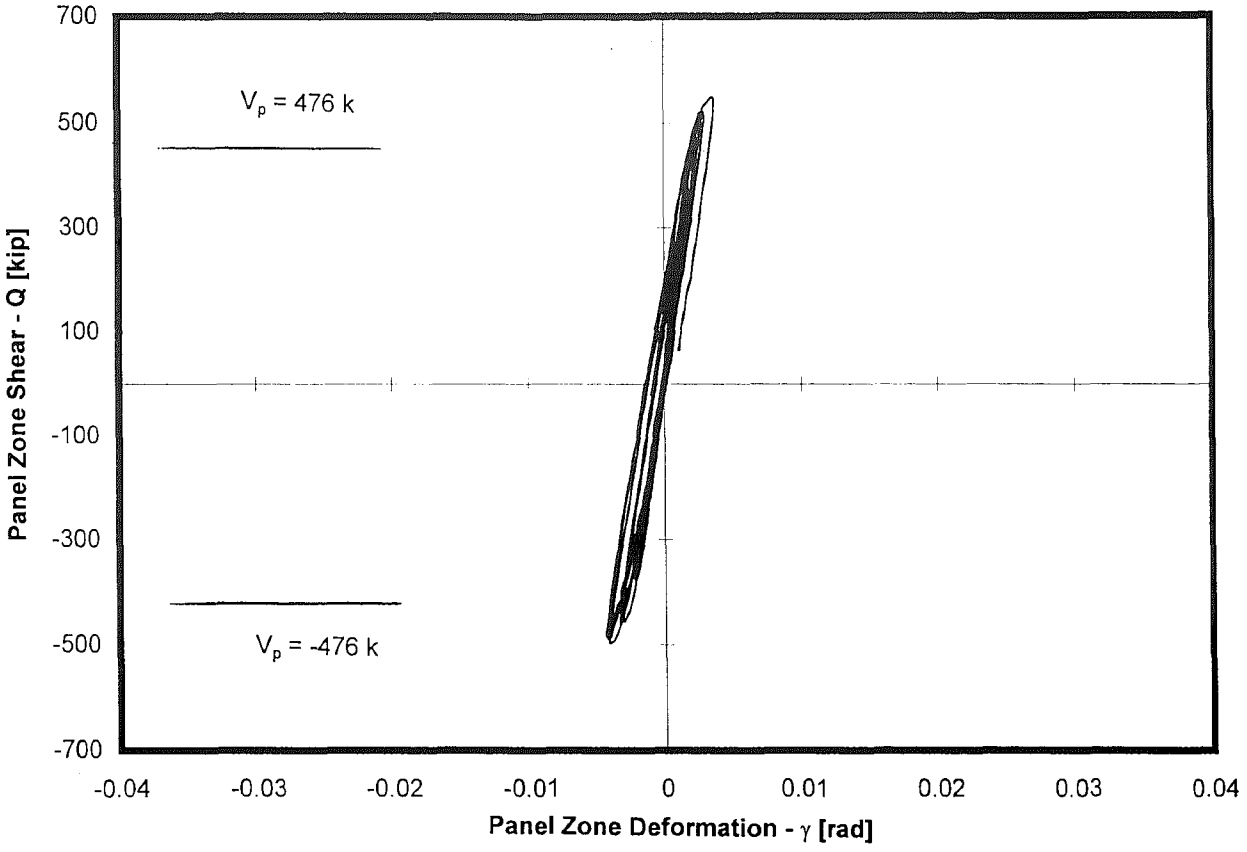

Figure 4.30 - South Panel Zone Shear vs. Panel Zone Deformation, Specimen 3

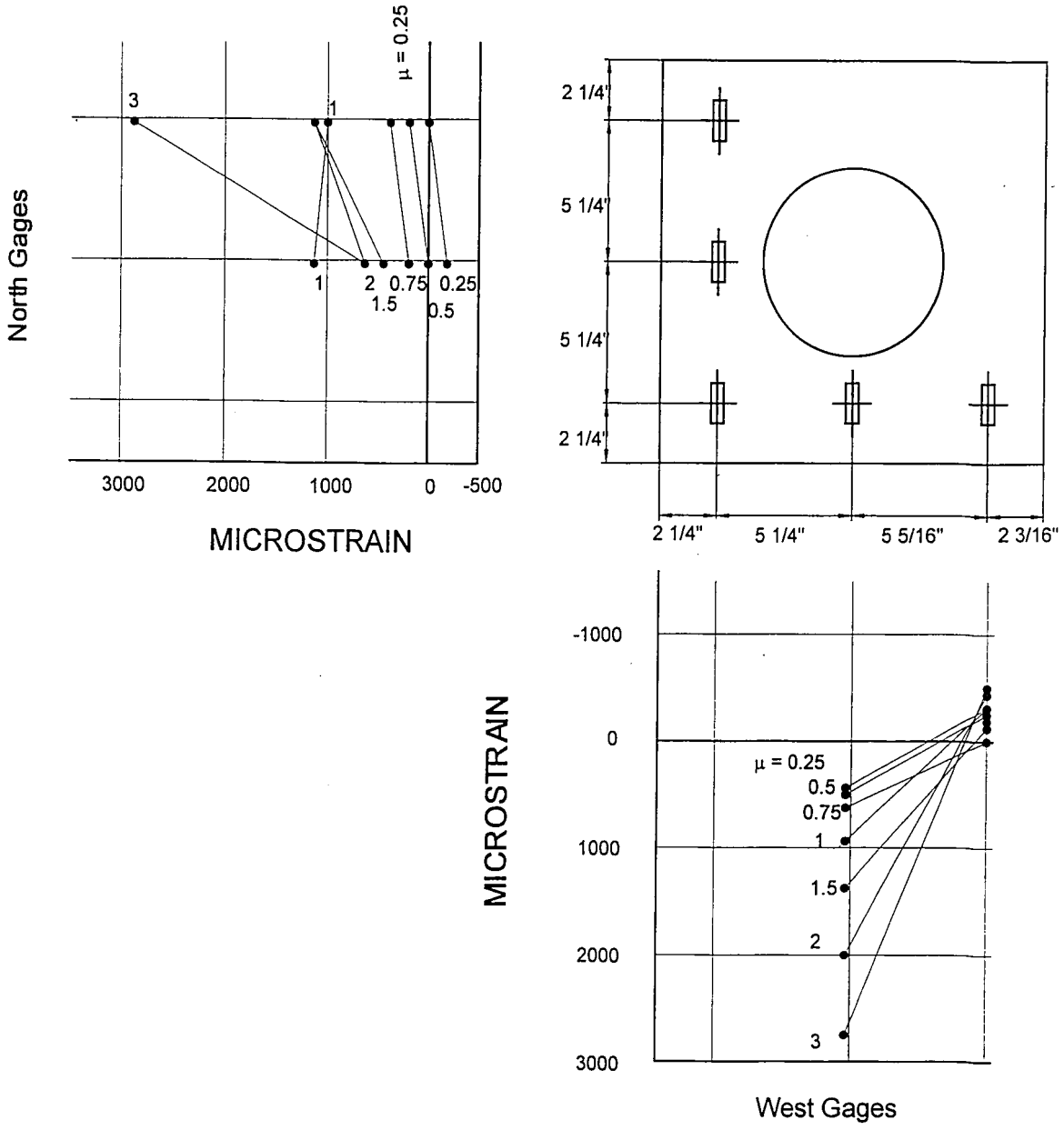

Figure 4.31 - Strain in Top Diaphragm (Pull Direction)
Specimen 1

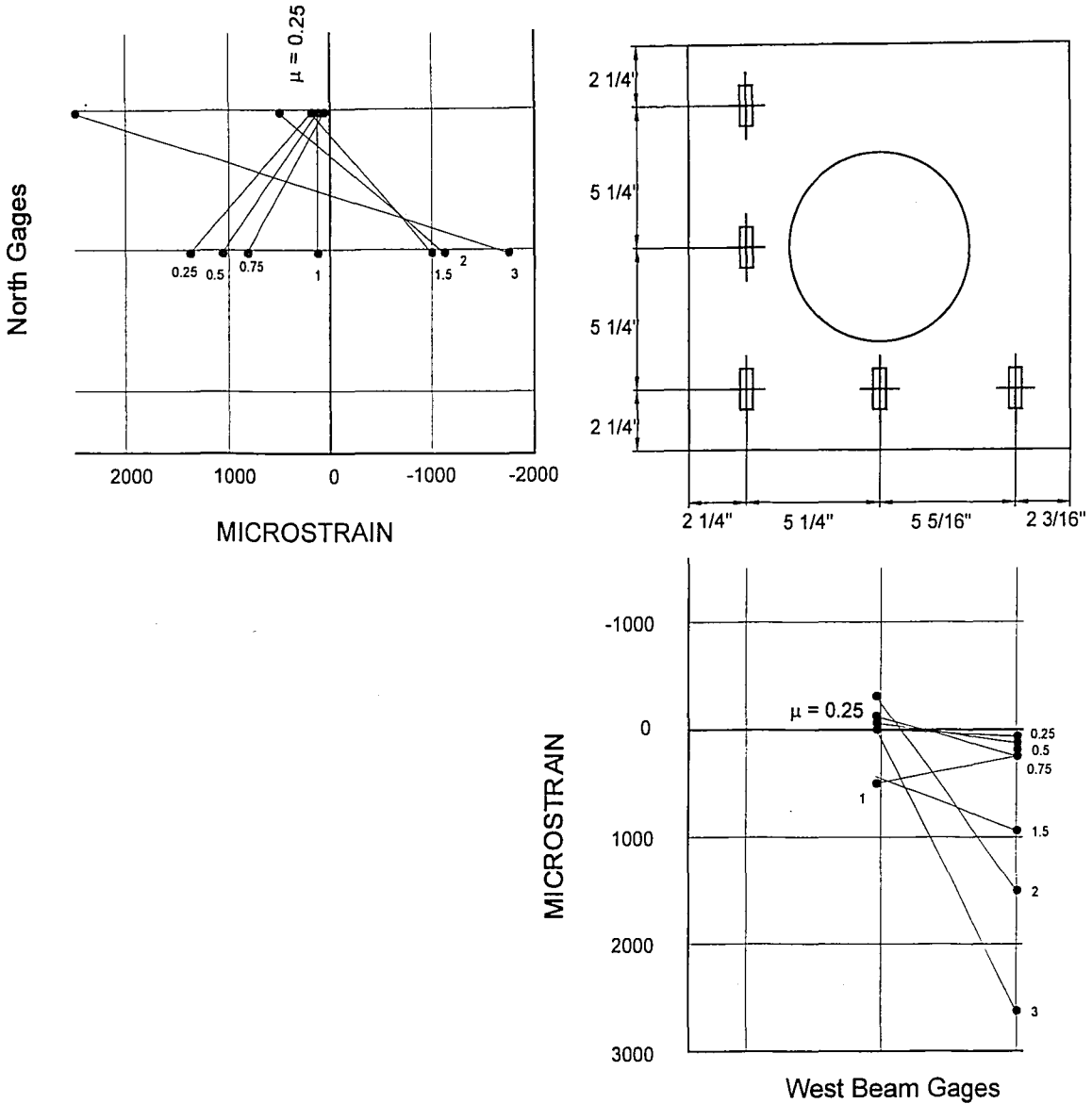

Figure 4.32 - Stain in Top Diaphragm (Push Direction)
Specimen 1

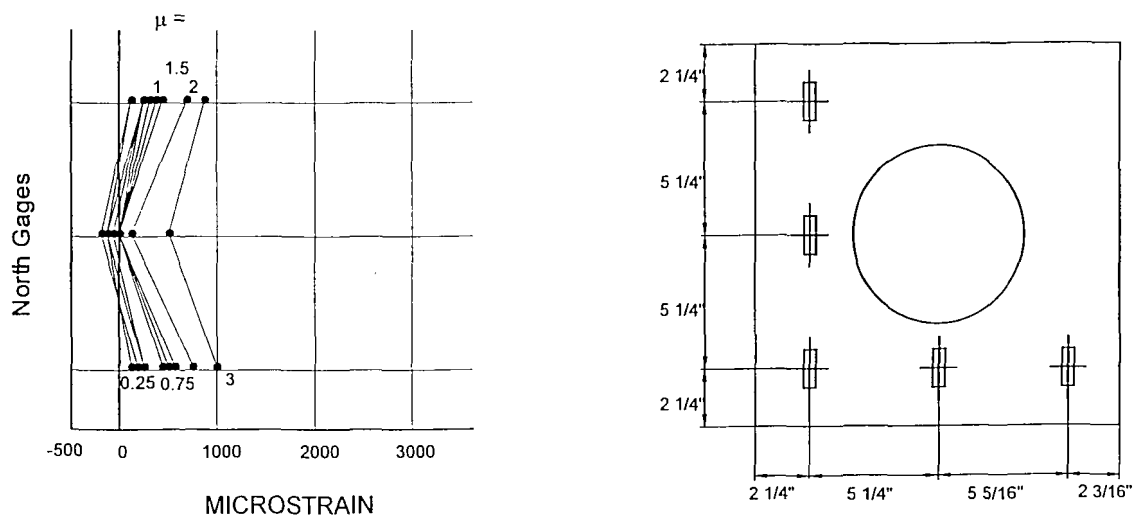

Figure 4.33 - Strain in Bottom Diaphragm (Pull - Direction), Specimen 1

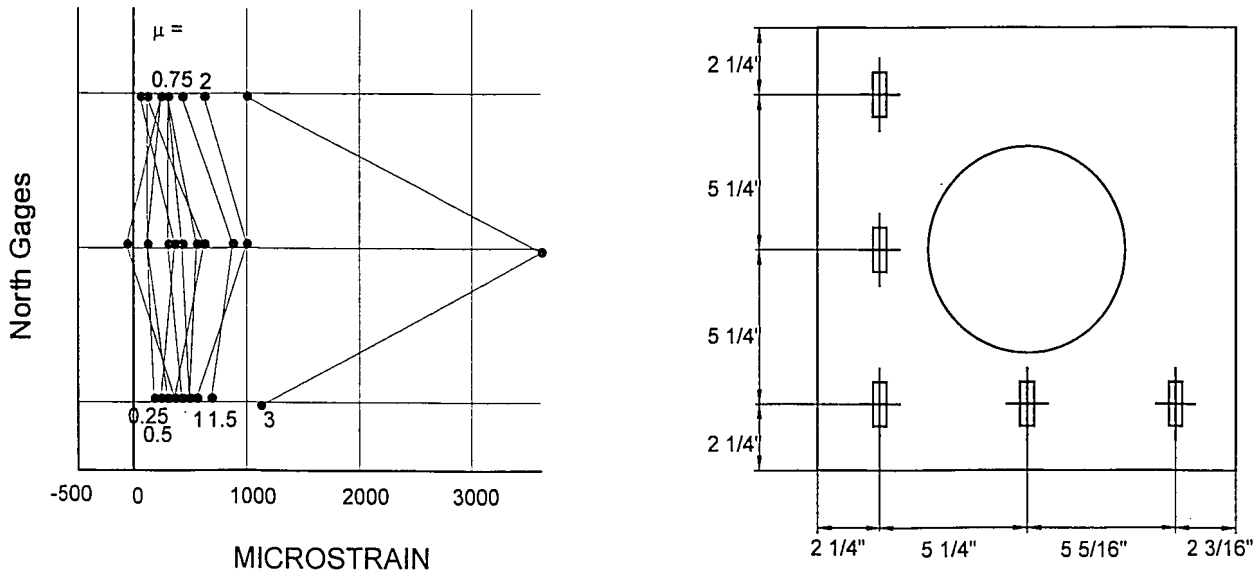

Figure 4.34 - Strain in Bottom Diaphragm (Push - Direction), Specimen 1

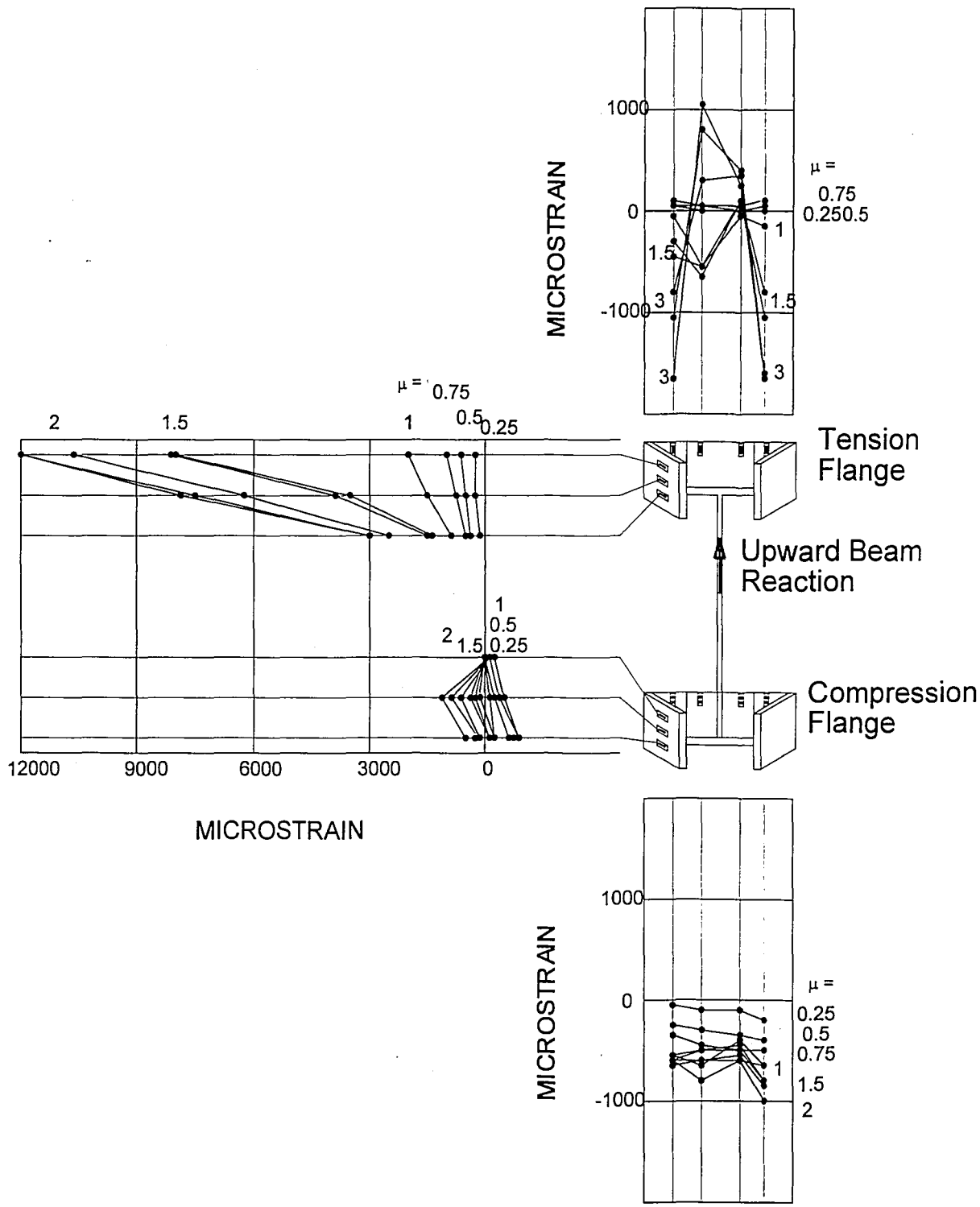

Figure 4.35 - Strain in Structural Tees (Pull - Direction)
Specimen 3

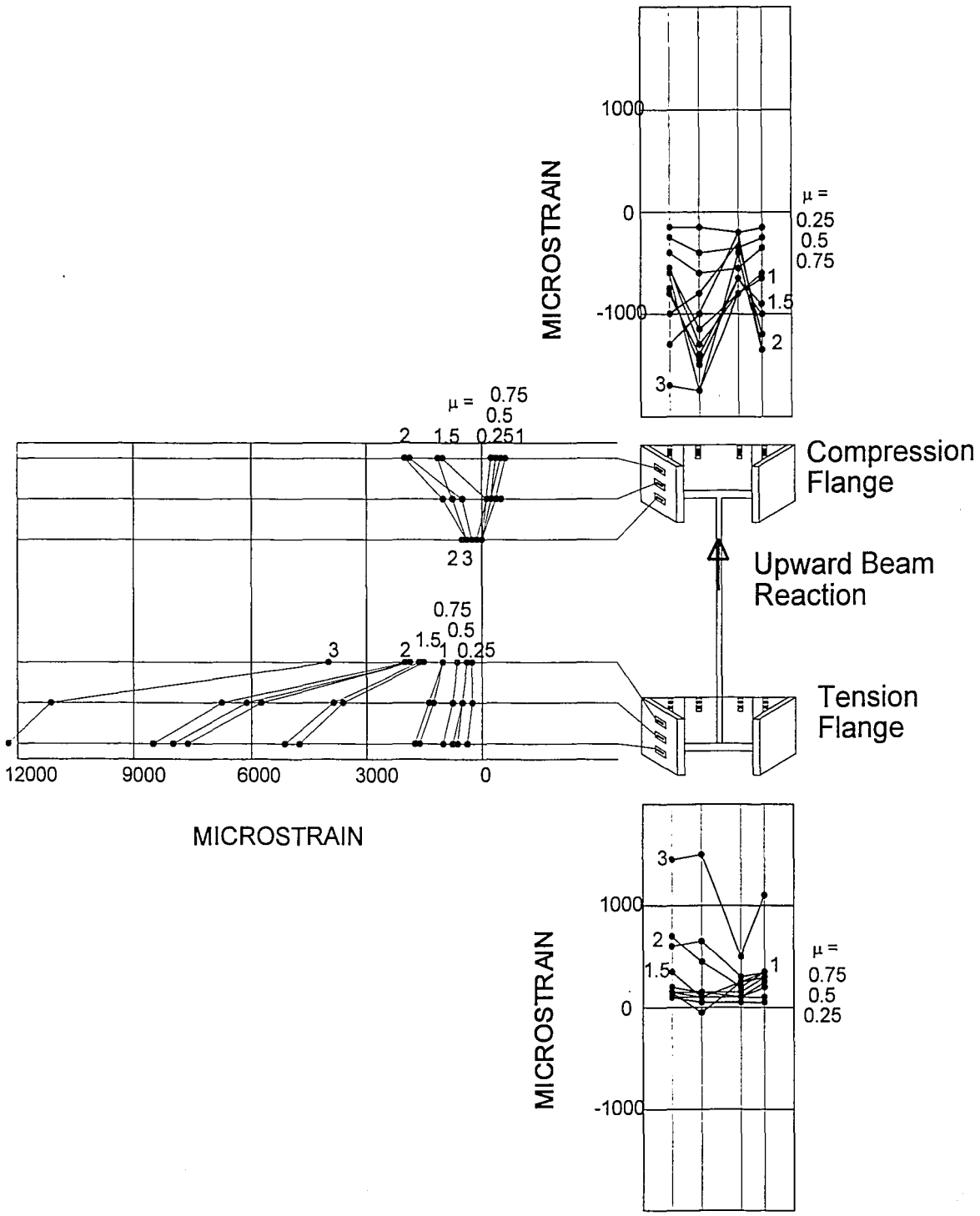

Figure 4.35 - Strain in Structural Tees (Pull - Direction)
Specimen 3

Chapter 5

Summary and Conclusions

5.1 Summary

This study consisted of testing two full scale concrete filled structural tube composite columns to wide flange beam moment connections with diaphragms under axial and lateral cyclic loading. Test specimens were designed to simulate as accurately as possible the physical domain near the connection between an interior column and two adjacent floor beams in a 20 story perimeter moment resisting frame. The experimental subassembly consisted of a CFT column taken from the center of the ninth floor extending to the center of the tenth floor at the inflection points, and the ninth floor beams extending from each face of the CFT column to the center of the prototype span. The axial (P), panel zone shear (V), and flexural (M) forces developed in the prototype member were determined and each test specimen was designed based upon a full scaling of the prototype member's forces.

Each subassemblage consisted of 16x16x1/2 structural steel tube filled with 6300 psi concrete, and two 12 foot long W24x62 beams on each side. Two different connection details were tested on the basis of assessing the effectiveness of the force transfer from the flanges of the beams through the panel zone. One connection (Specimen 1) was stiffened with an interior

diaphragm while the other connection (Specimen 2) had an exterior diaphragm. The experimental results from each test were analyzed for their strength, stiffness, ductility and failure mode. The combined force state in the test setup was introduced by subjecting each specimen to an axial load of 460 kips, representing the total load due to gravity and seismic overturning force effects, and a cyclically applied lateral force (H), simulating the lateral seismic loading.

5.2 Conclusions

Based on the analysis of the experimental results, the following conclusions are given:

(1.) Both of the specimens with interior or exterior diaphragms appear to have adequate cyclic strength and ductility when the yielding is designed to occur primarily in the beams.

(2.) The beams dissipated most of the energy in accordance with the weak beam - strong column theory by which both test specimens were designed.

(3.) The concrete contributed to the shear capacity of the panel zone.

(4.) The maximum beam moment for both specimens ranged between 1.16 M_p and 1.28 M_p.

(5.) The exterior diaphragm (Specimen 3) appears to be effective in developing the beam's capacity and inelastic rotation (θ_p).

(6.) Strain concentrations can develop in the connection elements which transfer the beam flange forces into the connection. These strain concentrations can lead to beam flange fracture and a deterioration in a beam's rotational capacity..

(7.) The initial elastic lateral stiffness of the CFT column is estimated reasonably well by the transformed section for lateral displacements corresponding to an inter-story drift not exceeding 0.3% to 0.6% of the story height.

(8.) In the weak beam - strong column design, the beams will account for most of the interstory drift, developing inelastic deformations.

References

(1.) ACI Committee 318, "Building Code Requirements for Reinforced Concrete (ACI 318-89)," *American Concrete Institute*, Detroit Michigan, Revised 1992.

(2.) American Institute of Steel Construction, "Load and Resistance Factor Design," *Manual of Steel Construction,* AISC Inc., Chicago, Illinois, 1992.

(3.) American Society for Testing and Materials, Standard Methods for Tension Testing of Metallic Materials, ASTM Designation E8-91, Philadelphia, 1991.

(4.) American Society for Testing and Materials, Standard Methods for Compression Testing of Cylindrical Concrete Specimens, ASTM Designation C39-72, Philadelphia, 1991.

(5.) Architectural Institute of Japan, "AIJ Standards for Structural Calculation of Steel Reinforced Concrete Structures," 1987.

(6.) Building Seismic Safety Council, "1991 National Earthquake Hazards Reduction Program (NEHRP)," Recommended Provisions for the Development of Seismic Regulations for New Buildings, Washington, DC, 1991.

(7.) Endoh, K., Yamamoto, I., Araki, S., Yagi, S., "Design and Construction of a 37 Storied Condominium with Concrete Filled Tubular Columns," Proceedings of the Third International Conference on Steel - Concrete Composite Structures, Fukuoka, Japan, 1991.

(8.) Furlong, R., "Strength of Steel-Encased Concrete Beam Columns," ASCE Journal of Structural Engineering, Vol. 93, No. ST5, 1967.

(9.) Furlong, R., "Design of Steel-Encased Concrete Beam Columns," ASCE Journal of Structural Engineering, Vol. 94, No. ST1, 1968.

(10.) Giroux, Y., Picard, A., "Rigid Framing Connections for Tubular Columns," Canadian Journal of Civil Engineering, Vol. 4, No. 2, June 1977.

(11.) Kanatani, H., Tabuchi, M., Kamba, T., Hsiaolien, J., Ishikawa, M., "A Study on Concrete Filled RHS Column to H-Beam Connections Fabricated With HT Bolts in Rigid Frames," Composite Construction in Steel and Concrete, Engineering Foundation, Henniker, New Hampshire, 1985.

(12.) Kato, B., Kimura, M., Ohta, H., Mizutani, N., "Connection of Beam Flange to Concrete-Filled Tubular Column," Proceeding - Composite Construction in Steel and Concrete II, Engineering Foundation, Potasi, Missouri, 1992.

(13.) Kimura, M., Ohta, H., Ishida, K., "Study On Influence of Replenishment on Mechanical Behavior of Concrete Filled Square Steel Columns With Inner Open Diaphragms," Proceedings of the Third International Conference on Steel-Concrete Composite Structures, Association for International Cooperation and Research on Steel Composite Structures, Fukuoka, Japan, 1991.

(14.) Krawinkler, H., Bertero, V., Popov, E., "Inelastic Behavior of Steel Beam-To-Column Subasseblages," Report to American Iron and Steel Institute, University of California, Berkeley, Califonia 1971.

(15.) Linderman, R., Anderson, J., "Steel Beam to Box Column Connections," Proceedings of Fourth U.S. National Conference on Earthquake Engineering, Palm Springs, California, May, 1990.

(16.) Matsui, C., Keira, K., Kowano, A., Tsuda, K., Sakai, J., "Development of Concrete Filled Steel Tubular Structures With Inner Ribs, "Proceedings of the third International Conference on Steel-Concrete Structures, Association for International Cooperation and research in Steel-Concrete Composite Structures, Fukuoka, Japan, 1991.

(17.) Matsui, C., "Local Buckling of Concrete Filled Steel Square Tubular columns," Composite Conference

(18.) Morino, S., Kawaguchi, J., Yasuzaki, C., Kanazawa, S., "Behavior of Concrete Filled Steel tubular Three Dimensional Subassemblages," Proceeding - Composite Construction in Steel and Concrete II, Engineering Foundation, Potosi, Missouri, 1992.

(19.) Packer, J., "Concrete-Filled HSS Connections", Journal of Structural Engineering, Vol. 121, No. 3, March 1995.

(20.) Picard, A., Giroux, Y., "Moment Connections between Wide Flange Beams and Square Tubular Columns," Canadian Journal of Civil Engineering, Vol. 3, No. 2, June 1976.

(21.) Ricles, J., Paboojian, S., "Seismic Performance of Composite Beam-Columns, "ATLSS Engineering Research Center, ATLSS Report No. 93-01, Lehigh University, Bethlehem, PA, January 1993.

(22.) Ricles, J., Suh, S., Sooi, T.K., Lu, L., "Concrete Filled Tube Panel Zone Under Shear," ATLSS Engineering Research Center, Lehigh University, Bethlehem, PA, 1994.

(23.) Shakie, K., "Composite Columns in Multi-Story Buildings," Proceeding - Composite Construction in Steel and Concrete, Engineering Foundation, Potosi, Missouri, 1987.

(24.) Tabuchi, M., Kanatani, H., Kamba, T., "Behavior of Tubular column to H-Beam Connections Under Seismic Loading," Proceedings of the Ninth World Conference on Earthquake Engineering, Tokyo, Japan, August, 1988.

(25.) Ting, L., Shanmugam, N., Lee, S., "Design of I-Beam to Box-Column Connections Stiffened Externally," AISC Engineering Journal, Vol. 30, No. 4, 4th Quarter, 1993.

(26.) Tsai, K.C., Lin, K.C., Liu, M.C., "Seismic behavior of Steel Beam-to-Box Column Connections," Earthquake Engineering, Tenth World Conference, Balkema, Rotterrdam, 1992.

(27.) Tomi, M., Yoshimura, K., Morishita, Y., "Experimental Studies on Concrete Filled Steel Tubular Stub Columns Under Concentric Loading," Proceeding of the International Colloquium on Stability of Structures Under Static and Dynamic Loads, SSRC/ASCE, Washington D.C., March 1977.

(28.) Yokoyama, Y., Morita, K., Kowamata, Y., Matsumura, H., "Structural Behaviors of Steel-Beam to concrete-Filled Square Tube Column Connections Reinforced With Inner Ring Stiffener," Proceedings of the Third International Conference on Steel-Concrete Composite Structures, Association for International Cooperation and Research on Steel-Concrete Composite Structures, Fukuoka, Japan, 1991.

(29.) Yura, J., Yarimci, E., Lu, L. "Techniques for Testing Structures Permitted to Sway," Experimental Mechanics, Vol. 7, No. 8, August 1967.

(30.) Zhijun, L., and Shanzhang, Y., "Experimental Study on Stiffener Rings Used for Beam-to-Concrete Filled Steel Tubular Column Joints," Proceedings of the Third International Conference on Steel-Concrete Composite Structures, Association for International Cooperation and Research in Steel-Concrete Composite Structures, Japan, 1991.

VITA

The author was born in Ridgewood, New Jersey on June 30, 1972. He is the only son of Garret John and Carolyn Vermaas. The author attended Eastern Christian High School in North Haledon, New Jersey. He received a Bachelor of Science in Civil Engineering from Lehigh University in May of 1994. There he was a member of Omicron Delta Kappa honor society, the president of Chi Epsilon Honor Society and also on the Dean's List. In August of 1994 he began working toward a Master of Science degree at Lehigh University at which time he worked at the Advanced Technology for Large Structural Systems (ATLSS) research center under Dr. Jim Ricles and Dr. T.K. Sooi and was a member of the Fritz Engineering Research Society. In July of 1995 the author started his career working for W. Thomas Zieman, P.E. in Fort Lee, New Jersey designing the rehabilitation phases for many large projects in New York City. The author is a member of the American Society of Civil Engineers, American Institute of Steel Construction, Nation Society of Professional Engineers, and the American Concrete Institute. The author now plans to work towards his Professional Engineering License in less than three years.

END OF TITLE